Application of MRI Connectivity in Stereotactic Functional Neurosurgery

Harith Akram

Thesis submitted for the degree of PhD in Neurosurgery

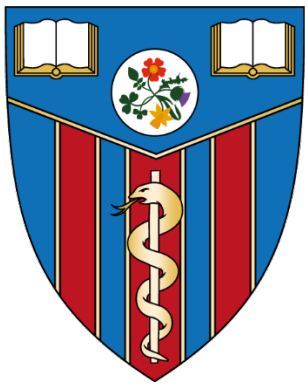

UCL Institute of Neurology

University College London

2018

I, Harith Akram, confirm that the work presented in this thesis is my own. Where information has been derived from other sources, I confirm that this has been indicated in the thesis.

MPhil / PhD programme:

UCL Institute of Neurology, Queen Square, London

Primary supervisor: Ludvic Zrinzo PhD FRCS

Secondary supervisors: Timothy Behrens PhD, John Ashburner PhD

Funding:

This work was funded by a grant from the Brain Research Trust (BRT) and supported by researchers at the National Institute for Health Research University College London Hospitals Biomedical Research Centre. The Unit of Functional Neurosurgery, UCL Institute of Neurology, Queen Square, London is also supported by the Parkinson's Appeal and the Sainsbury Monument Trust. The Wellcome Trust Centre for Neuroimaging is supported by core funding from the Wellcome Trust (grant reference 091593/Z/10/Z).

Author:

Harith Akram MBChB FRCS (Neuro.Surg)

Specialty Trainee in Neurosurgery

1) Unit of Functional Neurosurgery

Sobell Department of Motor Neuroscience and Movement Disorders

UCL Institute of Neurology, University College London

2) Victor Horsley Department of Neurosurgery

The National Hospital for Neurology and Neurosurgery

University College London Hospitals NHS Foundation Trust

Box 146, 2nd Floor, 33 Queen Square, London WC1N 3BG

Tel: +44(0)2031080023; Fax: +44(0)2031080142

Email: harith.akram.12@ucl.ac.uk

To my loving wife, Rebecca

and my children Francis and Noëlle

“If the human brain was so simple

that we could understand it,

we would be so simple that we couldn’t”

Emerson M. Pugh (1929 -)

Abstract

This thesis examines potential applications of advanced MRI-connectivity studies in stereotactic functional neurosurgery. Several new analysis methodologies are employed to: (1) build predictive models of DBS surgery outcome; (2) refine the surgical target and (3) help build a better understanding of the pathogenesis of the treated conditions and the mechanism of action of DBS therapy.

The experimental component is divided into three main parts focusing on the following pathologies: **(1)** Parkinson's disease (PD), **(2)** tremor and **(3)** trigeminal autonomic cephalalgias (TAC).

Section I: In the first experiment (chapter 3), resting state fMRI was used to find radiological biomarkers predictive of response to L-DOPA in 19 patients undergoing subthalamic nucleus (STN) DBS for PD. A greater improvement in UPDRS-III scores following L-DOPA administration was characterized by higher resting state functional connectivity (fcMRI) between the prefrontal cortex and the striatum ($p=0.001$) and lower fcMRI between the pallidum ($p=0.001$), subthalamic nucleus ($p=0.003$) and the paracentral lobule.

In the second experiment (chapter 4), structural (diffusion) connectivity was used to map out the influence of the hyperdirect pathways on outcome and identify the therapeutic 'sweet spots' in twenty PD patients undergoing STN-DBS. Clusters corresponding to maximum improvement in symptoms were in the posterior, superior and lateral portion of the STN. Greater connectivity to the primary motor area, supplementary motor area and prefrontal cortex was predictive of higher improvement in tremor, bradykinesia and rigidity, and rigidity respectively.

The third experiment (chapter 5) examined pyramidal tract (PT) activation in 20 PD patients with STN-DBS. Volume of tissue activation (VTA) around DBS contacts were modelled in relation to the PT. VTA/ PT overlap predicted EMG activation thresholds.

Sections II: Pilot data suggest that probabilistic tractography techniques can be used to segment the ventrolateral (VL) and ventroposterior (VP) thalamus based on cortical and cerebellar connectivity in nine patients who underwent thalamic DBS for tremor (chapter 6). The thalamic area, best representing the ventrointermedialis nucleus (VIM), was connected to the contralateral dentate cerebellar nucleus. Streamlines corresponding to the dentato-rubro-thalamic tract (DRT) connected M1 to the contralateral dentate nucleus via the dentato-thalamic area. Good response was seen when the active contact's VTA was in the thalamic area with the highest connectivity to the contralateral dentate nucleus.
Section III: The efficacy and safety of DBS in the ventral tegmental area (VTa) in the treatment of chronic cluster headache (CH) and short lasting unilateral neuralgiform headache attacks (SUNA) were examined (chapters 7 and 8). The optimum stimulation site within the VTa that best controls symptoms was explored (chapter 9). The average responders' deep brain stimulation activation volume lay on the trigemino-hypothalamic tract, connecting the trigeminal system and other nociceptive brainstem nuclei, with the hypothalamus, and the prefrontal and mesial temporal areas.

Acknowledgments

Spike Milligan received his lifetime achievement award in 1994 at the British Comedy Awards and famously declared: “I am not going to thank anybody, because I did it all on my own”. I certainly am in no position to adopt a similar stance. The work presented here is the product of endless collaboration and kind, constructive mentoring with selfless dedication by many a colleague who gave their time and effort to see it through. Moreover, the role luck played in all of this is not to be undervalued. As a senior house officer in neurosurgery ten years ago, I crossed paths with a recently appointed junior consultant in functional neurosurgery at the National Hospital for Neurology and Neurosurgery, Mr Ludvic Zrinzo. Ludvic Zrinzo’s dedication and pursuit of knowledge to better help his patients was contagious. I was fortunate to have him as a mentor, during my training in neurosurgery and later as a supervisor embarking on this work. I am also endlessly indebted to Ludvic Zrinzo’s mentor, Professor Marwan Hariz for his infinite encouragement and valuable advice, not to mention his never-ending support, even though he has often overestimated my aptitudes.

I must also thank Professor Timothy Behrens. Once again, chance played a part in our meeting in a Queen Square pub, after which he agreed to supervise this work. Professor Behrens along with Professor John Ashburner, my third supervisor, have been invaluable in the realization of this work and I am immensely thankful to them for all their help and for putting up with me, a clinician, for the past four years, which must have been hard at times.

I am grateful to my collaborators within the Unit of Functional Neurosurgery: Professor Patricia Limousin, Professor Thomas Foltynie, Professor Marjan Jahanshahi, Mr Joseph Candelario, Ms Catherine Milabo, Ms Maricel Salazar, Ms Linda Taib, Dr Dejan Georgiev, Dr Philipp Mahlknecht, Mr Jonathan Hyam and Dr Viswas Dayal. I extend my thanks to Dr Enrico Devita, Dr Mark White, Dr John Thornton, Dr Chris Lambert, Dr Antoine Lutti, Professor Nikolas Weiskoff and Professor Tarek Yousry in the UCL institute of Neurology.

I must also thank my collaborators in the Headache group at the National Hospital for Neurology and Neurosurgery: Dr Sarah Miller, Ms Susanne Lagrata and Dr Manjit Matharu.

I had the privilege of collaborating with numerous colleagues outside UCL: Dr Stamatios N. Sotiropoulos, Dr Saad Jbabdi and Dr Moises Hernandez Fernandez, Centre for Functional MRI of the Brain (FMRIB), John Radcliffe Hospital, Oxford; and Dr Rutger Nijlunsing, Dr Jonas Roothans and Dr Mattias Åström, Medtronic Eindhoven Design Center, The Netherlands.

I am most grateful to the Brain Research Trust (BRT) for their generous support of this work. The Unit of Functional Neurosurgery, UCL Institute of Neurology, Queen Square, London is also supported by the Parkinson's Appeal and the Sainsbury Monument Trust.

A special thank you goes to all the patients and families who found the strength to participate in clinical research despite their journey through difficult times.

I would like to thank my father, who gave me a set of screw drivers at a young age and encouraged me take my toys apart and put them back together again. My mother who has always smothered me with kindness and love. Most of all, I would like to thank my wife Rebecca, who has put up with me despite all my flaws – without her continuous support, kind-heartedness and motivation I would never have been able to complete this work. I dedicate this thesis to Rebecca, our son Francis and to our daughter Noëlle, who make it all worthwhile.

Table of Contents

List of Tables and Figures

Abbreviations

AC	Anterior commissure
AC-PC	Anterior commissure – posterior commissure
ALIC	Anterior limb of the internal capsule
AMT	Active motor thresholds
ART	Artifact Detection Tools
ASCII	American standard code for information interchange
BDI-II	Beck Depression Inventory II Score
BEDPOSTX	Bayesian Estimation of Diffusion Parameters Obtained using Sampling Techniques X
BET	Brain extraction tool
BG	Basal ganglia
BIS	Barratt impulsiveness scale
BOLD	Blood oxygen level dependent
CB	Connectivity based
CBT	Corticobulbar tract
CCH	Chronic cluster headache
CH	Cluster headache
CI	Confidence Interval
CompCor	Component-based noise correction method
CON	Connectivity
CPU	Central processing unit
CSF	Cerebro-spinal fluid
CSL	Computerised Speech Lab
CST	Corticospinal tract
CT	Computerized tomography
cZI	Caudal Zona incerta
DBS	Deep brain stimulation
DCM	Dynamic causal modelling
DF	Degrees of freedom
DICOM	Digital Imaging and Communications in Medicine
DLPFC	Dorso-lateral prefrontal cortex
DoF	Degrees of freedom

DRS	Dyskinesia Rating Scale
DRT	Dentato-rubro-thalamic
DT	Deterministic tractography
DWI	Diffusion weighted imaging
EMG	Electromyography
EPI	Echo Planar Imaging
EQ-5D	EuroQoL Score
EV	Explanatory variable
FA	Fractional anisotropy
fcMRI	Resting state functional connectivity
FDI	First dorsal interosseous
FDR	False discovery rate
FLIRT	FMRIB's linear image registration tool
fMRI	Functional MRI
FMRIB	Oxford Centre for Functional MRI of the Brain
FNIRT	FMRIB's non-linear image registration tool
FOG-Q	Freezing of gait questionnaire
FoV	Field of view
FSL	FMRIB’s software library
TS	Gilles de la Tourette syndrome
GLM	General linear model
GPe	Globus pallidus externus
GPGPU	General processing over GPU
GPi	globus pallidus internus
GPU	General processing unit
HAD-A	Hospital Anxiety and Depression Score Anxiety component
HAD-D	Hospital Anxiety and Depression Score Depression component
HADS	Hospital anxiety and depression scale
HAL	Headache load
HARDI	High angular resolution diffusion imaging
HDR	Hameodynamic response
HFS	High frequency stimulation
HIT-6	Headache impact 6
ICA	Independent component analysis
ICHD3-beta	International Classification of Headache Disorders 3-beta
IMPACT	Initiative on Methods, Measurement, and Pain Assessment in Clinical Trials

IPG	Implantable pulse generator
IQR	Interquartile range
LC	Levodopa challenge
LEDD	L-DOPA equivalent daily dose
LID	Levodopa induced dyskinesia
M1	Primary motor cortex
MCP	Mid-commissural point
MD	Mediodorsal thalamus
MEEPI	Multi-echo echo planar imaging
MER	Microelectrode recording
MIDAS	Migraine disability assessment score
MMS	Mini-mental score
MNI	Montreal Neurological Institute
MPM	Multi-parameter mapping
MPRAGE	Magnetization-prepared rapid gradient-echo
MPTP	1-methyl-4-phenyl-1,2,3,6-tetrahydropyridine
MRI	Magnetic resonance imaging
MT	Magnetization transfer
NAc	Nucleus accumbens
NBM	Nucleus basalis of Meynert
NHNN	National Hospital for Neurology and Neurosurgery
NHP	Non-human primate
NHS	National Health Service
NIfTI	Neuroimaging Informatics Technology Initiative
OCD	Obsessive compulsive disorder
ONS	Occipital nerve stimulation
OOr	Orbicularis Oris
PAG	Periaqueductal grey
PC	Posterior Commissure
PD	Parkinson's disease
PDQ-39	Parkinson's disease specific quality of life questionnaire
PDRP	Parkinson's disease related covariance pattern
PET	Positron emission tomography
PFC	Prefrontal cortex
PH	Posterior hypothalamus
PMA	Premotor area

PMC	Premotor cortex
PPC	Posterior parietal cortex
PPN	Pedunculopontine nucleus
PT	Probabilistic tractography
PTr	Pyramidal tract
PVG	Periventricular grey
PW	Pulse width
RMT	Resting motor thresholds
RoI	Region of interest
RsfMRI	Resting state functional magnetic resonance imaging
S1	Primary sensory cortex
SGCC	Subgenual anterior cingulate cortex
SAR	Specific absorption rate
SCCwm	subcallosal cingulate white matter
SD	Standard deviation
SE	Standard error
SF36	Short-Form 36 Score
SMA	Supplementary motor area
SN	Substantia nigra
SNR	Signal-to-noise ratio
SNr	Substantia nigra pars reticulata
SPECTS	Single Photon Emission Computed Tomography
SPG	Sphenopalatine ganglion
SSEPI	Single-shot Echo Planar Imaging
SSN	Superior salivatory nucleus
STN	Subthalamic nucleus
SUNA	Short lasting unilateral neuralgiform headache attacks with autonomic features
SUNCT	Short lasting unilateral neuralgiform headache attacks with conjunctival injection and tearing
TAC	Trigeminal autonomic cephalalgia
TCC	Trigemino-cervical complex
TE	Echo time
TETRAS	The essential tremor rating assessment scale
TFCE	Threshold-free cluster enhancement
THT	Trigemino-hypothalamic Tract
TMS	Transcranial magnetic stimulation

TR	Repeat time
TRG	Tremor research group
UPDRS	Unified Parkinson’s disease rating scale
UPDRS III	Unified Parkinson's disease rating scale motor score.
VAIC	Ventral anterior internal capsule
VBM	Voxel based morphometry
VIM	Ventrointermedialis
VL	Ventral lateral
VoP	Ventral oralis posterior
VP	Ventral posterior
VRS	Verbal rating scale
VTA	Volume of tissue activated
VTa	Ventral tegmental area
Y-BOCS	Yale-Brown obsessive-compulsive scale
ZI	Zona incerta
cZI	Caudal Zona incerta

Publications

The publications marked with an asterisk (*) are derived from work presented in the thesis. The remaining publications describe other collaborative work undertaken during the period of PhD study:

[1]* H. Akram, V. Dayal, P. Mahlknecht, D. Georgiev, J. Hyam, T. Foltynie, P. Limousin, E. De Vita, M. Jahanshahi, J. Ashburner, T. Behrens, M. Hariz, and L. Zrinzo, “Connectivity derived thalamic segmentation in deep brain stimulation for tremor.,” *Neuroimage Clin*, vol. 18, pp. 130–142, 2018.

[2] J. Gratwicke, L. Zrinzo, J. Kahan, A. Peters, M. Beigi, H. Akram, J. Hyam, A. Oswal, B. Day, L. Mancini, J. Thornton, T. Yousry, P. Limousin, M. Hariz, M. Jahanshahi, and T. Foltynie, “Bilateral Deep Brain Stimulation of the Nucleus Basalis of Meynert for Parkinson Disease Dementia: A Randomized Clinical Trial.,” *JAMA Neurol*, Dec. 2017.

[3]* H. Akram, S. Miller, S. Lagrata, M. Hariz, J. Ashburner, T. Behrens, M. Matharu, and L. Zrinzo, “Optimal deep brain stimulation site and target connectivity for chronic cluster headache.,” Neurology, pp. 10.1212/WNL.0000000000004646, Oct. 2017.

[4]* H. Akram, S. N. Sotiropoulos, S. Jbabdi, D. Georgiev, P. Mahlknecht, J. Hyam, T. Foltynie, P. Limousin, E. De Vita, M. Jahanshahi, M. Hariz, J. Ashburner, T. Behrens, and L. Zrinzo, “Subthalamic deep brain stimulation sweet spots and hyperdirect cortical connectivity in Parkinson's disease.,” NeuroImage, vol. 158, pp. 332–345, Jul. 2017.

[5]* P. Mahlknecht, H. Akram, D. Georgiev, E. Tripoliti, J. Candelario, A. Zacharia, L. Zrinzo, J. Hyam, M. Hariz, T. Foltynie, J. C. Rothwell, and P. Limousin, “Pyramidal tract activation due to subthalamic deep brain stimulation in Parkinson's disease.,” Mov Disord., vol. 339, no. 3, p. 1105, Jun. 2017.

[6]* H. Akram, C. Wu, J. Hyam, T. Foltynie, P. Limousin, E. De Vita, T. Yousry, M. Jahanshahi, M. Hariz, T. Behrens, J. Ashburner, and L. Zrinzo, “l-Dopa responsiveness is associated with distinctive connectivity patterns in advanced Parkinson's disease.,” Mov Disord., vol. 32, no. 6, pp. 874–883, Jun. 2017.

[7] B. C. M. van Wijk, A. Pogosyan, M. I. Hariz, H. Akram, T. Foltynie, P. Limousin, A. Horn, S. Ewert, P. Brown, and V. Litvak, “Localization of beta and high-frequency oscillations within the subthalamic nucleus region,” Neuroimage Clin, vol. 16, pp. 175–183, 2017.

[8] H. A. Roy, D. Pond, C. Roy, B. Forrow, T. Foltynie, L. Zrinzo, H. Akram, T. Z. Aziz, J. J. FitzGerald, and A. L. Green, “Effects of pedunculopontine nucleus stimulation on human bladder function.,” Neurourol. Urodyn., vol. 55, p. 118, Jun. 2017.

[9] L. Akbarian-Tefaghi, H. Akram, J. Johansson, L. Zrinzo, Z. Kefalopoulou, P. Limousin, E. Joyce, M. Hariz, K. Wårdell, and T. Foltynie, “Refining the Deep Brain Stimulation Target within the Limbic Globus Pallidus Internus for Tourette Syndrome,” Stereotact Funct Neurosurg, vol. 95, no. 4, pp. 251–258, 2017.

[10]* S. Miller, H. Akram, S. Lagrata, M. Hariz, L. Zrinzo, and M. Matharu, “Ventral tegmental area deep brain stimulation in refractory short-lasting unilateral neuralgiform headache attacks.,” Brain, vol. 139, no. 10, pp. 2631–2640, Oct. 2016.

[11] J. Pepper, L. Meliak, H. Akram, J. Hyam, C. Milabo, J. Candelario, T. Foltynie, P. Limousin, C. Curtis, M. Hariz, and L. Zrinzo, “Changing of the guard: reducing infection when replacing neural pacemakers,” Journal of Neurosurgery, pp. 1–8, Jun. 2016.

[12]* H. Akram, S. Miller, S. Lagrata, J. Hyam, M. Jahanshahi, M. Hariz, M. Matharu, and L. Zrinzo, “Ventral tegmental area deep brain stimulation for refractory chronic cluster headache.,” Neurology, vol. 86, no. 18, pp. 1676–1682, May 2016.

[13] A. Anzak, H. Tan, A. Pogosyan, S. Khan, S. Javed, S. S. Gill, K. Ashkan, H. Akram, T. Foltynie, P. Limousin, L. Zrinzo, A. L. Green, T. Aziz, and P. Brown, “Subcortical

evoked activity and motor enhancement in Parkinson's disease," Experimental Neurology, vol. 277, pp. 19–26, Mar. 2016.

[14] R. M. deSouza, H. Akram, H. L. Low, A. L. Green, K. Ashkan, and A. H. V. Schapira, "The timing of deep brain stimulation for Parkinson disease in the UK from 1997 to 2012.," Eur J Neurol, vol. 22, no. 10, pp. 1415–1417, Oct. 2015.

[15] J. A. Hyam, H. Akram, T. Foltynie, P. Limousin, M. Hariz, and L. Zrinzo, "What You See Is What You Get: Lead Location Within Deep Brain Structures Is Accurately Depicted by Stereotactic Magnetic Resonance Imaging.," Neurosurgery, vol. 11, pp. 412–9– discussion 419, Sep. 2015.

[16] A. Angeli, H. Akram, A. Zacharia, P. Limousin, M. Hariz, L. Zrinzo, and T. Foltynie, "Varying time-course of effects of high frequency stimulation of sub-regions of the globus pallidus in patients with parkinson's disease.," Parkinsonism and Related Disorders, vol. 21, no. 6, pp. 597–602, Jun. 2015.

[17] Z. Kefalopoulou, L. Zrinzo, M. Jahanshahi, J. Candelario, C. Milabo, M. Beigi, H. Akram, J. Hyam, J. Clayton, L. Kass-Iliyya, M. Silverdale, J. Evans, P. Limousin, M. Hariz, E. Joyce, and T. Foltynie, "Bilateral globus pallidus stimulation for severe Tourette's syndrome: a double-blind, randomised crossover trial.," The Lancet Neurology, vol. 14, no. 6, pp. 595–605, Jun. 2015.

[18] F. A. Wilkes, H. Akram, J. A. Hyam, N. D. Kitchen, M. I. Hariz, and L. Zrinzo, "Publication productivity of neurosurgeons in Great Britain and Ireland.," Journal of Neurosurgery, vol. 122, no. 4, pp. 948–954, Apr. 2015.

[19] H. Akram and M. Murphy, "Brainstem cavernous malformation," in Challenging Concepts in Neurosurgery, Oxford University Press, 2015, pp. 171–176.

[20] H. Akram, P. Limousin, J. Hyam, M. I. Hariz, and L. Zrinzo, "Aim for the Suprasternal Notch: Technical Note to Avoid Bowstringing after Deep Brain Stimulation.," Stereotact Funct Neurosurg, vol. 93, no. 4, pp. 227–230, 2015.

[21] L. Zrinzo, H. Akram, and M. Hariz, “Comment on "appropriate MRI sequences are required to accurately determine lead location after deep brain stimulation surgery".,” J Clin Neurosci, vol. 21, no. 12, pp. 2257–2258, Dec. 2014.

[22] I. Aviles-Olmos, Z. Kefalopoulou, E. Tripoliti, J. Candelario, H. Akram, I. Martinez-Torres, M. Jahanshahi, T. Foltynie, M. Hariz, L. Zrinzo, and P. Limousin, “Long-term outcome of subthalamic nucleus deep brain stimulation for Parkinson's disease using an MRI-guided and MRI-verified approach.,” Journal of Neurology, Neurosurgery & Psychiatry, vol. 85, no. 12, pp. 1419–1425, Dec. 2014.

[23] S. Sciacca, J. S. Smith, H. Akram, A. Asim, M. Matharu, and L. Watkins, “Rechargeable occipital nerve stimulator systems: a patient satisfaction study.,” Br J Neurosurg, vol. 28, no. 5, pp. 645–649, Oct. 2014.

[24] J. C. Clark, H. Akram, and R. F. Spetzler, “Fellowship training in the United States and Europe.,” WNEU, vol. 82, no. 3, pp. 350–351, Sep. 2014.

[25] A. Craig-McQuaide, H. Akram, L. Zrinzo, and E. Tripoliti, “A review of brain circuitries involved in stuttering.,” Front Hum Neurosci, vol. 8, p. 884, 2014.

[26] C. J. A. Cowie, J. D. Pešić-Smith, A. Boukas, R. J. Nelson, British Neurosurgical Trainees' Association, “Has the impact of the working time regulations changed neurosurgical trainees' attitudes towards the European working time directive 5 years on?,” Br J Neurosurg, vol. 27, no. 5, pp. 580–585, Oct. 2013.

[27] H. Akram, B. Mirza, N. Kitchen, and J. M. Zakrzewska, “Proposal for evaluating the quality of reports of surgical interventions in the treatment of trigeminal neuralgia: the Surgical Trigeminal Neuralgia Score.,” Neurosurgical FOCUS, vol. 35, no. 3, p. E3, Sep. 2013.

Preface

When my father was twelve, he travelled from Baghdad to London to the National Hospital for Neurology and Neurosurgery in Queen's Square. He was accompanying his disabled mother, a 40-year-old woman struck with Parkinson's disease in her early thirties. He was her carer, and would eventually also care for his father who suffered from intractable depression. My father used to walk him home from hospital, in his state of post-ictal confusion, following electroconvulsive therapy (ECT) sessions. My grandmother developed Parkinson's disease before the advent of L-DOPA, and underwent a pioneering procedure in 1962: stereotactic ablative surgery. Unfortunately, the procedure did not have the desired effect, most likely a result of inaccurate targeting. My father told me she 'lost her mind' in the weeks after surgery. I never met my grandfather; he died in hospital of a hypertensive intracerebral haemorrhage, a year before I was born. My grandmother I do remember; a wheelchair bound woman with snow white silky hair, covered elegantly with a paisley pattern headscarf around her head. I recall her embrace and kindness, but I also remember that she never smiled. I now recognise this as a classical symptom of her ailment. Without the benefit of CT and MRI, my grandmother's neurosurgeon had no reliable means of "seeing" the brain target, whether to plan surgery or confirm the result. Advanced imaging techniques have made functional neurosurgery safer, more accurate, and more effective.

I have been most fortunate to be taken under the wings of Ludvic Zrinzo and Marwan Hariz, pioneers and developers of the image guided and image verified approach to stereotactic functional neurosurgery. They have helped thousands of patients throughout their careers, both directly and indirectly by training others, engaging in research and sharing their knowledge.

This work explores the next frontier in advanced imaging techniques, focusing on the role brain connectivity studies can play in advancing the field of stereotactic functional neurosurgery; to ultimately help more patients, in memory of Khadija, my grandmother.

1. Introduction

"In a pitch-black night a blind man is the best guide; he knows the roads and paths better than any man who can see. When daylight comes, however, it is foolish to use blind old men as guides."

Heinrich Heine (1797 –1856)

1.1: Background

Deep brain stimulation (DBS) for central neuromodulation is a well-established therapy for a wide range of neurological conditions. This is particularly true in the discipline of movement disorders for the treatment of Parkinson's disease, essential tremor and dystonia [1,2]. Over 150,000 patients have received DBS worldwide [3]. Current research explores new brain targets and revisits those formerly used in ablative procedures for the treatment of psychiatric illnesses, such as obsessive-compulsive disorders (OCD), Gilles de la Tourette's syndrome (TS), medically refractory depression, and anorexia nervosa. DBS has also been used in the treatment of intractable, chronic pain to varying degrees of success. Various trials are currently underway for the treatment of a wide range of conditions such as dementia, epilepsy, and obesity making the field of DBS and functional neurosurgery one of the most rapidly expanding fields in neurosurgery. [4] [5,6]

DBS for movement disorders as we know it today was introduced in 1987 for the treatment of essential and Parkinsonian tremor [7]. High frequency stimulation in the subthalamic nucleus (STN) for Parkinson's disease was first reported in 1993 by Benabid and Pollak in Grenoble [8,9]. This was followed by the work of Coubes and Krauss et al on pallidal DBS for the treatment of dystonia in 1999 [10,11].

A contemporary DBS system comprises DBS lead(s) with a quadripolar electrode arrangement, extension cable(s), and a neurostimulator or implantable pulse generator (IPG) **(Figure 1-1)**. Novel lead design with segmented contacts allow for directional current steering [12,13]. The lead is implanted in the brain target area using a precise placement technique (e.g. stereotactic frame). This is performed unilaterally or bilaterally depending on the symptoms.

Figure 1-1: A Medtronic DBS lead (Model 3389)

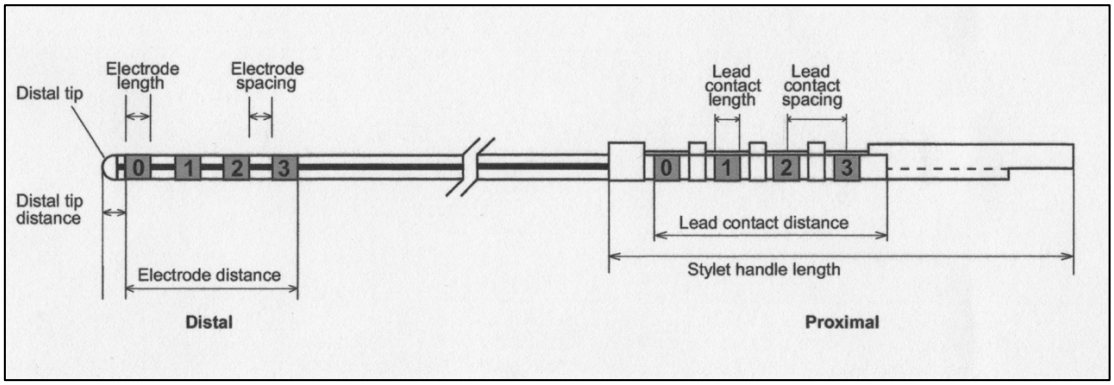

Medtronic 3389 DBS leads were used throughout this work. Distally, the electrode spacing is 0.5 mm, electrode length is 1.5 mm and electrode tip length is 1.5 mm. The diameter of the lead is 1.27 mm (Medtronic Inc.)

1.1.1: A brief history of functional neurosurgery

Functional neurosurgery involves carrying out an acute anatomical intervention to exact a chronic change in function. In line with this statement, functional neurosurgery may well be considered to be the oldest surgical discipline in human history [14]. Archaeological skull findings circa 10,000 BC have demonstrated the practice of trepanation by shamans [15]. Cave paintings showed that people believed the practice would cure epilepsy, migraine and mental disorders [16]. The trepanned bone was kept and may have been worn as a charm to keep evil spirits away [16]. Though one cannot possibly comprehend how this procedure would gain any popularity, it survived well into the middle ages and the Renaissance despite the likely lack of efficacy [17]. Nevertheless, evidence from seven out of eight skulls with trepanations from the 6th to 8th centuries found in southwestern Germany demonstrated clear evidence of healing, suggesting that many patients did survive [17].

Figure 1-2: Detail from The Extraction of the Stone of Madness,

A painting by Hieronymus Bosch depicting trepanation (c.1488–1516)

The modern practice of functional neurosurgery has somewhat more evidence and rather less superstition. This was made possible owing to the emergence and evolution of anatomical, physiological and imaging techniques that led to a better understanding of the disease process and how it is modulated by surgical intervention.

Surgical attempts to improve the functional deficit of movement disorders were first focused on creating lesions in the pyramidal system, resulting invariably in motor deficits [18-21].

Though the pathological involvement of the basal ganglia in Parkinson's disease and chorea was demonstrated in the nineteenth century [22-24], the basal ganglia were considered a surgical *noli me tangere* by Dandy, who speculated that the centre of consciousness lies therein [25]. This did not dissuade others for too long from operating on the basal ganglia. Myers resected the head of caudate in one patient with PD in 1939 significantly alleviating tremor and rigidity without damage to the pyramidal tract and resulting weakness [26]. He

later resected the pallidothalamic fibres in the ansa lenticularis which became a popular surgical option for movement disorders in the following decade [27-30].

The pivotal role the basal ganglia had in the surgical treatment of movement disorders was further consolidated in 1953 following a report of a surgical accident. Irving Cooper had planned to perform a cerebral pedunculotomy on a patient with post-encephalitic Parkinsonian syndrome, incidentally referred to him by Walter Freeman, to induce weakness and hence improve tremor. Cooper caused damage to the anterior choroidal artery during the approach that led him to ligate the artery and abandon the procedure. To his delight the patient's tremor disappeared following surgery without accompanying weakness. This outcome was attributed to an ischaemic lesion in the globus pallidus and ansa lenticularis [31,32]. The following year, Cooper reported a series of 34 patients with PD who underwent ligation of the contralateral anterior choroidal artery (6 bilateral) with no recurrence of rigidity or tremor one year or longer after surgery [33]. He conceded that although the procedure was effective, it would never be a routine operation due to the variability in the anatomy of the artery and the distribution of its vascular supply leading him to adopt chemo-pallidectomy and later cryotherapy as the procedure of choice all through the sixties [34]. Although Cooper used a probe of his design to perform these procedures and his complication rate was relatively low, others adopted a more open approach that carried significant morbidity and mortality [35]. A less invasive and more accurate approach was needed.

The word "stereotactic" is derived from the Greek for three-dimensional *"stereo"* and to touch *"tangere"*. Though the term is relatively recent, the basis of stereotaxy have been several hundred years in development [14,36]. The Cartesian coordinate system attributed to René Descartes (c.1596-1650), has allowed for the identification of a point in three-dimensional space by employing x, y and z coordinates in relation to a fixed point(s) or landmark(s). The discovery of X-Rays by Wilhelm-Conrad Röntgen in 1895 allowed for a degree of visualization of intracranial structures, which could be used as landmarks, in relation to the frame, for stereotactic targeting [37]. Sixteen months later, the French

photographer Gaston Contremoulins created a stereotactic device that implemented the newly discovered x-rays. The device was successfully used in humans to localize and extract intracranial bullets by the Parisian surgeon Charles Rémy in 1897 [38]. However, a systematic approach to stereotaxis was first applied in 1906 when Sir Victor Horsley and Robert Henry Clarke invented their renowned Horsley-Clarke apparatus, a stereotactic frame for animal studies **(Figure 1-3)** [39]. It was not until after the development of air ventriculography by Walter Dandy in 1918 that Ernst Spiegel and Henry Wycis developed their stereotactic frame to perform ablative procedures in humans in 1947 **(Figure 1-4)** [40]. The first operation they carried out was a thalamotomy for depression [40]. Spiegel and Wycis went on to publish the first human stereotactic atlas in 1952 [41]. And there it was, *"with a navigational system and a guiding map, human stereotactic neurosurgery was born"* [14]. Various stereotactic atlases and frames have been developed since, each with their inherent advantages and disadvantages [42-44].

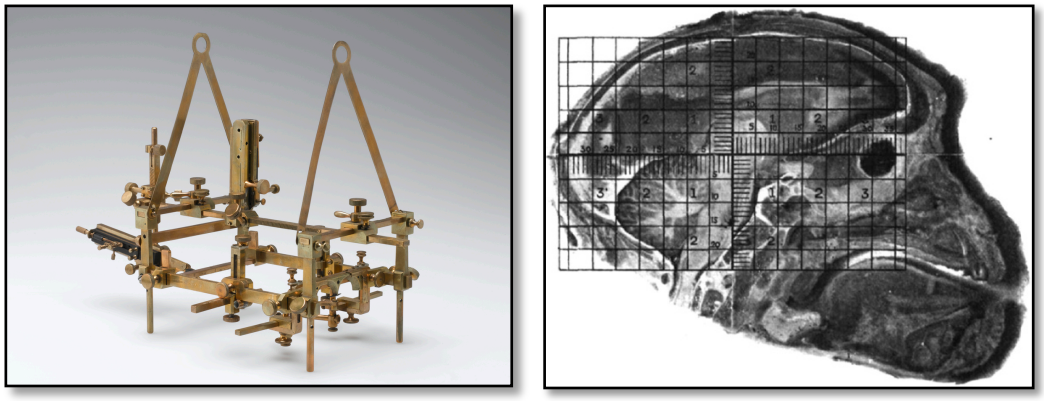

Figure 1-3: The Horsley-Clarke apparatus, the Science museum, London (left) and Cartesian coordinate grid overlaid on a non-human primate brain (right)

Figure 1-4: The Spiegel and Wycis stereotactic system

Spiegel and Wycis shifted their attention from the treatment of psychiatric illness to movement disorders. They used their frame to create a deep brain lesion by instilling alcohol in the globus pallidus interna (GPi) in a patient with Huntington's chorea [45]. They then started performing stereotactic pallidoansotomies in PD patients, ablating the same

areas that had been lesioned by Meyers, Fenelon, and Guiot via an open non-stereotactic approach [46].

Between 1960 and 1970, more than 40,000 stereotactic procedures were carried out [14,47]. The rise of functional neurosurgery procedures came to a halt following the discovery of L-Dopa in 1968. Nevertheless, the emergence late side effects of L-Dopa and its agonists became apparent in the mid-1980s. This necessitated a complementary surgical approach with medical therapy. The rediscovery of leksell's stereotactic pallidotomy by Lauri Laitinen in 1992 heralded the rebirth of stereotactic functional neurosurgery [48,49]. Marwan Hariz, Laitinen's apprentice, has likened this rebirth to "a phoenix rising from the ashes".

Ablative stereotactic surgical procedures gained momentum, however, they were not without drawbacks. Destructive surgery is irreversible (requiring high targeting accuracy to avoid neurological complications) and can carry a stigma. Furthermore, bilateral surgery in brain targets used in movement disorders can lead to unacceptable side effects such as balance, cognitive, speech and swallowing defects, especially when performed in the thalamus and basal ganglia and in a single session [50].

Deep brain stimulation offered an alternative to ablative surgery. Targeting is relatively more forgiving as the stimulation parameters can be adjusted to an extent. Moreover, bilateral surgery is better tolerated in the thalamus and basal ganglia. Having said that, it comes with the disadvantage of having an expensive implant that is prone to infections, device failure and battery depletion requiring further replacement surgery [50].

The concept of chronic subcortical stimulation was not new. It had been previously trailed in the treatment of patients with psychiatric disorders [51] and chronic pain [52]. In a famous animal experiment, Delgado was able to stop a bull mid-charge by delivering stimulation through chronically implanted subcortical leads controlled remotely using radio waves [53]. Delgado then worked with Sixto Obrador and Jose Martin-Rodriguez to implant bilateral electrodes to deliver chronic stimulation in the head of the caudate and septal regions for the treatment of brachial-plexus avulsion pain. This is thought to be the first implantation of a DBS device in Europe [54]. In further work by Carl-Willhelm Sem-Jacobsen, chronically

implanted depth electrodes were used to refine prefrontal leucotomy procedures by exploring the response to stimulation prior to making incremental, permanent lesions [55].

More, rather infamous work in the field of chronic deep brain stimulation for psychiatric disorders was carried out by the American psychiatrist Robert Heath in Tulane University, New Orleans in the 1950s [4]. Heath pioneered the concept of 'self-stimulation' through chronically implanted leads. His work began with a focus on treating schizophrenia, epilepsy and pain [56]. After some patients reported a sense of 'euphoria' when stimulating the septal area, Heath began to explore this further in an attempt to identify the pleasure centres in the brain [57]. Heath's work has raised considerable ethical concerns [4] and his experiments have been deemed "dubious and precarious by yesterday's standards" [56].

The list of subcortical structures targeted in DBS is extensive. Considering the role that the basal ganglia (BG) play in regulating and modulating internally and externally driven behaviours [58], it is no surprise that targeting these structures can have a significant impact on brain function. The success of the deep brain stimulation procedure hinges on proper patient and target selection and accurate lead placement with stimulation of neurones and pathways within a small region, while avoiding current spread to nearby structures causing unwanted neurological and/or behavioural side effects.

Though advancements in imaging techniques in the last century provided a window into the brain; targeting deep brain structures, whether for ablation or DBS, continued to pose challenges. ***Direct targeting*** is not possible using X-Rays because the targets cannot be visualised. This led to a reliance on various stereotactic atlases, employing references visible on air ventriculography (e.g. the anterior commissure and posterior commissure). ***Indirect targeting*** requires further intraoperative refinement of targeting variability, which can be achieved with electrophysiological mapping (i.e. micro/ macro electrode recording) and often intraoperative stimulation and testing [59]. CT and early MRI scans did not provide the spatial resolution and contrast for direct targeting or target verification. Additionally, MRI scans are susceptible to spatial distortion and artifacts, impinging on targeting accuracy [60].

Contemporary 1.5 and 3T MRI sequences, when meticulously calibrated and tested, can provide a map for direct targeting of many of the subcortical structures commonly used in functional neurosurgery (e.g. the STN, the GPi etc.) negating the need for surrogate markers required in indirect targeting [61,62]. Furthermore, immediate postoperative *stereotactic* MRI offers the ability to verify targeting accuracy by assessing electrode placement, guiding relocation of sub-optimally placed electrodes, auditing and ultimately improving targeting accuracy and precision, examining the effect of electrode placement on long-term therapeutic effects and side-effects and more recently, by utilising it in generating volume of tissue activation models around individual contacts to explore the anatomical basis to physiological observations and clinical responses [61].

Nevertheless, access to good quality and reliable MR imaging requires local expertise and the ungoverned use of MRI with DBS implants can raise safety concerns. However, when appropriate safety precautions are carried out, those risks can be reduced to acceptable limits that are far below the risk of other verification techniques commonly used in clinical practice [63].

1.1.2: Targeting neural circuits

Functionally distinct cortico-subcortical loops, which form elements of the motor, associative and emotive systems, pass through the basal ganglia and thalamic nuclei, often creating functional sub-regions within these structures with various degrees of overlap [58]. Localizing these sub-regions (e.g. the sensorimotor STN) is not easily achieved using conventional magnetic resonance imaging [58,64]. This underlying relationship between structure and function suggests that the efficacy of DBS, and avoidance of unwanted side effects, may be influenced by the precise stimulation site within the anatomical target. Those functional sub regions may show distinct electrophysiological features. This has been used as an argument for using MER to refine the final electrode location. However, there is a growing body of evidence suggesting that the use of surrogate electrophysiological markers is by no means a guarantee for a good long-term outcome.

Location of the best MER activity has been shown not to necessarily correlate with the best clinical response on macro-electrode testing intraoperatively [65]. It has been shown that a better predictor of good long-term clinical outcome was the DBS lead position within the MRI defined STN [66,67].

Additionally, using an image guided and verified approach is safer owing to the reduction in the number of passes through the brain. A blunt tipped probe is used to create a track to the target in contrast to MER, which commonly involves the insertion of two to five sharp microelectrodes and their cannulas. This is associated with an increased risk of intracranial haemorrhage, which can rarely lead to devastating complications and even death [68 69].

An additional gain when using an image guided and verified approach is the ability to carry out audit that can have a positive impact on future DBS procedures. There is no means to replicate an "ideal MER recording" in subsequent procedures. However, MRI verified surgery allows for constructing a 'DBS functional map' within the targeted structure through studying correlations between the contact location, side effects, and efficacy across a group. The data can then be replicated in future patients to improve targeting.

As an example of how audit can help finesse targeting, a recent study found that DBS electrodes placed along the medial border of the STN in PD patients led to more long term speech deterioration when compared to a slightly more lateral location [70].

Moreover, an image guided and image verified approach reduces the operative time and patient discomfort as surgery can be carried out under general anaesthesia [71], it allows for relocation of electrodes when results are suboptimal [72], and anatomical targeting errors can be detected and addressed before completing the procedure [73-75].

Using an image guided and verified approach thus carries significant advantages, however, at present, conventional MRI does not provide information on functional mapping within the brain target.

Structural and functional connectivity studies may provide the opportunity to examine the concept of "non-invasive" functional mapping against "invasive" mapping with MER. This

can provide new ways to define the sub-regions in target nuclei, such as the STN; where stimulation in the sensorimotor area gives the optimal results in PD patients [66,76,77].

In a contemporary, image guided and image verified functional neurosurgery approach, an MRI scan is performed with the frame on to calculate the stereotactic coordinates of the brain target visible on the scan. In some units, a stereotactic CT scan is performed and then co-registered with a preoperative non-stereotactic MRI using linear registration. Once the DBS leads are implanted, an intraoperative stereotactic MRI (or CT) is performed to confirm the final position of the electrodes. This is the approach used at the National Hospital for Neurology and Neurosurgery. Some continue to rely on surrogate electrophysiological markers obtained from the neural tissue local field potential using microelectrode recording to guide lead implantation. Following lead implantation, extension cables are tunnelled under the skin to connect the DBS lead(s) to an implantable pulse generator (IPG). The latter is internalised in a pectoral or abdominal pocket. The stimulation parameters are programmed and adjusted using an external programmer **(Figure 1.5)** to set up the active contacts (single, multiple adjacent, or interleaved), mode of stimulation (monopolar or bipolar), stimulation voltage (or amplitude), frequency and pulse width depending on stimulation efficacy and side effects. The patient is given a personal programmer to switch between different pre-sets of programs (if necessary), increase or decrease stimulation intensity (within a pre-set window), or to turn the device on and off. The different components of a contemporary DBS system are shown in **Figure 1-6**.

Figure 1-5:N-vision

Figure 1-6: A contemporary DBS system setup showing the different components [78]

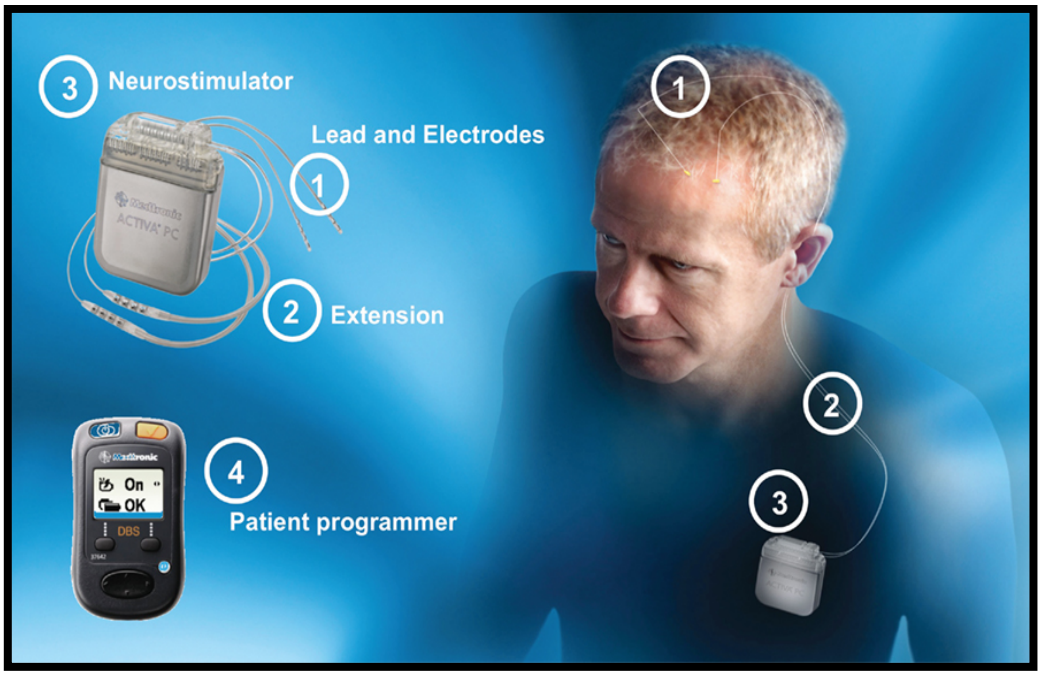

1.1.3: The role of MR connectivity

Structural and functional connectivity may allow the visualization of targets not readily visible on MRI, such as the ventrointermedialis (VIM) nucleus of the thalamus, used in the treatment of tremor. Defining white matter tracts using diffusion tractography techniques can also help targeting structures such as the medial forebrain bundle, possibly implicated in the treatment of depression [79].

The practice of exploring brain connectivity is not new. The structural connectivity of the human brain has been studied for centuries, employing various techniques to define neural connections. Gross anatomical studies in the 16th century carried out by the anatomist Andreas Vesalius defined various major white matter tracts in the brain. Centuries later, the development of the microscope opened the door for the study of the microstructural architecture of neural tissue. Tracer studies in non-human primates (NHP) allowed scientists to make some inferences about connections in the human brain. Brain lesions and tracer studies in humans similarly allowed for mapping brain connections.

In the context of this work, structural connectivity is used synonymously with diffusion connectivity.

1.1.4: Functional connectivity

Functional connectivity refers to correlations in activity between remote regions in the brain. The regions might be directly or indirectly (functionally) connected. This is traditionally studied using PET and or SPECT techniques. In this thesis, it is pertained to resting state fMRI experiments, by examining synchronicity in the haemodynamic response (HDR) on BOLD sequences thus determining correlations between different brain regions [80]. Further description of resting state functional connectivity analysis is provided in chapter 3.

1.1.5: Structural connectivity

Structural connectivity refers to direct anatomical connections, via axonal bundles between remote brain regions. This can be assessed using MR diffusion connectivity.

There is no 'standard' approach to acquiring and processing diffusion MRI data. This is partly due to the mixture of applications of diffusion imaging and the restraints associated with acquiring and processing higher quality data. As a result, a plethora of specialised software platforms have been developed, each offering different ways of data processing and visualization.

Applications of diffusion MRI can be broadly divided into two categories: (1) the study of the scale, density and organisation of brain tissue microstructure e.g. fractional anisotropy (FA), mean diffusivity (MD), neurite orientation dispersion and density imaging (NODDI), etc.; and (2) the study of macrostructural connectivity by means of tractography. The latter can be mostly subdivided into deterministic, probabilistic and global approaches [81].

1.1.5.1: Introduction to diffusion MRI acquisition

MRI is highly sensitive to water tissue content. As a result of Brownian motion, water molecules are mobile and not static. This motion can be random in isotropic environments (e.g. grey matter or CSF) or directional in anisotropic environments (e.g. axonal fibre bundles or blood vessels). A directional displacement of sensitised water molecules (phase shift) can result in a detectable MRI signal loss. This outlines the basic principle of diffusion imaging. In areas of restricted water diffusion, the orientation of white matter tracts can be

inferred from the signal loss incurred due to phase shift along the diffusion direction. This conventionally involves the use of a pulse-gradient spin echo sequence, were gradient pulses are applied on both ends of the 180° refocusing pulse. The signal is then acquired using a single-shot rapid image acquisition method such as echo-planar imaging (EPI). The strength and duration of the gradient pulse is directly related to signal loss along the diffusion direction or to the 'diffusion effect'. The factor that reflects the strength and timing of the gradients is termed the *b-value* (s/mm^2). Each diffusion direction is encoded in x, y and z coordinates of the corresponding gradients. Acquiring more diffusion directions results in higher angular resolution. This, however; comes at the expense of increased scanning time [81].

Other factors can influence the way diffusion MRI data is acquired. These include the static magnetic field strength, spatial resolution (voxel size), number of diffusion shells, number of averages acquired, phase encode direction, the quality and number of channels in the receive head coil, the use of in-plane acceleration or multi-slice acquisition, etc.

At the centre of any MRI acquisition there is a central trade-off between signal to noise ratio (SNR), image spatial resolution and scanning time. With an increase in the static magnetic field comes an increase in the intrinsic SNR (7T > 3T > 1.5T) but not without drawbacks, mainly increased inhomogeneity of both the main field (B0) and the RF transmit field (B1), resulting in worsening geometrical distortion, in addition to the increased specific absorption rate (SAR) resulting in safety implications [82].

Diffusion sequences are therefore highly customizable. Careful attention to optimising the scanning parameters should be sought to ensure that the appropriate sequences are acquired.

1.1.5.2: Modelling diffusion in a voxel

Several diffusion methods have been developed, each with its strengths and limitations. These include *diffusion kurtosis imaging* (DKI) [83]; *Q-space imaging* such as diffusion spectral imaging (DSI) [84] and hybrid diffusion imaging (HYDI) [85]; and *model based*

approaches such as the composite hindered and restricted model of diffusion (CHARMED) [86], NODDI [87] and diffusion basis spectral imaging (DBSI) [88]. The most popular diffusion models by far are Diffusion Tensor Imaging (DTI) and High Angular Resolution Diffusion Imaging (HARDI).

1.1.5.2.1: Diffusion Tensor Imaging (DTI)

DTI is one of the simplest models used to describe the anisotropic diffusion phenomenon in brain tissue. The use of the term is so ubiquitous, it has become - wrongly - synonymous with DWI and with tractography. DTI was first described in 1994 [89] as a three-dimensional model of Gaussian diffusion displacements in a voxel, depicted in a 3 X 3 covariance matrix:

$$D = \begin{pmatrix} D_{xx} & D_{xy} & D_{xz} \\ D_{yx} & D_{yy} & D_{yz} \\ D_{zx} & D_{zy} & D_{zz} \end{pmatrix}$$

In order to visualise the tensor as an ellipsoid (**Figure 1-7)**, the covariance matrix can be diagonalized to yield three eigenvalues ($\lambda 1 > \lambda 2 > \lambda 3$) and their corresponding eigenvectors ($\varepsilon 1$, $\varepsilon 2$ and $\varepsilon 3$).

Figure 1-7: The DTI ellipsoid

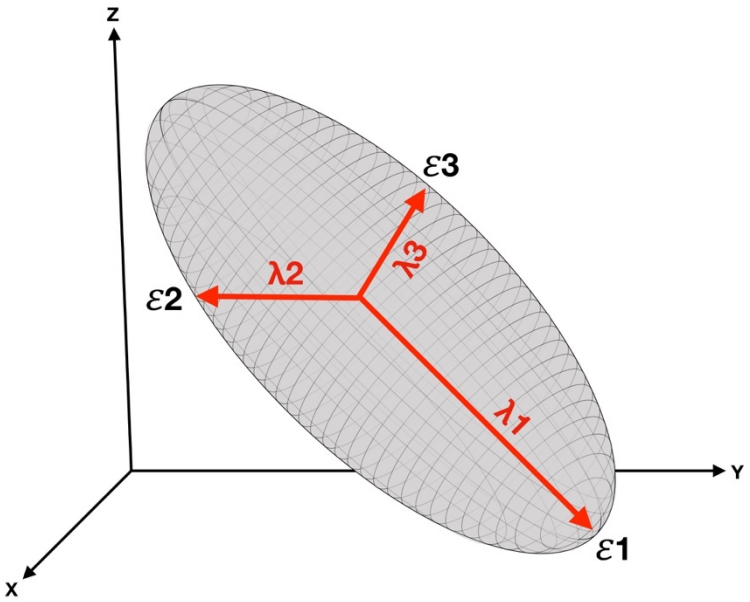

Several scalar matrices, to describe tissue diffusion properties on the microstructural level, can be derived from this tensor model such as FA, axial diffusivity, radial diffusivity and MD.

The DTI model has several limitations nonetheless, mainly its inability to resolve multiple fibre orientations in a voxel. Furthermore, the assumption of a Gaussian diffusion profile, which is at the heart of the DTI model, fails at higher b-values. This has necessitated the introduction of more complex models to describe the diffusion signal beyond the simple tensor [81].

1.1.5.2.2: High Angular Resolution Diffusion Imaging (HARDI)

In this diffusion method, higher b-values (1000 – 3000 s/mm^2) and number of diffusion directions (in a single shell) are needed when data is acquired. An ensemble of a finite number of diffusion tensors is modelled in each voxel [90]. This is a more complex model of diffusion than DTI and it allows for the resolution of multiple crossing fibres (e.g. in spherical deconvolution) [81]. This is the diffusion model used in the experiments in this thesis.

1.1.5.3 MR diffusion tractography

Tractography is a technique used to study white matter pathways and structural connectivity in brain tissue. It runs after diffusion modelling on the voxel level described previously. Tractography relies on indirect measurements to create 'tracts' through brain voxels. Inferences can be made from these tracts to represent white matter pathways [91]. These pathways have been validated in histological studies, correlating well with known anatomy [92]. The connectivity profile of a region of interest can be used to segment this region according to the maximum probability of connection to the cortex and or to other regions in the brain [93,94]. This technique has been applied to segment structures within the basal ganglia network [95-97].

Tractography is error prone and has several limitations, however; it remains the only non-invasive method available to measure the structural connectivity in the human brain tissue

in *vivo*. Tractography algorithms can be local or global, deterministic or probabilistic, model-based or model free.

1.1.5.3.1: Deterministic versus probabilistic tractography

Deterministic tractography is a technique that involves the creation of streamlines starting from a seed region of interest in white matter and passing through voxels by following the first eigenvector of the diffusion tensor (i.e. the principal direction of diffusion), effectively connecting the arrows in each voxel. Streamlines are then terminated when they reach a target seed or fall below a set curvature or FA value (e.g. in areas of low anisotropy). Deterministic tractography has been very successful in white matter - in *vivo* - dissection [98]. Since this method usually relies on the DTI model, diffusion data acquisition and processing are relatively fast. Despite its success in visualizing large white matter tracts, deterministic tractography has significant drawbacks. These include the inability to accurately visualize tracts in areas of low anisotropy (e.g. thalamus) or high noise (e.g. brainstem); and modelling errors in areas of high anatomical complexity (e.g. crossing or kissing fibres). Moreover, errors incurred during streamline visualization can get easily propagated resulting in anatomically erroneous connections [99]. Concerns regarding 'accuracy' and 'reproducibility' have also been recently raised [100]. Overall, deterministic tractography tends to 'underestimate' the number of streamlines in a pathway [101].

Probabilistic tractography does not utilise 'streamlining'. Instead, a function of uncertainty of the fibre orientation measurement is created in each voxel. This is often referred to as the orientation density function or ODF. Once fibre modelling is carried out in each brain voxel, tracts can be generated by the propagation of uncertainty over multiple iterations [91]. In contrast to deterministic tractography, probabilistic tractography can generate tracts in areas of low certainty (low anisotropy, high noise, etc.). It can also provide statistical metrics of connectivity. This method requires higher quality data (in a single shell i.e. HARDI or in a multi-shell form). It is also computationally demanding. These factors translate to relatively long acquisition and processing times. Having said that, with advancements in MR image acquisition (e.g. multiband acquisition) and processing (e.g. GPU processing),

these approaches are becoming more feasible in a clinical setting [102]. In a recent comparison of different tractography techniques, probabilistic tractography was shown to produce results closest to the ground truth, however; it also resulted in more false positives than deterministic approaches [101].

1.1.6: Limitations of MR connectivity techniques

In order to explore the clinical applications of MR connectivity, it is essential to understand the limitations of these techniques. Tractography makes inferences from water diffusion direction to produce models of white matter bundles. This is a gross representation of neural axons and is highly dependent on voxel size (spatial resolution), number of diffusion directions (directional resolution), field strength and many more highly customisable parameters from sequence acquisition to pre-processing, post-processing and study design, all of which can affect the results. Tractography does not provide information on directionality and struggles in regions with crossing or kissing fibres [103]. Furthermore, tractography has a propensity for favouring short, mesial and straight streamlines over long, lateral and tortuous ones [103].

Resting state functional MR connectivity can be heavily influenced by motion artifact and medications. The spatial resolution is considerably poor and single subject studies are often meaningless. Both structural and functional MR studies rely on image registration which can introduce errors that are unacceptable in stereotactic surgery.

In the experimental chapters of this thesis we have endeavoured to address the limitations of these techniques and we were conscious not to take our results on face value without the necessary rigorous appraisal.

1.2: Proposed model

Using structural and functional connectivity, the general aims of this work are to:

- Sub-segment basal ganglia structures using a non-biased-automated pipeline in DBS patients.
- Assess clinical outcome after DBS surgery using the above models.
- Generate a symptom-based predictive spatial model based on tractography data and electrode parameters, to allow individual based predictions regarding optimal electrode configurations.
- Explore basal ganglia networks, and examine distant brain regions that are influenced by DBS activity.

This work builds on previous work by Lambert et al [96]. It has been shown that it is possible to generate connectivity based sub-segmentation of multiple regions with no down-sampling of data within a clinically viable timeframe. The process is highly dependent on computing resources. In an example, the brainstem (18,000 voxels) was fully segmented and clustered in approximately 24 hours, with the majority of that time spent generating the initial tractography [104] [105]. Utilising this established framework, we provide and validate a system of methods to identify, for a given individual, the optimal DBS target location for their specific symptoms. We hypothesize that this would help to minimise side effects, improve safety, and facilitate the setting of DBS parameters. This also provides a unique insight into the mechanisms involved.

In this work, we employ connectivity analysis combined with spatial DBS information, volume of tissue activation and clinical outcome, within a generalized framework to attempt to “predict” optimal DBS lead location given the structural and diffusion weighted images. This would utilize far more anatomical information; rather than being limited to a certain grey-matter structure, it would take advantage of the regional information provided by the zone of stimulation or volume of tissue activation (i.e. both grey and white matter). Indeed, in vivo optogenetic studies using Parkinsonian rodent models suggest that it is inhibition of

the white matter afferent fibres, rather than the local cell bodies, that are responsible for the therapeutic effects of DBS [106], providing a neurophysiological rationale for this approach.

Furthermore, we employ a well-characterized and widely used approach with several available techniques [94-96,107] to parcellate the motor thalamus by clustering individual voxel tractography information based on cortical and cerebellar connectivity (chapter 6). This is yet to be implemented within a neurosurgical framework. We investigate whether this information can be used to help map the ventrointermedialis nucleus of the thalamus (VIM), a DBS target for tremor.

Another line of analysis is conducted for predominantly white matter targets, or ill-defined targets on structural imaging; such as the dentato-rubro-thalamic (DRT) tract and the caudal zona incerta (cZi) [a reticular nucleus] targeted in the treatment of tremor; and the ventral tegmental area targeted in the treatment of trigeminal autonomic cephalalgias (TAC). For these targets, we use probabilistic tractography to map these tracts and their relation to DBS contacts. These approaches help better understand the brain circuitry implicated in pathophysiology and DBS mechanism and refine target selection in the future.

The current project is cautious, taking a retrospective approach, and is done with patient safety in mind to allow a robust, well-understood, accurate technique to first be developed and thoroughly tested before being used to inform surgical decisions. Clearly there are more complicated and advanced models that could be attempted, for example considering local tissue impedance, tissue types etc., or performing longitudinal predictions of outcome (i.e. clinical stability), but these are secondary projects to the simpler and much more achievable primary aims.

1.3: Literature review

There are relatively few studies examining the role of connectivity in DBS surgery, and they can be broadly divided into three categories:

1.3.1: Studies that examine the connectivity of effective DBS targets in healthy subjects

This is the most common category. These studies examine simple connectivity patterns of effective DBS targets in healthy subjects not undergoing surgery [108-114]. This approach is useful in highlighting the common pathways implicated in DBS therapy but does not consider individual variations or differences in connectivity between healthy controls and patients. In certain studies, the scans were registered to a standard space e.g. MNI152 space, a process that readily introduces fusion co-registration errors, which can be paramount when studying small structures such as the STN.

The various reports, in each category, have been sub-grouped under three separate headings; movement disorders, pain and psychiatric disorders in the order of how established functional neurosurgery is in the treatment of these conditions.

1.3.1.1: Movement disorders

In a study that employed functional connectivity to investigate the VIM nucleus of the thalamus as a DBS target in the treatment of tremor, Anderson et al used resting state fMRI data acquired from 58 healthy subjects to map the functional connectivity between atlas defined regions of interest in the thalamus, the motor cortices and the motor activation region of the superior cerebellum as identified during a finger moving test. The researchers found consistent functional connectivity patterns between those regions of interest. There were inter-individual variations in the optimal DBS target in the thalamus [115]. In a similar study by Hyam et al, this time using structural connectivity (probabilistic tractography) in 17 healthy subjects from seeds in the VIM and the ventral oralis posterior (VoP) thalamic nuclei. Those regions of interest were identified on a structural MRI scan by an experienced neurosurgeon. Distinct connections between the VIM, M1, and the contralateral cerebellum were found. The VoP was connected to the SMA. Differences of connectivity between the VIM and VoP were identified in keeping with known anatomical data [116]. These findings support the role probabilistic tractography can play in distinguishing intimate nuclei within the thalamus depending on their connectivity patterns thus playing a role in the surgical planning.

In a study by Horn et al, machine learning techniques were applied to publicly available, state of the art diffusion and resting state functional MR data acquired from the human connectome project [117]. The connectivity profiles of the active contacts in 51 PD patients with STN DBS were explored using Lead-DBS toolbox [118]. The results were used alongside the efficacy profiles for DBS to train a connectivity model. The model was then used to predict efficacy in another dataset of 44 patients from a different centre based on connectivity. In the training dataset, structural connectivity between the DBS electrode and the SMA and functional anti-correlation to M1 correlated with clinical response. This same connectivity profile predicted response in the test group with an average error of 15%. The authors concluded that STN DBS connectivity in PD can predict clinical outcome across independent cohorts [119]. The authors submitted that specialized imaging in PD patients themselves is not necessary and connectivity data from matched controls is sufficient. This remains to be validated. PD patients have been shown to have altered functional and structural connectivity and replication of the study using patient specific data may yield different connectivity profiles and/ or average prediction error.

1.3.1.2: Pain

In a paper by Owen et al, the effective DBS contact location of a patient with cluster headache treated successfully with - what the authors term - posterior hypothalamic DBS was used as a seed to explore the structural connectivity of the target using probabilistic tractography in 13 healthy controls. The authors found consistent connections between the so called posterior hypothalamic region with the reticular nucleus and the cerebellum and in some patients, connections were also seen with the parietal cortices and the inferior medial frontal gyrus [120]. These findings shed a light on the possible pathways of action of DBS in cluster headache. The role of the so called posterior hypothalamic region in cluster headache was first pointed out after a PET study by May et al in 1998 that showed activation in what was termed the ipsilateral posterior hypothalamus during attacks [121]. A year later, another paper showed increased neuronal density in the same area in patients with cluster headache using voxel based morphometry analysis [122]. This led Franzini et al

to successfully treat a patient with refractory CH in 2001 with DBS [123], and report the first series of patients in 2003 [124]. Owen et al's work is the first to study the in vivo connections from the DBS target using probabilistic tractography.

1.3.1.3: Psychiatric disorders

Another DBS target, for which several trials are currently being carried out, is the anterior cingulate cortex [125-128]. Ablative surgery in this region is well established in the treatment of medically refractory depression with varied targeting strategies anywhere along the dorsal anterior cingulate to the subgenual cingulate cortex, albeit no evidence from blinded trials exists to support its efficacy. The practice declined in the last century with the development of effective drugs. In general, there was a move away from psychosurgery after the 50s and 60s. The poor regulation in the field during the lobotomy era and the lack of a consistent multidisciplinary approach gave way to poor surgical and ethical practices by some [51,129,130].

Johansen-Berg et al used the effective contact location from nine patients with medically refractory depression treated with cingulate cortex DBS to map the target's structural connectivity using probabilistic tractography in 17 healthy subjects. Using connectivity based parcellation of the anterior cingulate cortex, the authors defined two distinct regions: a pre-genual region, strongly connected to the medial prefrontal and the anterior mid-cingulate cortex and a sub-genual region with the strongest connections to the nucleus accumbens (NAc), amygdala, hypothalamus, and the orbitofrontal cortex. The location of the effective electrode contact points were within the sub-genual region; this finding supported the hypothesis that the treatment efficacy is mediated via the effects on a distributed network of frontal, emotive, and viscera-motor brain regions [112]. This study however, did not report on the outcome of DBS in these patients or indeed set out to correlate connectivity with outcome. Moreover, patients in the original trial by Mayberg et al had a short follow-up period (6 months) and were not blinded to stimulation making it difficult to disentangle a real treatment effect from a placebo effect [126].

Another study by Gutman et al used diffusion scans from 13 healthy subjects to compare the connectivity patterns of two DBS targets used in the treatment of refractory depression, the subcallosal cingulate white matter (SCCwm) and the anterior limb of the internal capsule (ALIC), in an attempt to explain the mechanisms of action of DBS. Group level tract maps were generated and compared for both targets. The authors found areas of overlap as expected and areas of distinct connectivity patterns for the two targets. The SCCwm had consistent ipsilateral connections to the medial frontal cortex, the anterior and posterior cingulate, medial temporal lobe, dorsal medial thalamus, hypothalamus, NAc and the dorsal brainstem. The ALIC seed in contrast demonstrated widespread projections to the frontal pole, medial temporal lobe, cerebellum, NAc, thalamus, hypothalamus and the brainstem. Connections to the frontal pole, medial temporal lobe, NAc, dorsal thalamus and the hypothalamus were common to both targets [110].

The above studies aim to explain the mechanism of action of DBS in the anterior cingulate region, whilst a study by Bhatia et al tried to compare targeting techniques using diffusion vs. conventional MRI targeting techniques. T1, T2 weighted images and diffusion acquisitions were taken in 59 healthy subjects. Targets were selected for both hemispheres using the T2 weighted and diffusion sequences. A significant difference was found within targets selected using diffusion from those selected using T2 sequences [131]. However, it must be emphasised that the findings are not coupled with any supporting clinical data or evidence of efficacy so no conclusions can be drawn about the role of diffusion connectivity in target selection in DBS surgery.

1.3.2: Studies that use patient specific connectivity data to directly plan surgery or predict outcome

These studies use patient specific connectivity data, either to directly perform targeting in DBS surgery or to perform post-hoc analysis, once DBS surgery was done using a traditional approach, looking at correlations between DBS lead contact location in relation to connectivity maps, and outcome [132]. These studies commonly use simple visualisation of the first order tensor fields (either directly or through streamline deterministic

tractography) to manually identify anatomical regions of interests within structures such as the thalamus [133], pedunculopontine nucleus (PPN) [134] or surrounding fibres [135]. The manual identification employed in these methods introduces observer bias, and does not take full advantage of the intrinsic information present in the data to allow these regions to be automatically segmented. Moreover, the assumptions made when employing deterministic tractography [135] only allow principle fibre bundles to be identified and fail to account for the complexity that naturally exists (i.e. multiple fibre tracts and crossing fibres).

Most of these studies focus on thalamic DBS targeting for tremor, DBS for pain and for depression/ OCD. It is imperative to highlight here that unlike DBS for tremor; DBS for pain and DBS for depression/ OCD remains experimental and there is no clear evidence to support the efficacy of these treatments, or even which target to choose. This "lack of evidence for efficacy", despite seemingly sound mechanistic imaging findings, reminds us of the limitations of such a "broad brush" technique when applied to the complex human brain affected by disease.

1.3.2.1: Movement disorders

Coenen et al published a case report in 2011 describing a patient with medically refractory, tremor dominant PD. The patient underwent a preoperative diffusion scan, followed by VIM DBS using traditional MRI landmarks for targeting. Intraoperative macrostimulation was used to confirm target accuracy. A postoperative CT scan showing the DBS lead was fused with the preoperative MRI to confirm lead location. DBS therapy was highly effective and preoperative whole brain deterministic tractography (DT) was then performed and the dentate-rubro-thalamic (DRT) tract was isolated. The active DBS contact was clearly located within the vicinity of the DRT, which has been implicated in the tremor circuit. The targets generally used for the treatment of tremor are the VIM, cZi and the posterior subthalamic region. This study showed that those targets may indeed form different nodes on one neural circuit [136]. In the same year the group reported the case of a patient with dystonic tremor who underwent bilateral VIM DBS insertion, this time guided by deterministic tractography in addition to traditional MRI landmarks, resulting in >90% tremor

control 3 months after surgery [137]. Although these are reports of single cases, they do provide a proof of concept for the use of diffusion connectivity in DBS surgical planning. The diffusion imaging parameters used were of poor quality with a limited number of diffusion directions and large voxel size. The authors used a deterministic tractography technique to model tracts that traverse the thalamus (an area of low anisotropy) where this technique has limitations.

On the same theme, Pouratian et al performed a post hoc analysis of six patients who underwent bilateral VIM DBS for tremor. Diffusion scans were performed preoperatively. Thalamic segmentation was attained using probabilistic tractography as described by Behrens et al [94]. Although the study had methodological weaknesses with suboptimal diffusion acquisition parameters and the scans were registered to the standard MNI152 space; the effective DBS contacts were located at the area of the thalamus with the highest probability of connection to the premotor and supplementary motor cortices [138]. Klein et al performed a post hoc connectivity analysis of 12 patients with intractable tremor who underwent VIM DBS using traditional MRI landmark targeting. The effective DBS contacts were used as seeds for probabilistic tractography using diffusion scans acquired before surgery. VIM stimulation resulted in a decrease in tremor magnitude and an improvement in the quality of life. Tractography initiated from the effective stimulation site reconstructed a highly reproducible network of structural connectivity comprising motor cortical, subcortical, cerebellar and brainstem. Connectivity to the primary motor cortex seemed to play a key role in successful stimulation [139], in contrast with Pouratian but in keeping with the findings by Coenen.

Groppa et al examined the effective DBS contact locations of seven patients with intractable essential tremor with thalamic DBS. The DRT was reconstructed using probabilistic tractography in 13 healthy controls using seeds in the cerebellum and the brainstem. The effective DBS contacts appeared to lie in the vicinity of the DRT [140].

Anthofer et al investigated the variability of probabilistic atlas-based VIM targets in relation to the surrounding major fibre tracts using deterministic tractography in 10 patients with

essential tremor who received VIM DBS. The DRT, pyramidal tract and lemniscus medialis where reconstructed by tractography in all 20 hemispheres. The distance from the probabilistic atlas-based VIM target to each tract along the x, y and z coordinates was measured. Considerable variability of the location of probabilistic atlas-based target points of the VIM, in relation to neighbouring major fibre tracts, in individual patients was found. These results suggest that individualized targeting to structures not directly visible on conventional MRI may be necessary [141]. A recent report by Coenen et al presents the results of a prospective trial in a group of 11 medically intractable tremor patients who underwent post-hoc deterministic tractography analysis after treatment with traditional thalamic deep brain stimulation. Tractography was processed postoperatively for evaluation, and the DRT was individually tracked. Electrode location was determined with helical CT fused to the preoperative MRI. The average follow-up period was 9 months (Range 3 - 17 months). The authors used the Essential Tremor Rating Score (ETRS) to assess treatment efficacy. This is described as moderate, good and excellent, without defining the degree of reduction in ETRS these categories reflect. Tremor was reduced in all patients with effective contacts located inside or in proximity to the DRT. The stimulation field around the DBS contacts was estimated. Moderate tremor reduction occurred in two patients in whom the stimulation field was centred on the anterior border of the DRT. When good and excellent tremor reduction was achieved (in nine patients), the stimulation field focused on the centre. The authors conclude that tractography can be used to optimize targeting in individual patients [132]. The authors employed a deterministic tractography approach to identify the DRT in each patient. Electrical stimulation field models were derived from individual active DBS contact impedance and stimulation amplitude. The methodology involved multiple registration steps, increasing the registration error margin. Each patient's postoperative CT scan (showing the DBS contacts) was fused to a preoperative MRI scan, which was then normalised to the brain MNI152 space. Each modelled DRT was also normalised to the brain MNI152 space to create a probabilistic DRT model. Stimulation fields were then simulated on the MNI152 brain. Modelling the

electrical stimulation field or activation volume is notoriously complex and current models assume an electrically homogenous and stable local medium, which the brain is certainly not [142,143]. Nevertheless, this is perhaps the most clinically relevant paper to date demonstrating the value of diffusion connectivity in predicting outcome from DBS tremor surgery.

In a study using diffusion connectivity in the operative planning, Schweder et al reported a case of a patient with PD who received bilateral pedunculopontine nucleus (PPN) DBS surgery. The targeting of the PPN was made using the fractional anisotropy (FA) map. Following surgery, the patient had a subjective improvement of 42% on the gait and falls questionnaire and 14% on the freezing of gait questionnaire (FOG-Q). Twelve months post-stimulation the patient underwent a further diffusion acquisition. When the pre-op probabilistic tractography pattern from the target seed was compared to the post-operative pattern, the authors found differences in the connectivity patterns between the two studies[144]. It is not apparent that any useful conclusions can be drawn from the comparison as the study had significant methodological weaknesses. The authors report a single case study. The efficacy of the PPN as a target remains contended. An improvement of 14% in the FOG-Q is very modest. Imaging parameters were poor with diffusion scans taken on a 1.5T MRI scanner along 32 directions with substantially large voxels (2.5 mm isotropic) in relation to the target in question, i.e. the PPN. The authors also performed post-op diffusion imaging in a patient with DBS electrodes implanted in the brainstem, yet they do not comment on safety issues or image artifact arising from the implanted leads. The differences in the tractography between the pre- and the 12 months post-operative imaging may be influenced by lead artifact, seed selection, registration error, various physiological factors or simply ageing, yet the authors do not account for those factors.

1.3.2.2: Pain

Owen et al performed a post-hoc analysis of diffusion connectivity data using seeds from the effective DBS contact location in four patients with medically refractory chronic pain who received DBS in the periaqueductal grey (PAG) and the periventricular grey (PVG)

areas. Probabilistic tractography was performed using diffusion scans acquired pre-operatively. The connectivity pattern was consistent with previously reported non-human primate (NHP) tracer studies, which used horseradish peroxide to trace connections between the PAG and the medio-dorsal thalamus (MD). Other connections to the precentral gyrus and central sulcus were also identified. The findings highlight the possible network involved in the pain pathway, which may allow for target refinement in the future [108]. The authors acknowledge the restrictions associated with diffusion imaging analysis in general, these difficulties become even more pronounced when tractography is performed in the brainstem due to the densely packed tracts and nuclei. Brainstem diffusion imaging can also be affected by physiological elements, such as the cardiac pulse and the respiratory cycle, more than the rest of the brain. Three sets of diffusion image acquisitions were taken on a 1.5T field MRI scanner along 60 diffusion directions. The three sets were then averaged to increase the signal to noise ratio (SNR). The voxel size was 2 mm isotropic (b=1000), which has limitations when tractography is performed outside the brainstem that are accentuated when within it. The authors do not comment on the postoperative structural MRI timing or acquisition parameters. Those were the structural scans used for registration. It is not clear if there were any registration errors especially that the structural and diffusion scans were acquired at different sittings. Brain shift can also occur in the immediate period following surgery, which may affect the accuracy of the registration. The authors conclude that probabilistic tractography, as a surgical planning tool may be a possibility in the future.

1.3.2.3: Psychiatric disorders

In a study utilizing functional connectivity to measure the effect of DBS on neural activity in OCD, Figee et al wrote a brief communication in *Nature Neuroscience* in 2013 detailing a study of 16 patients who received DBS in the NAc and ALIC for medically refractory OCD, and 13 matched controls. Resting state fMRI scans were acquired for the controls, and for patients one year after surgery in two states, on and off DBS. Patients completed an optimization phase during which they were evaluated every 2 weeks for severity of

symptoms and optimal stimulation parameters. The two dorsal contacts were active in all patients, implying that the most effective stimulation area was located at the border of the NAc core and anterior limb of the internal capsule. The authors state that patients showed stable clinical improvements with DBS for at least 1 year. The stimulators were turned off for 1 week, which resulted in a 50% increase in OCD symptoms, an 80% increase in anxiety symptoms and an 83% increase in depression symptoms The authors found the activity in the NAc to be lower in OCD patients in the off state compared to healthy controls, and this abnormal activity was normalized once DBS therapy was resumed. The abnormally increased functional connectivity between the medial and lateral prefrontal cortex (PFC) and the NAc was also normalized with DBS on [145].

In DBS for depression, Riva-Posse et al acquired preoperative diffusion imaging in 16 patients with treatment-resistant depression, who received subcallosal cingulate DBS. The activation volume around the contacts used for chronic stimulation was modelled for each patient retrospectively. Probabilistic tractography was used to delineate the white matter tracts traveling through each activation volume. Response was defined as 50% decrease in the 17-item Hamilton Depression Rating Scale. DBS responders shared bilateral pathways from their activation volumes to the medial frontal cortex via the forceps minor and the uncinate fasciculus; the rostral and dorsal cingulate cortex via the cingulum bundle; and subcortical nuclei including the NAc, caudate, putamen, and anterior thalamus. Non-responders did not show these connections. This meant that patient-specific; activation volume tractography modelling may identify critical tracts that mediate DBS antidepressant response, proposing a novel method for patient-specific target and stimulation parameter selection [146].

Another case report suggested a role that connectivity studies may have in predicting outcome from DBS therapy. McNab et al reported a case of a patient with bipolar disorder syndrome and medically refractory depression developed following a thalamic stroke. The patient was treated with bilateral DBS of the subgenual anterior cingulate cortex (SGCC) with no improvement in the depression scores post operatively. The patient died 16 months

following surgery. Pre-operative and post-mortem diffusion connectivity studies showed evidence of markedly reduced projections from the medial thalamus and the SGCC, to the amygdala on the right (stroke affected) side. The authors concluded that reduced amygdalo-thalamic and amygdalo-SGCC connections could be a predictor of poor outcome following SGCC DBS surgery for depression [147]. However, the SGCC is not an established DBS target for depression and attempting to infer mechanistic information from connectivity studies in this area may be of limited significance.

1.3.3: Studies that examine networks and connections between cortical and subcortical structures

These studies describe techniques to examine networks and connections between cortical and subcortical structures from a purely anatomical prospective, with no special attention to DBS targets [93,94,96,148].

In 2003, Behrens et al published the first report of the use of probabilistic tractography to delineate boundaries between different thalamic nuclei based on connectivity patterns between the thalamus and the different areas in the cortex. This displayed the role that probabilistic tractography could play in parcellating grey matter structures, that traditional maximum-likelihood or streamline approaches have failed to produce. The resulting thalamic segmentation corresponded well with previous histological findings and tracer studies in non-human primates. This has opened up the possibility for the use of this new technique to define potential DBS targets not traditionally visualized on structural MR imaging, such as the VIM nucleus targeted in the treatment of medically intractable tremor [94]. The technique was also validated by Johansen-Berg et al in 2004 [93].

Another notable report by Lambert et al in 2012 used a similar approach to sub-segment and define three major functional regions in the STN based on the maximum probability of connectivity between voxels in the STN, and cortical masks in the emotive, associative and sensorimotor regions. In vivo differentiation between the sensorimotor STN and the emotive and associative parts was only previously possible through invasive microelectrode recording techniques [96]. A similar technique was used by Chowdhury et al

in 2013 to segment the substantia nigra (SN) [97]. In 2014, Accola et al used high resolution MPM acquisitions to segment the STN based on iron content on magnetization transfer (MT) sequences; significant differences in iron contents were found in the emotive and motor areas [149]. Another study mapped the connectivity between the STN and the cortex in what is termed the hyperdirect pathway using both structural and functional connectivity studies; Brunenberg et al used high angular resolution diffusion imaging (HARDI) probabilistic connectivity and resting state fMRI to study the structural and functional connectivity of the STN in 10 healthy subjects. They described the hyperdirect pathway connecting the STN and the motor cortex, and they segmented the STN into associative (ventrolateral), motor (dorsolateral) and emotive (medial) functional sub-regions based on those connectivity patterns. The STN masks were derived from an MNI152 space atlas which might have introduced errors in delineating this small, and highly variable nucleus [150].

In the previous studies, MRI acquisitions were done with 1.5T or 3T magnetic field scanners. Lenglet et al, used ultra-high field MRI acquisitions at 7T to build models of connectivity between the basal ganglia and the thalamus using probabilistic tractography and resting state fMRI, the findings were in keeping with previously mapped connections found in tracer studies in NHPs [148].

In this work, we use functional and structural MR connectivity imaging acquired in patients set to undergo DBS surgery. We present several new analysis methodologies and applications: (1) build predictive models of DBS surgery outcome; (2) refine the surgical target and (3) help build a better understanding of the pathogenesis of the treated conditions and the mechanism of action of DBS therapy.

2. General Methods

2.1: Research questions and hypothesis

The main research questions are twofold.

1. Can brain connectivity imaging be used to predict clinical outcome of DBS surgery?

2. Can brain connectivity imaging be used to better target structures in DBS surgery?

2.2: Ethical Considerations

This protocol was granted ethical approval by West London REC 3 (REC reference number: 10/H0706/68). All subjects went through an informed consent process and provided signed consent. Participants were assessed to see if they were able to tolerate the lengthy imaging paradigm. They were given a copy of the patient information sheet to keep (participant consent and patient information sheet samples are included in the appendix). Patients were invited to attend the Department of Neuroradiology at the National Hospital for Neurology & Neurosurgery, Queen Square to undergo an additional scan within the month prior to surgery (and where possible during the surgical admission to reduce inconvenience of multiple visits). Any additional travel expenses were reimbursed, as is standard practice.

2.3: Finance and Insurance

The Brain Research Trust (BRT) provided a grant for £250,000 to finance this project. This study was sponsored by UCL. All researchers have medical indemnity insurance.

2.4: Data Handling

All personally identifiable data were kept in a locked filing cabinet in a secure building. The neuroimaging and clinical measures were acquired and stored anonymously using code numbers. A log of patient identifiers and their code numbers were stored securely and separately. Patients were further sub-classified per surgical target and symptom of interest. Imaging data were provided only with coded names. All digital data stored on laptops or personal computers logged on a local network were stored using code numbers, and are password protected with exclusive access only for the research team.

2.5: Patient selection

Suitable patients awaiting elective DBS surgery at the National Hospital for Neurology and Neurosurgery were contacted and invited to participate. The patients recruited to this study were selected per their clinical condition and the planned electrode target site. The primary pathologies included were PD treated with the STN as anatomical target, tremor (either in the context of PD or not) with the VIM of the thalamus or the cZi as target and CH and SUNA with the ventral tegmental area as target.

2.6: Imaging protocol

All pre-operative imaging was acquired on a Siemens Magnetom TrioTim Syngo MR B17 with a 3 Tesla field, at the department of neuroradiology, the National Hospital for Neurology and Neurosurgery. Pre-operative stereotactic and Post-operative stereotactic MR imaging was acquired as part of the DBS surgical process on a 1.5 Tesla Siemens Avanto interventional MRI scanner. This included a 1.5×1.5×2.0 mm^3 T2 weighted SPACE and a 3D MPRAGE (voxel dimension) sequence showing the implanted DBS electrode(s). The pre-operative imaging (non-stereotactic) research protocol included three different modalities; DWI acquisitions, followed by whole brain structural, multiparameter mapping

(MPM) scans, and a resting state fMRI scan with a total scanning time of 100 min. For detailed acquisition parameters, see Appendix 1.

Taking into consideration that the MRI protocol is relatively lengthy, patient selection was paramount. The scan had to be well tolerated, and appropriate counselling needed to be given during the consenting process. Whenever patients were not able to tolerate it, the scan was abandoned.

2.6.1: Diffusion Weighted Imaging (DWI)

Diffusion images were acquired using Siemens' 511E Advanced Echo Planar Imaging Diffusion WIP. In-plane acceleration was used (GRAPPA factor of 2) with partial Fourier 6/8. In plane resolution was 1.5×1.5 mm^2 (Field of view 219×219 mm^2, TR = 12200 ms, TE = 99.6 ms) and 85 slices were acquired with a 1.5 mm thickness. Diffusion-weighting with b=1500 s/mm^2 was applied along 128 directions uniformly distributed on the sphere and seven b=0s volumes were also acquired. To correct for distortions all acquisitions were repeated with a reversed phase encoding direction (left to right and right to left phase encode) giving a total of 270 volumes acquired ([128 +7] × 2). Total acquisition time was 62 minutes **(Table 2-1)**.

2.6.2: Multi Parameter Mapping (MPM)

A high-resolution quantitative **multi-parameter mapping (MPM)** approach was developed at the Wellcome Trust Centre for Neuroimaging (FIL) and validated and compared for reproducibility across both, the FIL and the National Hospital sites using two different Siemens Trio Tim scanners. **Quantitative anatomical MRI (qMRI)** is an MRI technique designed to give reproducible, absolute values. This is necessary when comparative studies are undertaken longitudinally (over time) or across multiple sites. The approach eliminates any deviations in the image values attributable to the scanner and reduces bias field artefact thus improving voxel based morphometry (VBM) analysis [151]. Using multi-parameter maps improve the segmentation of subcortical structures owing to the improved contrast-to-noise ratio that MT provides over T1w images [152]. The maps provided

longitudinal relaxation rate (R1 = 1/T1), effective proton density (PD*), magnetisation transfer saturation (MT) and effective transverse relaxation rate (R2* = 1/T2) images [152-154].

The acquisition consisted of three 3D FLASH acquisitions paired with B1 (transmit field mapping data to correct for the effect of inhomogeneous flip angles on the T1 maps) and B0 field map acquisitions. Spatial resolution=1×1×1 mm^3, repetition time=24.5 ms, multiple echo times, field of view=256 mm, flip angle=6 (PD), 21 (T1), 6 (MT) degrees, matrix=256×256, partitions=176; total acquisition time of 26 minutes [151].

Table 2-1: DWI acquisitions with alternating phase encoding

Acquisition number	Phase encoding directions	Rotation degree	TA (min.)	Diffusion directions
1	R >> L	90.00	04:41	20
2	L >> R	-90.00	04:41	20
3	R >> L	90.00	05:42	25
4	L >> R	-90.00	05:42	25
5	R >> L	90.00	04:53	21
6	L >> R	-90.00	04:53	21
7	R >> L	90.00	05:29	24
8	L >> R	-90.00	05:29	24
9	R >> L	90.00	05:05	22
10	L >> R	-90.00	05:05	22
11	R >> L	90.00	05:17	23
12	L >> R	-90.00	05:17	23
		Total	**62:23**	**270**

2.6.3: Resting state fMRI

Multi-echo Echo Planar Imaging (2D-MEEPI) sequences were obtained in two successive acquisitions with a total duration of 15 minutes. Spatial resolution=3×3×2.5 mm^3, repetition

time=60 ms (/slice), echo time=30 ms, flip angle=90 degrees, field of view=192 mm × 192 mm, 45 axial slices (2.5 mm thickness), matrix size=64×64 and a total of 512 scans. Patients were given instructions to keep their eyes open and gaze fixed on a cross hair.

2.7: The surgical procedure

Implantation of the DBS leads was performed using a stereotactic MRI guided and MRI verified approach without microelectrode recording (Leksell frame model G, Elekta Instrument AB, Stockholm, Sweden). Lead implantation was generally performed under general anaesthesia with staged implantation of the Implantable Pulse Generator (IPG) (Medtronic, Minneapolis, Minn., USA) except for patients treated for tremor where the target could not be directly visualised with structural imaging at 1.5T and intraoperative stimulation was necessary to confirm efficacy and avoid side effects. The location of the DBS leads was verified with a stereotactic MRI scan on a 1.5T T2-weighted stereotactic MR image, and a 3D MPRAGE scan was also acquired to rule out any immediate surgical complication e.g. haemorrhage. See **Figure 2-1** for STN visualization and target selection on MRI.

2.8: Data Collection:

The patients underwent all the routine pre-operative checks and screening brain scans prior to DBS surgery. Image acquisition was carried out pre-operatively, during the surgical admission whenever possible. The patients underwent DBS surgery following the routine hospital procedure. As part of this clinical protocol, whilst the patients were still in hospital, routine medications were withdrawn to allow the stimulator to be switched on and to establish optimal DBS settings (normally 2 days to 1 week after the DBS battery (IPG) is implanted). Standardised clinical and psychometric measures were normally taken at this point and these were made available for this study. For the STN-DBS group, each electrode contact was tested in turn and the clinical response documented, this was repeated in a

detailed manner using a screening sheet 6-12 months following surgery. Change in the clinical response was quantified using disease specific, standard, validated measures, as is routine practice for this surgical procedure.

Figure 2-1: STN visualization and target selection on MRI

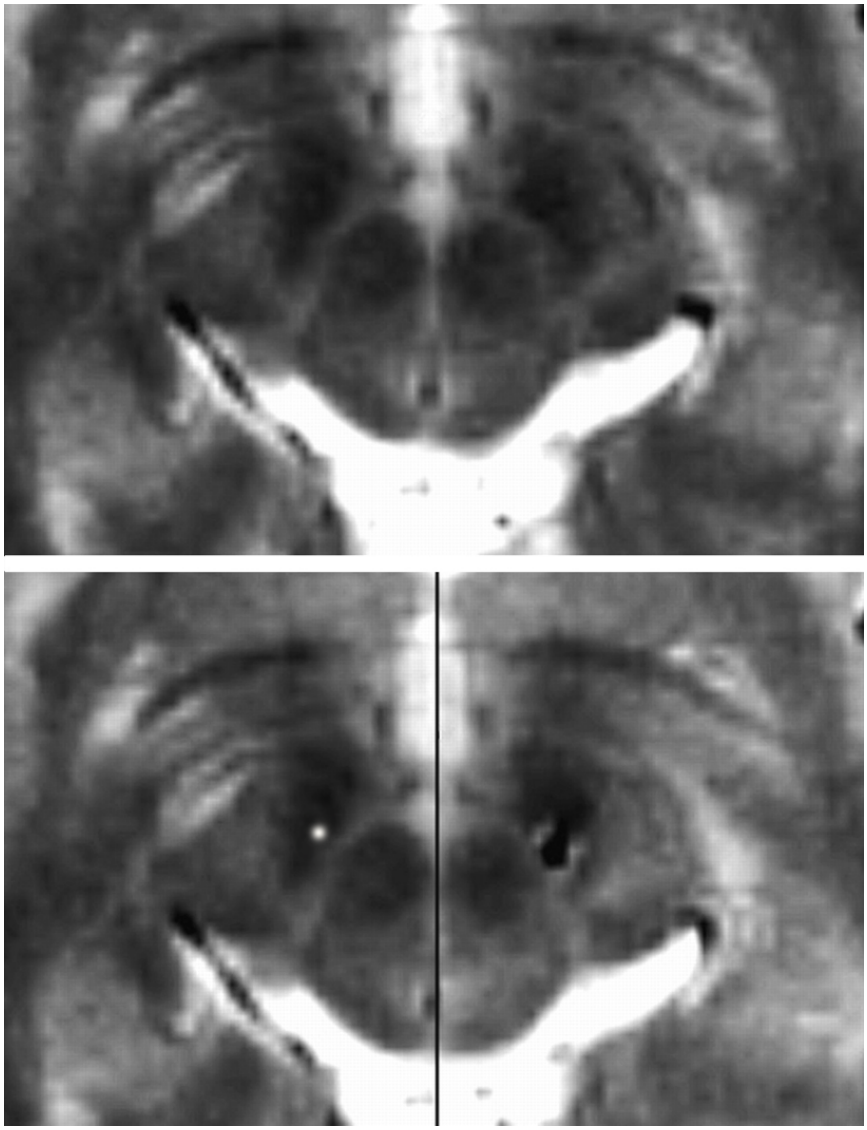

Top panel: Preoperative stereotactic T2-weighted axial MRI (1.5T, 2 mm thickness, no gap, TR 3500, TE 90.9) at the level of maximal rubral diameter (around 5 mm below the AC–PC plane). The subthalamic nucleus (STN) is visualised as the hypointense signal lateral to the red nucleus. Bottom left panel: The entry and target point are selected to maintain a parenchymal trajectory while maximising the length of the trajectory within the visible STN hypointensity from the AC–PC to target level. As a result, the final target point (white circle) is located at the target point originally described by Bejjani *et al*. Bottom right panel: Post-operative stereotactic T2-weighted axial MRI at equivalent level revealing electrode artefact at intended target [61].

2.8.1: Perioperative assessment and outcome measures

A detailed history was taken and a thorough clinical examination performed on every patient. Detailed neuropsychological assessment, including validated scales to assess mood, anxiety and impulsivity, were performed preoperatively.

Details of the specific outcome measures for each study are included in the corresponding chapters.

2.9: Statistical Considerations

2.9.1: Sample Size Calculation

No previous experience with similar diffusion imaging studies in similar subjects exists. Though previous authors have looked at power calculations for simple analysis of major tracts (e.g. pyramidal), they acknowledge varying reproducibility across tracts means that the numbers here cannot be generalised in a straightforward way to other pathways [155]. Using DWI data at 2mm isotropic resolutions in 60 directions with a b=1000s/mm^2, for between group comparisons at a threshold of $\alpha = 0.05$, a minimum number of participants are needed depending on region to ensure 80% power to detect major changes in tract volume. Similar studies looking at simple tractography from subcortical regions in deep brain stimulation have suggested 20 subjects as adequate [112]. The numbers proposed for the present study have been shown, through many diffusion imaging publications, to be appropriate for this type of research question.

We have recruited 20 patients with PD treated with STN DBS. For patients with other pathologies, a target of 6 – 12 patients was reached. This is due to the smaller number of patients with those pathologies who received DBS, which created a recruitment challenge.

2.10: Analysis

Detailed analysis is included in individual chapters.

2.10.1: Diffusion data pre-processing

All diffusion weighted imaging (DWI) scans (with accompanying b=0 scans) were converted from DICOM (Digital Imaging and Communications in Medicine) files to NIfTI volumes and the diffusion gradient direction values and vectors were extracted using *Volconv* (MJ White, NHNN Neuroradiology Department, London UK).

The diffusion data were acquired with reversed phase-encode blips (left-to-right and right-to-left), resulting in pairs of images with distortions going in opposite directions. From these pairs, the susceptibility-induced off-resonance field was estimated using a method described by Andersson et al [156] as implemented in FSL [157] and the two images were combined into a single corrected one using *Topup* (FSL v5.0), a tool for estimating and correcting susceptibility induced distortions prevalent in SSEPI DWI. The output from *Topup* was then fed into Eddy (FSL v5.0) for correction of eddy current distortions and subject movement [158].

The final step in diffusion pre-processing was registration. Patient averaged distortion corrected b=0 volume was registered to brain extracted structural image in native patient space (pre-implantation MPRAGE) with *Flirt* (FSL v5.0) using linear registration with six degrees of freedom, normal search and correlation ratio cost function. The resultant transformations were then composed with the transformations previously generated using non-linear registration between the structural in native patient space and the standard MNI152-1mm space producing diffusion-to-standard space transformations and their corresponding inversions.

The pre-processed data were fed into *BedpostX* (FSL v5.0) to estimate fibre orientations. Up to three crossing fibres were estimated in each brain voxel using model 2 and graphics processing unit (GPU) parallelization [159,160]. *Probtrackx* was then used on these estimates to obtain global connectivity (i.e. the probability of the existence of a path through the

diffusion field between any two distant points, a surrogate measure of anatomical connectivity) [103]. Using the obtained transformations to and from standard space, tractography protocols and masks were defined in MNI space.

2.10.2: Multi Parameter Mapping (MPM) pre-processing

This was carried out in the MPM toolbox (SPM12). MT, PD and T1 weighted imaging MR sequences were processed with paired B1 images; the resultant maps were quantitative MT, PD*, R1 (1/T1) and R2* (1/T2*) maps. The MT map was used for segmentation (SPM12). The resultant grey matter map was later used to create cortical masks for regions of interest (RoI). The grey matter, white matter and CSF maps were combined and binarised to form a brain mask to be used for brain extraction. The R1 map was then used for registration with the subject's diffusion space using FDT (FSL5.0 FMRIB) [151].

2.10.3: Resting State FMRI pre-processing

This section is described in Chapter 3.

2.10.4: DBS Volume of Tissue Activation (VTA)

In order to examine the effects of DBS on the surrounding brain tissue, there is a need to generate realistic, patient specific computational models of tissue activation around DBS electrodes. To date, there is no standardised method for producing these models. The models can therefore vary from simple, single cable models (generally assuming a surrounding axon diameter of 2.5 μm and a homogeneous medium) resulting in spherical volumes that can be quickly and easily produced; to overly complicated, pathway activation models that take into consideration local tissue conductivity and diffusivity (assuming larger diameter axons that require multiple stimuli to generate an action potential) [161].

In this work, we used SureTune® (Medtronic Inc. Minnesota), a DBS therapy planning platform to model VTAs around individual contacts (chapters 4, 5, 6 and 9) and to manually delineate STN volume meshes (chapters 4 and 5). The VTAs were created based on homogeneous finite element simulations of the distribution of the electric potential together

with coupled axon cable models. Axon models were composed of 21 nodes, with a diameter of 2.5 μm and oriented in the vicinity of the lead in a perpendicular orientation. Specific VTA thresholds were calculated for every electrical setting, taking into consideration the specific stimulation configuration, amplitude and pulse width as described by Åström and colleagues, in order to generate DBS therapy VTA [162]. Patient-specific tissue conductivity and patient-specific axon orientations were not considered.

This is a simplified linear model that does not account for local impedance inhomogeneity [163]. While it is important efforts are put into improving DBS models to resemble reality, it may not help to add details to a rough model when the basic knowledge of the DBS mechanisms of actions are still debated. Indeed, various models over- or under-estimate the VTA [142]. The presence of axons of different diameters and cell bodies, with variable action-potential thresholds, in the DBS region, complicates matters further. Our other justification for not using a more ***complex*** model is the fact that minute variations in VTAs are unlikely to have a large effect on statistical analysis and tractography results, due to the relatively larger spatial resolution of our structural and diffusion MRI data.

2.10.5: Sweet Spot Analysis

In order to generate statistically significant, probabilistic clusters predictive of efficacy and side-effects of DBS therapy, a novel analysis method was developed. This method was used in chapters 4 and 9.

In chapter 4, VTAs were generated around all individual DBS contacts at four different stimulation voltages (1,2,3 and 4 V) producing 32 different VTAs. In chapter 9, only VTAs corresponding to the active DBS contacts at the optimised stimulation amplitudes were generated. The VTAs were transformed from subject space to MNI space and a group average VTA region of interest was then generated from all individual VTAs.

A general linear model (GLM) was created with efficacy (chapters 4 and 9) and side-effects variables (chapter 4) that are associated with each VTA to test against each voxel in that VTA. A single-group average design was used. The variables were demeaned and single

group t-test with threshold-free cluster enhancement (TFCE) was used as test statistic [164]. Nonparametric permutation inference approach, similar to that commonly used for VBM and fMRI time series analysis, was carried out for each voxel (within the overall group average VTA region and not the entire brain) using *Randomise* (FSL5.0) with 5000 permutations to build up the null distribution to test against as previously described [165]. Raw t-stat (t statistic) images were then masked by the significant voxels from thresholded (α=0.05) t-stat images, also corrected for multiple comparisons.

2.10.6: Computational Resources

One of the obstacles when seeking to employ probabilistic tractography clinically is the computational resources needed to process the raw data in a feasible, timely fashion. Parallel processing, or general processing over GPU (GPGPU) techniques have been developed to use GPU cores instead of using the CPU when processing big datasets. This has shown very promising results when used in processing diffusion data [160]. For this reason, we decided to build a GPU cluster for the sole use in processing the diffusion data. The system has four CUDA enabled NVIDIA GeForce GTX TITAN GPU cards, with a combined sum of 11,520 cores (**Figure 2-2).**

2.11: Post-processing

Details of the specific post-processing for each study are included in the corresponding chapters.

2.12: Recruitment into the study

Table 2-2 gives a summary of the different conditions and number of patients recruited and needed in each category.

Figure 2-2: Gilgamesh, the high performance computer built for general processing over GPU (GPGPU).

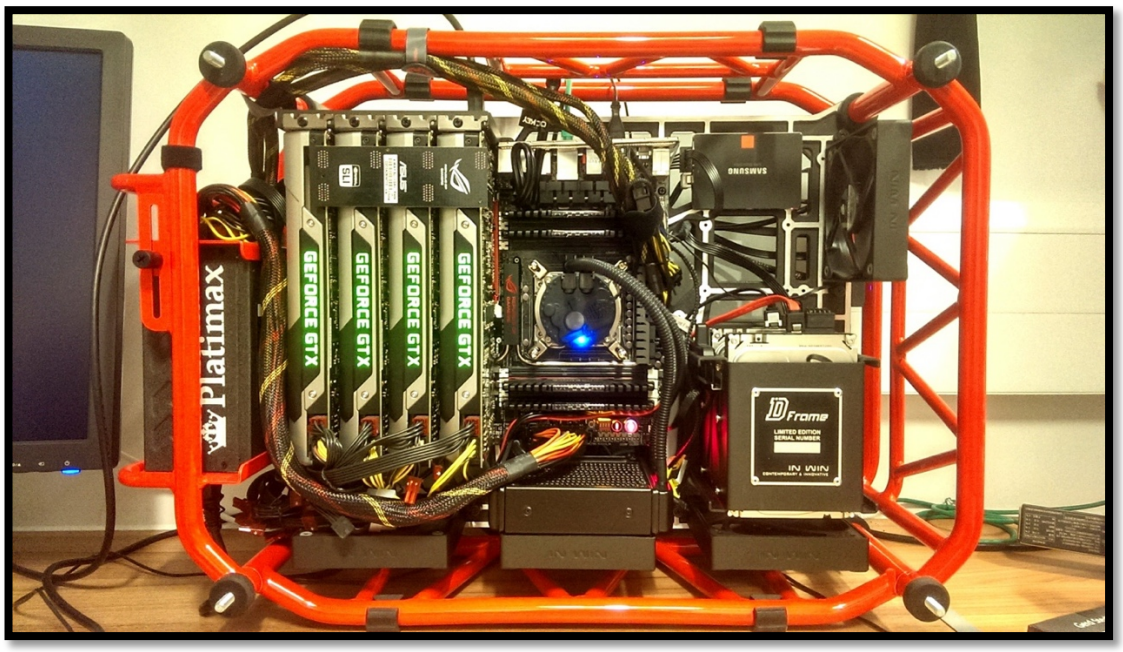

Table 2-2: Shows the various patient groups recruited with DBS target and number of patients recruited.

Patient group	DBS target	Recruited
Parkinson's disease (PD)	STN	21
Cluster headache	VTa	19*
SUNA	VTa	11**
Tremor dominant PD	VIM	4
Essential tremor	VIM	5
	Total	**60**

* 7 patients with CH underwent connectivity studies

** Only 3 patients with SUNA underwent connectivity studies, therefore, only clinical analysis of efficacy and side-effects was carried out

STN = subthalamic nucleus, VTa = ventral tegmental area, VIM = ventrointermedialis of the thalamus.

Section I:

Connectivity in Parkinson's Disease

"The pathological physiology of the Parkinsonian syndrome is the study of an organized chaos, a chaos induced in the first instance by destruction of important integrations and reorganized on an unstable basis in the process of rehabilitation" [166]**.**

Ivy Mackenzie (1877-1959).

3. Functional connectivity: L-DOPA Responsiveness in Patients with Advanced Parkinson's Disease

3.1: Abstract

Neuronal loss and dopamine depletion alter motor signal processing between cortical motor areas, basal ganglia and thalamus, resulting in the motor manifestations of Parkinson's disease. Dopamine replacement therapy can reverse these manifestations with varying degrees of improvement. To evaluate functional connectivity in patients with advanced Parkinson's disease and changes in functional connectivity in relation to the degree of response to L-DOPA, nineteen patients with advanced Parkinson's disease underwent resting state functional magnetic resonance imaging in the ON medication state. Scans were obtained on a 3 Tesla scanner in 3×3×2.5 mm^3 voxels. Seed based bivariate regression analyses were carried out with atlas-defined basal ganglia regions as seeds, to explore relationships between functional connectivity and improvement in the motor section of the Unified Parkinson's Disease Rating Scale (UPDRS-III) following L-DOPA challenge. False discovery rate (FDR)-corrected p-value was set at <0.05 for two-tailed t-test. A greater improvement in UPDRS-III scores following L-DOPA administration was characterized by higher resting state functional connectivity between the prefrontal cortex and the striatum ($p=0.001$) and lower resting state functional connectivity between the pallidum ($p=0.001$), subthalamic nucleus ($p=0.003$) and the paracentral lobule (supplementary motor area, mesial primary motor and primary sensory areas). Our findings show characteristic basal ganglia resting state functional connectivity patterns associated with different degrees of L-DOPA responsiveness in patients with advanced Parkinson's disease. L-DOPA exerts a graduated influence on remapping connectivity in distinct motor control networks, potentially explaining some of the variance in treatment response.

3.2: Introduction

Parkinson's disease is a neurodegenerative disorder that affects multiple systems in the brain in a progressive and, to some extent, a predictable fashion [167]. Considerable degeneration of dopaminergic neurons in the substantia nigra pars compacta leads to dopamine depletion in the striatum. This depletion causes dysfunction within the basal ganglia-thalamo-cortical 'motor' circuit, resulting in the hallmark motor triad of resting tremor, rigidity and bradykinesia. [168,169].

Numerous animal and human studies have demonstrated structurally and functionally segregated parallel circuits or loops that connect the cortex to the basal ganglia and thalamus [170-172]. This segregation is essential for motor processing and learning. Dopamine deficiency results in loss of this segregation and emergence of synchronized oscillations between basal ganglia structures and cortical areas. [173]. A correlation between motor deficits in Parkinson' and abnormal synchronized oscillatory activity, especially in the 'beta' band width (15-35hz) [174-176], has been shown at multiple levels in the motor circuit, which is also suppressed by dopaminergic therapies [177-179]. Alterations of basal ganglia physiology in Parkinson's disease, therefore, broadly consist of two elements: an increase in the neuronal discharge rate in the STN and globus pallidus internus (GPi) and the appearance of synchronized neuronal oscillations [180]. A new, dynamic 'center-surround model' has been proposed with excitatory input from the motor cortex directly influencing the STN through the 'hyper-direct' pathway and affecting the globus pallidus without passing through the striatum [181-184].

Functional connectivity of the brain can be explored using resting state fMRI. This offers a relatively simple and fast approach to map brain functional connectivity and pathological neural network changes. The technique does not rely on an experimental task design, making data analysis streamlined and less vulnerable to experimental bias [185].

The time course of low frequency (<0.1 Hz) fluctuations in blood oxygen level-dependent (BOLD) signal has a high degree of temporal correlation in functionally connected brain areas or 'nodes' [186]. Multiple statistical modeling techniques, such as seed-based

correlation mapping and independent component analysis (ICA), can then be used to examine this functional connectivity [185,187]. Resting state functional connectivity (fcMRI) has been used in various clinical applications [188]. For example, selective changes were found in individuals at risk of Alzheimer's disease [189] and also documented in patients with major depression [190]. Statistically significant positive correlations have been found between fcMRI and structural connectivity [191-194].

Resting state fMRI connectivity changes may relate to the abnormal synchronized oscillations in Parkinson's disease. Evidence for this relation has been demonstrated in numerous human and non-human primate studies. Correlation between the slow frequency (<0.1 Hz) of the BOLD signal in resting state fMRI and neural electrophysiological activity at higher frequencies [195], in the alpha band range [196], the gamma band range [197] and in the beta band range [198], provides inference between networks identified using fcMRI and their underlying neurophysiological correlates. This relation can be very useful in studying and understanding Parkinson's disease neurophysiology.

To date, several fcMRI studies have examined the connectivity profile in patients with Parkinson's disease compared to healthy controls and the effect L-DOPA therapy has on the connectivity pattern [199-207]. The majority of these studies, with the exception of one [206], were on patients in the early stages of Parkinson's disease. Limited information is available about the functional connectivity changes that occur later on in the course of the disease when complications of chronic L-DOPA therapy, such as levodopa induced dyskinesias (LID) and motor fluctuations, emerge.

Furthermore, patients can have varying degrees of response to L-DOPA in advanced Parkinson's disease. The emergence and progression of L-Dopa refractory signs represents one of the most challenging aspects of treating the disease. Furthermore, the degree of L-Dopa responsiveness is an important factor in patient selection for STN DBS. Greater than 25%–50% improvement in motor UPDRS (UPDRS III) following 'L-DOPA challenge' is generally considered a good outcome predictor for STN DBS in Parkinson's disease [208].

In this study, a seed-based approach to resting state functional MRI is used to examine differences in functional connectivity of the basal ganglia with cortical and subcortical areas in relation to the degree of clinical response to L-DOPA challenge in 19 patients with advanced Parkinson's disease and motor fluctuations. Our aim is to identify the fcMRI correlates associated with differences in treatment response to better understand the underlying neural network activity in advanced Parkinson's disease.

3.3: Materials and methods

3.3.1: Patients

Nineteen patients who met UK brain bank criteria for idiopathic Parkinson's disease were included (**Table 3-1**). Patients were recruited from the surgical waiting list for bilateral STN DBS after selection by a multidisciplinary team of specialized movement disorders neurologists and functional neurosurgeons. All patients underwent a neuropsychological assessment and a structural brain MRI to rule out dementia and significant brain atrophy, respectively. A formal L-DOPA challenge test was conducted, whereby the motor section of the unified Parkinson's disease rating scale (UPDRS III), was assessed in the OFF state at least 12 hours after omitting Parkinson's disease medications and repeated 30-60 minutes (or when clinically ON) after administration of the patient's regular medications supplemented with an additional dose of 50mg/12.5mg dispersible Madopar. Inclusion in the present study was limited to L-DOPA responsive patients with advanced Parkinson's disease with at least 25% improvement of UPDRS III between off and on medication states and who could tolerate lying flat for the duration of the scan.

3.3.2: Magnetic resonance imaging data acquisition

Imaging was acquired during admission before DBS surgery. Medications were optimised by a specialist neurologist to ensure patients were in the ON- state, with no concurrent head tremor or LID at the time of MRI. 3T Siemens Magnetom Trio Tim Syngo MR B17 was used with a well-padded 32 channel receive head coil to reduce discomfort and head motion during the scan.

3.3.3: Resting state functional MRI

Multi-echo Echo Planar Imaging (2D-MEEPI) sequences were obtained in two successive acquisitions with a total duration of 15 minutes. Spatial resolution=3×3×2.5 mm^3, repetition time=60 ms (x 45 slices = 2700 ms), echo time=30 ms, flip angle=90 degrees, field of view=192 mm × 192 mm, 45 axial slices (2.5 mm thickness), matrix size=64×64 and a total of 512 scans. Patients were given instructions to keep their eyes open and gaze fixed on a cross hair

3.3.4: Structural MRI

Multiple Parameter Mapping (MPM) sequences [151] were acquired for structural imaging just before the functional MRI scan. In brief, the whole protocol consisted of three 3D FLASH acquisitions performed with T1, Proton Density (PD), and Magnetization Transfer (MT) weighting; these were paired with B1 (transmit field mapping data to correct for the effect of inhomogeneous flip angles on the T1 maps) and B0 field map acquisitions. Spatial resolution=1×1×1 mm^3, repetition time=24.5 ms, multiple echo times, field of view=256 mm, flip angle=6 (PD), 21 (T1), 6 (MT) degrees, matrix=256×256, partitions=176; total acquisition time of 26 minutes.

3.3.5: Preprocessing

The structural scans were processed using the voxel based quantification (VBQ) toolbox in SPM12 to generate quantitative maps of multiple tissue properties (MT, PD*, R1 (1/T1) and R2* (1/T2*)) [151]. The MT maps, which provide high contrast to noise ratio, were segmented to generate white matter, grey matter and cerebrospinal fluid (CSF) maps using the 'Segment' toolbox in SPM12 [152,209].

The first three scans of each resting state session were discarded. The two sessions were concatenated to produce a single 506 scan time-series. Functional volumes underwent realignment, unwarping and slice-timing correction. The functional scans of each subject were rigidly registered to the anatomical (R1) scans and the corresponding CSF and white matter maps. Anatomical scans were then spatially normalized to MNI space (spatial

resolution=2×2×2 mm^3); the resultant transformation was further used to normalize the functional data. Functional outlier detection was carried out using Artifact Detection Tools (ART)-based scrubbing (www.nitrc.org/projects/artifact_detect/). The functional volumes were then inspected and smoothing was applied to reduce potential spatial and temporal artifacts using an 8 mm full width at half maximum Gaussian kernel.

In order to reduce spurious sources of variance in the functional data; denoising was carried out using component-based noise correction method (CompCor) [210]. The temporal time series with estimated subject motion (three rotation and three translation parameters, plus another six parameters representing their first-order temporal derivatives), as well as the BOLD time series within the subject-specific white matter mask (three principal component analysis parameters) and CSF mask (three principal component analysis parameters), were used as temporal covariates and removed from the BOLD data using linear regression. Ultra-low frequency fluctuations in the resulting residual BOLD time series were removed using a high-pass filter (1/128s, ≈0.0078 Hz). All processing steps were undertaken in MATLAB-based CONN toolbox [211].

With tremor and dyskinesias as potential sources of motion, the framewise displacement (FD) was calculated in order to precisely quantify the degree of motion correction performed for each volume of each subject [212]. In order to assess the possibility of movement confounding fcMRI analysis, a Pearson correlation was performed between the mean of each patient's FD values and the fcMRI of interest.

3.3.6: Analysis

Seed based analysis was performed. Regions of interest (ROI) were defined on the FSL Harvard-Oxford cortical structural atlas, the ATAG subthalamic nucleus atlas [213], and the ATAG MNI04 basal ganglia atlas. The right and left caudate, putamen, pallidum, STN, and thalamus were defined as ROIs for seed-to-voxel and ROI-to-ROI analysis. Those nodes largely incorporate the subcortical elements of the cortical-basal ganglia-thalamic loop implicated in motor control [214,215]. The paracentral lobules were used in the ROI-to-ROI analysis to further explore the strong fcMRI shown in the seed-to-voxel analysis.

Bivariate regression coefficients of the ROIs BOLD time series were measured before being entered into second-order between subject analysis. The connectivity of each of these network nodes to the rest of the brain was individually explored using seed-to-voxel analysis. FcMRI within cortico-basal ganglia-thalamic circuits was also explored using ROI-to-ROI analysis. Only the BOLD signal within each subject-specific gray matter mask was included in these calculations; normalizing each subject to the aforementioned atlases permitted second order analysis.

General linear models were generated to assess the relationship between the degree of improvement after L-DOPA (% improvement UPDRS-III) and connectivity. Thresholds for voxel-level height and cluster-level extent were set to a false discovery rate (FDR)-corrected P-value of <0.05. Seed-level correction was used to apply FDR separately for each seed ROI by implementing both a voxel-level height threshold and a cluster level extent threshold. Given the changes that occur in fcMRI with age (Ferreira, 2015), the primary effect of change in UPDRS III score with medication on functional connectivity was investigated while controlling for patient age in the GLM. In order to account for any effects related to differences in disease severity at the time of testing, the primary effect of L-dopa related change in UPDRS III score on cortico-basal ganglia-thalamic networks was investigated while controlling for UPDRS III OFF-medication score.

3.4: Results

3.4.1: Patients

Scanning proceeded with no adverse effects. The mean improvement in UPDRS III following L-DOPA administration was 26.3 points (60%, SD=20%) [95% confidence interval (CI): 21.5–31.1, P<0.0001]. There was no significant difference between the left and right UPDRS III OFF hemi-body scores [mean difference 2.4 points, P=0.12]. One patient had L-DOPA responsive tremor-dominant Parkinson's disease (UPDRS III OFF=33, ON=10). Mean Mini Mental State Examination Score (MMSE)=29.5/30 (SD=0.6). Modified Hoehn

and Yahr Staging was 3-4 for all patients. Mean levodopa equivalent dose (LED) was 1330 mg (SD=484.5). No significant correlation was found between daily LED and UPDRS-III OFF scores (r=0.16, P=0.5) or UPDRS-III improvement during L-DOPA challenge (r=0.32, P=0.18 and r=0.25, P=0.31 for raw and percentage change respectively). Detailed patient information can be found in **Table 3-1.**

Table 3-1: Patient information and L-DOPA challenge

		Range	Mean ± Std. Deviation
Age (yr.)	-	41-70	55.5 ± 9.9
Gender	15M, 4F	-	-
Hand dominance	19 RHD		
Disease duration (yr.)	-	4-22	11.2 ± 4.4
Duration of motor fluctuations (yr.)	-	1-9	3.4 ± 1.8
UPDRS III OFF (p)	-	20-73	43.8 ± 12.9
UPDRS III ON (p)	-	4-42	17.5 ± 9.9
Left hemibody UPDRS III OFF (p)	-	4-23	14.2 ± 6
Right hemibody UPDRS III OFF (p)	-	4-20	11.8 ± 4.7

RHD=right hand dominant, M=male, F=female, yr.=year, p=points

3.4.2: Quantification of Motion Correction

Mean framewise displacement (FD) values ranged from 0.3 mm to 2.8 mm (1.6 ± 0.7 mm). No volumes were discarded in preprocessing. There was no statistically significant correlation between FD measures and fcMRI calculations. (**Table 3-2**)

Table 3-2: Analysis of potential effects of motion correction (framewise displacement, FD) on resting state functional connectivity (fcMRI)*

	GP-PL	Thal-PL	STN-PL	Put-PL	GP-M1	Thal-M1	STN-M1	Put-M1	Caud-MFPC	Caud-LPFC	Put-LPFC
R	0.05	0.44	0.37	0.01	0.16	0.27	-0.01	0.04	0.13	0.34	0.39
p-value	0.88	0.18	0.27	0.98	0.64	0.43	0.99	0.90	0.71	0.31	0.24

* For each ROI-to-ROI analysis, a Pearson correlation was performed between mean FD values for each patient and the calculated fcMRI values.

GP = globus pallidus; Thal = thalamus; STN = subthalamic nucleus; Put = putamen; Caud = caudate; PL = paracentral lobule; M1 = motor cortex; MFPC = medial prefrontal cortex; LPFC = lateral prefrontal cortex

3.4.3: Basal ganglia and thalamic functional connectivity

Greater improvement in UPDRS III scores following L-DOPA administration was associated with higher fcMRI between the caudate and dorsolateral and medial prefrontal cortices and between the putamen and the inferior part of the left dorsolateral prefrontal cortex (DLPFC), centered on the inferior frontal gyrus. Greater improvement in UPDRS III scores was also associated with lower fcMRI between the basal ganglia and thalamus and the sensorimotor cortex, specifically, in the mesial areas with the portions of M1, SMA, and S1 residing in the paracentral lobule and superior portion of the cortical convexity. This was particularly notable for the pallidum and thalamus, and less prominent for the caudate and putamen. **(Table 3-3)**

The cluster for STN negative correlations with M1 and S1 was more diffuse. Greater improvement in UPDRS III scores was also associated with lower fcMRI between the thalamus and the posterior parietal cortex (PPC), between pallidum and PPC, between pallidum and lingual and fusiform gyri (visual association area), between STN and right PPC, between STN and left superior temporal gyrus, between STN and lingual gyrus, cuneus and precuneus (left) and between STN and posterior and caudal anterior cingulate cortices. **(Figure 3-1)**

Table 3-3: Functional connectivity of basal ganglia and thalamus with paracentral lobule in correlation with UPDRS III reduction following L-DOPA administration

	Paracentral lobule				*t*-score	FDR corrected P-value
	MNI coordinates			Cluster Size		
	x	y	z			
STN	+32	-16	+56	9445	-3.46	0.0032
Pallidum	+24	-48	+58	10407	-4.03	0.0010
Caudate	+14	-52	+62	2672	-3.72	0.0018
Putamen	-02	-12	+74	2123	-3.36	0.0040
Thalamus	+32	-30	+74	8093	-3.77	0.0017

MNI coordinates represent the centre of gravity of the cortical cluster

FDR=false discovery rate

Figure 3-1: Functional connectivity changes between cortical areas and subthalamic nucleus (A), globus pallidus (B), caudate (C), putamen (D) and thalamus (E) in relation to percentage improvement in UPDRS III with L-DOPA administration using a seed-to-voxel analysis

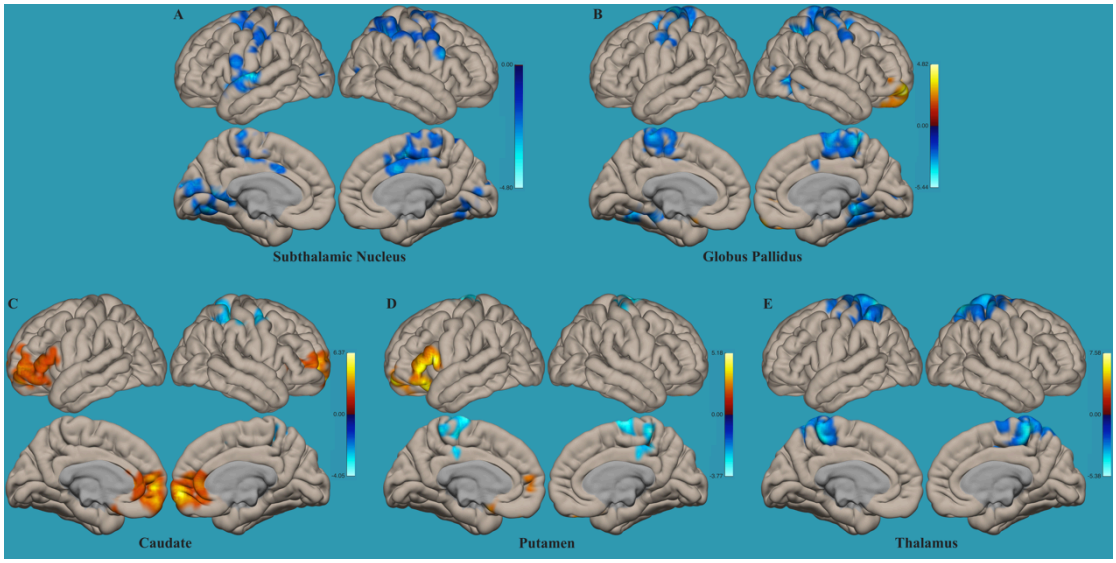

Colour scale represents t score values

Figure 3-2: Connectivity graph showing ROI-to-ROI analysis (*t*-score) against improvement in UPDRS III following L-DOPA administration

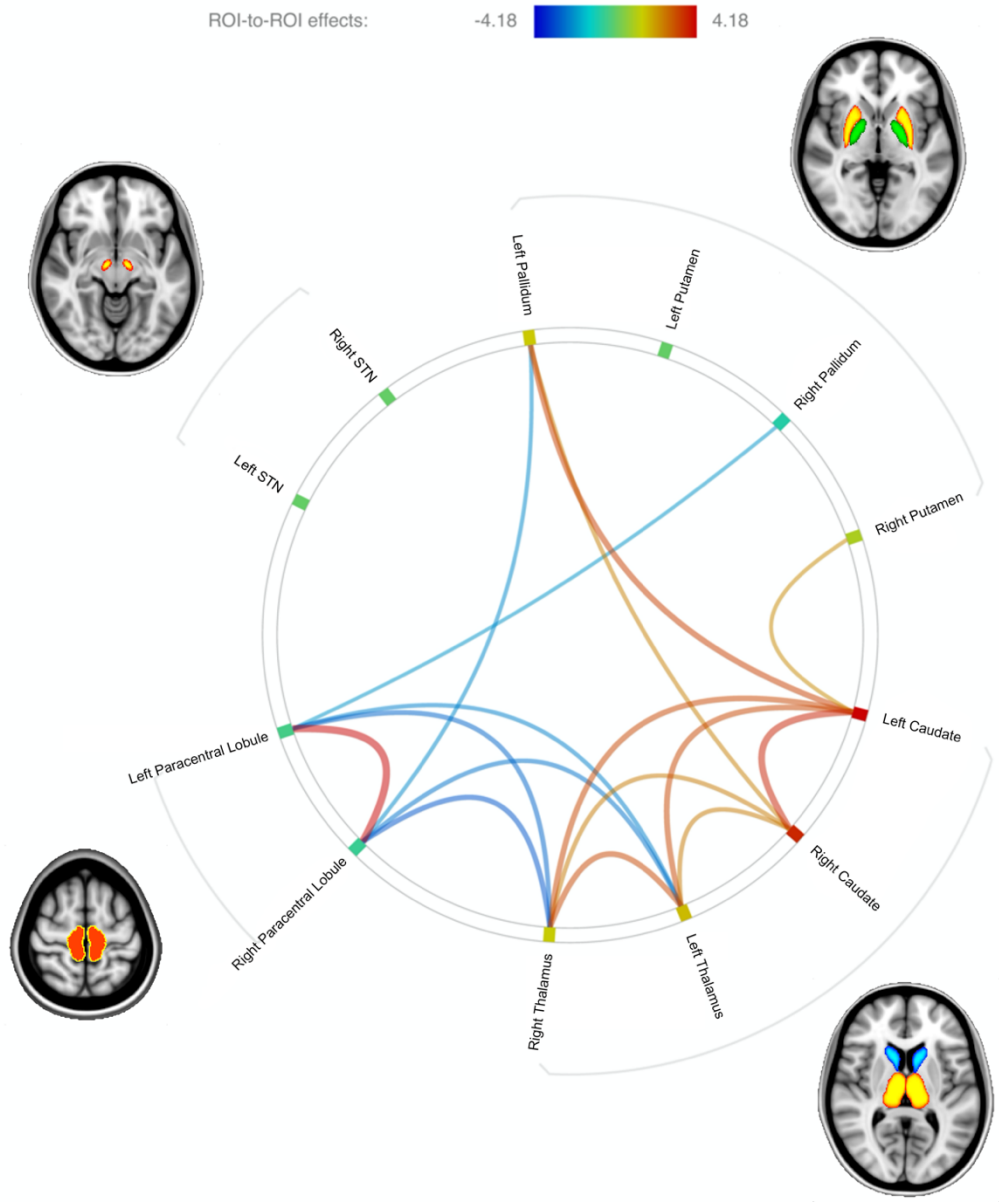

Line colors and width reflect the strength and polarity of connectivity as designated in the heat bar (correlations represented in orange and red; and anti-correlations represented in blue). The nodes on the perimeter of the connectivity circle are labeled and their colors correspond to those illustrated on the adjacent brain images.

ROI-to-ROI analysis showed that UPDRS III improvement with L-DOPA was positively associated with higher fcMRI between the caudate and the thalamus [t=3.27, corrected-p=0.03] and the caudate and the pallidum (t=3.38, corrected-p=0.01), on the left. A similar trend was also seen on the right side between the caudate and the thalamus but did not reach statistical significance after correcting for multiple comparisons (t=2.60, corrected-p=0.07. **(Figure 3-2)**.

3.5: Discussion

In In this work, resting state functional MRI was used to examine basal ganglia and thalamic functional connectivity in patients with advanced Parkinson's disease. Employing seed-to-voxel and ROI-to-ROI approaches, associations with the degree of response to L-DOPA were demonstrated. After adjusting for age and disease severity (baseline UPDRS III), significant associations were evident between L-dopa responsiveness and fcMRI between basal ganglia and cortex, and within basal ganglia and thalamus. The degree of response to L-DOPA, as measured by improvement of UPDRS III scores, was associated with increased fcMRI between the striatum and thalamus (caudate-pallidum and caudate-thalamus) and between the striatum and the PFC. The degree of response to L-DOPA was inversely associated with increased fcMRI between the thalamus, pallidum and STN and the paracentral lobule and parieto-occipito-temporal association areas. As there was no significant correlation between movement correction measures and fcMRI, it is more likely that these findings are the result of inherent differences in the basal ganglia-thalamic-cortical networks than the result of differences in patient movement.

Daily LED did not appear to correlate significantly with the degree of UPDRS-III response during the L-DOPA challenge or with the baseline UPDRS-III scores. This is likely due to the unpredictable bioavailability of dopamine in the brain following oral administration of levodopa mediated by erratic intestinal absorption, metabolism and transport across the blood brain barrier [216-218]. Levodopa dose was therefore discounted from the analysis.

A consistent pattern of change in metabolic activity in Parkinson's disease has been described previously in PET studies. Disease progression is often associated with increasing metabolism in the STN, GPi and thalamus as well as in the dorsal pons and M1, which progresses to declining metabolism in the PFC, SMA and inferior parietal regions. This pattern is shown to be reproducible and is referred to as a Parkinson's disease related covariance pattern (PDRP) [219-221]. Studies that used task-based fMRI to examine the activation patterns of the motor network in Parkinson's disease patients showed cortical activation abnormalities centered on a fronto-parietal cortical network comprising the pre-SMA, M1, and posterior parietal cortex, partially reversed with L-DOPA. Inconsistent results, potentially a consequence of disparities in selection and timing of the applied tasks, were found in those studies. [222].

Other studies have looked at group changes in activation in early or advanced PD patients in the presence and absence of L-dopa therapy, but none have sought to directly analyze the relationship between functional connectivity and degree of L-dopa response.

In a study that examined fcMRI changes in Parkinson's disease, a reduction in connectivity between the SMA, left dorsolateral PFC and left putamen was demonstrated. This connectivity pattern correlated with UPDRS III and was relatively normalized following L-DOPA administration [199]. Decreased connectivity between the PFC and the left putamen, right insula, right PMA, and left inferior parietal lobule was also demonstrated in another study of 18 Parkinson's disease patients and matched controls [202]. We showed in the present study that an increase in resting functional connectivity between the PFC, mostly in the inferior frontal gyrus (IFG), and the striatum was associated with a better response to L-DOPA. The IFG role is well described in the behavioral (proactive) inhibition network [223-229]. It has also been implicated in the pathogenesis of L-DOPA-induced dyskinesias (LID), possibly a reflection of motor inhibition network failure. Transcranial magnetic stimulation (TMS) over the right IFG reduces the extent of dyskinesia induced by a supra-maximal single dose of L-DOPA [206].

Changes in fcMRI between the STN, M1, SMA and PMA have been previously described in Parkinson's disease compared to controls. In a study of fcMRI of the STN in 31 Parkinson's disease patients with early stage disease during the medication-off state compared to 44 healthy controls, connectivity was increased to M1, SMA and PMA. A tremor-dominant subgroup showed localized increase in connectivity between the STN and hand area of M1 and the primary sensory cortex. In a non-tremor subgroup, increased connectivity was found between the STN and mesial cortical motor areas including the SMA [201].

The pattern of fcMRI changes shown in our study is supported by findings from a recent study that looked at differences in 'networks' identified on independent components analysis (ICA) in 27 Parkinson's disease patients and 16 controls. Significant functional connectivity increase in patients, between the sensorimotor network and the spatial attention network in the parietal cortex, was found and was correlated with UPDRS III [207]. Furthermore, L-DOPA has been shown to restore fcMRI in the sensorimotor network, especially in the SMA, when administered to drug-naïve patients [204].

Our analysis did not show a statistically significant correlation between improvement in UPDRS III and change in fcMRI between the putamen and the inferior parietal cortex. However, changes in fcMRI between these areas have been shown in Parkinson's disease patients when compared to controls [200].

We have shown that reduced resting functional connectivity between the striatum, pallidum and the thalamus is associated with a worse response to L-DOPA. It is conceivable that this finding is a result of the breakdown of segregation within the basal ganglia and the emergence of oscillatory activity within the sensorimotor network with dopamine depletion [173]. This pattern of fcMRI abnormality was also demonstrated in a study that focused on the functional connectivity between the striatum, thalamus and the brainstem. In that study, 13 patients with advanced Parkinson's disease compared with 19 controls showed lower functional connectivity patterns with the thalamus, midbrain, pons and cerebellum. A progressive 'gradient' of altered connectivity (posterior putamen > anterior putamen >

caudate) was observed in keeping with the pattern of dopaminergic loss in the pathogenesis of PD [203].

The shared findings of studies that investigated the way fcMRI is influenced by L-DOPA in Parkinson's disease [199-205,207], point towards an abnormal fcMRI pattern which is relatively restored following L-DOPA administration. We propose that the contrasting patterns of functional connectivity that we have observed in association with L-DOPA responsiveness are a reflection of the relative degrees of normalization of functional connectivity with dopamine therapy. On the one hand, improvement of motor symptoms with L-Dopa was associated with increased resting functional connectivity between the striatum and the DLPFC and IFC; and on the other hand with decreased resting functional connectivity of the STN and pallidum with the paracentral lobule and parieto-occipito-temporal association areas. It has been previously shown that PD patients can suppress involuntary movements albeit for short periods of time [230]. Given that we examined functional connectivity in the resting state, when patients were instructed to remain at rest and refrain from making any movements, the observed pattern of increased caudate-DLPFC/IFC functional connectivity with greater L-Dopa responsiveness may potentially reflect engagement of a goal-directed proactive inhibition network to withhold voluntary movement [229,231]. By contrast, the negative association between L-Dopa responsiveness and functional connectivity of the STN and pallidum with the M1 and posterior association areas may reflect engagement of a more 'reactive' inhibition pathway via the hyperdirect pathway [229,231] for withholding movements during the resting MRI in those with a worse response to levodopa medication. However, further work is needed to support this proposition.

Increased functional connectivity between the thalamus and the sensorimotor cortex has been previously demonstrated in fcMRI studies comparing PD patients to healthy controls [232]. This is consistent with primate models of PD where there is increased activity in the ventrolateral thalamus [215]. In our study, we demonstrated a negative correlation between thalamic-sensorimotor fcMRI and the response to L-DOPA. This once again supports the

hypothesis that in poor responders there is reduced fcMRI normalisation to dopamine than in good responders.

The validity of negative correlations, or anticorrelations, as neurophysiological findings in fMRI data has been a subject of debate. Analytic artifacts may arise from carrying out global signal regression to remove confounds due to noise in the BOLD time series, leading to anticorrelations even when they are not truly present [233-235, 236]. This had led to a widely accepted consensus not to interpret those findings when using global signal regression [233,237]. In our analysis, however, we applied the CompCor method of noise reductions, which does not rely on global signal regression and which has been shown to have higher sensitivity and specificity [238]. It is believed that the use of the ComCor method can generate valid anticorrelations between brain networks in fMRI [211]. We consider that the findings of negative correlations between subcortical and cortical areas in relation to the degree of response to L-DOPA here may have sound neurophysiological basis.

3.5.1: Limitations

All our patients were on optimal L-DOPA medication at the time of the MRI scan. For this reason, we cannot make any inferences on the acute effects of L-DOPA on the underlying pathophysiology as was demonstrated in other reports that compared changes in fcMRI before and after L-DOPA administration. [199-207]. In contrast with the majority of these reports our patients had advanced Parkinson's disease with severe motor fluctuations and, not infrequently, freezing of gait. We opted to only scan the patients in the ON state with their usual treatment regime firstly to reduce patient discomfort during the MRI scan and secondly to reduce motion artefact, which may degrade the quality of the resulting fMRI scans.

Another limitation associated with fcMRI techniques is that the technique is largely limited to group-level analysis. While this is useful in exploring group-wise changes, inferences on the individual level cannot be readily made, especially on a diagnostic/predictive capacity. This may limit the clinical application of the technique in individual patients.

Our analysis focused on fcMRI changes between cortico-subcortical structures in Parkinson's disease. We employed prior knowledge to define basal ganglia structures as ROIs for connectivity analysis. We have not explored cortico-cortical fcMRI changes and our findings, therefore, are limited to networks that include those predefined ROIs.

3.6: Conclusion

Differences in functional connectivity patterns of the basal ganglia, as mapped using resting state fMRI, are associated with different degrees of response to L-DOPA therapy in patients with advanced Parkinson's disease, at the group level. This is consistent with the hypothesis that the clinical effects of dopamine are a result of remapping of functional connectivity. Networks linked to cognitive (proactive) motor inhibition show relatively higher connectivity whilst networks linked to reactive motor inhibition show lower connectivity with better dopamine response. Furthermore, connectivity is relatively stronger in between basal ganglia structures with better dopamine response. Future studies may be able to validate these results and explore markers at the 'individual level' by employing machine learning algorithms to build predictive models of response to treatment, thus validating, or even corroborating the L-DOPA challenge test. The next step will be to explore the functional connectivity correlates predictive of response to STN DBS in this group once data become available. This could potentially aid with patient selection and help with understanding the mechanism of action of DBS.

4. Subthalamic deep brain stimulation sweet spots and hyperdirect cortical connectivity in Parkinson's disease

4.1: Abstract

The optimal stimulation site for subthalamic nucleus deep brain stimulation remains ill-defined. Previous studies disagree on whether contacts within the nucleus, or superior to it, give best improvement in motor symptoms. Furthermore, the role cortical connectivity has with respect to predicting the success of deep brain stimulation is yet to be established. Here, we aimed to identify subthalamic region stimulation clusters that predict maximum improvement in rigidity, bradykinesia and tremor, or emergence of side-effects; and secondly, to map-out the cortical fingerprint, mediated by the hyperdirect pathways that predict maximum efficacy.

High angular resolution diffusion imaging in 20 patients with advanced Parkinson's disease was acquired prior to bilateral subthalamic nucleus deep brain stimulation. All contacts were screened one-year from surgery for efficacy and side-effects at different amplitudes. Voxel-based statistical analysis of volumes of tissue activated models was used to identify significant treatment clusters. Probabilistic tractography was employed to identify cortical connectivity patterns associated with treatment efficacy.

All patients responded well to treatment (46% mean improvement off medication UPDRS-III [$p<0.0001$]) without significant adverse events. Cluster corresponding to maximum improvement in tremor was in the posterior, superior and lateral portion of the nucleus. Clusters corresponding to improvement in bradykinesia and rigidity were nearer the superior border in a further medial and posterior location. The rigidity cluster extended beyond the superior border to the area of the zona incerta and Forel-H_2 field. When the clusters where averaged, the coordinates of the area with maximum overall efficacy was X=-10(-9.5), Y=-13(-1) and Z=-7(-3) in MNI (AC-PC) space. Cortical connectivity to primary motor area was predictive of higher improvement in tremor; whilst that to supplementary

motor area was predictive of improvement in bradykinesia and rigidity; and connectivity to prefrontal cortex was predictive of improvement in rigidity.

These findings support the presence of overlapping stimulation sites within the subthalamic nucleus and its superior border, with different cortical connectivity patterns, associated with maximum improvement in tremor, rigidity and bradykinesia.

4.2: Introduction

Subthalamic nucleus (STN) high frequency stimulation is an established treatment in selected patients with advanced Parkinson's disease (PD) [8,239,240]. The STN is thought to comprise functional subdivisions implicated in motor, associative and limbic functions with degrees of overlap [241-246]. The motor subdivision occupies the so-called 'dorsolateral' aspect; nevertheless, the most effective target location has been contended. Authors have argued that contacts within the 'dorsolateral-STN' give the biggest improvement in UPDRS-III[66,76,77]; others have maintained that contacts 'dorsal' to the STN, in the zona incerta (ZI) area and Forel-H_2 field, have superior efficacy [142,247-253]. A third group found both locations, or border contacts to be equally effective [246,254-258].

This discrepancy is attributed to several factors. One is reliance on surrogate markers such as microelectrode recording [76,142,248,249,252,254,256-258] and non-specific atlas coordinates or deformable atlases [142,246,248,249,251,254,256,257] to identify the STN borders, not readily discernible on low or intermediate field MRI [259]. Another is using postoperative CT instead of stereotactic-MRI to confirm contact location within the target, overlooking errors introduced by brain shift or image co-registration [60,260]. Complicating matters further, is the STN's peculiar contour, double-oblique orientation and position within a junctional area where anatomical terms of location change, rendering localization description within the STN ambiguous [64,261,262]. The term "dorsal", used when referring to the STN, is synonymous with "posterior" in the pons and "superior" in the thalamus [263]. Here we use unambiguous anatomical terms (superior/ inferior) to describe location within the STN.

Lastly, overlooking the volume of tissue activated (VTA) and only examining centre of ***active*** contacts location ignores the effect contacts adjacent to the nucleus might have on nuclear cell bodies dendrites, as well as axons within the white matter outside the nucleus [264-269] and limiting the comparison to the most effective contacts that landed in the chosen, predetermined target.

A proposed mechanism of action of STN-DBS is through interrupting synchronised oscillations between STN and cortex [173-180] possibly through modulation of hyperdirect pathways [172,181-184,215,242,243,270-272]. The objectives of this study were to identify the optimal STN stimulation site separately for improvement in rigidity, bradykinesia and tremor; identify stimulation sites accountable for common side-effects encountered with STN-DBS one-year after surgery; and explore the cortical connectivity or ***fingerprint*** of stimulation volumes, through these hyperdirect pathways, in a bottom-up fashion, by proceeding stepwise through the following aims:

1. To create a ***group specific STN template*** by manually delineating, co-registering and averaging individual subthalamic nuclei
2. To screen all DBS contacts at amplitudes of 1,2,3 and 4 Volts for contralateral improvement in rigidity, bradykinesia and tremor; and emergence of side-effects
3. To generate VTA models for all DBS contacts at these amplitudes
4. To carry out a voxel based morphometry (VBM) style regression analysis of modelled VTAs and their associated efficacy and side-effect profiles
5. To use probabilistic tractography from modelled VTAs of all DBS contacts to predefined cortical areas excluding tracts passing through the thalamus and striatum and only including tracts passing through the internal capsule (hyperdirect pathway)
6. To generate a DBS-cortical connectivity matrix, using the output from the previous step, to test the predictive significance of cortical connectivity

4.3: Materials and methods

4.3.1: Patients

Twenty patients (four female), who met UK Brain Bank criteria for idiopathic Parkinson's disease [273], were included (**Table 4-1**). Patients on the surgical waiting list for bilateral STN-DBS were recruited after selection by a multidisciplinary team of specialized movement disorders neurologists and functional neurosurgeons. All patients underwent formal neuropsychological assessment and structural brain MRI to rule out dementia and significant brain atrophy, respectively. Patients underwent L-DOPA challenge test during the routine selection process. Those with an improvement <25% on the UPDRS-III were excluded. Inclusion in the present study was limited to patients who could tolerate and had no contraindications to a prolonged 3T-MRI scan.

4.3.2: Preoperative magnetic resonance imaging data acquisition

Imaging was acquired with patients in the ON-medication state, with no concurrent head tremor or dyskinesia. Imaging was performed on a 3T Siemens Magnetom Trio Tim Syngo MR B17 using a 32 channel receive head coil. Padding was used inside the head coil to reduce discomfort and head motion during the scan.

4.3.3: Diffusion weighted MRI

Details of diffusion weighted MRI acquisition and preprocessing are described in the general methods sections.

4.3.4: Surgical procedure and intraoperative magnetic resonance imaging data acquisition

Bilateral DBS (3389 Medtronic lead) implantation was performed under GA using a stereotactic MRI-guided and MRI-verified approach without microelectrode recording (Leksell frame G, Elekta) as detailed in previous publications [274,275]. Two stereotactic, pre-implantation scans were acquired, as part of the surgical procedure, to guide lead implantation; a T2-weighted axial scan (partial brain coverage around the STN) with voxel

size of 1.0×1.0 mm^2 (slice thickness=2 mm) and a T1-weighted 3D-MPRAGE scan with a $(1.5\ mm)^3$ voxel size on a 1.5T Siemens Espree interventional MRI scanner. Three-dimensional distortion correction was carried out using the scanner's built-in module. Target for the deepest contact was selected at the level of maximal rubral diameter (~5 mm below the AC-PC line). To maximise DBS trace within the STN, the target was often chosen 1.5 - 2 mm posterolateral to that described by Bejjani [276]. Stereotactic imaging was repeated following lead implantation to confirm placement. A dual channel implantable pulse generator (IPG) (Activa PC, Medtronic, Minneapolis, Minn., USA) was then implanted in the infra-clavicular region on the same day of lead implantation or within a week, as a staged procedure.

4.3.5: Outcome measures

4.3.5.1: DBS contact efficacy and side-effect profile screening

DBS efficacy and side-effects screening was performed one-year from surgery. Medications were withdrawn for twelve-hours before assessment. DBS was switched off and after a five to ten-minute washout period, hemi-body (upper limb) rigidity, bradykinesia and tremor scores were assessed and rated from 0-4 (0=normal, 1=slight, 2=mild, 3=moderate and 4=severe). Once baseline scores were documented, all contacts were screened one at a time using monopolar stimulation in four stimulation sessions with amplitudes of 1, 2, 3 and 4 volts, frequency of 130 Hz and pulse width of 60 μs until the effect was established. A washout period was allowed between stimulation sessions until baseline was reached. Scores were reassessed for every session whilst evaluating the emergence and progression of stimulation-related side-effects (i.e. facial pulling, dysarthria, diplopia and paraesthesia). An example screening sheet is provided in Appendix 2.

4.3.5.2: DBS contacts volume of tissue activated (VTA) modelling

Specific VTA thresholds were calculated for every electrical setting, taking into consideration the specific stimulation configuration, amplitude and pulse width as described

by Åström and colleagues, in order to generate DBS therapy VTA [162]. Intraoperative (pre- and post-implantation) stereotactic scans were co-registered. Scans were first manually aligned to a pre-implantation MPRAGE scan, before running automated co-registration with a restricted volume of fusion centred around the diencephalon/ mesencephalon. This was carried out to minimise registration error resulting from eventual brain shift incurred during surgery, despite minimal brain shift with our surgical technique [260]. Registration accuracy was carefully inspected and the process iterated if necessary.

Pre-implantation T2-weighted stereotactic scans were used to generate STN meshes. Two experienced practitioners (HA a functional neurosurgeon and PM a movement disorders neurologist) carried out the process independently with <15% interrater variability in identifying the boundaries of the STN across patients. The post-implantation MPRAGE was used to fit the DBS lead model within the MRI artefact produced by the leads. Individual VTAs were then generated around each DBS contact with voltages of 1, 2, 3 and 4 volts resulting in 32 VTAs per patient.

4.3.6: Image Pre-processing

Pre-implantation MPRAGE scans were brain extracted using *BET* (Brain Extraction Tool, FSL v5.0) [277]. A two-step procedure was used to register native scans to the MNI152 standard-space T1-weighted average structural template image (1mm resolution) [278]. The first step employed a linear (affine) transformation using *FLIRT* (FMRIB's Linear Image Registration Tool) using 12 degrees of freedom [279,280]. The output from this step was used to execute non-linear registration (second step) using *FNIRT* (FMRIB's Non-Linear Image Registration Tool) [281]. This process produced individual native-to-standard (MNI space) non-linear warp fields which were then applied to the STN and VTA volumetric meshes acquired from SureTune to transform all volumes to standard space.

4.3.7: Analysis

4.3.7.1: Model of VTAs and efficacy scores

Group-average, bilateral STN templates and total VTA areas were generated from standardised (MNI space) individual STN volumes and DBS contacts VTAs using *Fslmaths* (FSL5.0) (**Figure 4-1** and **Figure 4-2**).

Right sided individual contact VTAs were lateralised to the left by flipping the images along the x axis (x, y, z > -x, y, z) using *Fslswapdim* (FSL5.0). All VTAs were then merged using *Fslmerge* (FSL5.0) into a 4D data file. In each voxel, each of the VTAs (one for each of the 32 different stimulation conditions) was modelled as a linear combination of efficacy scores, and side-effects (0=absent, 1=transient or 2=persistent) within subject. A general linear model (GLM) was created with efficacy and side-effects variables to test against each voxel in corresponding VTAs in a single-group average design (each variable was tested individually). This analysis was carried out for each subject independently. The variables were demeaned and single group t-test with threshold-free cluster enhancement (TFCE) was used as test statistic [164]. Nonparametric permutation inference approach, similar to that commonly used for VBM and fMRI time series analysis, was carried out for each voxel using *Randomise* (FSL5.0) with 5000 permutations to build up the null distribution to test against as previously described [165]. Raw t-stat (t statistic) images were then masked by the significant voxels from thresholded (α=0.05) t-stat images, also corrected for multiple comparisons. The resultant images from each subject were combined to form a group average. Cluster-based inference using *Cluster* (FSL5.0) was carried out to extract the clusters and local maxima in outputs.

4.3.7.2: Tractography

Probabilistic tractography was generated in ProbtrackX2 GPU version (Behrens 2007) [282] (FSL5.0) (number of samples=5,000, curvature threshold=0.2, step length=0.5 mm subsidiary fibre volume fraction threshold=0.01) [283].

The combined (total) VTA areas were used to generate tractography (in MNI space) for the left and right hemispheres; additionally, tracts were generated from combined efficacy clusters instigating improvement in bradykinesia, tremor and rigidity as generated from the voxel-based morphometry (VBM) style DBS-contact VTA analysis in *Randomise* (FSL5.0).

Waypoints were used in the internal capsule to isolate the streamlines to three cortical target areas; (1) primary motor cortex (M1 [Brodmann's area 4]), (2) supplementary motor area (SMA) [Brodmann's area 6] and (3) prefrontal cortex (PFC). CSF termination and mid-sagittal exclusion masks were applied to exclude false positive streamlines and commissural tracts respectively. To improve connectional contrast between the three targets, each of them was used as a target, while the other two were used as exclusion masks. For instance, to track the STN-M1 pathway, M1 was used as target, while SMA and PFC were used as exclusion masks. This ensured that the tracked connection contained paths connecting STN to M1, and at the same time not connecting STN to any of the other two targets. Similarly, for the other two target regions.

4.3.7.3: DBS-Cortical connectivity

A connectivity matrix was generated between all seed points in the combined (total) VTA area mask and all points in the cortical target masks (i.e. M1, SMA and PFC) using the output from tractography. The streamline counts for each voxel were normalised by the total number of streamlines reaching all targets to acquire a proportional measure. A t-statistic was used to calculate the connectivity within the individual DBS-contact VTAs (inside) versus the connectivity outside the contact VTAs but within the combined (total) group average VTA and this value was used in subsequent regressions (denoted as CON). This value effectively reflected connectivity of voxels activated in a certain stimulation condition, using connectivity in inactive STN voxels as a baseline. An in-house MATLAB (MathWorks Inc.) script was used to test the relationship between the cortical connectivity of individual DBS-contact VTA voxels and the improvement in efficacy associated with each DBS-contact VTA. To account for the effect of VTA volume and stimulation amplitude on efficacy, these factors were used as nuisance covariates in the regression analysis. Efficacy for alleviation of a particular symptom was then modelled as a linear combination of the connectivity values to each of the three target areas, VTA volume and stimulation voltage, as shown below. Alleviation of three symptoms was individually explored (tremor,

bradykinesia and rigidity). All the explanatory variables (EVs) were normalised (demeaned and standard deviation made equal to 1), so that:

$$Efficacy = b_0 + b_1 \times CON_{VTA \rightarrow M1} + b_2 \times CON_{VTA \rightarrow SMA} + b_3 \times CON_{VTA \rightarrow PFC} + b_4 \times VOLTAGE + b_5 \times VTA\_VOLUME$$

CON: connectivity; VTA: volume of tissue activated; M1: primary motor area; PFC: prefrontal cortex; SMA: supplementary motor area, b_0-b_5: unknown model parameters.

4.4: Results

4.4.1: Patients

Scanning proceeded with no adverse effects. The mean pre-operative mini-mental score (MMS) was 29.6 (SD=0.6, Range=2). One patient had tremor-dominant PD without motor fluctuations. Six patients had no significant tremor and were therefore excluded from the tremor VTA efficacy and cortical connectivity analysis, but included in the rigidity and bradykinesia analyses. There was no surgical morbidity or mortality and all DBS leads landed within a mean (SD) of 0.8 (0.4) mm from the planned target. Patient demographics, improvement in UPDRS-III following L-DOPA administration (L-DOPA challenge, preoperatively), improvement in UPDRS-III one-year from surgery with DBS ON and OFF medications and change in L-DOPA equivalent daily dose are shown in **Table 4-1**.

4.4.2: VTA Modelling

Group average, statistically significant clusters correlated to stimulation efficacy and side-effect EVs within and around the STN are shown in **Figure 4-2** and **Figure 4-3**. Improvement in bradykinesia, rigidity and tremor with DBS was associated with VTA clusters in the posterior, superior and lateral STN with the bradykinesia and rigidity areas extending to the superior border and being more medial and posterior than that of tremor. The three clusters were averaged into a single area in the superior and lateral STN with

maximum intensity at X=-10(-9.5) Y=-13(-1) and Z=-7(-3) in MNI (AC-PC) space. Facial pulling was associated with VTA cluster in the region of the corticobulbar fibres. Acute dysarthria was associated with VTA cluster in the internal capsule. Diplopia was associated with the VTA cluster in the region of the mesencephalic oculomotor nerve fibres in the tegmentum. Paraesthesia was associated with the VTA cluster in the mid-portion and inferior STN. See **Table 4-2** for cluster volumes and MNI coordinates.

Table 4-1: Patient demographics, preoperative L-DOPA challenge, postoperative change in UPDRS III and medication requirement

	Mean	SD	SE	Minimum	Maximum	Range
Age*	56.3	10.2	2.3	41	71	30
Disease duration*	11.2	4.3	1.0	4	22	18
Duration of motor fluctuations*	3.1	2.0	0.4	0	9	9
UPDRS III OFF (LC)	43.8	13.0	3.0	20	73	53
UPDRS III ON (LC)	17.4	9.9	2.3	4	42	38
UPDRS III Improvement (LC) *95% CI:21.6-31.3, t:11.4, df:18, p<0.0001†*	26.5 **(61%)**	10.1 **(15.8%)**	2.3 **(3.6%)**	7 **(33%)**	47 **(91%)**	40 **(58%)**
UPDRS III (OFF Med. OFF DBS) **	50.5	17.2	3.9	24	96	72
UPDRS III (OFF Med. ON DBS) **	27.1	12.5	3.0	14	51	37
UPDRS III Improvement** *95% CI:16.8-29.4, t:7.5, df:16, p<0.0001†*	23.4 **(46%)**	12.8 **(17.4%)**	3.1 **(4.2%)**	8 **(22%)**	45 **(73%)**	37 **(51%)**
UPDRS III ON Med. OFF DBS**	27.6	14.1	3.2	10	62	52
UPDRS III ON Med. ON DBS**	13.3	9.1	2.2	3	34	31
UPDRS III Improvement** *95% CI:10.4-18.3, t:7.6, df:17, p<0.0001†*	14.3 **(52%)**	8.0 **(17.4%)**	1.9 **(4.1%)**	41 **(9%)**	28 **(81%)**	24 **(62%)**
LEDD (Preoperative)	1365.6	509.8	114	540	2550	2010
LEDD (Postoperative)	770.6	306.6	68.6	320	1266	946
LEDD Reduction with DBS *95% CI: 386.3-803.8, t:6, df:19, p<0.0001†*	595 **(44%)**	203.2 **(39.9%)**	45.4 **(39.8%)**	220 **(40.7%)**	1284 **(50.4%)**	1064 **(52.9%)**

*: At surgery; **: At 12 months; †: 2-tailed paired-t test; CI: Confidence Interval; Med: Medications; SD: Standard deviation; SE: Standard error; df: degrees of freedom; LC: L-DOPA Challenge (preoperative); LEDD: L-DOPA equivalent daily dose

Figure 4-1: STN and VTA modelling, co-registration and analysis pathways

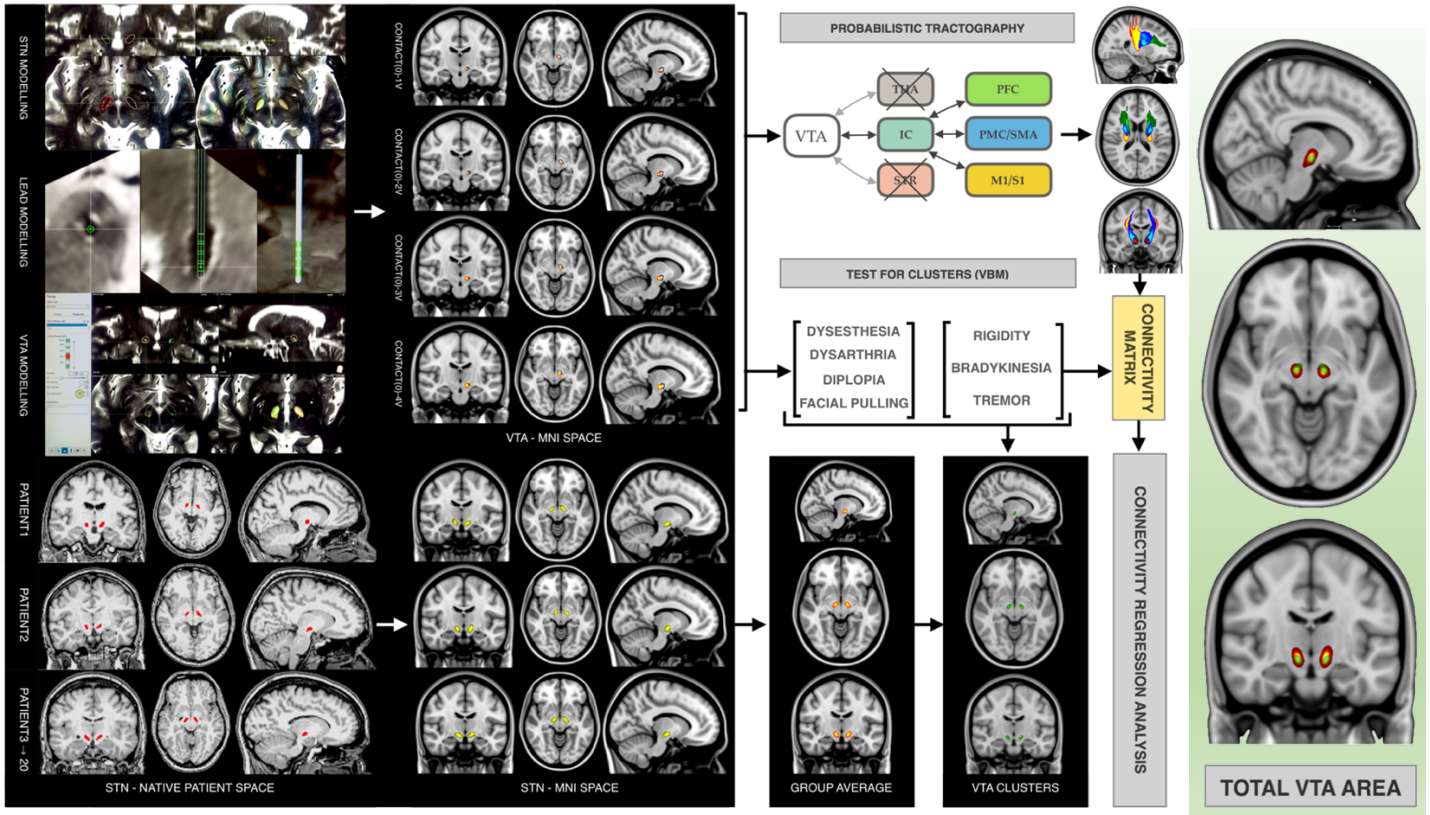

The graph on the left shows examples of STN, DBS lead and VTA modelling in SureTune package. Transformation from native space to MNI space is shown for STN and VTA models. Tractography to M1 is shown in red, to SMA in blue and to PFC in green. The graph on the right shows group average STN in green and total VTA area in red-yellow (IC: internal capsule; PFC: prefrontal cortex; SMA: supplementary motor area; M1: primary motor area; VTA: volume of tissue activated)

Figure 4-2: Volume of tissue activated significant clusters for maximum efficacy and emergence of side effects of subthalamic nucleus deep brain stimulation (z coordinate is in MNI space)

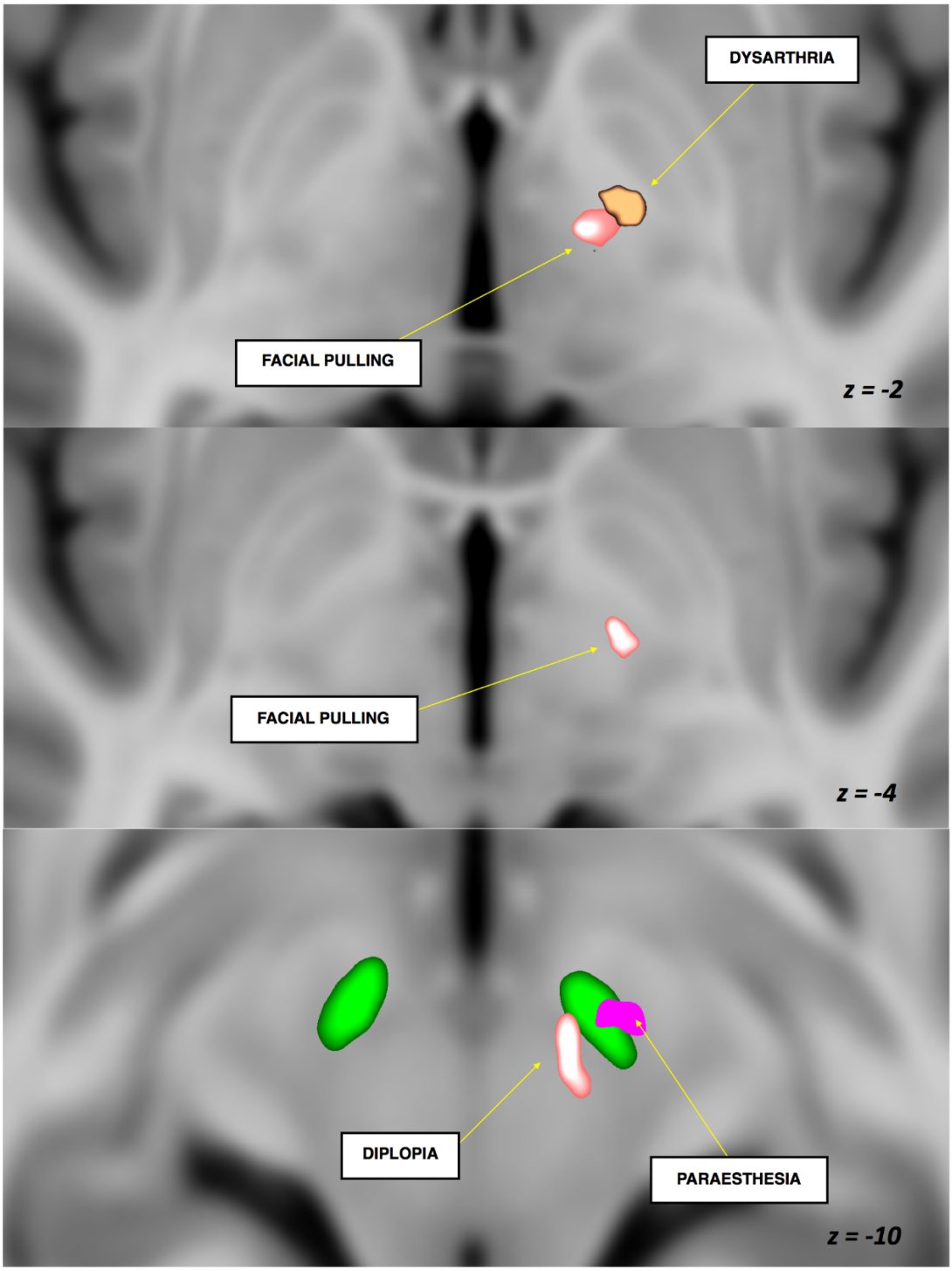

Group average STN is shown in green

Table 4-2: Volume of tissue activated significant clusters with maximum effect and centre of gravity coordinates in MNI and corresponding AC-PC space

VTA Cluster	VOL (mm^3)	P-VAL	Maximum effect coordinates MNI (AC-PC)			Centre of gravity coordinates MNI (AC-PC)		
			X	Y	Z	X	Y	Z
Rigidity	62	0.006	-9 (-8.5)	-13 (-1)	-7 (-3)	-11 (-10.5)	-15 (-3)	-7 (-3)
Bradykinesia	6	0.037	-11 (-10.5)	-14 (-2)	-7 (-3)	-11 (-10.5)	-14 (-2)	-7 (-3)
Tremor	11	0.014	-11 (-10.5)	-12 (0)	-6 (-2)	-12 (-11.5)	-12 (0)	-6 (-2)
Combined	26	-	-10 (-9.5)	-13 (-1)	-7 (-3)	-11 (-10.5)	-14 (-2)	-7 (-3)
Facial pulling	77	0.012	-11 (-10.5)	-19 (-7)	-1 (3)	-12 (-11.5)	-18 (-6)	-2 (2)
Dysarthria	149	0.002	-17 (-16.5)	-12 (0)	-5 (-1)	-15 (-14.5)	-11 (1)	-2 (2)
Diplopia	185	0.002	-7 (-6.5)	-12 (0)	-15 (-11)	-7 (-6.5)	-16 (-4)	-12 (-8)
Paraesthesia	475	0.002	-10 (-9.5)	-20 (-8)	-18 (-14)	-11 (-10.5)	-15 (-3)	-12 (-8)

VTA: Volume of tissue activation; VOL: Volume; P-VAL: p-value; AC: anterior commissure; PC: posterior commissure

Table 4-3. Model parameters that significantly contribute to the efficacy prediction

	Con STN-M1 (b1>0)	Con STN-SMA (b2>0)	Con STN-PFC (b3>0)	Voltage (b4>0)	VTA-Volume (b5>0)
Rigidity	p=0.035	p=0.0006	p=0.005	p=10-6	p=0.02
Bradykinesia	p>0.05	p=0.005	p>0.05	p=0.001	p>0.05
Tremor	p=0.04	p>0.05	p>0.05	p=10-7	p>0.05

P values correspond to testing each parameter being different from zero.

Con: connectivity

Figure 4-3: Volume of tissue activated significant clusters of subthalamic nucleus deep brain stimulation (MNI–Z = -7mm) *

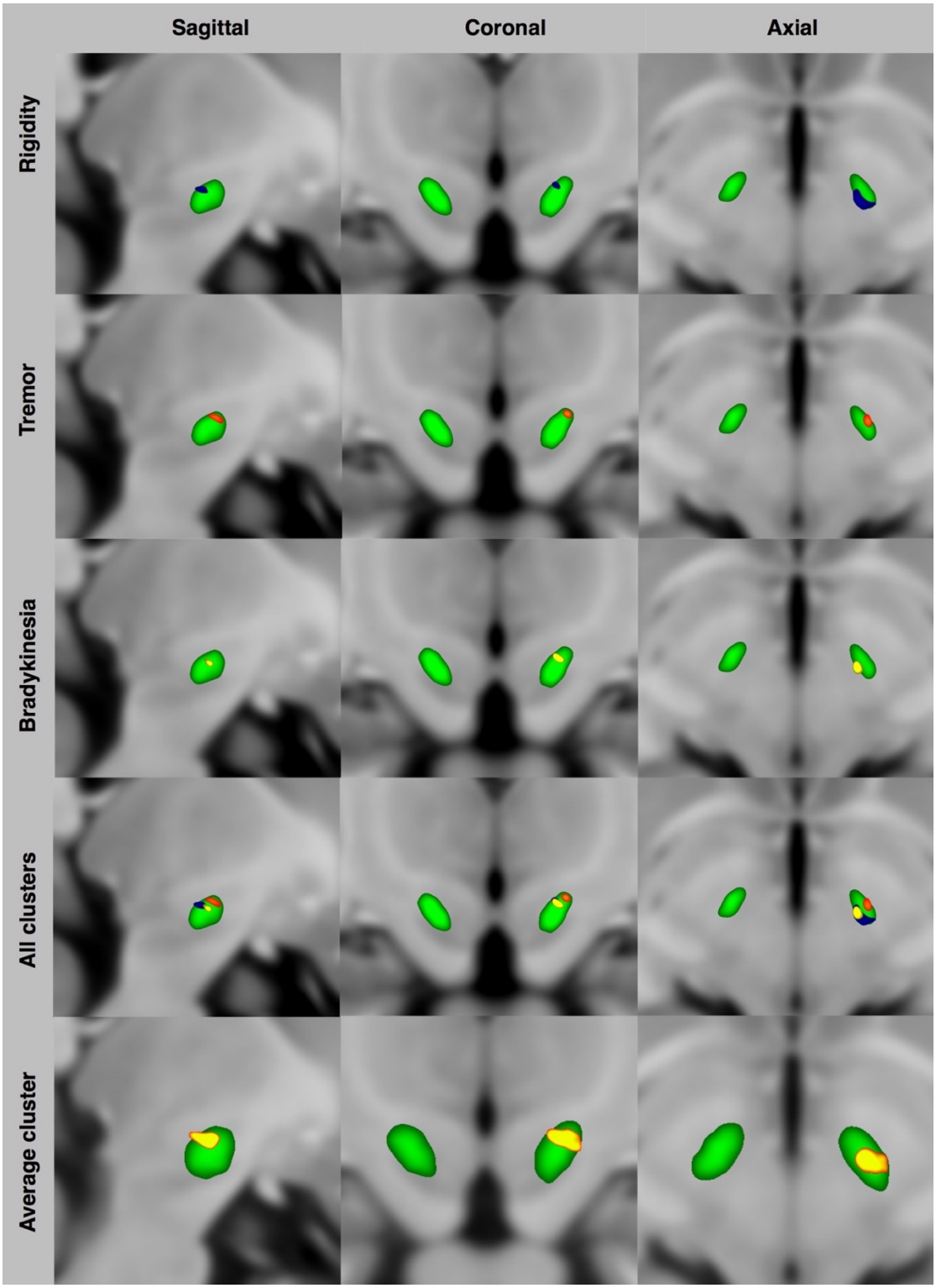

* Group average STN is shown in green. All clusters were corrected for multiple comparisons using non-parametric (gold-standard) approaches

4.4.3: Tractography

4.4.3.1: Tractography from combined, group average, entire VTA area

Six tracts were generated for each patient starting from the entire average VTA seed mask and ending in one of the predefined cortical targets in both hemispheres. Tracts to M1 ended mostly medially extending to the hand area. Group averages were produced for each tract class. The resulting six group average tracts are shown in **Figure 4-4**.

4.4.3.2: Tractography from bradykinesia, rigidity and tremor efficacy clusters

Eighteen tracts ([3 efficacy seed clusters × 3 cortical targets] × 2 hemispheres) for each patient were generated using seed masks corresponding to efficacy clusters in the STN as shown in Figure3. Tract group averages were again produced for each tract class (i.e. individual efficacy clusters to M1, SMA and PFC). Only tracts ending in the medial aspect (superior frontal gyrus) of M1, SMA and PFC survived. This is shown in **Figure 4.4**.

Figure 4-4: Group average tractography: from the combined overall average VTA mask– left and from the combined efficacy clusters - right to M1 (red), SMA (blue) and PFC (green)

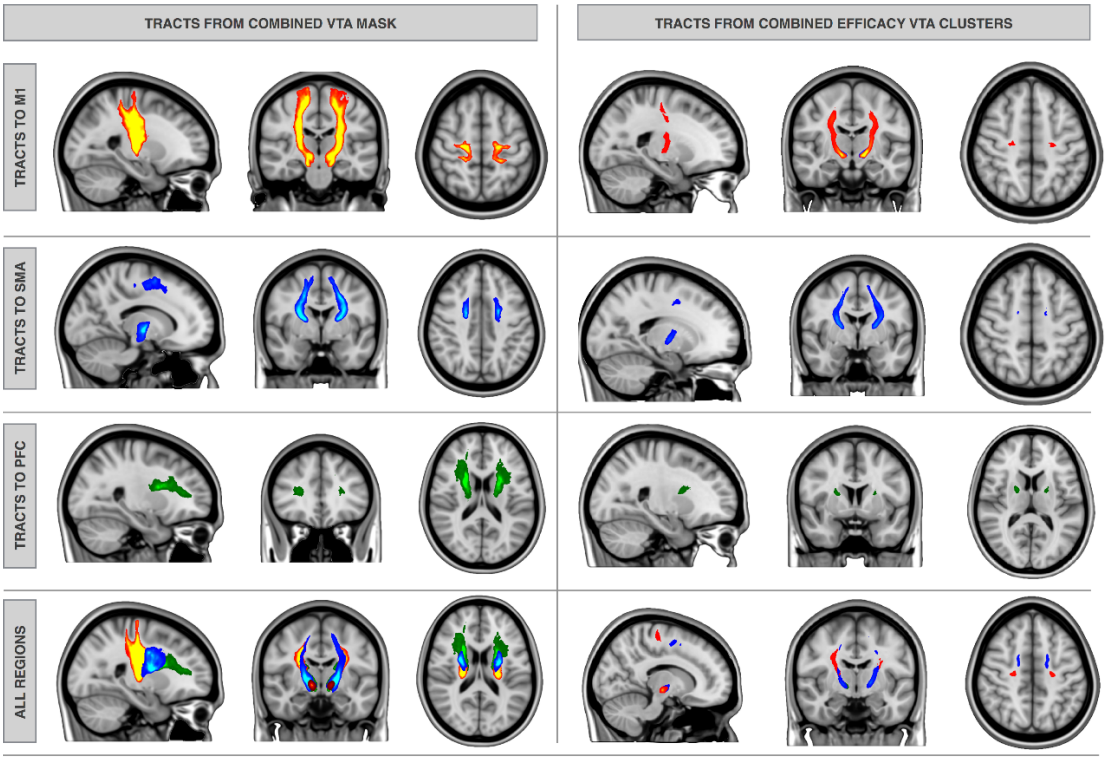

4.4.4: DBS-Cortical connectivity analysis

Rigidity, bradykinesia and tremor had different VTA-cortical connectivity predictive profiles. **Table 4-3** shows which model parameters significantly contribute to predicting efficacy for each symptom. In the case of rigidity, connectivity to SMA (b_2~32 [p=0.0006]) and PFC (b_3~26 [p=0.005]) were highly significant. The effect was about half of that explained by voltage (b_4~53 [p<0.0001]). For bradykinesia only connectivity to SMA was highly significant (b_2~23 [p=0.005]). The effect was about two-thirds of that explained by voltage (b_4~34 [p=0.001]). In the case of tremor, connectivity to the primary motor area was significant (b_1~27 [p=0.04]). The effect was about a third of that explained by voltage (b_4~80 [p<0.0001]).

Figure 4-5 shows the relationship between connectivity and efficacy for different stimulation amplitudes. Even if stimulation amplitude is a strong predictor of efficacy in all cases, the effect of connectivity can be also seen, particularly for rigidity and bradykinesia. For rigidity we can observe an upward trend for the efficacy as a function of the median connectivity to SMA. Particularly for intermediate voltages (2 and 3 Volts), being at an STN sub-region with higher connectivity to SMA leads to higher efficacy in alleviating rigidity. For bradykinesia, there is not a clear trend for high voltages (3 and 4 volts), but low/medium stimulation (1 and 2 volts) seems to benefit from being at a location with a high SMA connectivity. Thus, when voltage is low, exact contact location within the STN really matters. The profiles for tremor are much noisier and voltage amplitude clearly determines efficacy in this case.

Figure 4-5: Plots showing relationship between percentage improvement in efficacy and VTA-cortical connectivity with stimulation amplitude (right) for rigidity, bradykinesia and tremor

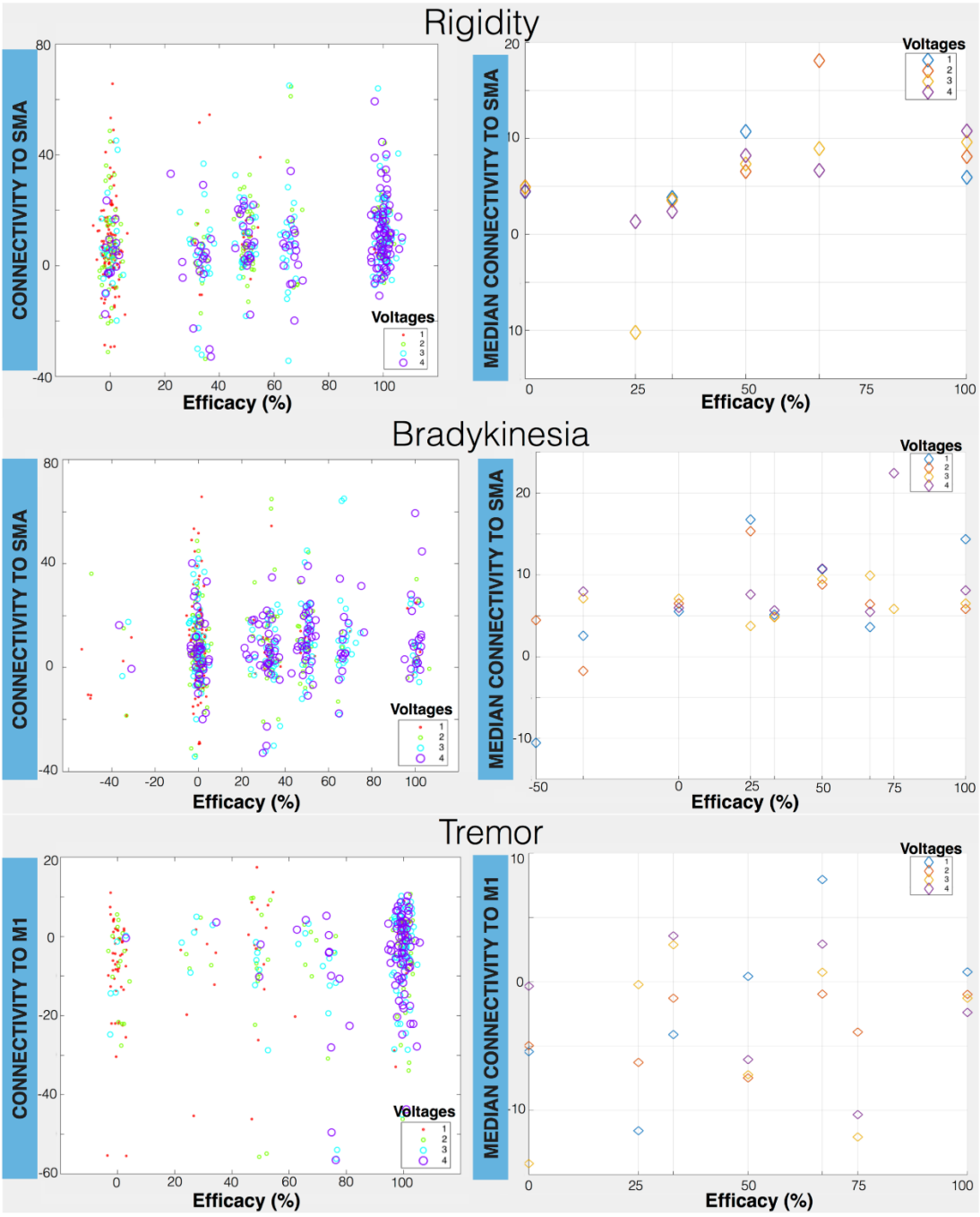

The connectivity of all voxels belonging to the respective VTA vs efficacy is illustrated with the scatter plots on the left. The median of these connectivity values is plotted vs efficacy on the right. Connectivity is defined as a t-score between the normalized streamline count of the activated STN region and the streamline count of the non-activated STN region, i.e. the latter is used as a "baseline" connectivity in each case.

4.5: Discussion

Voxel based statistical analysis of volumes of tissue activated, at increasing amplitudes, around individual DBS contacts, one year after STN DBS was used in 20 patients with Parkinson's disease (14 patients in the case of tremor) to (1) map out statistically significant clusters in the STN area, reflecting efficacy and side effects zones; (2) generate probabilistic tractography streamlines (hyperdirect pathways) from said volumes to predefined cortical areas [M1, SMA and PFC] and (3) identify the pattern of cortical connectivity that predicts response to treatment.

Appropriately selected patients responded well to DBS with reduction in LEDD and improvement in UPDRS-III both ON and OFF medications one-year post op **(Table 4-1)**.

4.5.1: Efficacy and side-effects clusters in the STN region

Using a statistical analysis approach akin to that used in voxel based morphometry, distinct clusters in the STN corresponding to improvement in rigidity, bradykinesia and tremor are demonstrated (**Figure 4-2** and **Figure 4-3**). All clusters are in the supero-lateral (motor) STN with overlapping bradykinesia and rigidity clusters. The tremor cluster is central within the supero-lateral STN whilst rigidity and bradykinesia appear to be more medial, posterior and superior. The rigidity cluster is the largest of the three and extends beyond the STN into the subthalamic region in the area of rostral ZI and Forel-H_2 field (pallido-thalamic fibres) whilst the bradykinesia cluster does not extend beyond the STN border [262]. The average cluster with overall maximum improvement in all motor symptoms lies in the superior-lateral portion of the STN.

This pattern could partly explain the disparity in the findings of previous reports exploring the best stimulation site. It is now apparent that improvement in different motor symptoms might be associated with stimulation of different sites in and around the STN. This is not a novel notion, Cintas and colleagues showed that improvement in tremor, rigidity and bradykinesia can follow stimulation in different contacts [252]. Clusters corresponding to

familiar side effects encountered with stimulation in well-established anatomical locations validate our findings (**Figure 4-2**).

It is paramount to highlight that the stimulation effect presented (for efficacy and side-effects) is a response to acute stimulation (during screening) and not long-term stimulation. This is an especially important point with regard to delayed emergence of side-effects resulting from chronic stimulation, particularly deterioration in speech intelligibility. The optimal DBS target may eventually vary according to emergence of such side-effects [284,285].

There are two main problems of carrying out a group analysis examining efficacy of individual DBS contacts. The first is the variability in the STN between individuals (and hemispheres in the same individual) and the method to describe contact locations. Using categorical, arbitrary division within the nucleus reduces sensitivity and specificity of the analysis. It also introduces observer bias. We overcame this problem by using a unique probabilistic STN template generated from our patient group, in order to visualise the resulting clusters, and co-registering volumes of tissue activation to MNI space. We tested voxels independently in the analysis across all contacts/ voltages for each individual, increasing the sensitivity and specificity of our approach.

The second problem is adjusting for baseline inhomogeneity. This is often overlooked and can produce statistical anomalies (e.g. a 5-point improvement from a baseline of 10 gives the same percentage of improvement of 30 from a baseline of 60) [286,287]. In order to overcome this, we examined efficacy clusters in each patient individually. The resultant clusters were then averaged across the entire group.

4.5.2: Tractography and cortical connectivity fingerprint

In vivo tractography studies in the region of the STN carry significant challenges. Motion artefacts, as a result of the highly pulsatile nature of the brainstem region, can degrade the MRI signal during diffusion image acquisition, reducing the signal-to-noise ratio (SNR). This is complicated by the presence of myriad criss-crossing axons and reticular brain regions [104,105]. One way of dealing with this is by using pulse-gating and respiratory rate monitoring

during diffusion imaging. Likewise, by acquiring multiple diffusion scans, at a high angular resolution (increasing acquisition time), SNR is improved [91,103].

Several studies have indeed used tractography to examine STN connectivity to cortical and subcortical areas but most used diffusion MR acquisition parameters more suited for conventional clinical application, such as mapping major white matter tracts prior to surgical intervention with low angular resolution (number of diffusion directions ≤ 64), low spatial resolution (voxel size ≥ 2mm) and low angular contrast (b-value=1000s/mm^2) [288-290]. Choosing the appropriate diffusion imaging parameters is of particular importance in the STN. This is in part due to its relatively small dimensions (12 mm in the longest axis and 4 mm in maximal thickness) [262] requiring small voxel dimensions; and low fractional anisotropy (grey matter) requiring higher diffusion sensitisation (b-value).

We acquired 270 diffusion scans per patient (in 2×128 directions sets) over 62 minutes. We meticulously and systematically corrected artefacts and examined the processed imaging data for quality control. We modelled three crossing fibres per voxel and used probabilistic tractography to ameliorate the crossing fibre problem.

Recently, there has been a tendency to use tractography in an exploratory fashion. Though there is a place for this in delineating large white matter bundles, the results should always be scrutinised for false positives. Tunnel effect, crossing and kissing fibres pose particular difficulties [92,103]. In order to keep the analysis focused, a set of tractography rules based on knowledge from neurophysiological and NHP tracer studies was used, without being too restrictive. The effect of STN-cortical connectivity was examined rather than simply described. The precise role of the cortico-STN hyperdirect pathway remains to be fully understood. It has been proposed that, through this pathway, direct cortical information reaches the STN before indirect cortical output via the cortico-basal ganglia route. This potentially allows for direct cortical modulation of STN output [291].

Our working hypothesis was that STN DBS exerted an effect through the hyperdirect pathway. The results suggest that ***three*** hyperdirect pathways connect the combined electrode stimulation area in and around the STN. Furthermore, distinct connectivity

patterns predict response to DBS. Connectivity to M1 appears to predict improvement in tremor; to SMA predicts improvement in bradykinesia; and to both SMA and PFC for improvement in rigidity. Purely visualising the tractography results from the subthalamic region to the distinct cortical areas is not informative by itself, however; the GLM analysis, examining the relationship with efficacy, illustrates that connectivity is indeed relevant to a degree that is comparable to that of DBS voltage.

This model fits with functional and anatomical expectations. A non-human primate tracer study examining the hyperdirect pathway shows that M1 STN terminals occupy the dorsolateral portion of the STN; whilst SMA and PFC terminals are more medially located, with areas of overlap between M1 and SMA; and SMA and PFC [241].

From a functional perspective; the primary motor area, SMA and PFC command sub-specialised roles in motor control. PET and SPECT studies have shown reduced metabolism in the PFC and SMA with Parkinson's disease progression [219-221]. The SMA is typically concerned with motor encoding and planning, whereas M1 is implicated with motor execution and the PFC plays a role in cognitive/ behavioural motor response selection and proactive motor inhibition [229,292,293]. DBS of the STN, by impacting on different fronto-basal ganglia pathways, has been shown to produce differential effects on reactive and proactive inhibition and on conflict resolution [294].

Resting tremor in Parkinson's disease is thought to be pathologically separate from bradykinesia and rigidity. The severity and magnitude of tremor is not related to the amount of dopamine deficiency in the substantia nigra and response to dopamine replacement can be poor in comparison to response in other motor symptoms [295-298]. Pathological oscillations in a cerebello-thalamo-cortical network, possibly triggered by pallidal dysfunction in Parkinson's disease, is thought to be culpable [299]. The cortical focus in this tremor network is in the primary motor cortex and not the SMA. This is supported by evidence from a transcranial magnetic stimulation (TMS) study that demonstrated tremor suppression following stimulation of the primary motor cortex [296].

A resting state functional MRI study has also shown increase in connectivity between the STN and hand area of M1 and the primary sensory cortex tremor-dominant subgroup; conversely, in a non-tremor subgroup, increased connectivity was found between the STN and wider cortical areas including the SMA as well as M1 [201]. Another study that used resting state fMRI showed that STN DBS modulates the hyperdirect M1-STN projections [300].

Two confounding factors are present when testing cortical connectivity of the volumes of tissue activated around each contact. The increase in tissue volume leads to an increase in the number of tractography voxel seeds. This, in turn, increases the number of streamlines from the VTA to the cortex in a non-linear fashion. The second confounding factor arises from the inexact relationship between stimulation amplitudes and increasing efficacy. Especially because the local population of neurons may have different action-potential thresholds. For this reason, voltage and seed volume effects were made covariates to study their effect on efficacy as well as that of the connectivity profile.

In the case of rigidity, an upward trend for all voltages was noted, particularly for low/medium voltages (e.g. 2 and 3 Volts) with higher connectivity to PFC and SMA, resulting in higher efficacy. For bradykinesia, the plot shows no clear trend for high voltages (3 and 4) but an upward trend for low voltages (1 and 2 Volts). In other words, when voltage is low, it matters most where the STN is stimulated. The tremor plot shows that voltage clearly determines efficacy in this case with a slight upward trend for voltages 1 and 3.

We focused the tractography analysis on hyperdirect pathways to three cortical areas known to be involved in tone control, motor initiation, planning and execution. We cannot rule out the existence of other cortical-STN pathways that may also influence outcome from DBS. Our analysis did not explore the influence of STN-subcortical connectivity (e.g. thalamic/ striatal). The reason for this is two-fold: the strength of tractography diminishes with distance rendering DBS-subcortical connectivity artificially stronger than DBS-cortical connectivity; and the combined VTA area ***clearly*** encroaches on the thalamic border as shown in **Figure 4-1**. It is, therefore, hardly surprising to find an increase in connectivity

between volumes of tissue activated and the thalamus, as was demonstrated in a recent study [289].

The efficacy cluster analysis we carried out does not address potential covariance within symptoms per se. We therefore cannot assert that the three areas are independent of each other based on the VBM analysis alone (especially in the case of rigidity and bradykinesia clusters), however; there is a clear difference in cortical connectivity pattern predictive of improvement in individual symptoms. This difference is supported by anatomical and functional studies as described in the discussion. We show that the average cluster lies in the dorsal-lateral portion of the STN in keeping with existing wisdom. We opted not to explore this relationship between the individual clusters further as this has little significance in clinical practice, as a well-placed DBS electrode can easily straddle the three areas. Nevertheless, carrying out the VBM analysis separately has produced convergent efficacy clusters in close proximity. This substantiates the novel technique used here.

4.5.3: Limitations

The limitations of the VTA model used in this study and the rationale behind using this model have been described in chapter 2 (2.10.4). Although the number of patients was relatively small (20 for the analysis of bradykinesia and rigidity analysis and 14 for the tremor analysis), we analysed two cerebral hemispheres independently by investigating hemi-body effects of stimulation doubling up the overall number in the analysis. Furthermore, testing the effect of stimulation for each individual contact at different voltages provided more data points per hemisphere. The main reason for the relatively small number of subjects stems from the difficulty in recruiting patients with advanced Parkinson's disease who are successfully selected for STN-DBS and can also tolerate having a lengthy MRI scan. We assessed stimulation efficacy in the upper limbs and not the lower limbs. We judged that this would give a more quantifiable and reproducible measure of improvement. Furthermore, patients with significant lower limb symptoms are seldom good candidates for STN-DBS. This does however mean that our results concerning the efficacy spots cannot directly be transferrable to patients with lower limb symptoms.

Another limitation is the inherent diffusion MRI imperfections as detailed in the discussion. Further improvements in diffusion imaging, with higher spatial and angular resolution and improved MRI gradients will add to the value of this modality [102,283].

Multiple registration steps introduce error to the system. Nonetheless; we meticulously confirmed registration accuracy at each step to alleviate the impact of this issue. Manual STN delineation introduces observer bias; however, using two experienced clinicians to perform this independently reduced inaccuracy. Furthermore, by using a group average imprecisions were minimized. Prior to carrying out the VTA cluster analysis, we lateralized the right sided DBS contacts and STN to the left. This approach is commonly used in imaging studies; however, it assumes no functional differences between the left and right STN. Given that the lateralised structures differ in size in our right hand dominant cohort, we must acknowledge the possible existence of different connectivity and efficacy relationships according to STN laterality. However, although reports have pointed to the existence of lateralised differences in emotional processing, no such differences have been established in motor processing [301].

Another limitation in the efficacy and side effect cluster analysis is the autocorrelation in the data. The VTAs, by definition, have a degree of overlap which increases the power but theoretically also increases the risk of false positives. This is certainly a weakness of the analysis. Having said that, spatial autocorrelation is a well-known phenomenon in VBM and fMRI analysis and permutation tests do not easily accommodate correlated datasets, as such dependence violates null-hypothesis exchangeability, however; it is suggested that non-parametric permutation testing is less amenable to false positives than parametric permutations [302]. We have also carried out the analysis for each subject separately to reduce the effect of inter-individual variability.

Lastly, the relatively long scan duration is a drawback. This was accepted to achieve the required SNR and resolution. However, novel MRI acquisition techniques (Simultaneous Multi-Slice Imaging and Multi-Band Imaging) [303] have been developed that will allow future studies to run similar protocols within half the time without compromising the SNR.

4.6: Conclusion

The optimal DBS site for patients with Parkinson's disease for tremor, bradykinesia and rigidity appears to correspond to different areas in the motor STN. Stimulation in the central portion of the superior STN is most effective for tremor, whilst stimulation in further medial and posterior areas, within the superior portion, gives highest improvements in bradykinesia and rigidity. DBS-cortical connectivity, along the hyperdirect pathways, to M1 is predictive of maximum improvement in tremor, to SMA is predictive of maximum improvement in bradykinesia and to both SMA and PFC is predictive of maximum improvement in rigidity.

5. Pyramidal tract activation due to subthalamic deep brain stimulation in Parkinson's disease

5.1: Abstract

Subthalamic deep brain stimulation (STN-DBS) is an effective treatment for Parkinson's disease (PD), but can have side effects caused by stimulus spread to structures outside the target volume such as the pyramidal tract. In this paper, we set out to assess the relevance of pyramidal tract activation with STN-DBS in PD.

In a multimodal, blinded study in 20 STN-DBS patients, we measured stimulation thresholds for evoking electro-myographic activity in orbicularis oris and first dorsal interosseous muscles at each of 150 electrode sites. We also modelled the electric field spread and calculated its overlap with the estimated anatomical location of corticospinal and corticobulbar tracts from primary motor cortex using 3 Tesla MRI probabilistic tractography.

Mean resting motor thresholds were significantly lower for the contralateral orbicularis oris (3.5±1.0 mA) compared with ipsilaterally (4.1±1.1 mA) and with the contralateral first dorsal interosseous (4.0±1.2 mA). The modelled volumes of corticobulbar and corticospinal tract activated correlated inversely with the resting motor threshold of the contralateral orbicularis oris and first dorsal interosseous, respectively. Active motor thresholds were significantly lower compared with resting motor thresholds by around 30% to 35% and correlated with the clinically used stimulation amplitude. Backward multiple regression in 12 individuals with a "lateral-type" speech showed that stimulation amplitude, levodopa equivalent dose reduction post-surgery, preoperative speech intelligibility, and first dorsal interosseous resting motor thresholds explained 79.9% of the variance in postoperative speech intelligibility.

In conclusion, direct pyramidal tract activation can occur at stimulation thresholds that are within the range used in clinical routine. This spread of current compromises increase in stimulation strengths and is related to the development of side effects such as speech disturbances with chronic stimulation.

5.2: Introduction

Subthalamic deep brain stimulation (STN-DBS) is an established treatment for motor fluctuations in patients with Parkinson's disease (PD) [304-306]. Although most eligible patients benefit from this therapy, there is still a large variability in the outcome. Spread of electrical field to surrounding structures is one of the main causes of side effects, and therefore precise position of the electrodes in the subthalamic area is a crucial factor in the size of the eventual benefit. An important structure in terms of side effect is the pyramidal tract, including the corticospinal tract (CST) and the corticobulbar tract (CBT), running through the posterior limb of the internal capsule and the cerebral peduncle (crus cerebri), surrounding the lateral aspects of the STN [307-309]. The distance between a DBS electrode in the STN and the cerebral peduncle carrying these fibres is in the range of a few millimetres and pyramidal side effects of stimulation are often observed, particularly at higher strengths of stimulation [310,311]. However, it can be clinically tricky to distinguish pyramidal from other side effects, for example, muscle spasms from dystonia related to DBS [312], pain [313], or speech disturbances, which may arise from either pyramidal tract stimulation or stimulation of the medial zona incerta, the prelemniscal radiations, or the fasciculus cerebellothalamicus [314,315].

Several studies have examined the spread of current from single stimuli through DBS electrodes placed in the STN to the adjacent pyramidal tract [310,316-318] These studies found motor-evoked potentials (MEP) in facial muscles and strictly contralateral arm and hand muscles by applying bipolar, high-amplitude stimulation through adjacent contacts. So far, however, a systematic assessment of the potential of electromyography (EMG) as an aid

in electrode localization in relation to the pyramidal tract and its relevance for clinical outcome has not been carried out.

Therefore, we explored the relationship between stimulation amplitude thresholds of the CBT and CST attributed to STN-DBS in a multimodal approach. We recorded MEPs elicited by single stimuli through all DBS electrodes using monopolar stimulation and amplitudes up to 6.0 mA. As a proof of concept, we created models of the volume of tissue activated (VTA) corresponding to each stimulus. Areas of overlap between said volumes and CST and CBT as generated by probabilistic tractography were calculated and correlated with EMG data. Finally, associations between MEPs and clinical effects and side effects were assessed to identify the potential for EMG in troubleshooting in PD patients treated with STN-DBS.

5.3: Methods

5.3.1: Participants and DBS implantation

Twenty-one patients with advanced PD who underwent STN-DBS were assessed post operatively. The surgical procedure has been previously described [61,63,67]. In brief, implantation of bilateral quadripolar DBS electrodes (3389 Medtronic, Minneapolis, MN) was performed without microelectrode recording and under general anaesthesia between May 2013 and July 2014 [71]. All patients had electrodes of 1.27 mm in width, with contacts of 1.5 mm in length, separated by 0.5 mm, and numbered from 0 to 3 (lowest to highest) in the left hemisphere and 8 to 11 in the right hemisphere. The STN was visualized and accurate lead placement verified on intraoperative, stereotactic T_2-weighted MRI sequences on a 1.5 Tesla (T) Siemens Avanto interventional MRI scanner (Siemens Healthcare, Erlangen, Germany).

5.3.2: Experimental design

Patients were assessed approximately 1 year after STN-DBS implantation. Four different authors independently evaluated neurophysiological (PM, neurologist), clinical (DG,

neurologist), speech (ET, speech therapist), and imaging (HA, neurosurgeon) assessments; each blinded to the other three assessments.

5.3.3: Clinical assessments

A standardized neurological examination including the UPDRS motor section (UPDRS-III) and the Dyskinesia Rating Scale was carried out off medication/on stimulation and on medication/on stimulation. *Off*-medication UPDRS-III scores, recorded preoperatively, were used as comparators to determine the motor benefit of STN-DBS. A repeat formal clinical screening of contacts was performed for each contact at 60 µs and 130 Hz in steps of 0.5 V every 10 seconds up to 4.0 V or until the patients experienced discomfort. Pyramidal side effects, defined as motor contractions of facial muscles, pharyngeal and/or laryngeal muscles, and the upper and lower limbs that are time-locked to stimulation, reproducible, appearing, and disappearing at the same thresholds [311], were systematically recorded.

5.3.4: EMG Recordings

EMG activity of the orbicularis oris muscle (OOr) and the first dorsal interosseous muscle (FDI) was recorded using 9-mm Ag-AgCl surface cup electrodes with the same equipment in a standardized fashion in an *on*-medication condition. We used a signal amplification gain of 2,000, recording frequencies at 10 kHz, and a band-pass frequency filter of 20 to 1,000 Hz. The signal was digitized and saved for offline analysis blinded to the conditions tested using Signal V4.08 (CED, Cambridge, UK). For the OOr, the active electrode was placed 1 cm lateral to the mouth corner, and the reference 2 cm lateral, for the FDI the muscle belly and the tendon of the same muscle, was used, respectively [318].

First, MEP were assessed while patients were sitting in a comfortable armchair and instructed not to speak and to relax, but not to sleep. Stimuli were elicited by the impulse generator on each of four contacts on each electrode in a monopolar stimulation mode. Stimulation at a low frequency of 3 Hz (allowing enough time for MEP recordings before subsequent stimuli) and at 60-µs pulse width (PW) was increased in 0.5-mA steps up to

6.0 mA or until bothersome side effects appeared. A PW of 60 µs was chosen because it is most widely used in clinical practice and has, in fact, been used in all our patients, allowing comparisons of EMG results with the clinically obtained data. Thirty sweeps of EMG triggered by the stimulation artifact were averaged per condition to detect the resting motor threshold (RMT) of pyramidal tract activation. RMTs were determined as the lowest stimulus intensity inducing MEPs clearly recognizable above background activity upon visual inspection (in most instances, this was the case when MEPs reached >10 µV in amplitude).

Second, active motor thresholds (AMTs) were assessed in 13 patients during sustained muscle contraction of approximately 25% of maximum voluntary force production (provided to the participants as visual feedback with a line on the EMG screen, which they were asked to match); first, of the FDI by squeezing a roll of tape, and second, of the OOr by forming a smiling mouth. For this condition, stimuli were only elicited by the clinically used contacts on each side. AMT was determined as the lowest stimulus intensity inducing MEPs clearly recognizable above background activity upon visual inspection.

Third, 7 patients underwent recordings of the same muscles with step-wise increasing pulse width (60, 120, 180, 240, and 450 μs) in order to calculate the chronaxies of the stimulated pyramidal fibres. **Figure 5-3.**

5.3.5: Speech assessments

Speech assessment was done in an *on*-medication condition preoperatively and postoperatively (on stimulation). It consisted of a standardized assessment of speech intelligibility [319] and 1-minute monologue on the topic of the patient's choice as described previously [70,314]. Analysis of speech intelligibility consisted of extracting percentage of words understood. Additionally, speech was perceptually classified into two groups according to our clinical experience and the literature: the “medial” speech type with strained-tight and continuous phonation, inaccurate articulation, and what sounds like breathing insufficiency [70,315] and the “lateral” speech type characterized by monotone-flat

intonation, fast rate of speech, and reduced movement of lips and tongue. Analysis was performed separately for these two groups.

5.3.6: MRI acquisition and processing

5.3.6.1: DBS contacts volume of tissue activated (VTA) modelling

DBS contacts volume of tissue activated (VTA) modelling was done on scans obtained intraoperatively on a 1.5 T Siemens Avanto interventional MRI scanner. Intraoperative MRI scans were uploaded and the post-implantation MPRAGE was used to fit the DBS lead model within the MRI artefact produced by the leads. Individual VTAs were then generated around each DBS contact with voltages of 0.5 to 6.0 mA in 0.5 mA steps. Binary image files of VTAs along with corresponding transformation matrices were exported and processed in MATLAB (MathWorks Inc.) using in-house software to generate Neuroimaging Informatics Technology Initiative (NIfTI) volumes for further analysis.

5.3.6.2: Diffusion weighted MRI and probabilistic tractography

Seventeen patients had undergone high angular resolution diffusion imaging in the week prior to STN DBS implantation on a 3T Siemens Magnetom using a padded 32-channel receive head coil to reduce discomfort and head motion. Details of diffusion weighted MRI acquisition and pre-processing are described in the general methods sections.

Two separate cortical seed masks were used to generate tractography for each hemisphere; the hand area in the primary motor cortex for the CST and the face area for the CBT as published previously [308,320]. Waypoints were used in the internal capsule and the crus cerebri to direct the streamlines. CSF termination and mid-sagittal exclusion masks were applied to exclude false positive streamlines and commissural tracts respectively. The generated tracks were visually inspected and group averages were created to improve the quality of the resulting templates. These were then transformed back to patients' native space using non-linear registration and the non-linear standard-patient space transforms. This allowed inclusion of the three patients with no preoperative diffusion data. Overlap

between The VTAs and the CST and CBT was then quantified using *fslmaths* (FSL V5.0) to generate overlap volumes and then *fslstats* (FSL V5.0) to measure those volumes.

5.3.7: Statistical analysis

Because data were largely non-normally distributed, as shown by the Shapiro–Wilk test, we used nonparametric tests for comparative statistics. Variables are given in medians (25th–75th percentiles), unless specified otherwise. The main neurophysiological outcome measure was defined as the threshold of stimulation strength in mA eliciting clear visually perceptible MEPs. As a proof of principle, motor thresholds of the OOr and the FDI were then correlated to MRI modelled volumes of CBT and CST activated, respectively. As volumes of overlap increased linearly with increasing stimulation strength (data not shown), we used volumes of overlap modelled at the maximum applied stimulation strength of 6.0 mA for correlations with motor thresholds. Linear regression analyses were additionally performed to assess the influence of volumes of CBT and CST activated on motor threshold of respective muscles as well as factors determining postoperative speech intelligibility. SPSS software (version 22.0; IBM Corp., Armonk, NY) was used for all statistical analyses. The local significance level was set at two-sided $P<0.05$.

5.4: Results

5.4.1: Patient characteristics and clinical assessments

One patient could not tolerate withdrawal from high-frequency stimulation for EMG measurements and was excluded. The remaining 20 patients (3 females, aged 60.6 [52.6-67.9] years; disease duration: 11.3 [7.2-13.8] years; stimulation duration: 1.0 [0.9-1.4] years) were eligible for analyses. UPDRS-III scores *off*-medication were 45.0 (35.5-51.5) preoperatively and 27.0 (17.0-35.0) postoperatively ($P<0.001$). Levodopa equivalent doses were 1,446 (1,177-1,978) preoperatively and 650 (500-953) postoperatively ($P<0.001$). Settings for chronic stimulation were as follows: 2.0 (1.5-2.1) mA amplitude; 130 (125-130) Hz frequency; and 60 μs PW in all patients. **Table 5-1**.

5.4.2: Muscle evoked potentials

A total of 150 contacts could be assessed at rest (in two patients only a unilateral assessment on the electrodes contralateral to the less affected side was possible, and two contacts of two other patients were dysfunctional as indicated by high impedance and were therefore not tested). Out of these, in 148 (98.7%) contacts it was possible to elicit MEPs in the contralateral OOr, in 138 (92.0%) in the ipsilateral OOr, and in 144 (96.0%) in the contralateral FDI using stimulation strengths up to 6 mA (for example see **Figure 5-1**). **Table 5-2** illustrates the RMTs, which were significantly lower in the OOr contralateral to the side of stimulation compared with the ipsilateral one and compared with the FDI.

At the maximum applied stimulation strength of 6 mA, MEPs reached mean amplitudes of 107.7±115.4μV in the contralateral OOr, compared with 36.4±41.1μV in the ipsilateral OOr ($Z=-8.4$, $p<0.0001$) and with 344.2±637.4μV in the FDI ($Z=-3.2$, $p=0.0027$). MEPs were elicited after a mean of 7.8±0.9ms in the contralateral, 7.8±0.9 ms in the ipsilateral OOr ($Z=-0.3$, $p=0.732$), and after 20.9ms±1.6ms in the FDI ($Z=-7.8$, $p<0.0001$). The latency was inversely correlated with the amplitude of the MEPs ($r=-0.369$, $p=0.0004$ for the contralateral OOr; $r=-0.118$, $p=0.303$ for the ipsilateral OOr; and $r=-0.344$, $p=0.0002$ for the FDI).

5.4.3: Influence of side and contact location on muscle evoked potentials at rest

Thresholds for the OOr (contralateral and ipsilateral) were significantly lower upon stimulation in the left compared with the right hemisphere, whereas there was no significant hemisphere effect with regard to the FDI **(Table 5-2)**. There were increasing thresholds along the axis of the electrode from the lowest to the highest contact for the FDI (from 3.1±0.8mA on contact 0, to 4.5±1.1mA on contact 3, $p<0.0001$ for trend; and from 3.8±0.9mA on contact 8 to 4.2±1.1mA on contact 11, $p=0.183$ for trend), but not for the contralateral or ipsilateral OOr. A regression analysis taking into account hemisphere and contact location confirmed these findings **(Table 5-2)**.

Hemisphere and contact location did not influence amplitude or latencies of MEPs.

5.4.4: Correlation with imaging data

CBTs and CSTs were successfully modelled, averaged and the average applied to each patient space. Next, VTAs were overlaid on CBTs and CSTs in each patient obtaining CBT volume activated and CST volume activated, respectively **(Figure 3.3.2)**. As volumes of overlap linearly increased with increasing stimulation strength, we used volumes of overlap modelled at the maximum applied stimulation strength of 6.0 mA for correlations with RMTs **(Table 3.3.3)**. The volume of CBT activated correlated inversely with the RMT of the contralateral OOr. Likewise, the volume of CST activated correlated inversely with the RMT of the FDI. For the ipsilateral OOr there was no such correlation. These findings were corroborated in a regression analysis, both unadjusted and adjusted for side and contact location **(Table 3.3.3)**.

The mean volume of overlap at the actual applied stimulation strength necessary for eliciting RMTs was higher for the OOr with 38.3±29.2 mm^3 (95%CI; 33.7–43.5mm^3) of CBT volume activated than for the FDI with 32.2±28.7 mm^3 (95%CI; 27.4–37.0mm^3) of CST volume activated ($Z=-5.0$, $p<0.0001$), but there was no difference between sides or across contacts.

5.4.5: Active motor thresholds

Thirteen patients underwent recordings of the three muscles during sustained contraction of (1) FDI by squeezing a roll of tape and (2) OOr by forming a smiling mouth. For these conditions stimuli were only elicited through the clinically used contacts on each side, with two patients having only unilateral assessments; thus a total of 24 contacts were assessed. **Table 3.3.3** presents the thresholds for the three sites of recording and for the two conditions tested. AMTs were significantly lower compared with RMTs **(Table 3.3.2)** by around 30%–35% in the contralateral OOr ($Z=-4.3$, $p<0.0001$), ipsilateral OOr ($Z=-4.1$, $p<0.0001$), and FDI ($Z=-4.2$, $p<0.0001$), respectively. AMT of the contralateral OOr was similar to the FDI, but significantly lower compared with the ipsilateral OOr **(Table 3.3.3)**. MEPs were elicited after a mean of 7.1±0.8ms in the contralateral, 7.1±0.9ms in the ipsilateral OOr ($Z=-0.4$, $p=0.700$), and after 20.4±2.1ms in the FDI ($Z=-4.1$, $p<0.0001$).

MEPs on activation occurred earlier than those at rest in all muscles (see above), however, achieving statistical significance in the FDI only (Z=-3.4, p=0.0008).

There were inverse correlation of AMT with the volume of CBT/CST activated, which reached statistical significance only for the combination of FDI AMT with volume of CST activated **(Table 3.3.3)**.

Interestingly, activation of the OOr led also to a lowering of the threshold in the FDI and vice versa, which was intermediate between RMT and AMT **(Table 3.3.3 and Figure 3.3.3)**.

5.4.6: Evaluation of the chronaxie

Seven patients underwent recordings of the three muscles with increasing pulse widths at the clinically used contacts, with two patients having bilateral assessments, thus assessing a total of 10 contacts. From the strength-duration curves **(Figure 3.3.3)** we determined a mean chronaxie of 142.5*μ*s for RMT of the contralateral OOr, of 163.2*μ*s for the ipsilateral OOr, and of 168.8*μ*s for the FDI. These values were not significantly different (all p-values for comparison >0.100).

5.4.7: Clinical-neurophysiological correlations

Neither motor improvement upon stimulation nor dyskinesias were significantly related to the motor thresholds for any muscles (all spearman rank correlations p>0.140). However, there was a direct correlation of the clinically used stimulation amplitude with the RMT (significant for the contralateral OOr, r=0.406, p=0.0128) and with the AMT, which was significant for all three muscles (contralateral OOr, r=0.604, p=0.0014; ipsilateral OOr, r=0.495, p=0.0119; and FDI, r=0.498, p=0.0132). RMT were higher than the amplitude used for clinical benefit in all patients on both sides (all p values for all three muscles <0.0001). The same was generally true for AMT, but p-values were less significant, likely due to a few DBS contacts where AMTs were lower than the clinically used stimulation amplitudes (five for the contralateral OOr, p=0.0226; two for the ipsilateral OOR, p=0.0002; and three for the FDI, p=0.0018).

Overall, 148 contacts were clinically screened for side effects using a frequency of 130 Hz and 60 μs. In 34 contacts (23.0%) contralateral facial pulling was noted at a mean threshold of 2.7±0.6mA. In 18 contacts (12.1%) contractions of the contralateral fingers/hand were noted at a mean threshold of 2.9±0.4mA. The clinical observation of contralateral facial pulling was noted at a similar amplitude to the RMT of the contralateral OOr in the same contacts (2.8±0.7mA; Z=-0.4, p=0.660), and contractions of the contralateral hand/fingers was noted at a similar mean threshold to the RMT of the FDI in the same contacts (3.2±0.9mA; Z = -0.9, p=0.352).

5.4.8: Speech assessments

Mean postoperative speech intelligibility was 89.0% (74.0-94.3). In the 8 participants with a “medial type” of speech, RMTs of the FDI were higher and volume of pyramidal tract activation was lower compared to the 12 participants with a lateral type of speech. In participants with a “lateral” type of speech, speech intelligibility correlated with the RMT of the FDI upon stimulation of the clinically used contacts ($r = 0.428$; $P = 0.0468$), but not with the RMTs of the OOr. AMTs were non-significantly correlated with speech intelligibility (e.g., FDI; $r = 0.345$; $P = 0.272$), but numbers for this analysis were small. Medial type of speech did not correlate with motor thresholds of any of the muscles (all $P > 0.1$).

A backward linear regression analysis incorporating other factors potentially impacting on speech (age, contact location, preoperative speech intelligibility, strength of stimulation, levodopa equivalent dose reduction) showed that 79.9% of the variance in speech intelligibility was explained by the four factors preoperative speech intelligibility ($P = 0.0034$), strength of stimulation ($P = 0.0001$), levodopa equivalent dose reduction post-surgery ($P = 0.0019$), and RMT of the FDI ($P = 0.0016$).

5.5: Discussion

In this multimodal study, we assessed the activation of the pyramidal tract attributed to STN-DBS in PD. We distinguished between CBT and CST by means of both neurophysiological assessment with EMG and imaging assessment with tractography and,

importantly, found strong correlations between outcomes of these assessment tools within the corticobulbar and the corticospinal system, respectively, arguing for the validity of our approach. The most relevant findings of our study are as follows: (1) Subthalamic DBS induces MEPs bilaterally in the face and contralaterally in the hand at thresholds of stimulation strengths, which are within the range used in routine clinical practice; (2) this activation most likely occurs because of direct stimulation of corticobulbar and corticospinal fibres, as shown by our imaging analysis and supported by the strength-duration curve calculations; (3) although motor improvement with STN-DBS was not related to the threshold of the MEPs, motor thresholds are directly correlated to amplitude used for chronic stimulation; and (4) development of the lateral type of speech disturbances with stimulation is significantly related to activation of the pyramidal tract.

5.5.1: Anatomical considerations

Using stimulation strengths up to 6.0 mA, it was possible to elicit MEPs in 99% of contralateral OOr, 92% of ipsilateral OOr, and 94% of FDIs. Median RMT was 3.0 mA for the contralateral OOr and 4.0 mA for the ipsilateral OOr and contralateral FDI. There was a significant hemisphere difference with higher thresholds upon stimulation in the right, as compared with the left STN, which could result from the fact that all our patients were right-handed. The increasing thresholds of FDI activation toward more superior contacts, also observed in an earlier study [310], may be attributed to a double oblique trajectory where electrode axes parallel the CBT coming from more anteriorly and include a small angle with the CST coming from more posteriorly [308]. Location of the CBT and CST within the internal capsule has been a matter of debate, but our analysis supports findings from recent studies suggesting that both the CBT and the CST run closely together within the posterior limb of the lower peduncular part of the internal capsule with a considerable level of overlap [308].

5.5.2: Neurophysiological considerations

The most likely mechanism of induction of MEPs is activation of the pyramidal tract and orthodromic conductance of the action potential to motor brainstem nuclei and the anterior

horn of the spinal cord, as suggested by multiple studies [310,317,318]. However, we here corroborate this hypothesis, for the first time, by correlating the threshold of facial MEPs to volume of corticobulbar activation and threshold for MEPs in the hand to corticospinal activation. The level of correlation was high and robust for the latter combination, whereas the correlation of corticobulbar volume activated with the OOr were slightly weaker contralaterally and not present ipsilaterally. Variability of the corticobulbar fibres at the level of the STN might be higher given that crossing of these fibres occurs slightly below and asymmetries between right and left and ipsilateral versus contralateral innervation have been demonstrated [321,322]. Ipsilateral fibres may additionally be located further away from the STN, which would be in line with our findings of a higher threshold for eliciting MEPs ipsilaterally than contralaterally. Also, chronaxie measurements of the three muscles were all well within the reported range of large myelinated axons [316,323,324], making it unlikely that electrophysiological characteristics of innervating systems are different. This is further supported by the similar latencies for ipsilateral and contralateral MEPs in the OOr arguing in favour of a bilateral, probably oligosynaptic, projection with contralateral predominance, as suggested previously [321]. Interestingly, we found a positive correlation of the latency with the amplitude of the MEPs. This may be explained by size principle in the recruitment of motoneurons with small and slower conducting ones reaching threshold before larger and faster conduction ones [325].

Importantly, thresholds for pyramidal side effects observed during the screening procedure were around 3 mA, similar to the RMT as assessed by EMG. Moreover, AMTs were significantly lower than RMTs, and also voluntary activation of corticobulbar or corticospinal fibres may enhance excitability of spinal or bulbar motoneurons, respectively. Median AMTs were as low as 2.5 mA, suggesting that activation of pyramidal fibres may occur with routinely used stimulation setting during activation that might not be evident at rest. The clinical implications of the stimulation of pyramidal fibres attributed to STN-DBS in PD have not been systematically studied so far.

5.5.3: Clinical implications

We found that in patients with lower AMTs and RMTs on the clinically used contacts, lower stimulation amplitudes for clinical benefit were used. This may point to (conscious or unconscious) avoidance of stimulation settings, which potentially activate the pyramidal tract in clinical routine. However, in our cohort, this did not translate into a significant relationship between motor improvement upon stimulation and the identified thresholds of pyramidal tract activation, but our cohort was rather small and patients were relatively early in their DBS treatment duration. With increasing disease and stimulation duration, higher stimulation current may be necessary to achieve sufficient symptom control at which point spread to the pyramidal tract might play a larger role. A contrasting interpretation, however, may be that stimulation of fibre tracts in close vicinity to the STN and the pyramidal tract, such as corticosubthalamic projections (e.g., the hyperdirect pathway), or pallidofugal fibres (e.g., ansa lenticularis or longitudinal fasciculus) might contribute to improved motor symptom control, as hypothesized by other studies [250,324,326], such that a slight stimulation of these fibres along with an unavoidable, but "subclinical" stimulation of the pyramidal tract could overall be beneficial. In line with these hypotheses, a recent study has shown that STN-DBS activates the cerebral cortex at 1 ms after stimulus onset, suggesting that antidromic activation of axons with cortical origin projecting to the subthalamic region could actually be part of the therapeutic mechanism of STN-DBS [305].

A further important observation was the strong correlation of the RMT of the FDI with postoperative "lateral type" speech intelligibility; RMT of the FDI was a significant factor in a logistic regression analysis along with preoperative speech intelligibility, applied stimulation strength, and levodopa dose reduction in combination explaining 80% of the variance in postoperative speech intelligibility. RMT of the OOr was not significantly associated with postoperative speech intelligibility. This might relate to the fact that speech intelligibility can be compromised by activation of fibres innervating a large number of different muscles in the face and pharynx and also to the greater variance of the OOr EMG signal. Also, CBT and CST in the tractography analysis and the EMG signal of the OOr and

FDI were very closely related, to the extent that EMG of the FDI might be the most practical marker of pyramidal activation and related clinical implications. Interestingly, the observed characteristics of the lateral type of speech were in line with speech changes in previous reports of pseudobulbar speech impairment upon lacunar cerebral infarction [327].Medial type of speech did not relate to any of the thresholds observed in line with earlier studies, suggesting that it relates to stimulation of structures outside the pyramidal tract, possibly the fasciculus cerebellothalamicus adjacent to the medial zona incerta and the prelemniscal radiations [314,328].

5.6: Conclusion

Subthalamic DBS induces MEPs at rest and upon activation bilaterally in the face and contralaterally in the hand at thresholds of stimulation strength that are within the range used in clinical routine. This spread of current compromises increase in stimulation strengths and is related to the development of speech disturbances with chronic stimulation. Our study suggests that EMG may detect such current spread and might thus represent a valuable tool in troubleshooting in PD patients treated with STN-DBS. Further studies will have to elucidate whether current spread to the pyramidal tract directly impacts on motor improvement attributed to subtle, subclinical corticobulbar and/or corticospinal stimulation.

Table 5-1: Characteristics of the study participants

	Mean ± standard deviation (median, 25th – 75th percentile)
Sex distribution	3 female, 17 male
Age	57.9 ± 9.7 (60.6, 52.6–67.9) years
Disease duration	10.9 ± 4.7 (11.3, 7.2–13.8) years
Stimulation duration	1.2 ± 0.7 (1.0, 0.9–1.4) years
Amplitude of stimulation	2.0 ± 0.7 (2.0, 0.5–3.5) mA
Frequency of stimulation	127 ± 29 (130, 125–130) Hz
Pulse width of stimulation	60 μs
UPDRS-III; pre-OP, Off Meds	43.8 ± 13.6 (45.0, 35.5–51.5)
UPDRS-III; post-OP, Off Meds, On Stim	27.4 ± 11.8 (27.0, 17.0–35.0)
Improvement pre- vs. post-OP	35.6 ± 19.7 (22.9–48.5) %
Levodopa equivalent dose pre-OP	1452 ± 517 (1446, 1177–1978) mg
Levodopa equivalent dose post-OP	776 ± 293 (650, 500–953) mg
Dyskinesia Rating Scale scores post-OP (On Meds, On Stim)	3.3 ± 3.2 (3.5, 0.0-6.0)

Table 5-2: Resting Motor Thresholds and effects of hemisphere and contact location

Muscle	Overall RMT (including all contacts from both electrodes) (mA)	Comparison versus OOr contra Z-score p-value	Comparison by hemisphere			Regression analysis Beta-coefficient (95%CI)	
			Left hemisphere (contacts 0–3)	Right hemisphere (contacts 8–11)	Z-scores	Hemisphere: Left versus right	Contact location: Inferior to superior
OOr contra	3.5 ± 1.0 (3.0; 3.0–4.0)		3.3 ± 1.1 3.0 (2.5–3.5)	3.6 ± 0.9 3.5 (3.0–4.0)	-2.7 p=0.0068	0.345 (0.025–0.666) p=0.0347	0.029 (-0.114–0.173) p=0.686
OOr ipsi	4.1 ± 1.1 (4.0; 3.5–5.0)	-7.5 p<0.0001	3.9 ± 1.2 3.5 (3.0–5.0)	4.4 ± 1.0 4.0 (3.5–5.1)	-2.8 p=0.0052	0.448 (0.086–0.809) p=0.0158	0.039 (-0.123–0.202) p=0.633
FDI	4.0 ± 1.2 (4.0; 3.0–5.0)	-5.0 p<0.0001	3.9 ± 1.2 4.0 (3.0–5.0)	4.1 ± 1.1 4.0 (3.0–5.0)	-2.2 p=0.0312	0.275 (-0.091–0.642) p=0.140	0.242 (0.077–0.407) p=0.0044

Results are reported in means ± standard deviation (medians, 25^{th} -75^{th} percentile). Two-sided, paired Wilcoxon signed rank test was used to calculate significance levels across muscles and between sides. A linear regression analysis was performed to evaluate effects of hemisphere of stimulation and contact location along the axis of the electrode (independent variables), and on motor threshold (dependent variable). Abbreviations: FDI = First Dorsal Interosseus muscle; mA = milliampere; µV = microvolt; MEP = Muscle Evoked Potential; OOr = Orbicularis Oris muscle; RMT = Resting Motor Threshold; 95%CI = 95% Confidence Interval

Table 5-3: Correlations of RMT with volumes of overlap

	Correlations Spearman rank coefficients (r)	**Regression analysis Beta-coefficient (95%CI)**	
Muscle	**Overall**	**Unadjusted**	**Adjusted for hemisphere and contact location**
OOr contra*	-0.349 p<0.0001	-0.021 (-0.030–-0.012) p<0.0001	-0.028 (-0.038–-0.009) p<0.0001
OOr ipsi*	-0.023 p=0.796	0.000 (-0.010–0.010) p=0.997	0.004 (-0.007–0.014) p=0.488
FDI**	-0.493 p<0.0001	-0.035 (-0.046–-0.024) p<0.0001	-0.033 (-0.045–-0.022) p<0.0001

*RMTs of the contralateral and ipsilateral OOr were correlated with volumes of corticobulbar tissue activated

**RMTs and MEPs of the FDI were correlated with volumes of corticospinal tissue activated

Beta-coefficients report the impact of volumes of overlap in voxels on RMT of respective muscles and were calculated with a linear regression analysis.

FDI = First Dorsal Interosseous muscle; OOr = Orbicularis Oris muscle; MEP = Muscle Evoked Potential; RMT = Resting Motor Threshold; 95%CI = 95% confidence interval

Table 5-4: Active motor thresholds

Condition	Muscle	Threshold (mA)	Correlation with Volumes of Overlap	Regression analysis Beta-coefficient (95%CI) p-value	
				Unadjusted	Adjusted for side and contact location
Activation of the OOr	OOr contra (AMT)*	2.4 ± 0.8 (2.5, 2.0–2.5)	-0.288 p=0.182	-0.011 (-0.029–0.006) p=0.182	-0.005 (-0.020–0.010) p=0.494
	OOr ipsi (AMT)*	2.9 ± 0.8 (3.0, 2.3–3.5)	-0.186 p=0.394	-0.009 (-0.032–0.013) p=0.394	-0.002 (-0.024–0.019) p=0.818
	FDI	3.2 ± 1.2 (3.0, 2.5–4.0)			
Activation of the FDI	OOr contra	3.1 ± 1.0 (3.0, 2.1–3.9)			
	OOr ipsi	3.8 ± 1.1 (4.0, 3.0–4.4)			
	FDI (AMT)*	2.6 ± 0.7 (2.5, 2.1–3.0)	-0.506 p=0.0162	-0.020 (-0.035–-0.004) p=0.0162	-0.012 (-0.028–0.004) p=0.137

Results are reported in means ± standard deviation (medians, 25^{th} -75^{th} percentile). Two-sided, paired Wilcoxon signed rank test was used to calculate significance levels across muscles and between sides. * True AMT conditions; OOr contralateral vs. ipsilateral: Z=-3.7, p=0.0002; OOr contralateral vs. FDI: Z=-1.6, p=0.111. Abbreviations: AMT = Active Motor Threshold; FDI = First Dorsal Interosseus muscle; mA = milliampere; mV = millivolt; MEP = Muscle Evoked Potential; OOr = orbicularis oris muscle.

Figure 5-1A: MEPs of the three muscles recorded in increasing stimulation strength (patient 17, contact 1-).

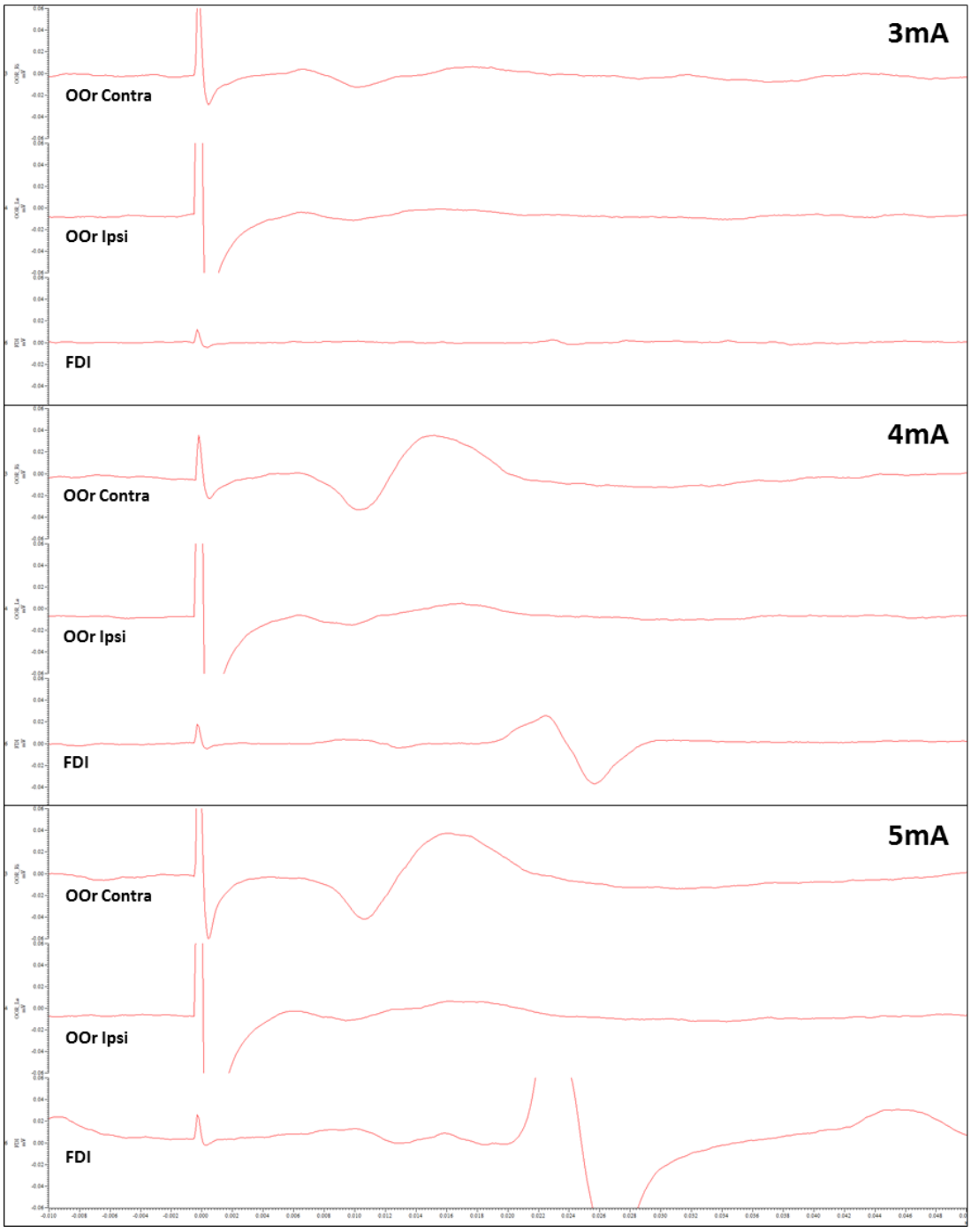

RMT for the contralateral OOr was reached at 3mA of stimulation strength, whereas ipsilateral OOr and FDI showed MEPs starting from 4mA.

Figure 5-1B: MEPs of the three muscles recorded in increasing stimulation strength (patient 13, contact 8-)

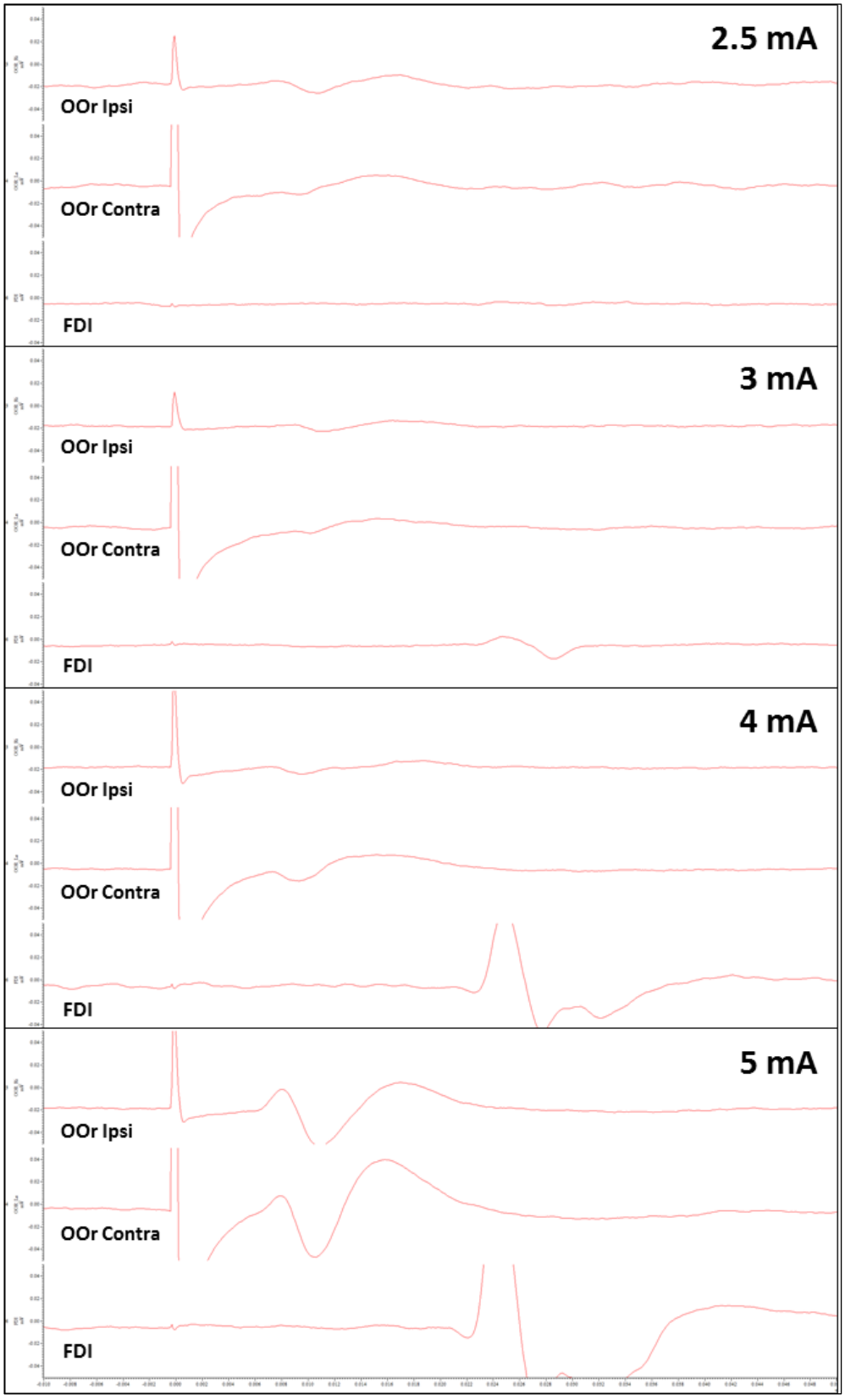

RMT for the contralateral OOr was reached at 2.5mA of stimulation strength, whereas ipsilateral OOr and FDI showed MEPs starting from 3mA.

Figure 5-2: Probabilistic tractography derived corticospinal tract (CST, orange) coming from the precentral cortex in and around the hand motor knob and corticobulbar tracts (CBT, blue) coming from the laterally and caudally adjacent precentral motor cortex.

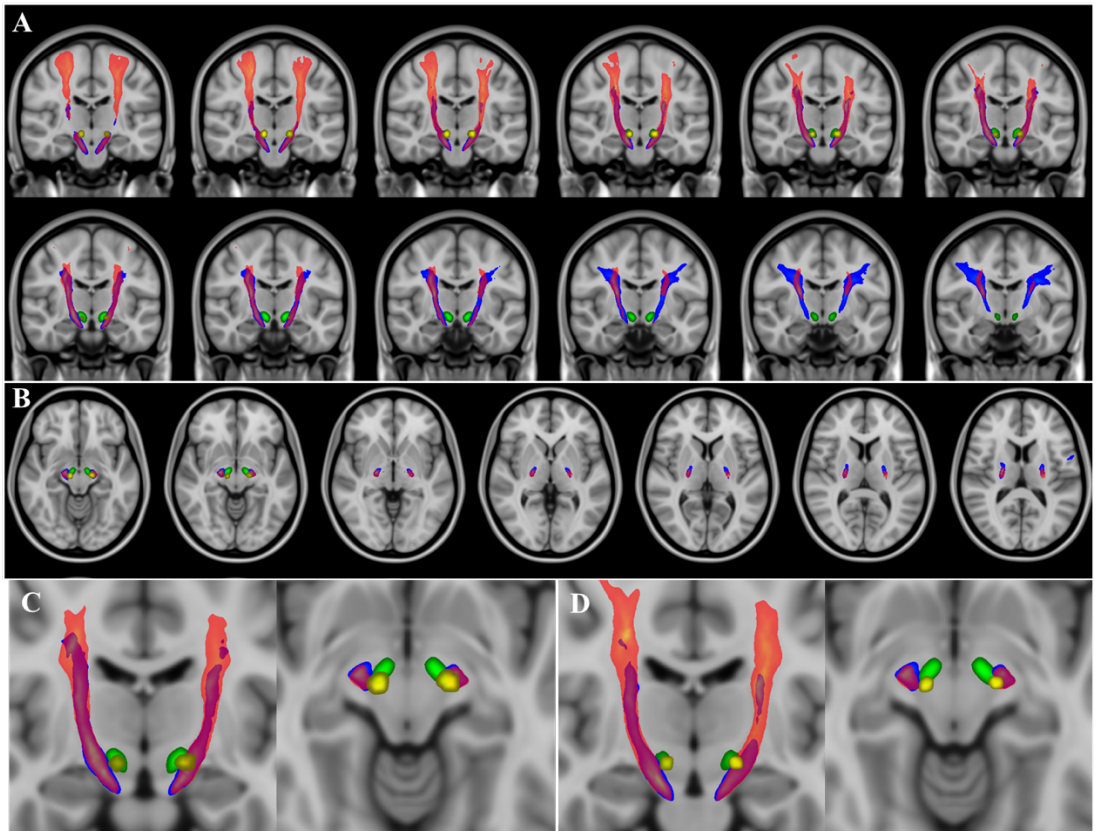

The subthalamic nucleus (STN) of subject number 13 is depicted in green and the volume of tissue activated (VTA) on the highest contacts (3- and 11-) is depicted in yellow. On coronal (A) and axial (B) slices it can be appreciated that the CBT is located more anteriorly than the CST with diminishing distance towards caudally and a great level of overlap at the level of the STN. Enlarged images show level of overlap between CBT/CST and VTA (i.e. volume of corticobulbar/corticospinal tract activated) at 4 mA (C) and 2 mA (D) of stimulation strength as an example, which was greater for the left than for the right side in this case.

Figure 5-3: Strength-time duration curves depicting the relationship between pulse width and amplitude necessary for induction of RMT in the three muscles

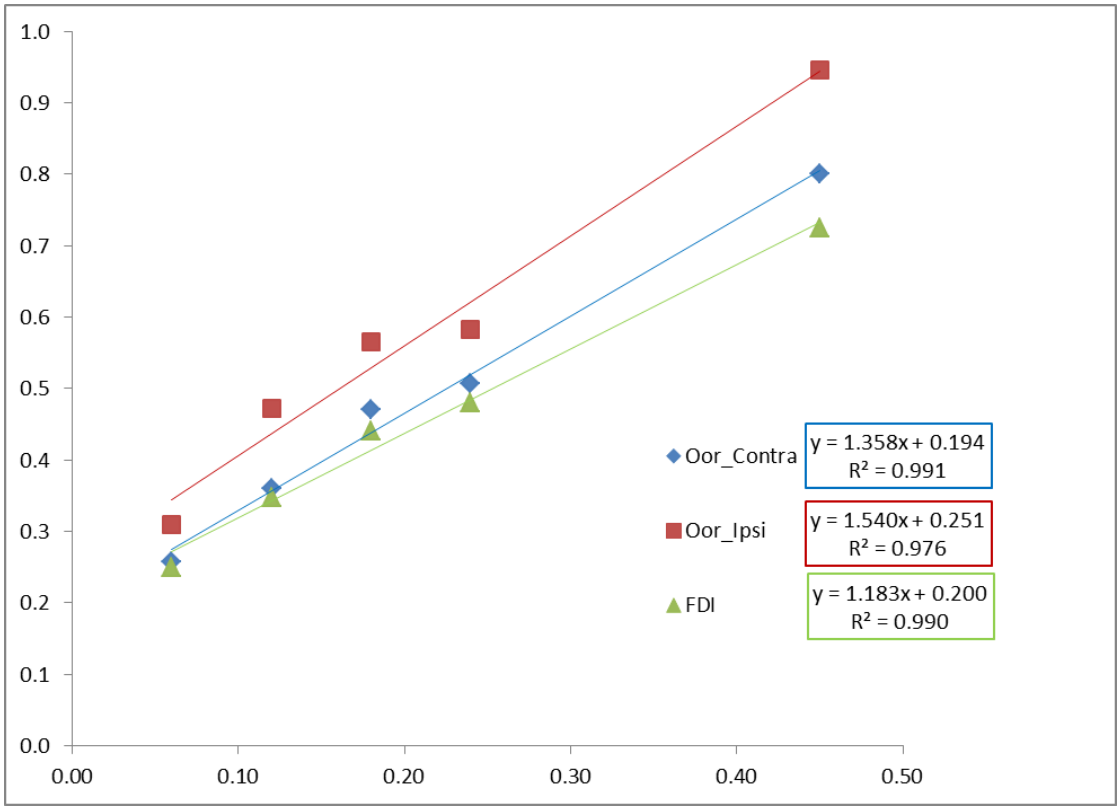

The data were linearized by plotting pulse width (x-axis; µs) against the product of amplitude and pulse width (y-axis; mA*µs). To further confirm that motor responses in the OOr and FDI were due to stimulation of large diameter myelinated fibres in the pyramidal tract, we calculated the strength-duration time constant for these effects based on the Weiss's law (Weiss, 1901, Ranck 1975). The time constant is given by the (negative) intercept of the linear regression line on the duration axis and was 142.5 µs for the contralateral OOr, 163.2 µs for the ipsilateral OOr, and 168.8 µs for the FDI. These chronaxies are well within the reported range of large myelinated axons as pyramidal tract fibres [316,323,324], making it unlikely that electrophysiological characteristics of innervating systems are different.

Section II:

Connectivity in Tremor

“When the hand trembled to receive

A thrilling clasp, which seemed so near,

And the heart ventured to believe,

Another heart esteemed it dear”

***Frances*, Charlotte Brontë** (1816–1855)

6. Connectivity derived thalamic segmentation in deep brain stimulation for tremor

6.1: Abstract

The ventral intermediate nucleus (VIM) of the thalamus is an established surgical target for stereotactic ablation and deep brain stimulation (DBS) in the treatment of tremor in Parkinson's disease (PD) and essential tremor (ET). It is centrally placed on a cerebello-thalamo-cortical network connecting the primary motor cortex, to the dentate nucleus of the contralateral cerebellum through the dentato-rubro-thalamic tract (DRT). The VIM is not readily visible on conventional MR imaging, so identifying the surgical target traditionally involved indirect targeting that relies on atlas-defined coordinates. Unfortunately, this approach does not fully account for individual variability and requires surgery to be performed with the patient awake to allow for intraoperative targeting confirmation. The aim of this study is to identify the VIM and the DRT using probabilistic tractography in patients that will undergo thalamic DBS for tremor. Four male patients with tremor dominant PD and five patients (three female) with ET underwent high angular resolution diffusion imaging (HARDI) (128 diffusion directions, 1.5 mm isotropic voxels and b value = 1500) preoperatively. Patients received VIM-DBS using an MR image guided and MR image verified approach with indirect targeting. Postoperatively, using parallel Graphical Processing Unit (GPU) processing, thalamic areas with the highest diffusion connectivity to the primary motor area (M1), supplementary motor area (SMA), primary sensory area (S1) and contralateral dentate nucleus were identified. Additionally, volume of tissue activation (VTA) corresponding to active DBS contacts were modelled. Response to treatment was defined as 40% reduction in the total Fahn-Tolosa-Martin Tremor Rating Score (FTMTRS) with DBS-ON, one year from surgery. Three out of nine patients had a suboptimal, long-term response to treatment. The segmented thalamic areas corresponded well to anatomically known counterparts in the ventrolateral (VL) and ventroposterior (VP)

thalamus. The dentate-thalamic area, lay within the M1-thalamic area in a ventral and lateral location. Streamlines corresponding to the DRT connected M1 to the contralateral dentate nucleus via the dentate-thalamic area, clearly crossing the midline in the mesencephalon. Good response was seen when the active contact VTA was in the thalamic area with highest connectivity to the contralateral dentate nucleus. Non-responders had active contact VTAs outside the dentate-thalamic area. We conclude that probabilistic tractography techniques can be used to segment the VL and VP thalamus based on cortical and cerebellar connectivity. The thalamic area, best representing the VIM, is connected to the contralateral dentate cerebellar nucleus. Connectivity based segmentation of the VIM can be achieved in individual patients in a clinically feasible timescale, using HARDI and high performance computing with parallel GPU processing. This same technique can map out the DRT tract with clear mesencephalic crossing.

6.2: Introduction

The ventral intermediate nucleus (VIM) of the thalamus is an established surgical target, for stereotactic ablation and deep brain stimulation (DBS) in the treatment of tremor in Parkinson's disease (PD), essential tremor (ET) and multiple sclerosis [329-336]. A subjacent area, the caudal zona incerta (cZI), is another effective DBS target for the treatment of tremor [284,337-340].

The VIM is centrally placed on a cerebello-thalamo-cortical network in which pathological oscillations, possibly triggered by pallidal dysfunction in the case of PD, is thought to be culpable for tremor [299]. The cortical focus in this tremor network is in the primary motor cortex, connected to the dentate nucleus of the contralateral cerebellum through the dentato-rubro-thalamic tract (DRT) via the VIM [341-346].

The VIM is not readily visible on conventional, stereotactic MR imaging sequences used in image guided and image verified surgery [347-350]. Identifying the nucleus traditionally involves indirect targeting relying on atlas-defined coordinates in relation to the anterior commissure (AC) – posterior commissure (PC) points as landmarks, along with other

identifiable structures such as the lateral thalamic / internal capsule border [262]. Needless to say, this approach does not fully account for individual variability. Furthermore, surgery often needs to be performed with the patient awake to allow for intraoperative confirmation of targeting, thus increasing patient discomfort [351]. Moreover, intraoperative confirmation is not always readily feasible e.g. when performing a thalamotomy using Gamma Knife [352] or focused ultrasound [353].

To overcome this, various imaging techniques have been proposed to identify the VIM. Ultra-high field MRI provides high contrast-to-noise ratio in-between thalamic nuclei, better segmenting the nucleus, however, this modality is not readily available in a clinical setting [354]. Another technique relies on contrast in coloured fractional anisotropy (FA) maps, a product of diffusion tensor imaging (DTI) [355,356]. Simple visualisation of the first order tensor fields in DTI has also been used to generate deterministic tractography models of the DRT, which is then targeted by DBS [132,136,357,358]. This modality is commonly accessible in clinical settings and imaging is relatively swift to acquire and process; however, it carries limitations related to disentangling crossing fibres, tracking in areas of low anisotropy (e.g. the thalamus) [80] and overall accuracy [100].

An emerging modality utilises high angular resolution diffusion imaging (HARDI) and probabilistic connectivity based segmentation of the thalamus [80,94,359-361]. This technique successfully models crossing fibres and grey matter (low anisotropy) connectivity and achieves high signal-to-noise ratio, but requires prolonged image acquisition and large computational resources which are impractical in clinical practice. Novel MRI acquisition techniques, such as Simultaneous Multi-Slice Imaging and Multi-Band Imaging [303] have reduced scanning time. Furthermore, advances in computer processing techniques and relying on graphical processing units to carry out diffusion analysis have facilitated the use of this modality in clinical practice [160,282].

The objectives of this study were to examine the feasibility of using probabilistic, connectivity based segmentation techniques to segment the thalamus in a group of PD and ET patients one year from VIM DBS; to generate probabilistic tractography models of the

DRT tracts and to carry out a post-hoc analysis of the relation of the segmented VIM and DRT with volume of tissue activation (VTA) models around active contacts of the DBS lead. We show that the VIM is best segmented based on connectivity to the contralateral dentate nucleus and that patients with good response to treatment had active contact VTAs within the segmented VIM.

6.3: Materials and methods

6.3.1: Patients

Four male patients with tremor dominant PD who met UK brain bank criteria [273] and five patients (three female) with ET were recruited, following selection for VIM-DBS, by a multidisciplinary team of specialized movement disorders neurologists and functional neurosurgeons (**Table 6-1**). Formal neuropsychological assessment and structural brain MRI were performed to rule out dementia and significant brain atrophy, respectively. PD patients underwent the L-DOPA challenge test during the routine selection process. The motor subsection of the unified Parkinson's disease rating scale (UPDRS-III) was assessed in the OFF state at least 12 hours after omitting PD medications. The assessment was then repeated 30 minutes (or when clinically ON) after administration of the patient's regular medications topped-up with an additional dose of 50mg/12.5mg dispersible Madopar/ Benserazide. Patients with ET underwent assessment with the Fahn-Tolosa-Marin Tremor Rating Scale (FTMTRS) [362]. The scale consists of three sections rating severity of tremor from 0 (none) to 4 (severe). The first section assesses severity and location of tremor, the second section assesses ability to perform specific motor tasks, such as writing, drawing and pouring, and the third section assesses patient-reported functional disability resulting from the tremor (speaking, eating, drinking, hygiene, dressing, writing, working and social activities) [363]. Inclusion in the present study was limited to patients who could tolerate lying flat for the duration of the preoperative scan and who have no contraindications to 3T MRI.

6.3.2: Preoperative diffusion weighted MRI acquisition and preprocessing

Details of diffusion weighted MRI acquisition and preprocessing are described in the general methods sections.

6.3.3: Surgical procedure and intraoperative MRI acquisition

DBS leads (3389 Medtronic) were implanted under local anaesthesia using a stereotactic MRI-guided and MRI-verified approach without microelectrode recording (using a Leksell frame model G, Elekta Instrument AB, Stockholm, Sweden), as detailed in previous publications on subthalamic nucleus DBS for PD [274,275]. All patients had unilateral surgery except for one patient with PD tremor who underwent bilateral surgery.

Three stereotactic, pre-implantation scans were acquired, as part of the surgical procedure, to guide lead implantation; a proton-density and a T2 weighted axial scan (partial brain coverage around the thalamus and cZI) with voxel size of 1.0×1.0 mm^2 and slice thickness of 2 mm [62,364]; and a T1 weighted 3D-MPRAGE scan with a 1.5 mm isotropic voxel size on a 1.5T Siemens Avanto interventional MRI scanner. Three-dimensional distortion correction was carried out using the scanner's built-in module. Once scans were reoriented to have slices parallel with the anterior commissure (AC) – posterior commissure (PC) line, the trajectory was planned such that the deepest contact targeted the cZI and the proximal contacts targeted the VIM at the level of the AC-PC. The thalamo-capsular border, visualised on the proton-density scan, was used to aid the identification of the laterality of the VIM on imaging, which was then indirectly targeted using atlas coordinates in relation to the mid-commissural point - [X=12-14 mm, Y= (AC-PC length/3) - 2 mm anterior to PC, Z=0]. The cZI was identified on the axial T2-weighted scan medial to the postero-medial border of the STN. The MPRAGE scan was used to plan the lead's entry point over the coronal suture ± 1 cm anteroposteriorly, with the lead trajectory avoiding the ventricles and sulci. A 1.5 mm thick radiofrequency probe (RF) was inserted first into the deepest target (cZI), using impedance recording. The last 6 mm of the trajectory were traversed using 2 mm steps whilst simultaneously assessing the implantation effect on tremor in the outstretched contralateral upper limb. The RF lead was then replaced with the DBS lead,

temporarily fixed in situ. Fibrin sealant (Tisseel, Baxter, USA) was used in the burr hole to prevent CSF leak and pneumocephalus [260]. An external stimulator was then used to deliver monopolar stimulation to each contact using increasing amplitudes to assess efficacy and side-effect profile. Transient tingling in the palm upon stimulation was considered a sign of good placement. Patients were stressed, using verbal recollection and arithmetic tasks, to elicit the tremor. Thresholds for capsular effects and dysesthesia were also assessed. In the case of poor response or unacceptable side-effects, the lead was removed and the process repeated following appropriate targeting adjustments. Imaging was repeated immediately following lead implantation to confirm lead placement. The specific absorption rate (SAR) was kept < 0.4 W/kg by reducing the number of acquired T2 weighted slices covering the distal leads to 12-14. The leads were then connected to an implantable pulse generator (IPG) (Activa SC or PC, Medtronic, Minneapolis, Minn., USA) implanted in the infra-clavicular region on the same day or within a week.

6.3.4: Outcome measures

6.3.4.1: Effective stimulation parameters

All DBS contacts were screened by a movement disorders neurologist once implantation effects had worn off (2-14 days). Patients were then followed-up in clinic to adjust and fine tune stimulation parameters in the first 12 months after surgery.

6.3.4.2: Fahn-Tolosa-Marin Tremor Rating Scale

All patients underwent assessment both in the OFF and ON DBS states 12 – 24 months from surgery. This was carried out by an experienced movement disorders neurologist. The assessment was carried out with DBS ON first and then 10 minutes after switching stimulation off. Good response to DBS was defined as an improvement ≥ 40% in total FTMTRS with ON stimulation.

6.3.4.3: DBS contacts volume of tissue activated (VTA) modelling

SureTune® (Medtronic Inc. Minnesota), a DBS therapy planning platform was used to model VTAs around individual contacts. The platform applies neuron models coupled to finite element simulations as described by Åström and colleagues in order to generate DBS therapy VTA [162]. Intraoperative MRI scans were uploaded and a two-step linear registration was used to co-register the pre-implantation and post-implantation stereotactic MPRAGE scans. The first step involved manually aligning the volumes with the pre-implantation MPRAGE. The second step employed automated co-registration with a restricted volume of fusion centred around the diencephalon/ mesencephalon. This was carried out to minimise registration error resulting from eventual brain shift incurred during surgery, despite minimal brain shift with our surgical technique [260]. Registration accuracy was carefully inspected and the process iterated if necessary. All volumes were realigned with a plane parallel to the AC-PC line.

Post-implantation MPRAGE scans were used to fit the DBS lead model within the MRI artefact produced by the leads. Individual VTAs were then generated around active DBS contacts with corresponding stimulation amplitudes. Binary image files of VTAs with corresponding transformation matrices were exported and processed in MATLAB (MathWorks Inc.) using an in-house software to generate Neuroimaging Informatics Technology Initiative (NIfTI) volumes for further analysis. Right sided individual contact VTAs were lateralised to the left by swapping the x axis (x, y, z > -x, y, z) using *Fslswapdim* (FSL v5.0).

6.3.5: Image Pre-processing

Pre-implantation MPRAGE scans were brain extracted using *BET* (Brain Extraction Tool, FSL v5.0) [277]. Two-step transformation was used to register native scans to the MNI152 standard-space T1-weighted average structural template image (1mm resolution) [278]. The first step employed linear (affine) transformation using *FLIRT* (FMRIB's Linear Image Registration Tool) using 12 degrees of freedom, correlation ratio cost function and normal search [279,280]. The output from this step was used to execute non-linear registration (second

step) using *FNIRT* (FMRIB's Non-Linear Image Registration Tool) [281]. This process produced individual native to standard (MNI space) non-linear warp fields, which were then applied to VTAs acquired from SureTune in order to transform all volumes to standard space.

6.3.6: Analysis

6.3.6.1: Regions of interest (ROI) definition

Cortical reconstruction and volumetric segmentation of the MNI-152, T1 weighted (1mm) volume was performed with the Freesurfer image analysis suite. Resulting ROIs were used for connectivity based thalamic segmentation and tractography of the dentato-rubro-thalamo-cortical tract (DRTC). Cortical volumetric masks of the primary motor cortex (M1 [Brodmann's area 4]), primary sensory cortex (S1 [Brodmann's areas 3,1,2]), supplementary motor area (SMA), premotor cortex (PMC) (both constituting Brodmann's area 6) and subcortical thalamic volumetric masks were generated. Cerebellar masks of the superior cerebellar peduncle and the cerebellar white matter (containing the dentate nucleus) were manually segmented using ITK-SNAP [365] **(Figure 6-1)**.

6.3.6.2: Tractography

Probabilistic tractography was generated in ProbtrackX2 GPU version (Behrens 2007) [282] (FSL v5.0) (number of samples=5000, curvature threshold=0.2, step length=0.5 mm subsidiary fibre volume fraction threshold=0.01). The process repetitively samples from the distributions of voxel-wise principal diffusion directions generated in *BedpostX*, each time computing a streamline through these local samples to generate a 'probabilistic streamline' or a 'sample' from the distribution on the location of the true streamline, building up a spatial 'connectivity distribution' or global connectivity (i.e. the probability of the existence of a path through the diffusion field between any two distant points, a surrogate measure of anatomical connectivity) [103]. Streamlines truly represent paths of minimal hindrance to diffusion of water in the brain, but they are reasonable indirect estimates of long-range white matter connections [283].

6.3.6.3: Connectivity based thalamic segmentation

Thalamic segmentation was carried out for all patients using probabilistic tractography. The resulting volumes were used to create group averages. Seed voxels in the thalamus were classified according to the probability of connection to the defined cortical and cerebellar target masks (ipsilateral S1, M1, SMA/PMC and contralateral cerebellar masks). This process has been previously described by Behrens et al [94]. CSF termination and contralateral cerebrum/ ipsilateral cerebellum exclusion masks were applied to exclude false positive streamlines and commissural tracts.

6.3.6.4: Tractography of the dentato-rubro-thalamo-cortical pathway

Probabilistic tractography was generated, for each patient, from the cerebellar seed to the contralateral M1 target using the contralateral thalamic mask as waypoint and the ipsilateral cerebrum and contralateral cerebellum as exclusion masks. CSF termination masks were used to exclude false positive streamlines. The process was repeated using the M1 mask as seed and the cerebellar mask as target. The two resulting tracks were merged to create a single DRTC tract. All tracks were then used to create group averages.

6.4: Results

6.4.1: Patients

Preoperative scanning and surgery proceeded with no adverse events. The mean pre-operative UPDDRS-III tremor subsection score (highest possible score = 28) for the PD patients was 12.5 (8-17) points off medications and 9.8 (8-12) points on medications with a modest average improvement of 18%. Two out of the four patients with PD did not show improvement in tremor with levodopa administration.

The ET group had a preoperative FTMTRS score of 81.6 (55-97) points.

All patients were right hand dominant. There was no surgical morbidity or mortality. One patient with PD had bilateral surgery in one procedure. The remainder had left sided surgery making up a total of 10 implanted DBS leads (five in each group) **(Table 6-1)**.

6.4.2: DBS profile

All patients improved with DBS albeit to varying degrees (**Table 6-1**). PD3 had a marked improvement in tremor following lead implantation (bilateral DBS). The tremor re-emerged a week later just before IPG insertion. Once DBS was switched on there was a significant improvement in tremor, however, 24 hours later, the patient became agitated. This was felt to be largely due to sleep deprivation and resolved on resumption of normal sleep. ET1 had a significant improvement at 2 Volts, however, mild slurring and slowing of speech occurred at 2.5 Volts. ET2 had tingling and discomfort in the right side of the face, right arm and part of the right leg when stimulating the deepest contact (cZI) and facial pulling at 1.9 Volts when stimulating the second deepest contact. ET4 developed very mild balance deterioration and a feeling of exhaustion and ET5 developed mild and transient paraesthesia with stimulation.

6.4.3: Postoperative clinical outcomes

All PD patients experienced tremor rebound when DBS was switched off. The mean improvement in FTMTRS was 58% in the PD group and 34% in the ET group, comparing off to on stimulation. Three out of five patients in the ET group had a poor response to treatment (<40%) **(Table 6-1)**.

6.4.4: Connectivity-based thalamic segmentation

Appropriate thresholds of (1,000) and (100) samples per voxel were applied to cortical and cerebellar group average thalamic clusters respectively using *Fslmaths* (FSL v5.0). The clusters were in the ventrolateral thalamus with some overlap between SMA/PMC and M1 clusters; and between M1 and S1 clusters. The contralateral cerebellar (dentate) cluster lies completely within the inferior portion of the M1 cluster **(Figure 6-1)**. Cluster-based inference using *Cluster* (FSL v5.0) was carried out to extract the clusters and local maxima in outputs **(Table 6-2)**.

Table 6-2: Connectivity-based thalamic clusters of cortical and cerebellar areas showing volumes and MNI (AC-PC) coordinates of maximum intensity and centre of gravity (Left hemisphere)

Thalamic Cluster	VOL (mm^3)	Maximum intensity coordinates MNI (AC-PC)			Centre of gravity coordinates MNI (AC-PC)		
		X	Y	Z	X	Y	Z
S1	704	-17 (-16.5)	-23 (-11)	4 (8)	-17 (-16.5)	-22 (-10)	4.8 (8.8)
SMA/PMC	743	-15 (-14.5)	-8 (4)	5 (9)	-13 (-12.5)	-10 (2)	5.6 (9.6)
M1	1021	-20 (-19.5)	-19 (-7)	8 (12)	-16 (-15.5)	-19 (-7)	6 (10)
Dentate	141	-10 (-9.5)	-18 (-6)	-3 (1)	-15 (-14.5)	-17 (-5)	1.5 (5.5)

MNI: Montreal Neurological Institute; AC-PC: anterior commissure – posterior commissure; VOL: volume; S1: primary sensory area; M1: primary motor area; SMA: supplementary motor area; PMC: premotor cortex

Table 6-1: Demographics, preoperative UPDRS-III (PDT patients), FTMTRS (ET patients), postoperative FTMTRS ON/ OFF DBS and stimulation parameters

Patient		PD1	PD2	PD3	PD4	Mean	ET1	ET2	ET3	ET4	ET5	Mean
Age (yr.)*		67	63	64	67	**65.3**	56	49	66	78	70	**63.8**
Surgery		Left	Left	Bilat.	Left		Left	Left	Left	Left	Left	
Disease duration (yr.)*		5	6	10	10	**7.8**	10	10	6	12	11	**9.8**
Follow-up (month)		36	23	19	15	**23.3**	35	31	27	13	12	**23.6**
Preop. UPDRS-III tremor subsection (PD patients)	OFF MED.	12	8	17	13	**12.5**	-	-	-	-	-	
	ON MED.	12	8	11	8	**9.8**	-	-	-	-	-	
	IMP (%)	0 (0%)	0 (0%)	6 (35%)	5 (38.4%)	**2.8 (18.4%)**	-	-	-	-	-	
Preop. FTMTRS (ET patients)		-	-	-	-		55	66	93	97	97	**81.6**
Postop. FTMTRS	OFF DBS	32	33	129	55	**62.3**	44	71	93	89	63	**72**
	ON DBS	14	15	44	24	**24.3**	29	47	81	47	36	**48**
	IMP (%)	18 (56%)	18 (55%)	85 (66%)	31 (56%)	**38 (58%)**	15 (34%)	24 (34%)	24 (13%)	24 (47%)	24 (43%)	**24 (34%)**
ACTIVE CONTACTS	X-	1	2	2	0		1	0 plus 1	1	0 plus 3	3	
	X+	-	-	10	-		-	-	-	-	-	
	AMP (Volt)	2	2	2.6	1.8	**2.1**	2	2	2	2.5	2.5	**2.2**
	PW (μS)	60	60	60	60	**60**	60	60	60	60	60	**60**
	FREQ (HZ)	130	150	130	130	**135**	130	180	130	150	180	**154**

6.4.5: Tractography of the DRTC

Left and right group average streamlines connect the dentate nucleus to the contralateral primary motor cortex, passing through the contralateral red nucleus and thalamus. The path through the thalamus clearly traverses the cerebellar cluster and overlapping portion of the M1 cluster **(Figure 6.2)**.

6.4.6: VTA Modelling and relationship to thalamic clusters and DRTC

VTA volumes corresponding to the active contacts stimulation for the seven patients with good response were averaged taking the median voxels. The good response group average fell on the dentate-thalamic cluster at the level of the AC-PC extending inferiorly into the cZI, on the DRTC. The three patients with poor response fell adjacent to, or on the DRTC but outside the dentate-thalamic cluster. See Figure 3 for group average responders VTA and non-responders VTAs in relation to the DRTC and the dentate-thalamic cluster.

6.4.7: Feasibility of stereotactic DBS targeting of the dentate-thalamic cluster

Employing the methods described, segmentation and registration of the dentate-thalamic cluster was achieved in less than 10 minutes per subject using a local, purpose built GPU high performance computer with 10,752 Compute Unified Device Architecture (CUDA) cores. Diffusion preprocessing, using the same cluster, was achieved in under 45 minutes. See **figure 6-4** for individual dentate-thalamic clusters registered to post- and preoperative stereotactic MPRAGE scans.

Neuroinspire™ surgical planning software (Renishaw PLC, United Kingdom) was used to carry out mock stereotactic targeting. The package has the capability of loading NIfTI volumes as well as DICOM image formats. The dentate-thalamic cluster voxels were subtracted (removed) from the stereotactic preoperative MPRAGE scan using *Fslmaths* (FSL V5.0). This process resulted in a new NIfTI volume with the clusters “punched out”. Planning was then carried out routinely with the added identification of the dentate-thalmic cluster, at the level of the AC-PC as demonstrated in **Figure 6-5**.

Figure 6-1: Thalamic clusters with corresponding cortical and cerebellar ROI masks (S1: blue - M1: red - SMA/PMC: green - dentate: yellow)

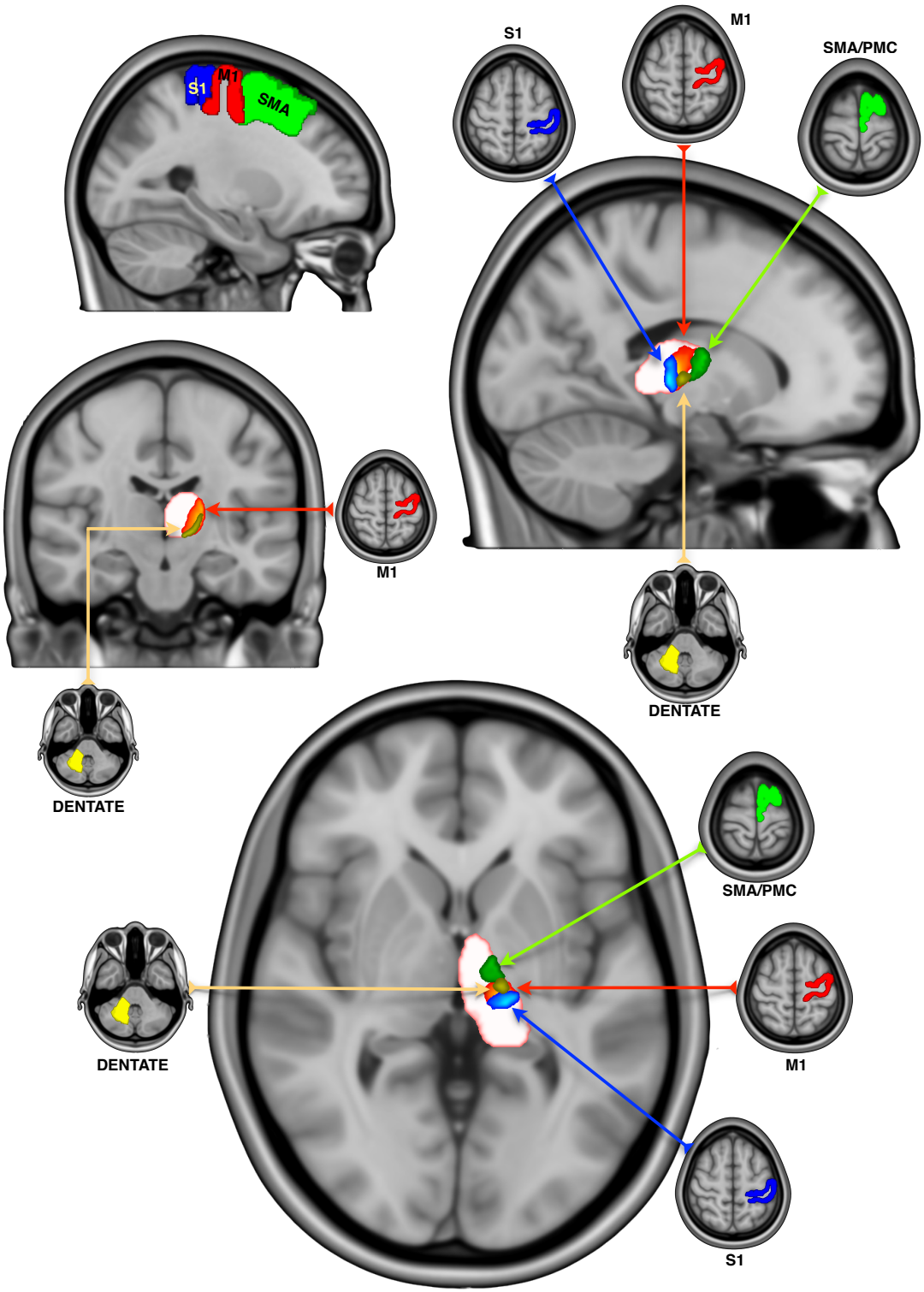

S1: primary sensory area; M1: primary motor area; SMA: supplementary motor area; PMC: premotor cortex

Figure 6-2: The left (blue) and right (red) dentato-rubro-thalamo-cortical tracts shown with decussation in the midbrain and path through the thalamic clusters

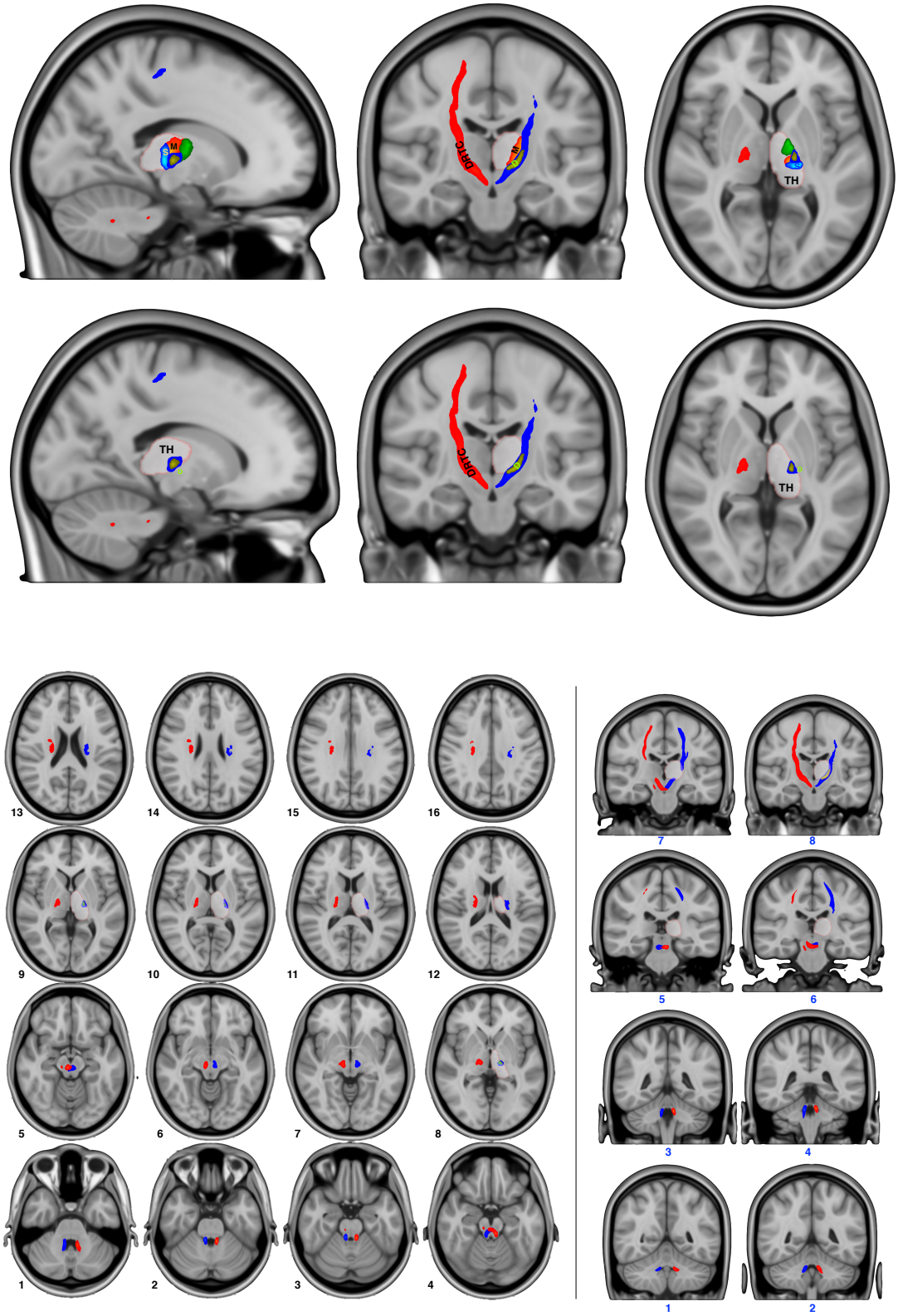

Figure 6-3: (A) Responders group average VTA (hot) and (B) non-responders VTAs (copper) in relation to the DRTC and the dentate-thalamic cluster

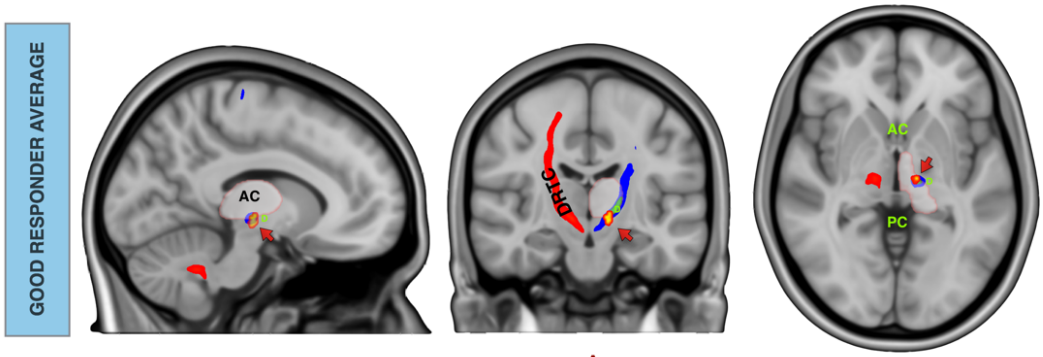

A.

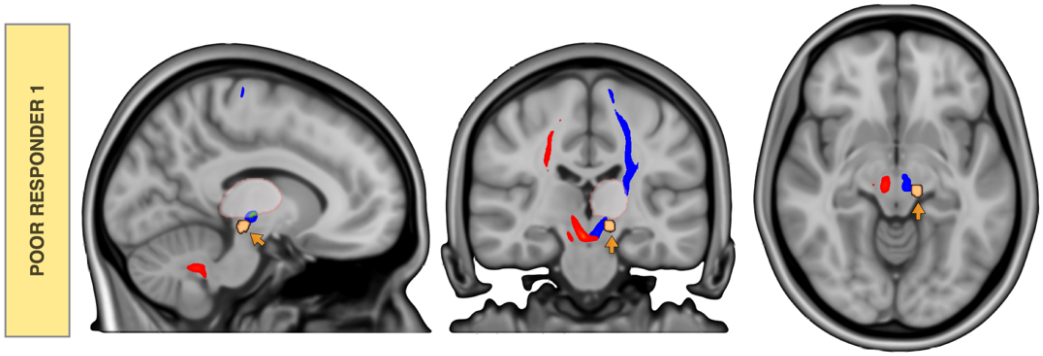

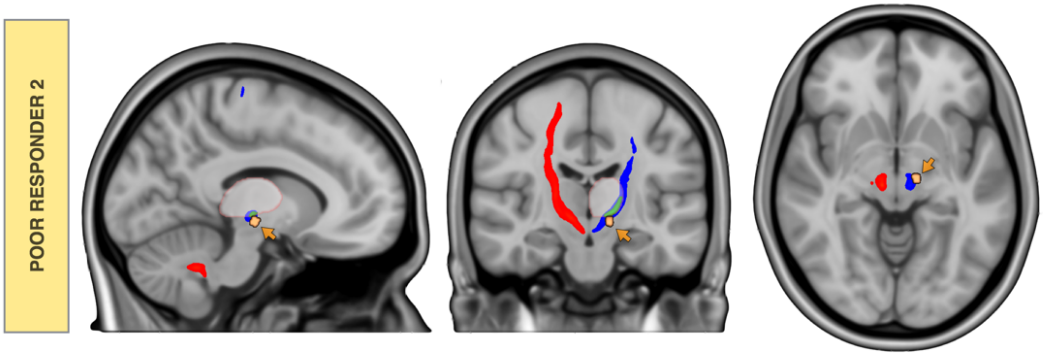

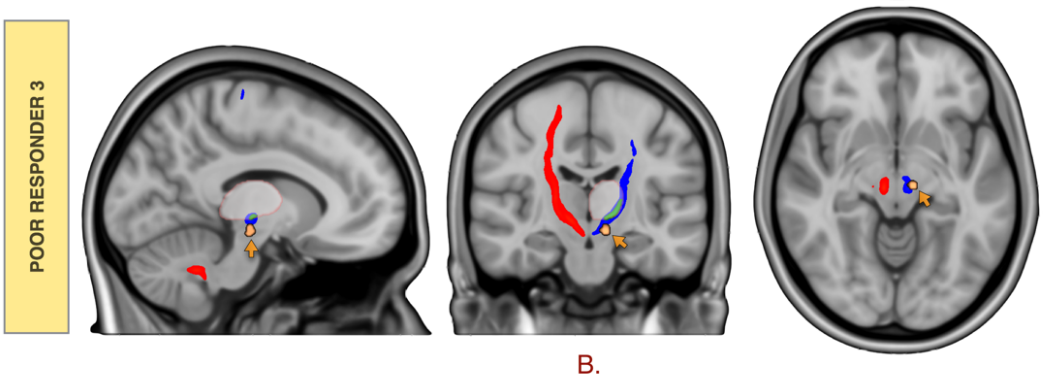

B.

Figure 6-4: Individual dentate-thalamic clusters registered to postoperative (top) and preoperative (bottom) stereotactic scans

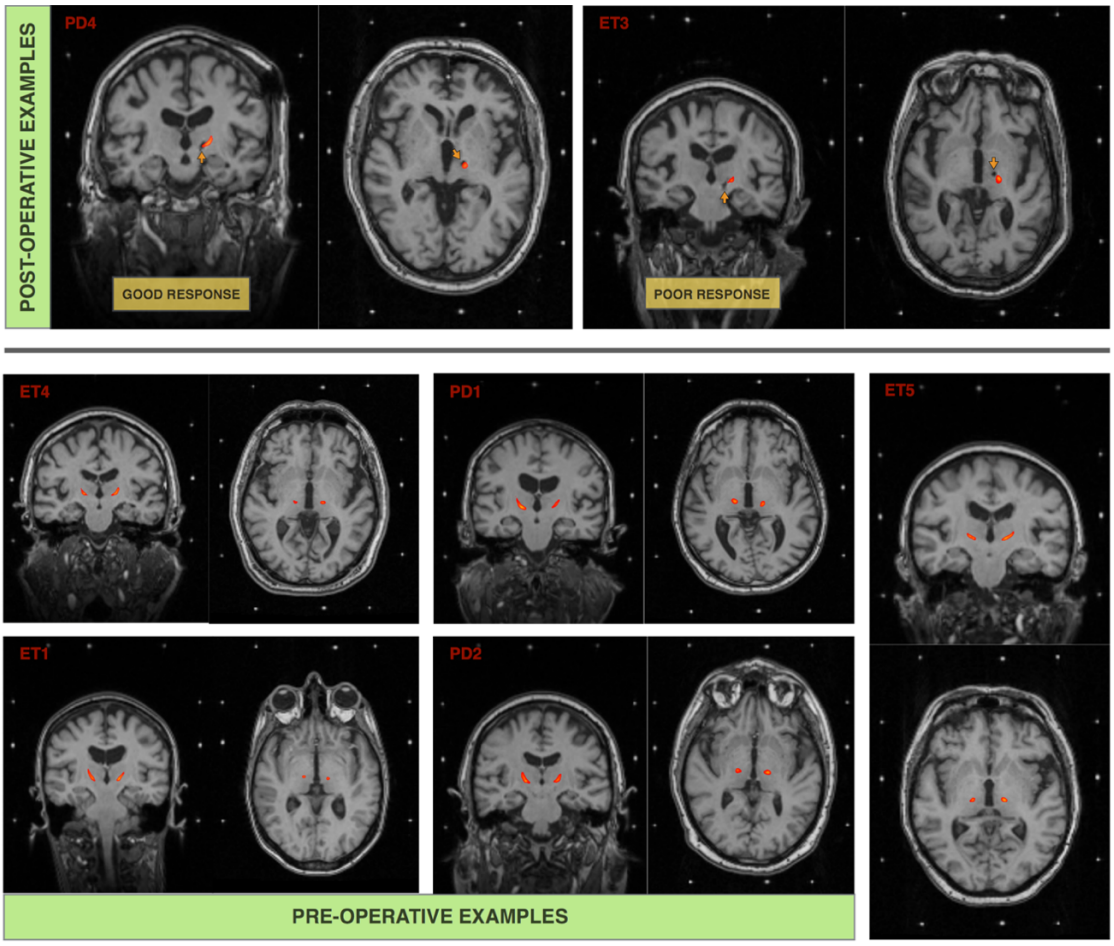

The arrows point to the DBS lead artefact in relation to the dentate-thalamic cluster

6.5: Discussion

In this work, we segmented the VIM nucleus of the thalamus, using connectivity based probabilistic techniques, applied to individual HARDI datasets, in five patients with ET and four patients with PD tremor, one year from thalamic DBS. Furthermore, we generated probabilistic streamlines representing the DRTC tracts, clearly connecting the M1 area with the contralateral dentate nucleus of the cerebellum via the VIM showing clear crossing in the brainstem. Three out of nine patients had a suboptimal, long-term response to treatment as demonstrated on improvement on FTMTRS. Post-hoc analysis of active DBS-contacts VTA models, showed that a good response is seen when the VTA was in the segmented VIM.

Figure 6-5: Left VIM DBS planning using Neuroinspire™ surgical planning software using preoperative stereotactic T2-weighted slab registered to MPRAGE T1 NIfTI volume with dentate-thalamic clusters punched-out

Individualised, image guided and image verified targeting of the VIM has been a quest of many in the field of functional neurosurgery. Inter-individual variability in the VIM's location has been illustrated in several studies. This was clearly shown in a functional connectivity study that analysed resting state fMRI scans in 58 healthy subjects [115]. Considerable individual variability of atlas-based VIM targeting was again demonstrated in a study that examined the VIM's relation to surrounding major fibre tracts using deterministic tractography in 10 patients with thalamic DBS for ET [141].

In 2003, Behrens et al published a report detailing the use of probabilistic tractography in delineating boundaries between different thalamic nuclei, based on connectivity patterns between the thalamus and various cortical areas [94]. This was the first time probabilistic tractography was used to parcellate grey matter structures, obtaining the quality of results that traditional maximum-likelihood or streamline approaches have failed to produce [366]. The resulting thalamic segmentation corresponded well with previous histological findings [367] and tracer studies in non-human primates [368-375]. This technique was further validated

in another study in 2004 [376]. Other grey matter structures have also been segmented with a similar approach [96,97,112].

Several studies have since used probabilistic tractography to examine VIM connectivity to cortical and cerebellar areas [139,140,377], or to segment the VIM based on said connectivity [138]. Interestingly, a post hoc analysis with connectivity based segmentation of six patients with bilateral VIM DBS showed the effective DBS contacts to be in the thalamic region with the highest probability of connection to the premotor and supplementary motor cortices [138]. This goes against prior anatomical knowledge [367] and the consistent findings from other connectivity studies [115,139,140,377] and transcranial magnetic stimulation (TMS) studies [296]. It is likely that this inconsistency resulted from using diffusion MR acquisition parameters intended for conventional clinical applications, such as mapping major white matter tracts prior to surgical intervention with low angular resolution (number of diffusion directions = 20), low spatial resolution (isotropic voxel size = 2 mm) and low angular contrast (b-value=1000 s/mm^2) [138].

Choosing the appropriate diffusion imaging parameters is paramount to achieving accurate segmentation of grey matter structures such as the thalamus [359-361]. In vivo probabilistic tractography studies in the cerebellum, brainstem and diencephalon carry significant challenges. Motion artefacts, caused by the highly pulsatile nature of the region, can degrade the MRI signal during diffusion image acquisition, reducing the signal-to-noise ratio (SNR). This is complicated by the presence of myriad criss-crossing axons and reticular brain regions [104,105]. One way of dealing with this is by using pulse-gating and respiratory rate monitoring during diffusion imaging. Likewise, by acquiring multiple diffusion scans, at a high angular resolution (increasing acquisition time), SNR is improved [91,103].

We acquired 270 diffusion scans per patient (in 2 × 128 directions sets) over 62 minutes. We meticulously and systematically corrected artefacts and examined the processed imaging data for quality control. We modelled three crossing fibres per voxel and used probabilistic tractography to ameliorate difficulties posed by crossing or kissing fibres and

tunnelling effect [92,103]. To keep the analysis focused, a set of tractography rules based on knowledge from anatomical studies was used, without being too restrictive.

Our analysis shows that the thalamic area, with highest connectivity to the contralateral dentate nucleus lies within the much larger area with highest connectivity to M1 in a ventro-lateral position. The area with highest connectivity to the SMA and PMC was anterior to the M1 area. The area with highest connectivity to S1 was posterior to the M1 area. This is in keeping with known anatomical information [378]. The ventral posterior (VP) thalamic nuclear complex relays impulses of sensory systems to S1, whilst ventral lateral (VL) nuclear complex relays information from the cerebellum, basal ganglia and substantia nigra (SN) [378]. The VL complex is generally subdivided into the pars anterior (VLa), pars posterior (VLp) and pars medialis (VLm). The VLa relays afferents from the globus pallidus interna (GPi) to the PMC and SMA [262,379-384]; whilst the VLm relays input from the SN to the PMC and prefrontal cortex [368,385,386]. The VLp, receives a large, topographically organised input from the cerebellar nuclei, projecting principally to M1 [378,380,382,387,388]. The VIM corresponds to the inferior part of the VLp [368].

It is important to bear in mind that the subdivisions of the thalamus by [389] or [390] are primarily based on histochemical staining of serial sections of human thalami, rather than anatomical connectivity. It is entirely possible that the optimal “functional” target straddles these subdivisions. Moreover, it is mechanistically likely that network connectivity of the target area will be a better predictor of efficacy than its histochemical properties.

Previous work focused on relation of DBS contacts to areas with cortical connectivity rather than cerebellar connectivity [138]. We have shown these areas to be non-specific and with varying degrees of overlap. Whilst the dentate-thalamic area is more representative of the actual VIM, it is harder to segment due to inherent difficulties in diffusion connectivity techniques highlighted above. This is, to our knowledge, the first time such a parcellation has been made possible, on the individual level, using in vivo 3T MRI.

Deterministic approaches have so far failed to produce anatomically accurate representations of the DRTC, generally showing the tract to arise from the ipsilateral, not

the contralateral dentate nucleus [132,136,358], or stopping at the upper brainstem decussation level [357]. This may not be problematic when the DRTC itself is being targeted, as it is the case in these reports; however, to accurately segment the VIM based on cerebellar connectivity, the crossing cerebellar streamlines must be mapped. We show clear crossing of the DRTC from the contralateral dentate nucleus, which passes through the segmented dentate area in the thalamus all the way to M1. The average VTA of the responders group lies in the inferior dentate thalamic area and on the DRTC in the CZi, possibly capturing the DRTC fibres as they enter the VIM.

6.5.1: Using the FTMTRS as an outcome measure

Despite the prevalence of tremor amongst movement disorders, there is no universally accepted method of quantifying and rating its severity [362,363,391-393]. Several tremor scales exist but they are often disease specific [394]. In 2013, a task force established by the Movement Disorders Society reviewed several rating scales for the assessment of tremor and recommended the use of five severity scales, one of which was the FTMTRS. The scale was assessed for reliability, validity and sensitivity to change [395]. Moreover, in view of the mixed patient group in this study, the FTMTRS has the advantage of being non-disease specific [396].

In this study, we examined the change in FTMTRS with DBS-OFF and -ON, 12 - 24 months from surgery. We did not calculate the improvement in FTMTRS in relation to preoperative baseline scores. This was since FTMTRS scores were not part of the routine preoperative assessment for PD patients which is a limitation of this study. It is interesting to notice the apparent 'lesion effect' in three out of five ET patients (two responders and one non-responder) illustrated by reduction in FTMTRS in the postoperative DBS-OFF measurements when compared to baseline. Indeed, the overall percentage of improvement with DBS-ON would have been higher had the preoperative FTMTRS been used as a denominator in the ET group.

6.5.2: Limitations

The limitations of the VTA model used in this study and the rationale behind using this model have been described in chapter 2 (2.10.4).

By employing multiple registration steps, we have introduced error to the system. Nonetheless; we meticulously confirmed registration accuracy at each step to alleviate the impact of this issue.

Lastly, the relatively long scan duration is a drawback. This was accepted to achieve the required SNR and resolution. However, since this study was conducted, novel MRI acquisition techniques, such as Simultaneous Multi-Slice Imaging and Multi-Band Imaging [303] have been developed that will allow future studies to run similar protocols within half the time without compromising the SNR. Further improvements in diffusion imaging, with higher spatial and angular resolution, better MRI gradients and shorter acquisition times with emergence of multi-band acquisition will add to the value of this modality [102,283]. Lastly, the number of patients in this study is relatively small with mixed aetiologies. However, the data suggest that imaging can be used to optimise efficacy of tremor control. We intend to expand our experience with this technique in each pathology in the coming years.

6.6: Conclusion

Probabilistic tractography techniques can be used to segment the VL and VP thalamus based on cortical and cerebellar connectivity. The thalamic area, best representing the VIM, is connected to the contralateral dentate cerebellar nucleus. Patients with VTAs in this area attained good treatment response, whilst those with VTAs outside it did not. Connectivity based segmentation of the VIM can be achieved in individual patients in a clinically feasible timescale, using HARDI and high performance computing with parallel GPU processing. This same technique can map out the DRTC with clear mesencephalic crossing. Future studies may focus on improving data acquisition and processing time; and apply this technique prospectively in patients undergoing thalamic DBS or lesioning for tremor.

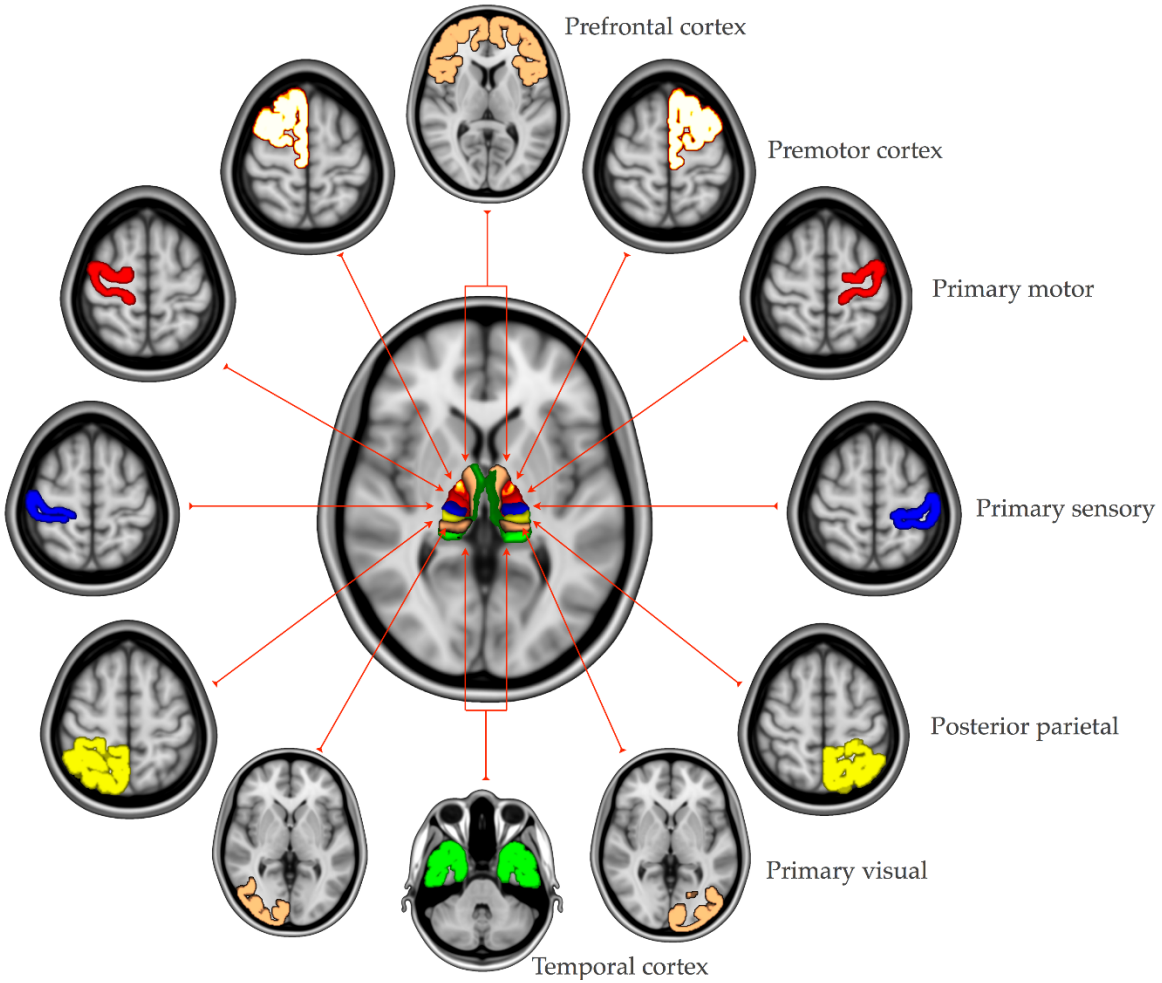

Connectivity based thalamic segmentation

Section III:

DBS for Trigeminal Autonomic Cephalalgias and Connectivity in Cluster Headache

"Of pain you could wish only one thing: that it should stop. Nothing in the world was so bad as physical pain. In the face of pain there are no heroes."

George Orwell, 1984

7. Ventral Tegmental Area Deep Brain Stimulation for Refractory Chronic Cluster Headache

7.1: Abstract

Cluster headache (CH) has a prevalence of 0.1-0.2%. Ten to 15% of patients have a chronic form (CCH) at times intractable to medical therapies. We present outcomes in a cohort of medically-intractable CCH with ventral tegmental area (VTa) deep brain stimulation (DBS). In an uncontrolled open-label prospective study, twenty-one patients (17 male; mean age 52 years) with medically refractory CCH were selected for ipsilateral VTa-DBS by a specialist multi-disciplinary team including headache neurologist and functional neurosurgeon. Patients had also failed, or were denied access to occipital nerve stimulation within the UK National Health Service. The primary endpoint was the improvement in the headache frequency. Secondary outcomes included other headache scores (severity, duration, headache load), medication use, disability and affective scores, quality-of-life (QoL) measures and adverse events. Median follow-up was 18-months (range 4-60). At the final follow-up point, there was 60% improvement in headache frequency (p=0.007) and 30% improvement in headache severity (p=0.001). The headache-load (a composite score encompassing frequency, severity and duration of attacks) improved by 68% (p=0.002). Total monthly triptan intake of the group dropped by 57% post-treatment. Significant improvement was observed in several QoL, disability and mood scales. Side-effects included diplopia, which resolved in two-patients following stimulation adjustment, and persisted in one-patient with a history of ipsilateral trochlear nerve palsy. There were no other serious adverse events. This study supports that VTA-DBS may be a safe and effective therapy for refractory CCH patients who failed conventional treatments. This study provides Class IV evidence that ventral tegmental area deep brain stimulation decreases headache frequency, severity and headache load in patients with medically intractable chronic cluster headaches.

7.2: Introduction

Cluster headache (CH) is a trigeminal autonomic cephalalgia (TAC)[397] characterized by attacks of severe, strictly unilateral cranial pain associated with ipsilateral cranial autonomic features.[398,399] CH has a prevalence of 0.1-0.2% and chronic cluster headache (CCH) occurs in 10-15% of sufferers whose attacks occur for more than one year without remission, or with remissions lasting less than one month.[400] [401-403] [404]

Standard medical therapy comprises acute and prophylactic treatments, which are usually effective.[405] However, in a small but significant number of highly disabled individuals, attacks are intractable. For these patients, peripheral [occipital nerve stimulation (ONS) and/or sphenopalatine ganglion stimulation] and central neuromodulation [ventral tegmental area (VTa) deep brain stimulation (DBS)] have been carried out with promising results.[68,123,124,406-408]

Here we investigate the efficacy of VTa-DBS when used as a humanitarian intervention in patients who had exhausted every other option available to them with the framework of the UK NHS. We present a prospective study of 21 consecutive patients with CCH, treated using a magnetic resonance imaging (MRI)-guided and MRI-verified approach to VTa-DBS, focusing on changes in headache characteristics, quality of life, disability and mood.

7.3: Methods

Standard Protocol Approvals, Registrations, and Patient Consents

The UK National Institute for Health and Care Excellence (NICE) published guidance concerning DBS for intractable TACs in March 2011 (https://www.nice.org.uk/guidance/ipg381/chapter/1-Guidance), advising arrangements for clinical governance, consent, audit and research. In keeping with this, and under the supervision of our institution's Clinical Effectiveness Supervisory Committee (CESG), we offered VTa-DBS to CCH patients who had failed ONS or in whom NHS funding for ONS had been declined. The procedure was provided on the basis of a "humanitarian

intervention". Patients were provided with CESG approved patient information booklets and gave written consent.

7.3.1: Patient selection

Included patients fulfilled the ICHD-II diagnostic criteria for CCH[397] and had experienced highly disabling, medically refractory symptoms for at least two years. CCH was classified as medically intractable if patients failed adequate trials of at least five of the following seven drugs: verapamil, lithium, methysergide, topiramate, melatonin, gabapentin, and valproate. A failed trial was defined as an unsatisfactory response, side effects intolerance or contraindication to the agent's use.[409] All patients were considered for ONS prior to DBS and had either been refused funding or had failed to respond adequately. Sphenopalatine ganglion stimulation was not available in the UK during the study period. Referrals were made by a single tertiary specialist headache clinic to a DBS multidisciplinary team at the same centre. Neuropsychological evaluations and MRI brain scans were performed to rule out cognitive impairment, brain lesions or significant brain atrophy.

7.3.2: Outcome measures and follow up

Outcome data were collected and recorded prospectively and included headache frequency, headache severity, headache load, disability scores, affective scores, quality of life measures, adverse events (including surgical complications, stimulation-induced adverse events and morbidity) and reduction in preventative and acute treatment.

Headache severity was measured on the verbal rating scale (VRS) for pain (0 being no pain, and 10 being the worst pain imaginable). Patients reported the mean headache intensity during individual attacks. The individual scores were then averaged over the observation period. Headache frequency was defined as the number of CH attacks/day. Headache load (HAL) was defined as ∑ [severity (on the verbal rating scale)] x [duration (in hours)] of all headache attacks occurring over a 2 week period. These measures were assessed using headache diaries collected preoperatively (baseline), at commencement of DBS therapy, at 3 months, 6 months, 12 months and yearly thereafter. Patients with

multiple headache types kept separate diaries for CH attacks and other headache syndromes; headache parameters were calculated for each headache type.

Responders were defined as patients with sustained HAL reduction ≥30% since this was deemed meaningful in line with the Initiative on Methods, Measurement, and Pain Assessment in Clinical Trials (IMMPACT) guidelines.[410]

Disability measures, quality of life and affective scores were collected using questionnaires. The Short Form-36 (SF36) measuring both the physical component summary (PCS) and mental component summary (MCS) scores was used to assess health-related quality of life at baseline and after stable improvements in responders, or after a year of continuous stimulation in non-responders.[411] Since specific tools for measuring the disability of CH have not yet been validated, disability was assessed using the Migraine Disability Assessment Scale (MIDAS)[412] and the Headache Impact Test-6 (HIT-6).[413] MIDAS and HIT-6 have been used extensively to assess primary headache disorders. They have previously been used to assess the disability of CH and hemicrania continua patients treated with ONS.[414,415] The Hospital Anxiety and Depression Scale [(HAD-A) and (HAD-D)][416] was used to evaluate the presence and degree of anxiety, and depression before and after surgery. Other questionnaires included the Beck Depression Inventory II (BDI-II) and the EuroQol (EQ-5D).

7.3.3: Surgical procedure

DBS leads were implanted using a stereotactic MRI-guided and MRI-verified approach without microelectrode recording as detailed in previous publications (Leksell frame model G, Elekta Instrument AB, Stockholm, Sweden).[61,274] The first 11 patients, had lead implantation performed under local anaesthesia; in the remaining 10 patients leads were implanted under general anaesthesia.[61] The anatomical target was the ipsilateral VTa. The location for the deepest contact of the 3389 Medtronic lead was defined on a 1.5T T2-weighted axial stereotactic MR image at a level immediately above the mammillary bodies, anteromedial to the hypointense red nucleus and posterolateral to the hypointense mammillothalamic tract. Immediately after lead implant, location was verified with a

stereotactic MRI scan **(Figure 7-1)** in patients without ONS. Postoperative stereotactic CT scan was performed in patients with implanted ONS hardware. The lead was then connected to a single or dual channel Implantable Pulse Generator (IPG) (Medtronic, Minneapolis, Minn., USA) implanted in the infra-clavicular region on the same day of lead implantation or within a week, as a staged procedure under general anaesthesia.

7.3.4: DBS programming

In the weeks following surgery, open label programming was conducted to define optimal stimulation parameters. Six patients (29%) had a delay of one to three months before their stimulation was started. This was because they reported a clear 'stun' effect period post-operatively, during which attacks improved without any stimulation. In these patients, DBS was not initiated until they reported a return to baseline in terms of attack frequency. All devices were programmed with a frequency of 185Hz and a pulse width of 60μs as described by Franzini et al [124]. Voltages were adjusted according to self-limiting side effects (diplopia, vertigo, oscillopsia and ophthalmoplegia) in single or multiple steps, depending on the patient. Stimulation parameters were kept constant for the first three months and were adjusted after this if patients were not responding.

7.3.5: Statistical analysis

IBM SPSS Statistics package v22 was used for all the statistical analyses.

Percentage change from baseline was used where appropriate. The data at baseline was assessed for normality using Kolmogorov-Smirnov test and by inspecting the Q-Q plot and frequency distribution histogram prior to determining appropriate statistical tests. Whenever the distribution was not normal, non-parametric tests were used and the median was given instead of the mean. Wilcoxon signed-rank test was used to compare treatment effect at each time-point from baseline. To adjust for multiple comparisons, Bonferroni corrections were applied by multiplying each test-statistics p-value by the number of comparisons. Statistical significance was set at 5%. Raw and normalized data were tested and descriptive statistics were reported where applicable.

7.3.6: Research questions

When carried out in patients with refractory CCH;

1) Does VTa-DBS improve headache frequency, severity and headache load? (Class 4 evidence)
2) Does VTa-DBS improve disability, mood and quality of life? (Class IV evidence)
3) Is VTa-DBS safe? (Class IV evidence)

7.4: Results

7.4.1: Patient sample

Between April 2009 and November 2013, 21 patients (17 male) with a mean (SD) age of 52 (10) years, underwent VTa-DBS for CCH. CCH was the sole headache diagnosis in sixteen patients (76%). Other primary headaches were present in the remaining 5 patients (24%), including episodic migraine, sporadic hemiplegic migraine and short-lasting unilateral neuralgiform headache with conjunctival injection and tearing (SUNCT). The mean (SD) time from CH onset until surgery was 15 (7) years. The mean (SD) time from CH onset until the last follow-up point was 18 (8) years. Sixteen patients received unilateral DBS electrode implantation (8 left) for strictly unilateral cluster CH; the remaining five patients (24%) underwent bilateral DBS electrode implantation for side-variable CH attacks. Six (29%) patients had prior ONS implanted with limited or short lasting effect with a median time of 4 years prior to undergoing DBS. Of these, three patients had the ONS removed before undergoing DBS surgery **(Table 7-2)**. Co-morbidities in this patient group included depression (n=10), previous suicide attempts or ideation (n=4), cancer (n=3), other chronic headache syndromes (n=5), epilepsy (n=3), Parkinson's disease (n=1), chronic fatigue syndrome (n=1), stroke (n=1), heart disease (n=1), hereditary spastic paraparesis (n=1) and temporo-mandibular joint dysfunction (n=1). Four patients were smokers and three were ex-smokers.

Implanted leads were within a mean (SD) of 0.8 (0.4) mm from the planned target. Postoperatively three patients complained of intermittent diplopia that resolved in two

patients following stimulation parameters adjustment and persisted in the other patient who had a previous history of ipsilateral trochlear nerve palsy following a head injury; this diplopia persisted even when stimulation was switched off. One patient developed a keloid scar over the IPG incision. A superficial wound infection developed in one patient, which resolved with antibiotics treatment. There was no surgical mortality or other significant morbidity. Post-operative follow up ranged from 4 months to 5 years with 19 patients having at least one year follow up.

7.4.2: Frequency and severity of headache attacks (VRS)

At the final follow up point, there was a 60% overall improvement in the median headache frequency from 5 to 2 attacks/day (p=0.007). The percentage of patients who had at least 30% and 50% reduction in median frequency of attacks was 62% and 52% respectively.

The overall improvement in median headache severity was 30% from 10 to 7 points on the VRS (p=0.001). The percentage of patients who had at least 30% and 50% reduction in median headache severity on the VRS was 43% and 24% respectively at the final follow up point (**Table 7-3** shows effect of DBS on CH attack frequency, severity and duration at last follow-up).

7.4.3: Headache load (HAL)

Eleven patients (52%) showed a maximum reduction in the HAL of more than 80% during the follow up period. Within three months of surgery, the median change in HAL was 62%, at 6 months it was 59% and at twelve months it was 79% **(Table 7-1, and Figures 7-2a, 7-2b)**.

The percentage of patients who had at least 30% and 50% reduction in headache load was 81% and 76% respectively at the final follow-up point. Four patients (19%) failed to respond to treatment (< 30% reduction in HAL). Three of these had also failed to respond to ONS treatment previously. The subset of patients with prior ONS (n=6) had a failure rate of 50% (n=3). There was no change in the median HAL at 3 months, deterioration of 3% at 6 months and of 23% at 12 months (n=6). In this subgroup, the three patients who improved

had a modest but meaningful reduction of the median HAL of 34%, 30% and 34% at 3, 6 and 12 months respectively.

7.4.4: Reduction in acute and preventative treatment

Seven patients were on preventative medications prior to DBS insertion. Six continued to take preventative medications after surgery although, four of these reduced the dose of a medication and three stopped at least one medication. One patient increased the dose of verapamil as it had an improved effect on preventing attacks post-DBS. Eleven patients were taking triptans prior to treatment and 12 were using oxygen. At the last follow-up point, seven patients were using triptans and 11 were using oxygen. One patient started to use triptans again post treatment as it was found to be effective whereas previously it had not. The total monthly triptan intake of the whole group was 873 doses pre-treatment and 376 doses post-treatment - a reduction of 57% **(Table 7-5)**.

7.4.5: QoL, mood and disability measures

Median improvement in HIT-6 was 4 points (corrected-p=0.018) at 6 months and 6 points (corrected-p=0.034) at 12-months. The PCS section of the SF-36 scores showed an improvement of 13% (corrected-p=0.038) at 6-months **(Table 7-4 and Figure 7-3)**.

7.5: Discussion

This open-label prospective study suggests that MRI-guided and MRI-verified DBS of the VTa is a safe and effective procedure in patients with CCH whose symptoms are refractory to other treatments. Symptomatic improvement was sustained over time and was accompanied by significant improvements in a number of quality of life scales.

In 1998, a positron emission tomography study reported increased activation in the posterior hypothalamic region during CH attacks, though the maximal activation was centred over the VTa.[417,418] This led to the first DBS procedure in 2001 with attacks disappearing within 48 hours of starting stimulation.[123] This pioneering group referred to the anatomical target as the “posterior hypothalamus (PH)” rather than the VTa, and went on to report the first series of 5 patients in 2003 and 19 patients in 2013.[124,419] To date,

different centres have published data on over 70 patients with DBS for medically-intractable CCH with varying response rates but an overall good safety record with the exception of one fatal intracerebral haemorrhage during a microelectrode guided procedure.[68,69,406,407,419]

A randomized controlled crossover trial of DBS for CCH did not show any significant difference between sham and active stimulation during the blinded crossover period (Fontaine et al 2009). However, 1-year outcome revealed that 6/11 patients had >50% reduction in attack frequency and three patients were pain-free. The difference in outcome may be explained by the short 1 month crossover period within 3 months of surgery. Such a design does not allow for residual micro-lesion effects in the postoperative period or the observed increase in stimulation efficacy over 3-months of continuous stimulation in open-label trials.

Our study shows a clear reduction in the headache frequency and severity of CCH attacks with VTa-DBS, with greater benefit on frequency. However, using one aspect alone - headache severity or headache frequency - may not represent the real response of CCH attacks to an intervention. Therefore, this study introduces the concept of HAL that may provide a more meaningful measure of symptom severity. VTa-DBS resulted in significant improvement in the HAL as early as three months post operatively which continued until the final follow-up point. Nevertheless, the clinical meaningfulness of HAL as a primary end-point needs validation by studies in larger cohorts.

The monthly triptan intake of the group as a whole dropped by 57% (497 doses/month). Using current UK costing estimates [420] this can be calculated to be a saving of £8291 a month for the 21 patients or around £395 a month per patient on triptans alone.

None of the quality of life, disability and mood outcome measures deteriorated following surgery and a number improved significantly from baseline (HIT-6, SF36-PCS and EuroQol). The largest improvement was seen in in the SF36-PCS at 6 months.

Improvement in quality of life measures did not have the same magnitude as that observed with HAL. The relatively long duration of the disease (average 15 years) may have resulted

in socio-economic and psychosocial adjustments to chronic illness that are unlikely to improve immediately following improvement in the headache symptoms. Other factors to consider are other co-morbidities in our cohort of patients.

The brain region used for DBS was first described as a surgical target by Sano *et al* who performed stereotactic lesions in 51 patients with pathologically aggressive behaviour.[421] Although this area has been widely described as the 'posterior hypothalamus', the anatomical accuracy of this label has been contested. The mammillo-thalamic tract represents the posterior border of the hypothalamus and the target area lies posterior to this within the ventral tegmentum of the midbrain.[418,422] This brain region has also been used as a target in DBS for depression.[423]

Our general practice is to perform DBS surgery under general anaesthesia when the brain target can be well visualized with MRI to guide electrode insertion.[61,274] However, we elected to perform surgery under local anaesthesia for the first eleven patients. This allowed intraoperative testing with macro-stimulation to study any possible intraoperative side effects of stimulation. With higher voltages these included tachycardia, raised blood pressure, vertical diplopia and a feeling of "panic" or "impending doom". These effects were reproducible in all tested patients. Once the procedure was well established locally, we performed the surgery under general anaesthesia, relying on MRI-verified targeting.

Limitations apply to any open-label study. A placebo effect cannot be excluded; however, this is unlikely to be large with follow up over one year. Moreover, there were a number of incidents where attacks recurred when stimulation was inadvertently switched off.

The six patients who had a short lasting or no response to ONS therapy prior to receiving DBS had a much higher failure rate and no overall improvement in HAL. Furthermore, those who did respond to DBS showed a very modest improvement in HAL when compared to that seen across the entire patient group. Moreover, two of the five patients with bilateral CCH were non-responders. A failure to respond to ONS and the presence of bilateral symptoms may be predictors of poor outcome following DBS; however, these patient subgroups are too small to draw any firm conclusions.

Lack of response to VTa-DBS in some patients has been reported in previous series in spite of well positioned DBS electrodes.[422] Despite an increase in HAL in these patients **(Figure 7-2b)**, our cohort of patients experienced significant improvement as a group. Further work into structural and functional connectivity may reveal underlying differences between responders and non-responders, improving patient selection and outcome of DBS in CH. This study suggests that MRI-verified VTa-DBS may be a safe and effective treatment for drug-refractory CCH and could be considered for suitable patients who fail conventional treatment. We also noted positive effects of DBS for CCH on patient-reported quality of life, disability and mood.

Table 7-1: Median Headache Load

	Baseline	**3 Months**	**6 Months**	**12 Months**	**Last F/U**
Median	696	258 *(n=17, p=0.002)*	198 *(n=16, p=0.01)*	156 *(n=20, p=0.003)*	208 *(n=21, p=0.002)*
MAD	235	175	155.5	146	162
Median Improvement (%)		62%	59%	79%	68%

Median Headache Load at baseline and at postoperative follow-up points with percentage of improvement in Headache Load relative to baseline. MAD: Median Absolute Deviation. P values are Bonferroni corrected; they represent change relative to baseline

Figure 7-1: Immediate post-operative stereotactic axial T2-weighted and coronal T1-weighted MR images demonstrating the deep brain stimulation lead in the left ventral tegmental area

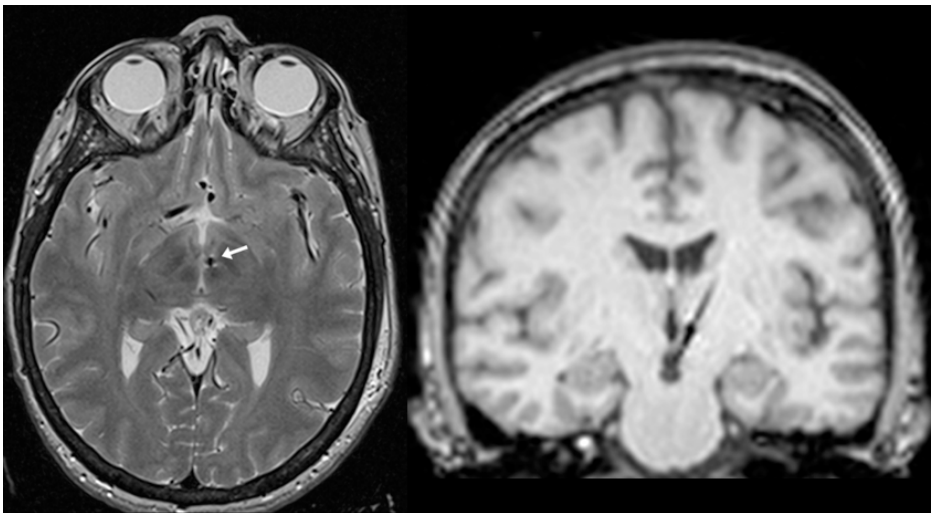

Table 7-4: Quality of life, disability and mood

	Baseline			6 Months				12 Months			
	Med	**MAD**	**n**	**Med**	**MAD**	**n**	**p-val**	**Med**	**MAD**	**n**	**p-val**
MIDAS	137	74	18	100	91	18	0.16	29	29	17	0.08
HIT-6	69	4	19	65	5	19	0.02*	64	8	16	0.03*
HAD-A**	(11)	(5)	19	(9)	(5)	19	0.22	(9)	(5)	17	0.5
HAD-D**	(12)	(6)	19	(10)	(6)	19	0.22	(10)	(5)	17	0.32
BDI-II	28	11	18	25	12	18	0.27	20	8	15	0.47
SF36-PCS	32	6	14	36	9	14	0.04*	35	6	13	0.27
SF36-MCS	32	9	14	36	12	14	1.10	34	16	15	1.94
Euro-QoL	0.65	0.09	11	0.68	0.07	11	1.25	0.71	0.07	10	0.08
Euro-Scale	49	19	11	55	15	11	0.28	45	17	10	1.89

*: p value ≤0.05; Med: Median

** Normally distributed data presented in mean and SD instead of median and MAD

Quality of life, disability and mood data at baseline, 3, 6 and 12 months post-surgical follow-up

MIDAS: Migraine Disability Assessment Score, HIT6: Headache Impact-6, HAD-A: Hospital Anxiety and Depression Scale (Anxiety component), HAD-D: Hospital Anxiety and Depression Scale (Depression component), BDI-II: Beck Depression Inventory II, SF36-PCS: Short Form 36 Physical Summary Score, SF36-MCs: Short Form 36 Mental Summary Score. MAD: Median Absolute Deviation. P values are Bonferroni corrected

Table 7-2: Patient demographics

Patient	Age (years) at time of implant	Sex	Duration of CH from onset to time of implant (years)	Other headache types	Laterality of DBS electrode	MRI scan result	Total duration of DBS therapy at last follow up (years)
1††	59	M	16		Left	Normal	1.5
2	50	F	6	Episodic migraine	Right	Normal	0.8
3	40	M	27	SUNCT Post traumatic migraine	Right	Normal	2.0
4††	49	M	23		Right	Normal	1.0
5	51	M	23		Left	Normal	1.5
6	54	F	16		Left	Normal	5.0
7	61	M	16	Episodic migraine	Right	Normal	5.0
8	43	F	6		Bilateral	Normal	1.5
9†	47	M	9		Right	Right petrous bone cholesteatoma	1.3
10†	61	M	21		Bilateral	Normal	1.5
11	41	M	6		Bilateral	Normal	1.6
12	37	M	20		Right	Normal	4.5
13	46	M	5	Sporadic hemiplegic migraine	Bilateral	Normal	0.8
14†	55	M	22		Left	Normal	1.8
15	71	M	30	SUNCT	Left	Left cerebello-pontine angle arachnoid cyst	3.5
16††	35	F	13		Bilateral	Normal	1.2
17	43	M	18		Left	Normal	1.8
18	70	M	10		Right	Normal	3.5
19	70	M	18		Left	Mature infarct in the right cuneus	3.5
20	48	M	11		Right	Normal	1.0
21	57	M	9		Left	Developmental venous anomaly (DVA)	0.3
Median (range)	50 (35-71)		16 (5-27)				1.5 (0.3-5)

† Patients with implanted occipital nerve stimulator (ONS), †† denotes removal of the ONS prior to DBS. SUNCT: short-lasting unilateral neuralgiform headache with conjunctival injection and tearing, CH: cluster headache, M: male, F: female.

Table 7-3: Effect of DBS on headache characteristics

	Follow-up after DBS (years)	Median frequency/day (range)		Median severity on VRS (range)		Median duration in HOURS (range)		Headache Load		Percentage of improvement of the headache load	Patients estimation of benefit since implantation
		Before	After	Before	After	Before	After	Before	After		
1	1.5	2 (1-2)	2 (1-2)	7 (6-8)	7 (7-8)	2.5 (1-4)	2 (1-3)	840	260	69%	0%
2	0.8	3 (2-3)	3 (2-3)	7 (7-10)	5 (3-6)	3 (0.25-3)	0.5 (0.5-0.6)	696	239	66%	70%
3	2.0	5 (4-5)	1 (1)	10 (9-10)	8 (8)	1.5 (0.5-2.5)	1 (1-1.5)	764	78	90%	75%
4	1.0	3 (2-3)	2 (1-2)	6 (5-6)	3 (2-6)	2 (2-4)	2 (1-4)	379	208	53%	60%
5	1.5	4 (3-4)	0 (0-1)	10 (10)	0	5 (5-6)	6 (6-8)	1341	0	100%	95%
6	5.0	5 (4-6)	3 (2-3)	10 (9-10)	9 (6-10)	3 (3-4)	1.5 (0.75-4)	1995	529	73%	30%
7	5.0	3 (2-3)	0 (0-1)	10 (9-10)	8 (8-9)	2 (0.75-3)	0.3 (0.25-0.7)	474	270	43%	50%
8	1.5	5 (3-5)	0 (0-1)	9 (6-9)	6 (6)	2 (2-2.75)	2.5 (2.5)	1964	347	82%	99%
9	1.3	4 (4-6)	2 (2-4)	8 (8)	6 (6-9)	1.5 (0.3-1.5)	1 (0.3-1.25)	532	180	66%	80%
10	1.5	7 (5-7)	7 (5-7)	9 (7-9)	8 (7-9)	1.5 (0.8-1.8)	1.2 (0.75-22.0)	519	603	-16%	25%
11	1.6	6 (4-5)	1 (0-4)	8 (5-9)	8 (8)	2 (0.5-3)	0.5 (0.5-2.5)	221	20	91%	70%
12	4.5	4 (3-4)	0 (0)	10 (10)	0	1 (0.75-1)	0 (0)	751	0	100%	99%
13	1.4	7 (5-7)	3 (3-4)	10 (10)	7 (4-9)	3 (1-4)	1.5 (1-2)	2020	743	63%	30%
14	1.8	6 (5-8)	5 (4-6)	10 (9-10)	10 (10)	1 (1-2)	1.5 (0.5-3)	961	1255	-31%	5%
15	3.5	10 (6-10)	8 (4-8)	8 (5-9)	8 (8-9)	0.5 (0.25-0.5)	0.5 (0.2-3)	153	330	-115%	0%
16	1.2	4 (2-4)	4 (2-7)	10 (10)	10 (10)	2(1.5-3)	1.5 (1.5-2)	706	700	0.9%	0%
17	1.8	10 (7-10)	9 (8-10)	10 (8-10)	10 (10)	0.6 (0.3-2)	1 (1-2)	372	135	64%	0%
18	3.5	8 (8)	0	10 (9-10)	0	0.3 (0.3-1)	0	524	0	100%	100%
19	3.5	8 (4-8)	8 (5-8)	10 (10)	9 (8-9)	1.5 (0.25-2.5)	0.2 (0.2-1.25)	250	80	68%	0%
20	1.0	6 (4-6)	1 (0-2)	7 (5-7)	3 (3-4)	1 (1-1.5)	1 (1)	461	46	90%	70%
21	0.3	2 (1-2)	0	8 (7-8)	0	2 (2-3)	0	720	0	100%	99%
Median (range)	1.5 (0.3-5)	5 (2-10)	2 (0-10)	10 (6-10)	7 (0-10)	1.75 (0.3-5)	1 (0-6)	696 (153-2020)	208 (0-1255)	68% (-115-100)%	60% (0-100)%

Effect of DBS on CH attack frequency, severity and duration at last follow-up

VRS: Verbal rating scale (0 = no pain to 10 = very severe pain); The Headache score was derived from the two week diaries patients kept prospectively at baseline and prior to each assessment using the formula: Σ [duration (min) x severity (VRS)]

Table 7-5: Use of preventive and acute treatments

	Preventative Treatment		Acute Medication	
	Prior to DBS (daily dose)	**After DBS (daily dose)**	**Prior to DBS**	**After DBS**
1	Nil	Nil	Rizatriptan tablets 10mg x2/day	Rizatriptan tablets10mg x2/day
2	Verapamil 720mg, Baclofen 15mg	Verapamil 720mg	Oxygen daily	Oxygen once week
3	Nil	Nil	Nil	Nil
4	Nil	Nil	S/C sumatriptan x2/day, nasal sumatriptan x3/day	Nasal sumatriptan x1-2/day
5	Nil	Nil	Nil	Nil
6	Nil	Nil	Nil	Nil
7	Methysergide 12mg	Methysergide 9mg	S/C sumatriptan x2/day, oxygen daily	S/C sumatriptan x2/week, oxygen x2/week
8	Nil	Nil	Nasal sumatriptan x3/day, oromorph 20mg x2/week, nasal lidocaine daily	Nil
9	Nil	Nil	S/C sumatriptan x2/day, oxygen daily	Oxygen daily
10	Nil	Nil	S/C sumatriptan x2/day, oxygen daily	S/C sumatriptan x2/day, oxygen daily
11	Nil	Nil	S/C sumatriptan x2/day, frovatriptan 2.5mg x1/day, oxygen daily	S/C sumatriptan x2/day, frovatriptan 2.5mg x1/week, oxygen daily
12	Verapamil 360mg, Lithium 1200mg	Verapamil 360mg, Lithium 1200mg	S/C sumatriptan x4/day	Nil
13	Nil	Nil	Nasal sumatriptan x1/day, oxygen daily	Nasal sumatriptan x2/day, oxygen daily
14	Nil	Nil	Oxygen daily	Oxygen daily
15	Nil	Melatonin 16mg	Oxygen once week	Oxygen daily
16	Baclofen 60mg, Melatonin 14mg	Levitracetam 1g, Melatonin 2mg, Baclofen 60mg	Oxygen daily	Oxygen daily
17	Verapamil 720mg	Verapamil 960mg	S/C sumatriptan x4/day, oxygen daily	S/C sumatriptan x4/day, oxygen daily
18	Gabapentin 3600mg,	Gabapentin 300mg	Nasal sumatriptan x3/day, oxygen daily	Nil
19	Verapamil160mg, Melatonin 9mg	Melatonin 15mg	Oxygen daily	Oxygen daily
20	Melatonin 16mg	Nil	Nasal sumatriptan x2-3/month	Nil
21	Nil	Nil	Nil	Nil

Use of preventive treatments and acute treatments for CH prior to and after D

Figure 7-2: Median Headache Load Evolution

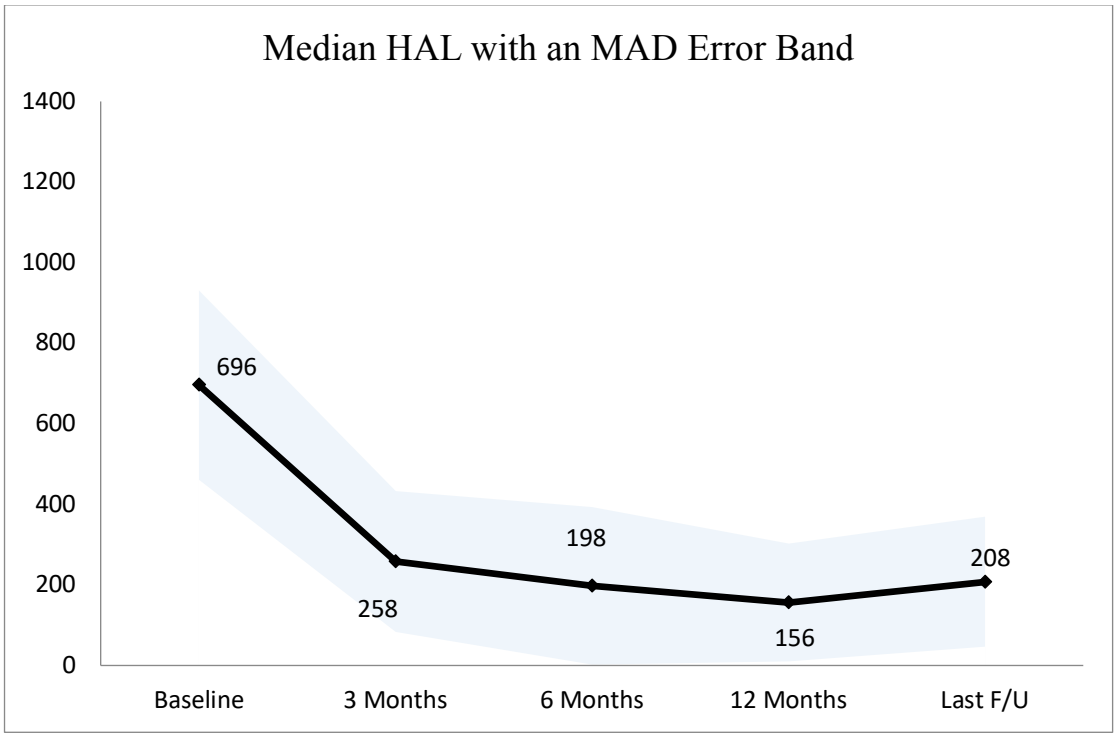

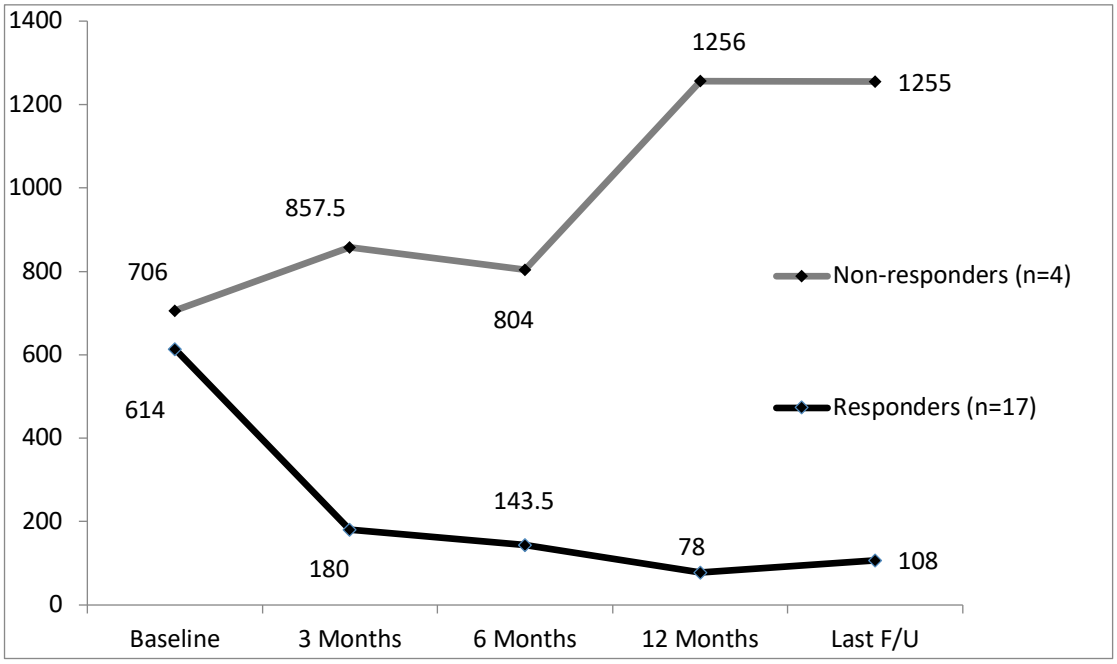

MAD: Median Absolute Deviation

2a: Median Headache Load (HAL) at baseline and over the course of follow-up

2b: Median HAL of Responders and Non-responders

Figure 7-3: Improvement in quality of life, disability and mood

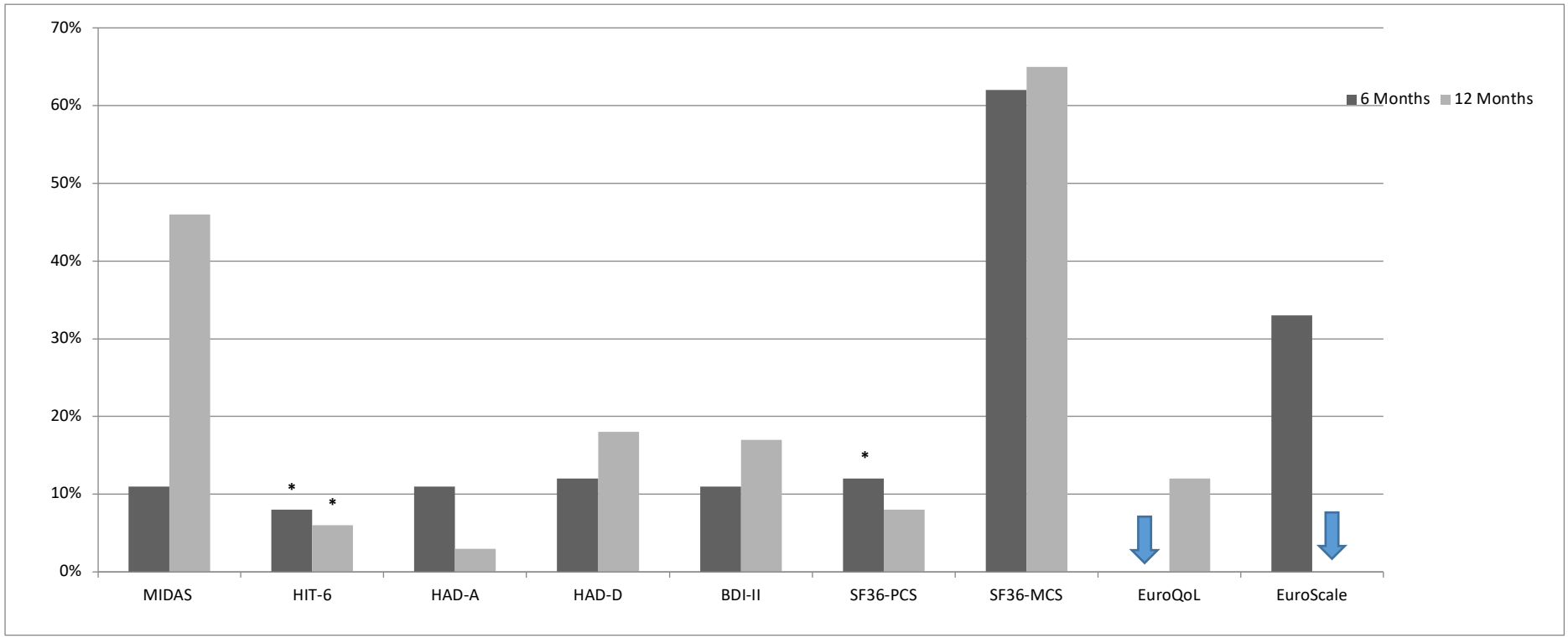

*: p value ≤0.05. P values are Bonferroni corrected; they represent individual tests at each time point relative to baseline (number of comparisons = 2 for tests at 6 and 12 months)

Median percentage of improvement in quality of life (SF36, EuroQoL), disability (MIDAS, HIT6), and mood (HADS-A, HADS-D, MIDAS: Migraine Disability Assessment Score, HIT6: Headache Impact-6, HADS-A, HADS-D: Hospital Anxiety and Depression Scale, BDI-II: Beck Depression Inventory II, SF36-PCS: Short Form 36 Physical Summary Score, SF36-MCs: Short Form 36 Mental Summary Score.

8. Ventral tegmental area deep brain stimulation in refractory short-lasting unilateral neuralgiform headache attacks

8.1: Abstract

Short-lasting unilateral neuralgiform headache attacks are primary headache disorders characterized by short lasting attacks of unilateral pain accompanied by autonomic features. A small minority are refractory to medical treatment. Neuroimaging studies have suggested a role of the posterior hypothalamic region in their pathogenesis. Previous case reports on deep brain stimulation of this region, now understood to be the ventral tegmental area, for this disorder are limited to a total of three patients. We present a case-series of 11 new patients treated with ventral tegmental area deep brain stimulation in an uncontrolled, open-label prospective observational study. Eleven patients with refractory short-lasting unilateral neuralgiform headache attacks underwent ipsilateral ventral tegmental area deep brain stimulation in a specialist unit. All patients had failed, or been denied access to, occipital nerve stimulation within the United Kingdom's National Health Service. Primary endpoint was change in mean daily attack frequency at final follow-up. Secondary outcomes included attack severity, attack duration, headache load (a composite score of attack frequency, severity and duration), quality of life measures, disability and affective scores. Information was also collected on adverse events. Eleven patients (six male) with a median age of 50 years (range 26-67) were implanted between 2009 and 2014. Median follow-up was 29 months (range 7-63). At final follow-up the median improvement in daily attack frequency was 78% (IQR 33%). Response rate (defined as at least a 50% improvement in daily attack frequency) was 82% and four patients were rendered pain free for prolonged periods of time. Headache load improved by 99% (IQR 52%). Improvements were observed in a number of quality of life, disability and affect measures. Adverse events included mild incision site pain, subcutaneous displacement of the implantable pulse generator, transient oscillopsia and minor wound infection. One

patient required removal of the system due to wound infection. Ventral tegmental area deep brain stimulation may be an effective treatment option for refractory short-lasting unilateral neuralgiform headache attack patients who have failed other therapies.

8.2: Introduction

Short-lasting unilateral neuralgiform headache attacks are a rare form of primary headache disorder characterised by frequent attacks of excruciating unilateral pain occurring in the trigeminal distribution, centred on the eye and temple, with associated autonomic features. They are included in the group known as the trigeminal autonomic cephalalgias and The International Classification of Headache Disorders (ICHD3-beta) describes two subtypes **(Table 8-1)**: short-lasting unilateral neuralgiform headache attacks with conjunctival injection and tearing (SUNCT) and short-lasting unilateral neuralgiform headache attacks with cranial autonomic features (SUNA) [424]. The disorder is said to be chronic when it occurs for more than a year with remission periods lasting less than one-month. Short-lasting unilateral neuralgiform headache attacks can be difficult to treat medically. In the past, intractable patients have been subjected to destructive procedures of the trigeminal nerve with poor long-term results [425]. Peripheral (occipital nerve stimulation [ONS]) and central (ventral tegmental area [VTa] deep brain stimulation [DBS]) neuromodulation techniques have been carried out with more promising results [426-429].

To date there are three published case reports of DBS for short-lasting unilateral neuralgiform headache attacks [426-428]. We present a consecutive series of 11 patients with intractable chronic short-lasting unilateral neuralgiform headache attacks treated with VTa-DBS as a humanitarian intervention reporting on changes in attack characteristics, quality of life, headache disability, affect scores and adverse events.

8.3: Methods

This was an observational study based on a prospective, open label cohort initiated in 2009. Under the supervision of our institution's Clinical Effectiveness Supervisory Committee with arrangements for clinical governance, consent and audit, we offered VTa-DBS to medically

intractable short-lasting unilateral neuralgiform headache attacks who had failed ONS or had been declined NHS funding for ONS. The procedure was provided on the basis of a "humanitarian intervention". In addition, ethic board approval for data collection and publication was granted by Northwick Park Hospital Research Ethics Committee, Hampstead, London, UK.

All patients were seen by a single specialist headache team at the National Hospital for Neurology and Neurosurgery, Queen Square, London UK and referred to a single multidisciplinary DBS team at the same centre. All patients fulfilled the International Classification of Headache Disorders-2 criteria at diagnosis but also met revised ICHD-3beta criteria [424,430]. Patients with prolonged attacks had a trial of Indomethacin (oral or intramuscular) to rule out Indomethacin-sensitive headaches [431]. Unlike chronic cluster headache or chronic migraine, intractability is not defined for short-lasting unilateral neuralgiform headache attacks [409]. Patients were considered suitable for VTa-DBS if they had had disabling medically intractable chronic short-lasting unilateral neuralgiform headache attacks for at least two years and had failed adequate trials of lamotrigine, topiramate, gabapentin, pregabalin and at least one of either carbamazepine or oxcarbazepine [429]. Disability was defined as a Headache Impact Test Score (HIT-6) in the severely affected range (i.e. above 60). Agents were selected on the basis of reported efficacy in this disorder and local experience [432,433]. A failed trial was defined as lack of response, intolerable side effects or contradiction to the use of the drug. One patient (P9) did not meet the criteria for medical intractability as they had not trialled carbamazepine or oxcarbazepine but this patient was implanted primarily for co-existent intractable chronic cluster headache. All patients were considered for ONS prior to VTa-DBS and had either been declined funding or failed to respond. Microvascular decompression of the trigeminal nerve was not being offered to this patient group during the study period. Neuropsychological evaluations and MRI brain scans were performed to exclude possible contraindications to surgery such as significant cognitive impairment, brain lesion or significant brain atrophy.

8.3.1: Outcomes

The two primary outcome measures were the change in median daily attack frequency in the two weeks prior to implant and the two weeks before final follow-up, and clinical response to VTa-DBS, defined as an at least 50% reduction in daily attack frequency. Secondary outcomes included reduction in the daily attack severity and frequency, headache specific disability scores, quality of life and affect scores.

Outcome data was collected and recorded prospectively. Patients were seen at three monthly intervals post implant over the first year and six monthly thereafter. Timing of additional appointments was dependent on clinical condition. Data collected included demographics, diagnosis, previous and current treatments, attack frequency, attack severity, headache load, headache disability scores, quality of life scales, affective scores, DBS settings and complications.

Headache load (HAL) is a composite score defined as Σ(severity [verbal rating scale]) x (duration [hours]) of all attacks over a two week period [434]. Patients were asked to record these data in a headache diary completed for at least two weeks before every assessment. Headache severity was measured on a verbal rating scale (VRS; 0=no pain – 10=excruciating pain). Patients with multiple headache types were able to differentiate their phenotypes and kept a separate diary for each headache syndrome.

Although specific tools for measuring the associated disability of trigeminal autonomic cephalalgias have yet to be validated, Migraine Disability Assessment Scores (MIDAS) and Headache Impact Test-6 Scores (HIT-6) were recorded pre and post-DBS to monitor disability. These scores have been widely used in the assessment of primary headache disorders and have previously been used to monitor response to cluster headache, hemicrania continua and short-lasting unilateral neuralgiform disorders in ONS [415,429,435]. Beck Depression Inventory II Score (BDI-II), Hospital Anxiety (HAD-A) and Depression (HAD-D) Scores were used to monitor mental state pre- and post-ONS implant and quality of life was assessed using the EuroQoL (EQ-5D) and Short-Form 36 (SF36).

Data were collected prospectively and entered onto a clinical database (Microsoft Excel, Microsoft Corporation, Redmond, WA, USA).

8.3.2: Surgical Procedure

Deep brain stimulation surgery was performed with the Leksell frame (model G, Elekta Instrument AB, Stockholm, Sweden), using an MRI-guided and MRI-verified approach without microelectrode recording. This approach has previously been described for alternative DBS targets [61,274]. Surgery was performed under local anaesthesia for patients one to four and under general anaesthesia for all others (P5-11). The anatomical target was the VTa ipsilateral to the side of attacks. The location of the deepest contact of the Medtronic 3389 lead was defined on an axial 1.5T T2-weighted stereotactic MRI image at a level immediately superior to the mammillary bodies, anteromedial to the hypointense red nucleus and posterolateral to the hypointense mammillothalamic tract, midway on a line joining the center of the nucleus ruber to the center of the mamillary body. Immediate postoperative low energy stereotactic MRI [63] with frame still on the head, was used to verify electrode location (in patient 9 with ONS in situ, an immediate postoperative CT scanning was used) **(Figure 8-1)**. All DBS leads were located within 1mm of the intended target point. The lead was then connected to a Medtronic implantable pulse generator (IPG) located in the infra-clavicular region.

8.3.3: DBS Programming

All patients underwent initial programming to define optimal stimulation parameters. The contact point that produced typical patient complaints of transient vertical diplopia, vertigo, oscillopsia and ophthalmoplegia at the lowest amplitudes was chosen as the initial stimulation contact. Four patients had stimulation started immediately. The remaining seven patients had a delay of four to seven weeks before stimulation was started due to the presence of a stun effect post-operatively where attacks transiently improved without use of stimulation. In those with a stun effect, DBS was not initiated until attacks returned to normal pre-surgical frequency. All devices were programmed with frequency of 185Hz

and a 60µs pulse width. Voltage was adjusted according to patient reported side effects (see above) aiming for a maximum of 4.0V. Adjustments in voltage were undertaken in single or multiple steps dependent on patient tolerability. Stimulation parameters remained constant for three months after each re-programming session. Adjustments in stimulation parameters were made depending on clinical response.

8.3.4: Statistics

All statistical analyses were conducted using IBM SPSS Statistics version 22 (IBM Corp. Int.). In descriptive analysis, continuous variables were summarized using median and interquartile range and categorical variable using percentages. Wilcoxon signed-rank tests were used to measure changes in baseline values. A last observation carried forward technique was used in the case of missing data. All statistical tests were two-sided with a significance level of 5%.

8.4: Results

8.4.1: Patient demographics

Eleven patients (six male) with short-lasting unilateral neuralgiform headache attacks underwent VTa-DBS between October 2009 and September 2014. Patient demographics and baseline headache characteristics are shown in **Table 8-2**. Median age at implant was 50 years (range 26-67). Three patients were diagnosed with SUNA and eight SUNCT. Nine patients had been chronic since onset. Median duration of the chronic phase was 9 years (range 4-20). Five patients had additional headache syndromes including chronic migraine (three patients), chronic cluster headache (three patients) **(Table 8-2)**. In those with cluster headache, attacks of short-lasting unilateral neuralgiform headache attacks were ipsilateral to their cluster attacks in all but one patient (P9) who had left sided cluster attacks and unilateral but side variable SUNCT attacks (more common on the left). Eight patients had unilateral DBS electrodes implanted and three had bilateral implants (P7, P9 and P10) for side variable attacks **(Table 8-3)**. Two patients (P5 and P9) had previously undergone ONS implantation with little (P9) or no effect (P5) on their SUNCT. Patient 5

had had the ONS device removed prior to VTa-DBS and Patient 10 still had the ONS in-situ given its partial effect on their cluster headaches.

All patients had undergone MRI brain scans prior to VTa-DBS of which two showed evidence of neurovascular conflict of the ipsilateral trigeminal nerve.

Patients had tried a median of 11 treatments (IQR 3) including oral preventative drugs and injectable treatments **(Table 8-4 and 8-5)**. Nine of ten patients that received lidocaine infusions reported transient benefit and ten patients failed to receive any benefit from greater occipital nerve blocks.

8.4.2: Follow up and final outcome

Post-operative follow-up ranged from seven to 63 months with a median of 29 months (IQR 20). One patient had her DBS system removed at time of follow-up. At final follow up, median attack frequency had reduced by 78% (IQR 33%) from 45 (IQR 10) to 2 (IQR 180) attacks per day (p=0.003) **(Figure 8-2A and 8-2B and Table 8-6)**. A positive clinical response, defined as at least a 50% reduction in attack frequency, was seen in 82% (9 patients). Of the two who failed to respond, one (P5) had the stimulator switched off for around 12 months during the 32-month follow-up due to tolerability issues but still obtained a more than 30% reduction in attacks. The other (P6), reporting a 25% reduction in attack frequency at follow-up did not have an implant in-situ having had the DBS system removed 17 months into her 24 month follow-up due to a wound infection. Previous to implant removal, the patient was reporting a 90% reduction in daily attack frequency **(Figure 8-2B)**. Patient estimate of improvement was 70% (IQR 95%) **(Table 8-6)** and all patients said they would recommend the treatment to others. The median time to reach a 50% improvement was 1 month (range 1-2 months). Only one responder had the system switched off for any period of time (P6) and attack frequency returned to baseline within 1 month of DBS removal. In those with co-existent headache disorders, cluster headache attacks decreased in two patients (P3 and P9) by 72% and 25% respectively. Migrainous headaches failed to respond in the three patients (P3, P6 and P10) reporting them.

8.4.3: Attack severity, duration and headache load

At final follow-up, median attack severity reduced by 50% from 10 (IQR 2) to 5 (IQR 10) points on VRS (p=0.020). Median attack duration reduced by 99% (IQR 100) from 7200 to 30 seconds but this change was not statistically significant (p=0.066). Headache load showed a median reduction of 99% (IQR 52) (p=0.026). Neither of the patients categorized as clinical non-responders (P5 and P6) showed a more than 50% reduction in HAL. One patient (P9) who recorded a 66% reduction in attack frequency failed to show a matching response to HAL (48% reduction) **(Table 8-6)**.

8.4.4: Headache associated disability scores, quality of life and affect measures

Baseline median MIDAS and HIT-6 scores were 81 (IQR 254) and 70 (IQR 12) respectively, both scores being within the severely affected range **(Table 8-7)**. At final follow-up statistically significant reductions were seen in HIT-6 but not MIDAS. Median HIT-6 fell by 15 points (p=0.015) well above the three point minimally important change [436]. MIDAS fell by 39 points (p=0.678) which although not statistically significant is above the nine-point difference separating moderate from severe disability. Summary measures of the physical (SF-36P) and mental (SF-36M) SF-36 scale showed a non-significant improvement **(Table 8-6)**. No significant change was seen in the separate domain scores of SF-36 scale **(Figure 8-3)**. Euro-QoL 5D and EuroScale scores did not show any significant change post implant **(Table 8-7)**. Prior to implant all affective scores indicated the presence of moderate mood disorders. Post treatment, both HAD-A and BDI-II scales indicated mild disorder scores but HAD-D continued to indicate moderate levels of depression **(Table 8-7)**. Despite this clinical change, there was no statistically significant change in affective scores at follow-up.

8.4.5: Adverse Events

Adverse events were recorded if any issues had arisen during the time of treatment. Events were classified as “hardware related” if they involved a malfunction of any device component, “biological” if they involved pain or other biological reactions related to the

device or the surgical procedure to implant it and “stimulation-related” if they were thought to be related to stimulation. One hardware related event was noted with a patient requiring surgical revision of their IPG due to the IPG moving or “flipping”. Biological adverse events included mild to moderate neck stiffness in three patients, keloid scar in one patient and persistent pain over wound sites in two patients. One patient suffered a small wound dehiscence in the first three weeks post-operatively with no evidence of wound infection. One patient suffered a wound infection at the lead/cable connector site 17 months post-implant (P6). Due to the risk of spread of infection, the whole DBS system was removed. All patients reported transient stimulation related adverse effects (described in DBS programming section above) related to DBS programming resolving within minutes to hours. One patient complained of symptoms compatible with oscillopsia on reading for six weeks after their initial programming session that resolved spontaneously. One patient (P5) complained of intolerable worsening of chronic nausea with any change in stimulation, however, with blinded changes in stimulation and in a 12-month period without stimulation there was no change in the nausea and it was judged that this complaint was not related to stimulation. A total of two surgical interventions were required during follow-up **(Table 8-8)**.

8.4.6: Concomitant drug use

Nine patients were taking preventative medications for short lasting unilateral neuralgiform headache attacks at time of implant **(Table 8-9)**. At final follow-up, four patients had stopped all preventatives for their SUNCT/SUNA and a further two had been able to reduce their doses of one or more medications.

8.4.7: Stimulation parameters

A summary of stimulation parameters is given in **Table 8-10**. Median stimulation amplitude at follow-up was 3.0V. Subjects had a median of 6 changes to stimulation parameters during follow-up.

8.5: Discussion

Previous case reports of VTa-DBS treatment in short lasting unilateral neuralgiform headache attacks have suggested a benefit in three patients [426-428]. Our open-label prospective series of eleven patients suggests that VTa-DBS may be an effective and safe treatment in patients with intractable short lasting unilateral neuralgiform headache attacks who have proved refractory to all other available treatment modalities. In our group of eleven patients there was a significant reduction in daily attack frequency of 78% with four patients remaining pain free for prolonged periods of time. Overall nine patients had a positive response to VTa-DBS with a 50% or more reduction in attack frequency. Improvement was seen in headache specific disability scores (HIT-6) but not in quality of life scales or measures of depression.

Deep brain stimulation for another trigeminal autonomic cephalalgia chronic cluster headache (CCH) was first undertaken by Leone *et al* in 2001 [123]. This procedure was based on the findings of a 1998 study which showed increased activation on positron emission tomography in the posterior hypothalamic region during cluster headache attacks [121]. To date, there is now published data on over 70 patients with intractable CCH treated with DBS. One series which pools 58 of these patients reports that 62% showed a 50% or greater reduction in attack frequency [406]. Similar findings of activation of the ipsilateral inferior posterior hypothalamic region was also observed during SUNCT attacks and therefore the same DBS target was proposed to be potentially beneficial in the treatment of short lasting unilateral neuralgiform headache attacks [437]. Only three case reports have been published, all showing substantial and sustained reductions in attack frequency without any serious adverse events [426-428]. Since the initial work of May and Leone, further anatomical clarification of the surgical target has been undertaken and the target has been shown to be in the ventral tegmental area of the midbrain rather than the posterior hypothalamic region [418,422].

Our series shows improvements in both attack frequency (78%) and severity (50%) with VTa-DBS. This finding has been described in CCH cases treated with VTa-DBS but not

short lasting unilateral neuralgiform headache attack cases [406]. This series also reports the headache load (HAL) as an outcome measure for the group. This composite score reflects all three domains of headache burden (frequency, severity and duration). Attack frequency has always been the focus of previous outcome reports for VTa-DBS for headache. However, the use of a single outcome may not represent the actual benefit perceived by the patient. Headache load showed a significant improvement (99%) at final follow-up. In our group, only one patient showed a discrepancy between attack frequency and HAL response (P9). This patient exhibited a 66% reduction in attack frequency (and so a positive response to VTa-DBS) but a 48% reduction in HAL. It is interesting to note that this patient stated they had not perceived any benefit from the treatment. The clinical usefulness of HAL as a primary outcome measure needs validation in larger cohorts in the future.

As in previous VTa-DBS for primary headache series our subjects reported a delay in clinical response. In CCH this delay is several months long but in the short lasting unilateral neuralgiform headache cases ranged from days to a maximum of three months [406,426,427,435,438,439]. In our series, the time taken to see positive clinical response was 1 month (range 1-2 months). This delay likely reflects the neuroplastic response underlying successful VTa-DBS treatment.

Clinically and statistically important differences were seen in HIT-6 scores following VTa-DBS but no significant improvement was seen in quality of life measures. Factors to consider in this observation include the small sample size, the long duration of chronic pain (9 years) and co-morbidities in these patients all of which may have resulted in psychosocial issues unlikely to improve with change in symptoms. Similar observations have been made in VTa-DBS for CCH [438]. Little has been published regarding quality of life data in the trigeminal autonomic cephalalgias including short lasting unilateral neuralgiform attack disorders and no specific headache disability or quality of life scales exist for these disorders. It has been suggested that in headache disorders, generic scales (such as SF36) may not be useful in measuring changes over time and that disorder

specific measures (such as HIT-6) may be more representative [440]. Until such scales have been developed the quality of life tools available may not accurately reflect the headache groups they are applied to.

One serious adverse event of subcutaneous infection leading to system removal occurred in our series. Infection of the DBS system has been reported by two other CCH series (4/19 and 1/11 patients) [419,441], although their operative technique differed from our unit. A report from Belgium on the death of a patient from an intracerebral haemorrhage following microelectrode (MER) guided DBS for CCH has raised serious safety concerns regards this procedure [68]. However, there is no recognised neuronal firing pattern or "signature" for the VTa, casting doubt on the clinical utility of MER for this anatomical target. Moreover, the target area is visible on a stereotactic thin-slice T2-weighted MRI. Hence, the use of an MRI-verified surgical technique without the use of MER provides direct visualisation of the individual target area and is associated with a significantly lower risk of haemorrhage during DBS procedures [69]. The use of microelectrode recording when targeting this area has also been avoided by using an endoventricular approach to DBS lead placement [442] . The stimulation induced ophthalmic side effects reported by our patients have all been documented in CCH series and, much like our series, have all been transient. It is likely that this transient vertical diplopia is due to stimulation of the nearby rostral interstitial nucleus of the medial longitudinal fasciculus that forms part of the vertical gaze center [443].

The main limitation of this study is the lack of placebo control. Although there is undoubtedly a placebo effect for headache treatments, it is unlikely our findings can be explained by this alone. Placebo response rates for ONS in migraine are low (below 20%) and there is no reason to expect the contrary in this disorder or procedure [444-446]. Likewise, the intractable nature of the group, the sustained response and the re-emergence of attacks when stimulation was stopped all argue against a placebo response. Although a previous randomized controlled trial of DBS in CCH failed to show a difference between sham and active stimulation this was likely due to methodological issues with short 1-month crossover periods. Unfortunately, given the rarity of short lasting unilateral neuralgiform headache

attacks, it seems unlikely that high quality, properly powered randomised control trials of VTa-DBS will ever be performed.

Microvascular decompression, occipital nerve stimulation and deep brain stimulation have all been found to be effective in open-label series with response rates of over 75% [426,428,429,447]. The invasiveness of surgery, associated risks, the need for implanted hardware and the cost of treatment will all influence individual patient options. With these in mind, we may in the future recommend that patients with intractable short lasting unilateral neuralgiform headache attacks first undergo microvascular decompression if they have ipsilateral neurovascular compression of the trigeminal nerve, that ONS be reserved for those without neurovascular compression or failing microvascular decompression and DBS (as the most invasive neuromodulation option) be left as an option when patients have failed all other procedures.

This study suggests that VTa-DBS may provide an effective and sustained benefit in intractable short lasting unilateral neuralgiform headache attacks. However, MRI-verified VTa-DBS should be reserved for those patients having failed all other medical and surgical options available to them.

Table 8-1: International Classification of Headache Disorders diagnostic criteria for short lasting unilateral neuralgiform headache attacks

Short lasting unilateral neuralgiform headache attacks
• At least 20 attacks suffered • Moderate to severe unilateral head pain with trigeminal distribution, lasting 1-600 seconds and occurring as single stabs, series of stabs or in a saw-tooth pattern • At least one cranial autonomic symptom or sign ipsilateral to the pain: • Conjunctival injection and/or lacrimation 1. nasal congestion and/or lacrimation 2. eyelid oedema 3. facial sweating 4. facial flushing 5. fullness in the ear 6. ptosis and/or miosis • Attacks occur at least once a day for more than half the time the disorder is active
Short lasting unilateral neuralgiform headache attacks with conjunctival injection and tearing
• As short lasting unilateral neuralgiform headache attacks • Autonomic symptoms of both conjunctival injection and lacrimation
Short lasting unilateral neuralgiform headache attacks with autonomic features
• As short lasting unilateral neuralgiform headache attacks • Autonomic symptoms include only one of or neither of conjunctival injection and lacrimation

Table 8-2: Patient demographics

	Age/ years	Sex	SUNCT/SUNA	Chronic duration	Side	Other Headaches	Attack Frequency/ Day	Average Attack duration	Triggered attacks/ Spontaneous attacks/Both*	MRI for neurovascular conflict**
1	56	M	SUNCT	14	R	NIL	20	5min	Spontaneous	NIL
2	63	M	SUNCT	16	R	NIL	360	10 sec	Both-touch/wind	Right
3	39	M	SUNCT	9	R	CCH (R) CM	20	15 sec	Spontaneous	NIL
4	67	M	SUNCT	13	L	CCH (L)	40	10min	Spontaneous	NIL
5	64	F	SUNCT	9	R	NIL	6	3min	Spontaneous	NIL
6	55	F	SUNCT	20	L	CM	120	2 min	BOTH – touch/chewing/ wind	NIL
7	41	F	SUNCT	4	L 90% R 10%	NIL	200	3 min	Spontaneous	NIL
8	26	F	SUNA	8	R	NIL	800	2 sec	BOTH – talking/touch/ eating/wind	NIL
9	50	M	SUNCT	6	L 70% R 30%	CCH (L)	3	5min	Spontaneous	NIL
10	42	F	SUNA	19	L 40% R 60%	CM	95	2min	Spontaneous	NIL
11	46	M	SUNA	9	R	NIL	45	30 sec	Spontaneous	Right
Median (IQR)	*50 (22)*	*6M 5F*	*8 SUNCT 3 SUNA*	*9 (7)*	*6 R 2 L 3L/R*	*3 CCH 3 CM*	*45 (20)*	*2 min (5)*	*8 Spontaneous 3 Both*	*2 Ipsilateral NVC*

*In case of triggered attacks, typical triggers are listed ** Neurovascular conflict of trigeminal nerve at level of root entry zone seen on MRI

M, male; F, female; SUNCT, short lasting unilateral neuralgiform headache attacks with conjunctival injection and tearing; SUNA, short lasting unilateral neuralgiform headache attacks with autonomic features; R, right; L, left; L/R, left or right; CCH, chronic cluster headache; CM, chronic migraine; MO, medication overuse; NVC, neurovascular conflict

Table 8-6: Headache characteristics before and after treatment

	Follow Up/ months	DAILY ATTACK FREQUENCY			ATTACK SEVERITY			HEADACHE LOAD			ATTACK DURATION (seconds)			Estimated Improvement[ŦŦ]	Patient recommend[ŦŦ]
		Pre DBS	Post DBS	% Change	Pre DBS	Post DBS	% Change	Pre DBS	Post DBS	% Change	Pre DBS	Post DBS	% Change		
1	63	20	6	70	8	2	75	69	3	96	18000	30	99	95	Yes
2	40	360	0	100	7	0	100	14	0	100	10	0	100	100	Yes
3	33	10	0	100	10	0	100	7	0	100	15	0	100	100	Yes
4	41	40	2	95	7	7	0	94	1	99	36000	1	100	70	Yes
5	32	6	4	33	10	10	0	42	35	17	10800	7200	33	5	Yes
6 ≠	29	120	90	25	9	10	0	225	304	0	7200	7200	0	0	Yes
7	23	200	58	71	10	5	50	1400	304	78	10800	60	99	70	Yes
8	14	800	0	100	10	0	100	62	0	100	2	0	100	100	Yes
9	7	3	1	66	10	10	0	23	12	48	18000	18000	0	0	Yes
10	29	95	0	100	10	0	100	44	0	100	7200	0	100	100	Yes
11	28	45	5	89	8	8	0	56	12	79	2160	18000	-7	58	Yes
MEDIAN (IQR)	*29 (20)*	*45 (20)*	*2 (10)*	*78* (33)*	*10 (2)*	*5 (10)*	*50* (100)*	*62 (202)*	*3 (35)*	*99* (52)*	7200 (17985)	30 (7200)	99 (100)	*70 (95)*	

The average daily attack frequency and severity is listed before and after treatment. Headache load, a composite score reflecting attack frequency, severity and duration is also shown. Patient satisfaction is shown using their estimated level of improvement and their recommendation of treatment to other patients.

*p<0.05; Ŧ Patient estimate of improvement at final follow-up; ŦŦ Patient asked if they would recommend the procedure to another person with short lasting unilateral neuralgiform headache attacks; ≠ Deep brain stimulation system removed at time of follow-up; DBS, Deep brain stimulation

Table 8-7: Headache specific disability, affect and quality of life score changes with deep brain stimulation

	Pre-DBS Median (IQR)	Post-DBS Median (IQR)	Median % Change % (IQR)	P-value
MIDAS	81 (254)	65 (12)	0 (63)	0.678
HIT-6	70 (12)	65 (14)	8 (19)	0.015*
HAD-A	12 (11)	8 (13)	17 (28)	0.035*
HAD-D	12 (8)	11 (10)	0 (42)	0.721
BDI-II	23 (23)	16 (29)	0 (24)	0.929
SF-36 Physical	23 (26)	29 (18)	0 (24)	0.594
SF-36 Mental	30 (27)	46 (27)	23 (39)	0.208
Euro-QoL	0.63 (0.18)	0.64 (0.18)	0 (1.0)	0.208
Euro-Scale	30 (50)	32 (50)	0 (45)	0.483

IQR, Interquartile range; MIDAS, Migraine Disability Assessment Scale; HIT-6, Headache Impact Test; HAD-A, Hospital Anxiety and Depression scores-anxiety specific; HAD-D, Hospital Anxiety and Depression scores – depression specific; BDI-II, Becks Depression Inventory; SF-36, Short Form 36.

Table 8-8: Adverse events related to deep brain stimulation

Adverse Event (n)	***Resolution (surgical/medical/spontaneous/no intervention)***
Hardware Related	
IPG "flips" or moves in chest skin pocket (1)	Surgical intervention – repositioning of IPG
Biological	
Neck stiffness (3)	No intervention
Pain over wound site (2)	No intervention
Keloid scar over IPG site (1)	No intervention
Wound infection (1)	Surgical intervention – removal of system
Wound dehiscence, no infection (1)	Medical
Stimulation Related	
Diplopia, nausea, vertigo, ophthalmoplegia with changes of programming (11)	Spontaneous
Possible worsening of nausea (1)	Medical – DBS switched off with no change in symptoms. *Decision made symptoms not related to DBS*
Oscillopsia when reading (1)	Spontaneous resolution after 6 weeks
	TOTAL SURGICAL INTERVENTIONS = 2

IPG, implantable pulse generator; DBS, deep brain stimulation

Figure 8-1: 1.5T MRI scan showing DBS lead placement

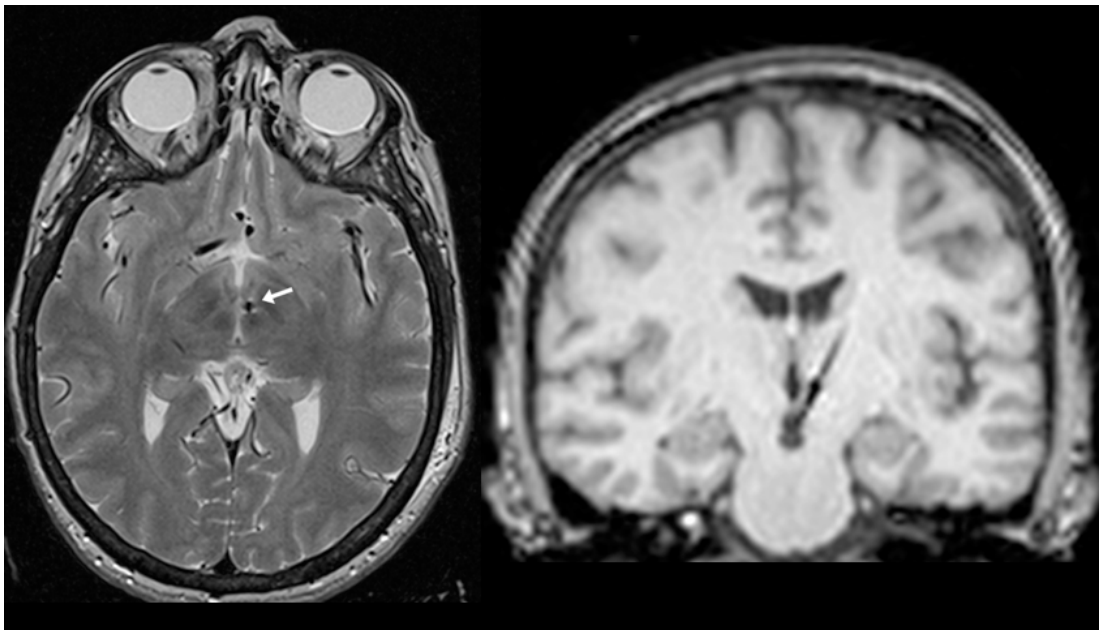

Post-operative 1.5T T2-weighted, 2mm-thick, axial stereotactic MRI immediately after implant shows the DBS lead positioned in the right ventral tegmental area of the midbrain (white arrow)

Figure 8-2: Reduction in daily attack frequency following deep brain stimulation

Figure 8-2A

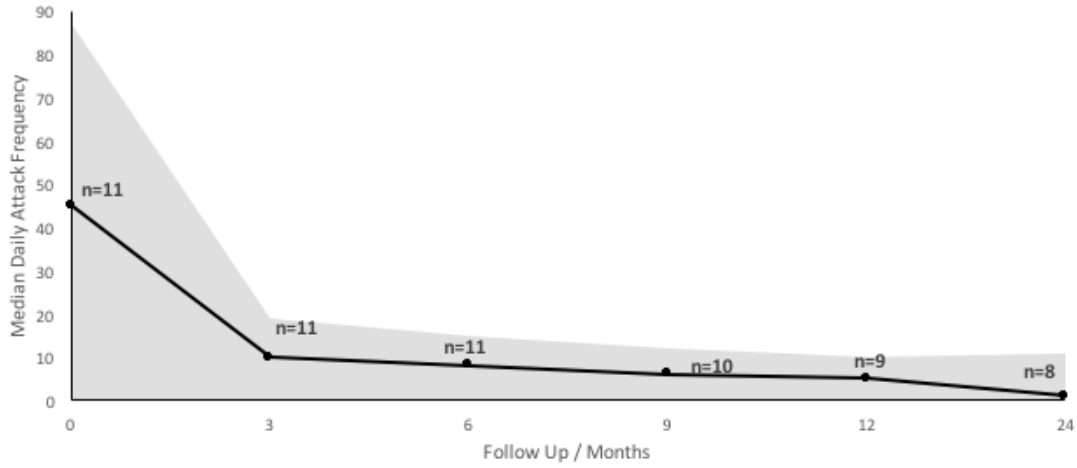

Figure 8-2B

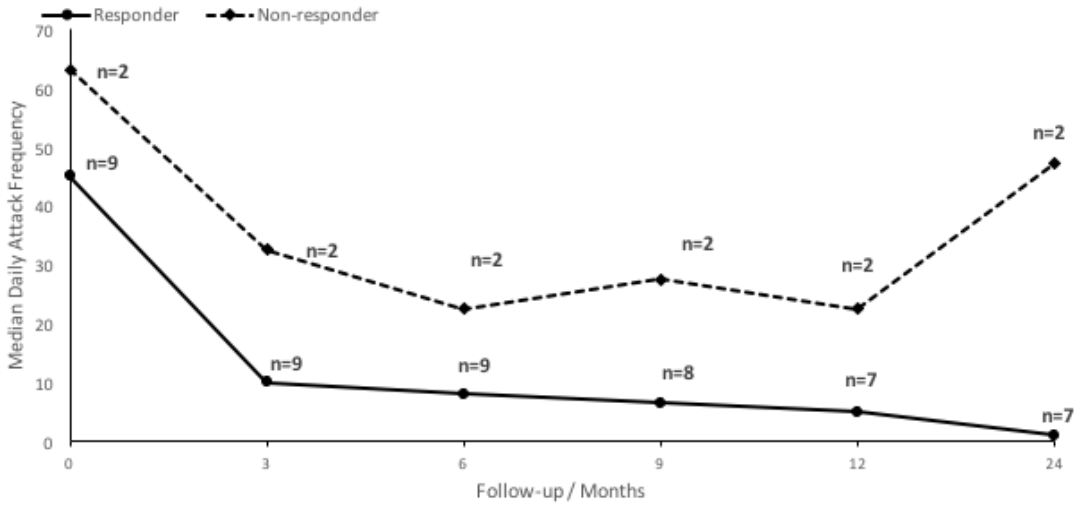

(A) Reduction in median daily attack frequency in the whole cohort with shaded area representing median absolute deviation error band. (B) Reduction in median daily attack frequency of responders and non-responders following implant

Figure 8-3: SF36 domain scores pre and post-DBS

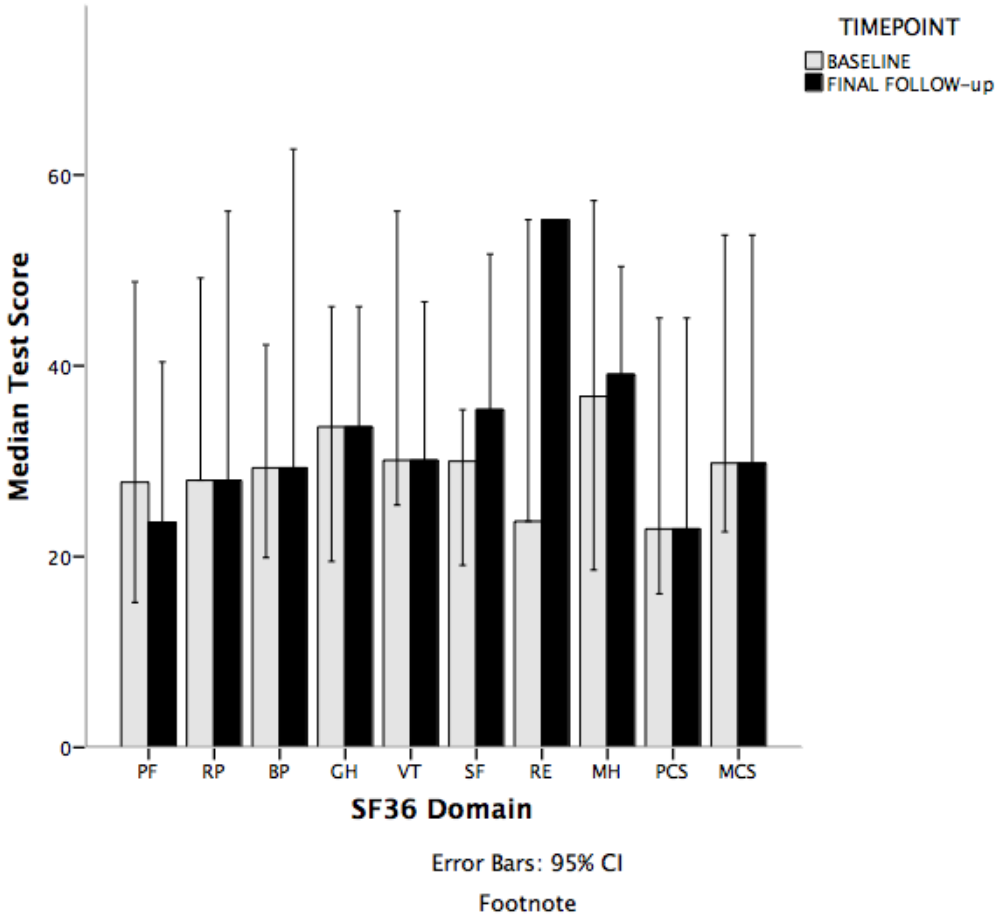

PF, physical functioning; RP, role-physcial; BP, bodily pain; GH, general health; VT, vitality; SF, social functioning; RE, role-emotional; MH, mental health; PCS, physical composite score; MCS,mental health composite score

Table 8-4: Preventative medications previously tried by patients undergoing deep brain stimulation

	Lamotrigine	Topiramate	Gabapentin	Pregabalin	Carbamazepine	Oxcarbazepine	Other
1	600mg	350mg	3600mg	600mg	1600mg	NT	*Melatonin, Indomethacin*
2	400mg	400mg	DUK	DUK	800	300	*Melatonin, Baclofen, Phenytoin*
3	600mg	1000mg	3600mg	600mg	DUK	NT	*Duloxetine, Melatonin, Venlafaxine*
4	200mg	200mg	3600mg	300mg	NT	1500mg	*Duloxetine, Melatonin*
5	600mg	400mg	DUK	DUK	900mg	300mg	*Duloxetine, Mexiletine, Melatonin, ONS (removed)*
6	200mg	450mg	2400mg	50mg	1200mg	1200mg	*Duloxetine, Lacosamide, Phenytoin, Baclofen, Zonisamide*
7	400mg	300mg	2700mg	300mg	DUK	2400mg	*Duloxetine, Indometacin*
8	1200mg	400mg	1800mg	300mg	1200mg	1200mg	*Duloxetine, Baclofen, Lacosamide, VNS*
9	400mg	200mg	600mg	600mg	NT	NT	*ONS(in-situ)*
10	400mg	200mg	900mg	600mg	DUK	2100mg	*Duloxetine, Mexiletine, Lacosamide, Ketamine*
11	200mg	25mg	300mg	1200mg	NT	1500mg	*Duloxetine, Indometacin*

NT, drug not tried; DUK, dose unknown; ONS, occipital nerve stimulation; VNS, non-invasive vagal nerve stimulation (GammaCore)

Table Legend: The daily dose of the preventative medications with stated efficacy in short lasting unilateral neuralgiform headache attacks taken by each patient prior to undergoing deep brain stimulation. A list of additional medications trialled for the condition is also shown.

Table 8-5: Injectable transitional treatments given for short lasting unilateral neuralgiform headache attacks prior to deep brain stimulation

	Lidocaine Infusion (7-10 days)			Greater Occipital Nerve Injection (lidocaine and steroid)		
	Response*	**Number of treatments**	**Duration of response (days)**	**Response****	**Side of injection**	**Duration of response (days)**
1	Yes	1	10 days	No	Right	3 days
2	Yes	1	On infusion only++	No	Right	0 days
3	Yes	1	On infusion only++	No	Right	0 days
4	Yes	1	On infusion only++	No	Left	0 days
5	Yes	2	On infusion only++	No	Right	0 days
6	No	1	Nil	No	Left	0 days
7	Yes	7	1 month	No	Left	0 days
8	Yes	1	On infusion only++	No	Right	0 days
9	N/A	-	-	No	Bilateral	0 days
10	Yes	4	10 days	Yes	Bilateral	2 weeks
11	Yes	2	Infusion only++	No	Bilateral	5 days

*Response defined by at least 50% reduction in daily attack frequency

** Response defined by at least a 50% reduction in attack frequency for at least one week post procedure

++ Patient reported response only during time on treatment and which stopped as soon as infusion ended

N/A, patient not tried treatment

Table 8-9: Summary of changes in preventative medications following deep brain stimulation

	Medication Prior to DBS	Medication Post DBS	Reduction in Dose
1	Pregabalin 600mg Lamotrigine 600mg	Pregabalin 600mg Lamotrigine 600mg	No No
2	Lamotrigine 700mg Carbamazepine 800mg	Lamotrigine 400mg Oxcarbazepine 300mg	Yes Yes (relative doses)
3	Lamotrigine 600mg	Nil	Yes
4	Nil	Nil	N/A
5	Lamotrigine 600mg Topiramate 400mg	Lamotrigine 600mg Lacosamide 50mg	No No
6	Zonisamide 100mg Lamotrigine 200mg	Zonisamide 100mg Lamotrigine 200mg	No No
7	Oxcarbazepine 1800mg Topiramate 300mg	Nil	Yes Yes
8	Lamotrigine 600mg Lacosamide 300mg	Lamotrigine 600mg Lacosamide 300mg	No No
9	Lamotrigine 400mg (+ONS)	Nil (+ONS)	Yes
10	Topiramate 200mg	Nil	Yes
11	Nil	Nil	N/A

DBS, deep brain stimulation; N/A, not applicable as patient not on medication

Table 8-10: Summary of deep brain stimulator settings for each patient

	Implant Location	Amplitude Range (V)	Frequency (Hertz)	Pulse width (μs)	Contact points settings*
1	Right	1.3-3.0	185	60	C+/1-
2	Right	1.5-3.0	185	60	C+/1-
3	Right	2.4-3.0	185	60	C+/0-, C+/0-1-
4	Left	1.3-3.5	185	60	C+/1-, C+/1-2-
5	Right	0-2.6	185	60	C+/0-, C+/1-
6	Left	0.0-3.0	185	60	C+/0-, C+/0-1-
7	Bilateral	2.2-3.0	185	60	Left (Activated from onset): C+/1-, C+/0-1 Right (Activated after 7 months): C+/8-
8	Right	3.0-3.5	185	60	C+1-, C+/0-1-
9	Bilateral	3.0	185	60	Left (Activated from onset): C+/0-, C+/1-, C+/0-1 Right (Not activated at follow-up)
10	Bilateral	3.0-3.5	185	60	Left: C+/0-, C+/0-1- Right: C+/9-, C+/8-9-
11	Right	1.5-2.8	185	60	C+/1-, C+/0-
Median (IQR)	*6 Right* *2 Left* *3 Bilateral*	*1.5 (2.7)-3 (0.5)*	*185*	*60*	

*Lead set as cathode and contact point as anode

9. Optimal deep brain stimulation site and target connectivity for chronic cluster headache

9.1: Abstract

High frequency deep brain stimulation (DBS) in the ventral tegmental area (VTa) is a safe and effective treatment for patients with refractory chronic cluster headache. Whereas the stimulation target was revealed on functional imaging studies, the mechanism of action of this treatment is yet to be understood. Furthermore, the optimal stimulation site within the target area has not been fully determined. Seven patients (5 male) with refractory chronic cluster headache were studied. High spatial, high angular resolution diffusion 3T MRI was acquired preoperatively. DBS electrode implantation into the VTa was performed using an MRI-guided and MRI-verified approach, unilaterally in 5 patients and bilaterally in two. Volumes of tissue activation were generated around active lead contacts using a finite element model. Twelve-months after surgery, voxel-based morphometry was used to identify voxels associated with higher reduction in headache load, defined as ∑ [severity (on the verbal rating scale)] x [duration (in hours)] of all headache attacks occurring over a 2-week period. Probabilistic tractography was used to identify the brain connectivity print of the DBS activation volumes in responders, defined as patients with a reduction of ≥ 30% in headache load. There was no surgical morbidity. Average follow-up length was 34 (±14) months. Patients showed a 76% (±33) reduction in headache load, 46% (±41) in attack severity, 58% (±41) in headache frequency, and 51% (±46) in attack duration at the last follow-up. All patients, except one, responded to treatment. Greatest reduction in headache load was associated with activation in an area cantered at 6 mm lateral, 2 mm posterior and 1 mm inferior to the third ventricle's mid-commissural point. Average responders' deep brain stimulation activation volume lay on the trigemino-hypothalamic tract, connecting the trigeminal system and other brainstem nuclei associated with

nociception and pain modulation, with the hypothalamus, and the prefrontal and mesial temporal areas.

9.2: Introduction

Chronic, high frequency deep brain stimulation (DBS) in the ventral tegmental area (VTa) has been shown to be a safe and effective treatment modality for patients with refractory chronic cluster headache (CCH) [68,123,124,406-408,448,449].

The underlying pathophysiology in cluster headache (CH) is not fully understood [450-457]. Though the exact trigger site for CH attacks is not clear, the hypothalamus has been implicated in the disease process [121,122,458-460] and pathological activation of the trigemino-parasympathetic brainstem reflex is thought to be responsible for simultaneous activation of trigeminal nerve and craniofacial parasympathetic nerve fibres, respectively, leading to the characteristic ipsilateral cranial pain and autonomic features [455,461]

The periodicity of individual attacks, the relapsing-remitting course and the seasonal recurrence of headache bouts are all suggestive of possible hypothalamic role in CH [398,455]. This is supported by neuro-endocrinological studies [458,459] and neuroimaging studies [121,122]. The latter pointed to increased activity and neuronal density in what was termed 'the posterior hypothalamic region' ipsilateral to the headache attacks [121,122,460]. However, further investigation of the area referred to in these studies has shown it to lie in the ventral tegmental area (VTa) and not the hypothalamic region [418,422,448]. These findings led to the emergence of this region as a target for DBS for CCH [68,123,124,406,407,419,448,462]

Occipital nerve stimulation (ONS) and cervical spinal cord stimulation for CH are thought to work through activation of the trigemino-cervical complex (TCC) [463,464]. The exact mode of action of DBS for CH and the neural networks involved remain poorly understood. Furthermore, the optimal stimulation site is yet to be identified [68,123,124,406,407,418,419,422]. Activation of the trigeminal nerve and ganglion have been demonstrated with hypothalamic stimulation [417], possibly mediated by the trigemino-hypothalamic tract (THT) described in non-human studies [465,466].

The objectives of this study were to identify the optimal VTa stimulation site for improvement in headache load and to explore the connectivity or ***fingerprint*** of stimulation tissue volumes in responders to identify the THT, by proceeding through the following steps:

1. To generate volume of tissue activated models for all active DBS contacts
2. To carry out a voxel based morphometry (VBM) style regression analysis of modelled activation volumes and their associated efficacy profiles
3. To perform tractography from modelled activation volumes of active DBS contacts in responders using a probabilistic approach and state of the art high angular resolution diffusion imaging (HARDI)

9.3: Materials and methods

The DBS procedure was provided on the basis of a "humanitarian intervention" for patients who had failed ONS or in whom National Health Service funding for ONS had been declined. This was in keeping with the UK National Institute for Health and Care Excellence (NICE) guidance (https://www.nice.org.uk/guidance/ipg381/chapter/1-Guidance). All patients were given information booklets approved by our institution's Clinical Effectiveness Supervisory Committee and provided written informed consent.

9.3.1: Patients

Seven patients (5 male) were recruited. Five patients belonged to a cohort that has been published previously concerning efficacy and safety of DBS for CCH [448]. All patients fulfilled the ICHD-II and ICHD-III beta diagnostic criteria for CCH and had experienced highly disabling, medically refractory symptoms for at least two years [397,424]. CCH was classified as medically intractable if patients failed adequate trials of at least five of the following seven drugs, where at least two came from the first three drugs listed: verapamil, lithium, methysergide, topiramate, melatonin, gabapentin, and valproate. A failed trial was defined as an unsatisfactory response, side effects intolerance or contraindication to the agent's

use [409]. Referrals were made by a single tertiary specialist headache clinic to a DBS multidisciplinary team at the same centre. Neuropsychological evaluations and MRI brain scans were performed to rule out cognitive impairment, brain lesions or significant brain atrophy. Inclusion in the present study was limited to patients who could tolerate lying flat for the duration of the preoperative scan and who had no contraindications to 3T MRI. Sphenopalatine ganglion stimulation was not available in the UK during the study period.

9.3.2: Preoperative magnetic resonance imaging data acquisition

Imaging pertinent to this study was performed prior to surgery on a 3T Siemens Magnetom Trio TIM Syngo MR B17 using a 32 channel receive head coil. Padding was used inside the head coil to reduce discomfort and head motion.

9.3.2.1: Diffusion weighted MRI

Details of diffusion weighted MRI acquisition and preprocessing are described in the general methods sections.

9.3.2.2: Surgical procedure and intraoperative magnetic resonance imaging data acquisition

DBS leads were implanted under general anaesthesia using a stereotactic 1.5 T MRI-guided and MRI-verified approach (Leksell frame model G, Elekta Instrument AB, Stockholm, Sweden) without microelectrode recording as detailed elsewhere [69,448]. The anatomical target was the ipsilateral VTa. Two patients with bilateral CCH underwent bilateral surgery in a single procedure. Two stereotactic, pre-implantation scans were acquired, as part of the surgical procedure, to guide lead implantation: a T2 weighted axial scan (partial brain coverage around the midbrain and hypothalamus with voxel size of 1.0×1.0 mm and slice thickness of 2 mm; and a T1 weighted 3D-MPRAGE scan with a 1.5 mm^3 isotropic voxel size on a 1.5T Siemens Avanto interventional MRI scanner. Three-dimensional distortion correction was applied using the scanner's built-in module. Once scans were reformatted parallel to the anterior commissure (AC) – posterior commissure (PC) line, the deepest contact location of the 3389 Medtronic lead was defined on the T2-

weighted MRI at a level immediately above the mammillary bodies, anteromedial to the hypointense red nucleus and posterolateral to the hypointense mammillothalamic tract. The MPRAGE scan was used to plan the lead's entry point over the coronal suture ± 2cm in the sagittal plane and at a laterality of 3-5cm ensuring a trajectory avoiding the sulci and lateral ventricle. Stereotactic imaging was repeated immediately following lead implantation to confirm lead placement. Care was taken to keep the specific absorption rate (SAR) < 0.4 W/kg; this was generally achieved by reducing the number of acquired T2 slices covering the distal leads to 12-14 [63]. The leads were then connected to an implantable pulse generator (IPG) (Activa SC or PC, Medtronic, Minneapolis, Minn., USA) implanted in the infra-clavicular region on either on the same day of lead implantation or within a week of it, as a staged procedure.

9.3.3: DBS programming

In the weeks following surgery, open label programming was conducted to define optimal stimulation parameters. All devices were programmed with a frequency of 185Hz and a pulse width of 60μs [124]. Voltages were adjusted according to self-limiting side effects (diplopia, vertigo, nausea, oscillopsia and ophthalmoplegia) in single or multiple steps, depending on the patient. Stimulation parameters were kept constant for the first three months and were adjusted after this if patients were not responding.

9.3.4: Outcome measures and follow-up

Outcome data were collected and recorded prospectively. These included daily attack frequency, attack severity, attack duration, headache load and adverse events (including surgical complications, stimulation-induced adverse events and morbidity). Headache severity was measured on the verbal rating scale (VRS) for pain (0 being no pain, and 10 being the worst pain imaginable). Attack frequency was defined as the number of CH attacks/day and duration as the time in hours of each recorded attack. The individual scores from both of these were then averaged over the 2-week observation period. Headache load (HAL) was defined as ∑ [severity (on the verbal rating scale)] x [duration (in hours)] of

all headache attacks occurring over a 2-week period. We have introduced this measure previously and suggested that it effectively reflects response to treatment [448]. These measures were assessed using 2-week duration headache diaries collected preoperatively (baseline), at commencement of DBS therapy, at 3 months, 6 months, 12 months and yearly thereafter.

Responders were defined as patients with sustained HAL reduction ≥30% since this was deemed meaningful in line with the Initiative on Methods, Measurement, and Pain Assessment in Clinical Trials (IMMPACT) guidelines [410].

9.3.5: Analysis of activation volumes

9.3.5.1: DBS contacts volume of tissue activated modelling

SureTune® (Medtronic Inc. Minnesota), a DBS therapy planning platform (pre-release Beta version) was used to model activation volumes around individual contacts. The platform applies neuron models coupled to finite element simulations as described by Åström and colleagues in order to generate DBS therapy activation volumes [162]. Post-operative, stereotactic MPRAGE scans were manually aligned with pre-implantation stereotactic MPRAGE scans. Automatic co-registration was then carried out with a restricted volume of fusion centred on the hypothalamus/ mesencephalon. This was carried out to minimise registration error resulting from brain shift incurred during surgery despite minimal brain shift with our surgical technique [260]. Registration accuracy was carefully inspected and the process iterated if necessary. All volumes were realigned with a plane parallel to the AC-PC line.

The post-implantation MPRAGE was used to fit the DBS lead model within the MRI artefact produced by the leads. Activation volumes were generated around active DBS contacts with corresponding voltages. Binary image files of activation volumes with corresponding transformation matrices were exported and processed in MATLAB (MathWorks Inc.) using an in-house software to generate Neuroimaging Informatics Technology Initiative (NIfTI) volumes for further analysis.

9.3.5.2: Inter-subject alignment

Pre-implantation MPRAGE scans were brain extracted using *BET* (Brain Extraction Tool, FSL v5.0) which deletes non-brain tissue from a whole head MRI [277]. Two-step transformation was used to register native scans to the MNI152 standard-space T1-weighted average structural template image (1mm resolution) [278]. The first step employed linear (affine) transformation using *FLIRT* (FMRIB's Linear Image Registration Tool) with 12 degrees of freedom, correlation ratio cost function and normal search [279,280]. The output from this step was used to execute non-linear registration (second step) using *FNIRT* (FMRIB's Non-Linear Image Registration Tool) [281]. This process produced individual native to standard (MNI space) non-linear warp fields which were then applied to the DBS activation volumes acquired from SureTune in order to transform all volumes to standard space.

9.3.5.3: Average DBS activation volume and efficacy cluster

All lateralized volumes were merged using *Fslmerge* (FSL v5.0) into a 4D data file. A single-group average (one-sample t-test) general linear model (GLM) design was used to test against percentage improvement in HAL.

Nonparametric permutation inference was then carried out on each voxel using *Randomise* (FSL v5.0) with 5000 permutations to build up the null distribution to test against. Percentage improvement in HAL was demeaned and single group t-test with threshold-free cluster enhancement (TFCE) was used as test statistic [164]. Cluster-based inference using *Cluster* (FSL v5.0) was carried out to extract the clusters and local maxima in outputs.

9.3.6: Analysis of white matter tracts

9.3.6.1: Tractography

Probabilistic tractography was generated in ProbtrackX2 GPU version (Behrens 2007) [282] (FSL v5.0) (number of samples=5000, curvature threshold=0.2, step length=0.5 mm subsidiary fibre volume fraction threshold=0.01). The process repetitively samples from the distributions of voxel-wise principal diffusion directions generated in *BedpostX*, each time

computing a streamline through these local samples to generate a 'probabilistic streamline' or a 'sample' from the distribution on the location of the true streamline, building up a spatial 'connectivity distribution'. Streamlines truly represent paths of minimal hindrance to diffusion of water in the brain, but they are reasonable indirect estimates of long-range white matter connections [283].

Probabilistic tractography was generated, for all responders, using the DBS activation volume as seeds and the cerebellum and contralateral hemisphere as exclusion mask. CSF termination masks were used to exclude false positive streamlines.

9.4: Results

9.4.1: Patients

Scanning and surgery proceeded with no adverse effects. The mean (SD) follow-up was 33 (14) months (median = 34 months). Six patients responded to DBS. The patient who did not respond (CH2) was also the only patient to have received ONS prior to DBS. This was removed after five years for lack of response. There was no surgical morbidity or mortality. Two patients underwent bilateral surgery making up a total of nine implanted DBS leads. **Table 9-1** shows demographics, disease duration, length of follow-up, stimulation amplitudes and change in headache load, attack severity, attack frequency and attack duration at the final follow-up point from baseline along with patient's estimated percentage of improvement after surgery.

9.4.2: Stimulation-induced adverse events

There were no serious adverse effects from DBS. Two patients developed transient dizziness, one patient developed nausea and one patient developed intermittent diplopia, all improved with adjusting stimulation amplitude. One patient (CH2) developed troublesome diplopia, oscillopsia and nystagmus with DBS amplitudes above 2 volts.

9.4.3: DBS activation volume modelling and efficacy cluster

Responders average DBS activation volume, non-responder (CH2) DBS activation volume and statistically significant cluster correlated to higher stimulation efficacy (improvement in HAL) are shown in **Figure 9-1**. The responders average activation volume lies in the ventral tegmental area in the area between the red nucleus and the mammillo-thalamic tract. The cluster predictive of improvement in HAL lies in the superior, posterior and lateral portion of the group average activation volume. The activation volume for the non-responder lies outside the efficacy cluster. See **Table 9-2** for average activation and cluster volumes with MNI coordinates

Table 9-1: Patients' demographics, disease duration, length of follow-up, stimulation amplitudes and outcome after surgery

Patient		CH1	CH2	CH3	CH4	CH5	CH6	CH7	Mean	STD	Med.
Gender		F	M	M	M	M	F	M			
Age (yr.)*		50	47	56	45	47	61	42	**50**	**7**	**47**
Duration of symptoms (yr.)*		5	21	9	4	10	16	25	**13**	**8**	**10**
Side		Right	Left	Left	Bilat.	Right	Bilat.	Left			
Length of follow-up (month)		48	34	33	48	41	14	14	**33**	**14**	**34**
HAL	**Pre. HAL**	696	756	720	967	461	520	983	**729**	**199**	**720**
	Post. HAL	70	588	0	0	18	294	146	**159**	**216**	**70**
IMP%		90	15	100	100	96	43	85	**76**	**33**	**90**
Severity (VAS)	**Pre. severity**	9	9	10	10	6	10	6	**9**	**2**	**9**
	Post. severity	7	7	0	0	4	8	6	**4**	**4**	**6**
IMP%		22	22	100	100	33	20	0	**46**	**41**	**22**
Frequency (day)	**Pre. freq.**	3	2	2	7	3	9	2	**5**	**3**	**3**
	Post. freq.	3	2	0	0	0.43	5	1	**2**	**2**	**1**
IMP%		0	0	100	100	86	44	50	**58**	**41**	**50**
Duration (min)	**Pre. duration**	180	180	180	150	120	30	300	**147**	**83**	**180**
	Post. duration	45	180	0	0	100	30	90	**53**	**60**	**45**
IMP%		75	0	100	100	17	0	70	**51**	**46**	**70**
Patient estimated IMP%		60	15	100	100	65	60	30	**66**	**31**	**60**
DBS amplitude (volt)		3.5	2.4	3	3.5	3.7	3.6	3.5	**3.3**	**0.5**	**3.5**

DBS: deep brain stimulation; STD: standard deviation; Med.: median; yr.: year; min: minute; Bilat.: bilateral; IMP%: percentage of improvement; freq.: frequency.

9.4.4: Tractography

Group average streamlines generated from individual responders DBS activation volume are shown in **Figure 9-2**. Anteriorly, the streamlines traverse the hypothalamus and then split into two pathways; an infero-lateral pathway towards the mesial temporal lobe and amygdalar complex, possibly via the amygdalofugal pathway, and an antero-superior pathway towards the prefrontal area via the anterior limb of the internal capsule. Posteriorly,

the streamlines run medial to the red nucleus towards the periaqueductal grey and then caudally through the pons and upper medulla in a dorso-lateral position towards the trigeminal tract and nuclei

Table 9-2: Group average activation volume and high efficacy cluster with MNI (AC-PC) coordinates of maximum intensity and centre of gravity (Left hemisphere)

DBS Cluster	VOL (mm^3)	Maximum intensity coordinates MNI (AC-PC)			Centre of gravity coordinates MNI (AC-PC)			p-value
		X	Y	Z	X	Y	Z	
Average responders	254	-3 (-3)	-13 (-2)	-8 (-3)	-4 (-4)	-12 (-1)	-8 (-3)	-
Maximum efficacy	14	-6 (-6)	-13 (-2)	-6 (-1)	-4 (-4)	-12 (-1)	-5 (0)	<0.001

MNI: Montreal Neurological Institute; AC-PC: anterior commissure – posterior commissure; VOL: volume. AC-PC coordinates are in relation to mid-commissural point

Figure 9-1: Average DBS activation volume (green) with DBS efficacy cluster (red) and activation volume for the non-responder (blue)

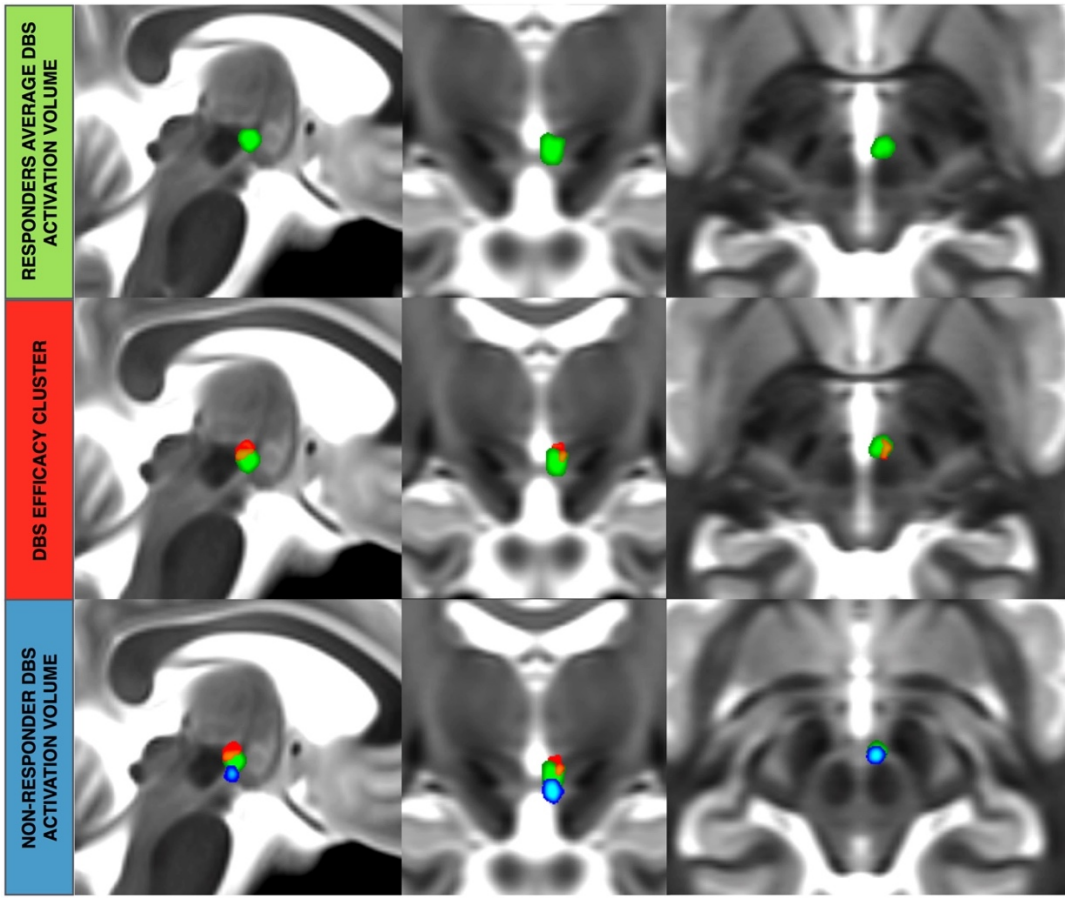

Figure 9-2: Group average probabilistic tractography streamlines (red-yellow) with group average DBS tissue activation volume (green)

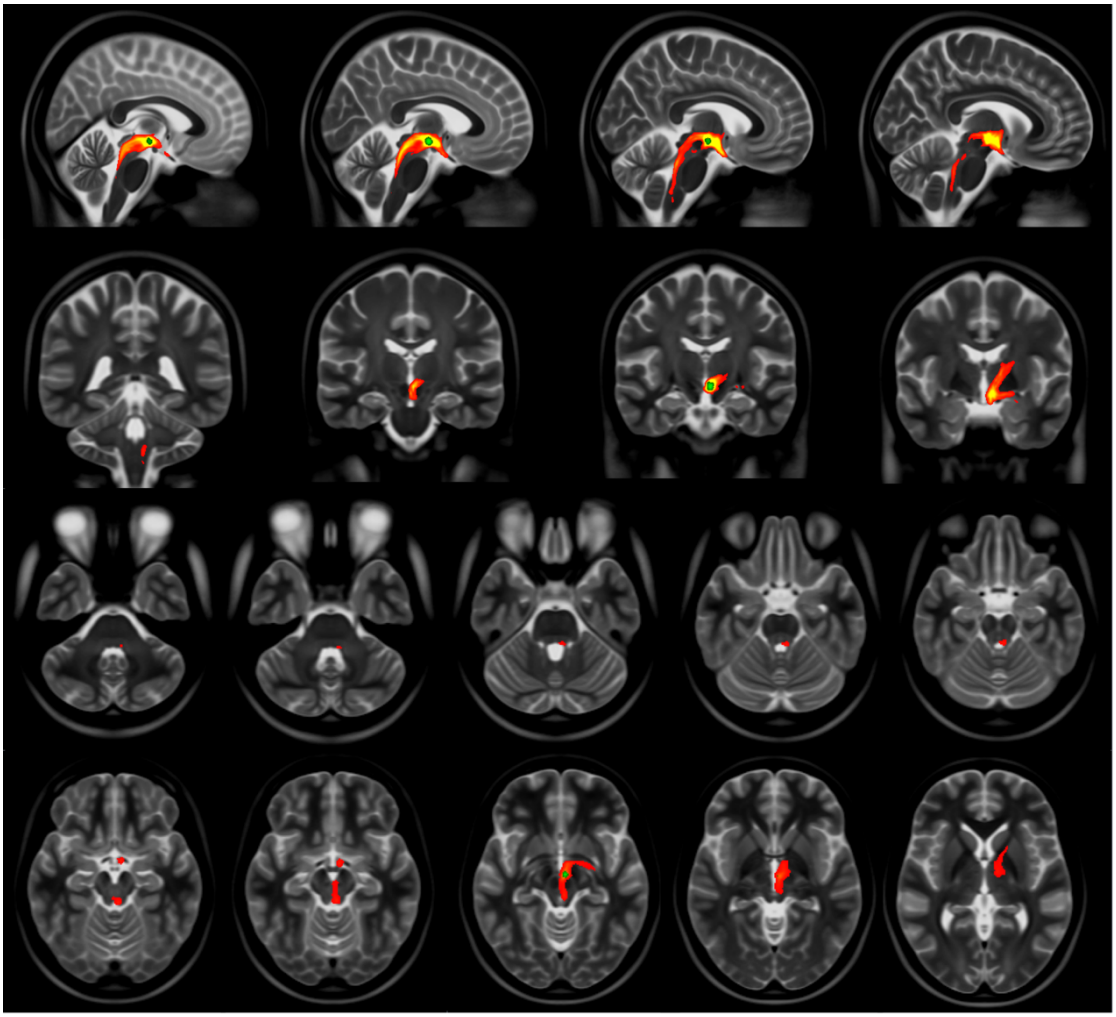

9.5: Discussion

Voxel based statistical analysis of active DBS contacts activation volumes, at the last follow-up point after VTa DBS was used in 7 patients with medically refractory chronic cluster headache to identify a statistically significant cluster in the stimulation area, reflecting the highest efficacy zone. The responders' activation volumes (six patients, eight DBS contacts) were also used to generate probabilistic tractography streamlines to identify the trigemino-hypothalamic tract.

We show that patients were appropriately selected **(Table 9-1)** as demonstrated in disease duration and headache characteristics. Furthermore, six out of seven patients had indeed responded well to DBS as demonstrated by the improvement in headache load, duration, frequency and severity.

9.5.1: Optimal VTa stimulation site

The first patient [123] and patient series [124] to undergo DBS for CCH, had the target in what was termed the hypothalamic grey. The target came to light after a positron emission tomography (PET) study found increased activation in this area in CH patients during attacks [121]. The target in this area, which we identify as the VTa, is not readily demarcated. This is due to three factors; firstly, the target has to be identified using surrounding landmarks on MRI (e.g. the red nucleus, the mammillothalamic tract); secondly, the stimulation amplitude (an average of 3.3 volts in this study) covers a comparatively large brain tissue area around the active DBS contact, hence allowing some leeway in targeting accuracy; and thirdly, PET studies are subject to misalignment during the co-registration process, potentially introducing a spatial error [467]. This has been reflected in the discrepancy in the reported coordinates of activation with another PET study [468] and with a functional MRI study [469].

The original target's coordinates were 2 mm lateral to the midline, 6 mm behind the mid-commissural point (MCP) and 8 mm below the AC-PC [123]. This is the same area identified in an earlier PET study [121]. The target was then modified to 2 mm lateral to the midline, 3 mm posterior and 5 mm below the MCP [124]. This last "Franzini" target has been generally adopted in the other surgical series [422,438,470].

A study of ten patients with CCH implanted with unilateral DBS leads using Franzini's target employed postoperative AC-PC coordinates of the active DBS contact centres, projected on the Schaltenbrand atlas [262] and a three-dimensional 4.7 Tesla MRI atlas of the diencephalon-mesencephalic junction atlas to identify the anatomical location of the effective DBS electrodes [422]. Five patients responded to treatment. The mean coordinates of the active contacts in the responders were 3 mm lateral, 3.5 mm posterior and 3.3 mm below the MCP. The study, however, did not find a statistically significant difference between the responder and non-responder groups. The authors pointed out the limitation from the method used to localize the contacts, i.e. projection of AC–PC coordinates on

atlases [422]. These coordinates are within 1.5 mm from the co-ordinates of the average volume of DBS activation (maximum intensity point) in the responders in our study.

Our voxel based morphometry, regression analysis shows the coordinates of the higher efficacy predictive cluster (maximum intensity point) to be further lateral and superior (6 mm lateral, 2 mm posterior and 1 mm inferior to the MCP). This seems to be supported by the relation of the DBS activation volume of the single non-responder in our study to the efficacy cluster lying outside it as shown in **Figure 9-1**.

9.5.2: Tractography of the trigemino-hypothalamic pathway (THT)

The difficulty in explaining the mechanism of action of DBS in CH is partly caused by the lack of a definitive understanding of the pathophysiological process itself [471,472]. Some authors suggest that simple local blockade of the 'posterior hypothalamic grey' or VTa activity is not a likely mechanism for improvement in headache. However, many patients experience a micro-lesion or "stun" effect with complete abolition of attacks for a few days or even weeks following DBS lead implantation alone, suggesting disruption of pathological neural activity in the region [448,455,471]. However, this does not explain the latency in achieving maximal DBS efficacy that has been seen across several studies, including our own. Increased threshold for cold pain at the site of the first trigeminal branch ipsilateral to the stimulated side in chronically stimulated patients could be caused by modulation of the anti-nociceptive system [473], however; a generic anti-nociceptive effect does not explain why DBS is effective for the trigeminal autonomic cephalalgias but not "atypical facial pain" [455,471,472,474]. DBS has been shown to modulate a complex network of pain-processing areas [417]. Stimulation induced local activation around the active DBS contact as well as distant activation in the ipsilateral thalamus, somatosensory cortex and precuneus, the anterior cingulate cortex and the ipsilateral trigeminal nucleus and ganglion; coupled with deactivation in the middle temporal gyrus, posterior cingulate cortex, inferior temporal gyrus bilaterally and contralateral anterior insula [417]. This study was the first to document a functional connection between the hypothalamus and the trigeminal system in human beings in vivo. The activation in the trigeminal system however does not seem to provoke

CH pain attacks or the typical sensations that commonly accompany trigeminal activation [417]. This connection has been previously observed following injection of the neuropeptide orexin B into the 'posterior hypothalamic region' of the rat which increased spontaneous activity in the caudal trigeminal nucleus (with discharges persisting for several minutes) and heightened responses in the nucleus to dural stimulation and noxious thermal stimulation of the face. [466]

The connection between the trigeminal system and the hypothalamus is crucial in integrating somatosensory and visceral information (e.g. innervation from cranial skin, intracranial blood vessels, and meninges) with endocrine and autonomic responses [465]. Single-unit recording and antidromic microstimulation techniques in rats have established a direct two-way connection between the posterior hypothalamus and the spinal trigeminal nucleus through the THT [465].

Other brainstem nuclei have neurons that respond to noxious and innocuous somatosensory and visceral stimulation [475-479]. These nuclei also give efferents to the hypothalamus, such as the parabrachial nuclei [480-482], nucleus of the solitary tract [483,484], periaqueductal gray [485-488], and caudal ventrolateral medulla [489,490] suggesting that somatosensory signals reach the hypothalamus through several polysynaptic pathways [465].

Previous work has explored the structural connectivity of the DBS target using probabilistic tractography in healthy controls[491]. Comparable connections to the frontal and temporal areas were described alongside connections to the periaqueductal grey. At the time, image acquisition parameters were not sufficient for accurate tracking in the brainstem which we present here.

Our tractography results show that the DBS activated area, posterior to the hypothalamus, in the ventral tegmentum lies on a tract that connects the hypothalamus, prefrontal and mesial temporal regions anteriorly with brainstem areas in the proximity of the parabrachial nuclei, nucleus of the solitary tract, periaqueductal grey and ending in the region of the trigeminal nucleus and tract and the superior salivatory nucleus (SSN) **(Figures 9-2 and 9-3)**.

Although this finding does not explain the mechanism of action of DBS, it confirms the relevance of the target site by means of its connections to anatomically relevant brainstem areas. One possibility is by exerting a top-down anti-nociceptive effect, while another possibility, is by modulation of the trigeminal parasympathetic reflex, commonly activated in primary headache disorders [492] and is thought to mediate the cranial autonomic symptoms in CH [493]. This pathway can be triggered by hypodermic capsaicin injection in the first trigeminal nerve division area [494] as well as a variety of trigeminal nociceptive triggers [472]. Nociceptive trigeminal activation, in the first division of the trigeminal nerve, is relayed into the spinal trigeminal nucleus and the C1/C2 dorsal horns (i.e. the trigemino-cervical complex or TCC) [495] which has a reflex connection to the SSN in the pons [496]. The output is then carried via the parasympathetic pathway of the facial nerve, through the geniculate ganglion within the greater superficial petrosal nerve [497] to the sphenopalatine ganglion (SPG) [472,498].

It must be noted however, that the pain and the autonomic phenomenon can at times occur independently [461] especially in patients taking preventive medications, suggesting either anatomically separate pathways albeit partly, or different activation thresholds mediating these two features [400,498]

9.5.3: The use of improvement in HAL as a determinant of treatment response

The International Headache Society guidelines for cluster headache clinical trials advocate a reduction of 50% in headache frequency as a marker for treatment response [499]. Though we present change in headache frequency, severity and duration following treatment as suggested by these guidelines; it is our experience that patients who achieve a significant improvement in only one of the variables can be extremely satisfied with the therapy provided. For example, a patient with 6 attacks of one-hour duration per day with severity of 8/10 who, after DBS, then experiences 5 attacks of one-hour per day with a 2/10 severity will not be a responder in terms of headache frequency but is certainly a responder in terms of headache load and quality of life. Within this group we have had patients who had >30% response in terms of headache load but <50% response to headache frequency who were,

nevertheless, very pleased with the improvement in their symptoms. We have therefore opted to use the reduction in HAL as the marker for treatment response as we have done so in a previous publication [448]

Figure 9-3: Illustration showing two cross-sections in the pons at the level of the trigeminal nerve, main sensory and mesencephalic trigeminal nuclei (top); and spinal trigeminal nucleus and tract, superior salivatory nucleus and solitary tract (bottom)

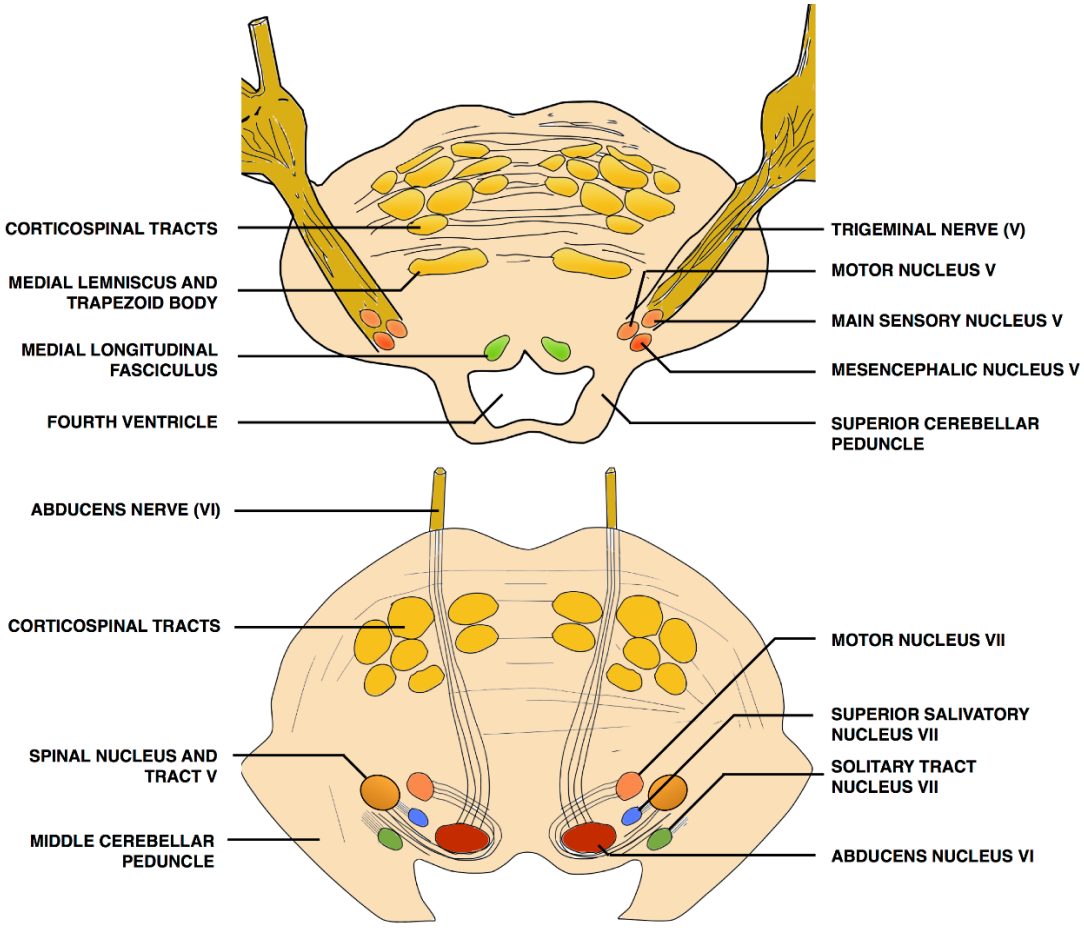

9.5.4: Limitations

The principal weakness in this study is the small number of patients. Cluster headache is an orphan condition with a prevalence of 0.1-0.2%, with only 10-15% of sufferers developing the chronic form, a small minority of which will be refractory to medical therapies and hence qualify for neuromodulation [400-404]. This explains the reason the number of patients treated with DBS in the literature remains in double digits [448]. As a result of the small population in our study, we identified a single non-responder in keeping with our

published failure rate of 19% [448]. This patient had also failed to respond to ONS which raises the possibility of other unidentified disease factors related to failure as opposed to DBS active contact location. Unfortunately, this does not allow a two group statistical analysis of the tractography results, however, the single group regression analysis we carried out was able to identify the voxels that predict the highest improvements in HAL.

The limitations of the VTA model used in this study and the rationale behind using this model have been described in chapter 2 (2.10.4). A further limitation is due to inherent diffusion MRI imperfections. In vivo tractography studies in the brainstem carry significant challenges. Motion artefacts, as a result of the highly pulsatile nature of the region, can degrade the MRI signal during diffusion image acquisition, reducing the signal-to-noise ratio (SNR). This is complicated by the presence of myriads of criss-crossing axons and reticular brain regions [104,105]. One way of dealing with this is by using pulse-gating and respiratory rate monitoring during diffusion imaging. Likewise, by acquiring multiple diffusion scans, at a high angular resolution (increasing acquisition time), SNR is improved [91,103].

In this study, 270 diffusion scans per patient (in 2 × 128 directions sets) were acquired over 62 minutes. We meticulously and systematically corrected artefacts and examined the processed imaging data for quality control. We modelled three crossing fibres per voxel and used probabilistic tractography to ameliorate the crossing fibre problem. Further improvements in diffusion imaging, owing to higher spatial and angular resolution, better MRI gradients and shorter acquisition times with emergence of multi-band acquisition will add to the value of this modality [102,283].

By employing multiple registration steps, we have introduced error to the system. Nonetheless, we meticulously inspected registration accuracy at each step to alleviate the impact of this issue. Prior to carrying out the VBM cluster analysis, we lateralized the right sided DBS contacts to the left. This is an approach commonly used in imaging studies, however, it assumes no functional / structural differences between the left and right hemispheres, in the regions of interest at the least.

Lastly, the relatively long scan duration is a drawback. This was chosen to achieve the SNR and resolution needed, however, since the conduction of this study, novel MRI acquisition techniques, such as Simultaneous Multi-Slice Imaging and Multi-Band Imaging [303] have been developed which allow a similar protocol to be run within half the time without compromising the SNR.

Despite these caveats and drawbacks, the methodology used has confirmed anatomical connections that have been implicated in the pathophysiology of cluster headache.

9.6: Conclusion

Following VTa-DBS in patients with medically refractory chronic cluster headache, the largest reduction in headache load appears to correspond to activation in an area 6 mm lateral, 2 mm posterior and 1 mm inferior to the MCP. Active contact DBS activation in responders lies on the trigemino-hypothalamic tract, connecting the trigeminal system and other brainstem nuclei linked with nociception and pain modulation with the hypothalamus, prefrontal and mesial temporal areas.

10. General Discussion

10.1: Contributions to the field of functional neurosurgery

This thesis presents a study into the application of MRI connectivity in the field of functional neurosurgery. The methods and models used, albeit in selected patient groups undergoing DBS surgery, could be applied to other patient groups. This will help refine targeting, build predictive models of treatment and map out the underlying brain networks to better understand the mechanism of action of DBS. This is not restricted to patients undergoing DBS but includes ablative stereotactic procedures.

10.1.1: Connectivity in Parkinson's Disease

In this chapter, we explored the applications of functional connectivity, structural connectivity and neurophysiology (EMG) to build predictive models of response to L-DOPA and STN-DBS. We also mapped out hyperdirect pathways and explored their influence on efficacy. Understanding the relationship between the functional connectivity and clinical effects of dopamine helps shed light on the disease process in the advanced stage. We inferred that networks linked to cognitive (proactive) motor inhibition show relatively higher connectivity whilst networks linked to reactive motor inhibition show lower connectivity with better dopamine response. Furthermore, connectivity was relatively stronger in between basal ganglia structures with better dopamine response. Future studies may be able to validate these results and explore markers at the 'individual level' by employing machine learning algorithms to build predictive models of response to treatment, thus validating, or even corroborating the L-DOPA challenge test. This could potentially aid with patient selection and help with understanding the mechanism of action of DBS.

We identified in the second experiment the optimal STN deep brain stimulation site for patients with Parkinson's disease for tremor, bradykinesia and rigidity. These appeared to correspond to different (though closely related) areas in the motor STN. Stimulation in the

central portion of the superior STN was most effective for tremor, whilst stimulation in further medial and posterior areas, within the superior portion, gave highest improvements in bradykinesia and rigidity. These areas, although distinct, could readily be targeted with a single DBS electrode. The findings should, however, help refine the targeting strategies. We showed that DBS-cortical connectivity, along the hyperdirect pathways, to M1 was predictive of maximum improvement in tremor, to SMA was predictive of maximum improvement in bradykinesia and to both SMA and PFC was predictive of maximum improvement in rigidity. This revealed the diffuse cortical involvement in DBS for PD. Future developments, especially in the field of adaptive stimulation [500,501] will benefit from this understanding.

We used DBS volume of tissue activation models in this thesis. The overlap between the models and corticospinal tracts identified on tractography correlated well with EMG findings. Despite the limitations of said models, we showed that they can be validated using a multimodal imaging-neurophysiology approach. This spread of current compromises increase in stimulation strengths and is related to the development of speech disturbances with chronic stimulation. Furthermore, we proposed that EMG may be used to detect such current spread and may thus represent a valuable tool in troubleshooting in PD patients treated with STN DBS.

10.1.2: Connectivity in Tremor

Probabilistic tractography techniques were successfully used to segment the VL and VP thalamus based on cortical and cerebellar connectivity. The thalamic area, best representing the VIM, was connected to the contralateral dentate cerebellar nucleus. Connectivity based segmentation of the VIM were achieved in individual patients in a clinically feasible timescale, using HARDI and high performance computing with parallel GPU processing. This same technique can map out the DRTC tract with clear mesencephalic crossing. Future studies may focus on improving data acquisition and processing time; and apply this technique prospectively in patients undergoing thalamic DBS or lesioning for tremor.

10.1.3: DBS of Trigeminal Autonomic Cephalalgias and Connectivity in Cluster Headache

In this chapter, we first established the safety and efficacy of DBS in the ventral tegmental area (VTa) for two trigeminal autonomic cephalalgias (TAC) entities; chronic cluster headache and SUNA. We also noted positive effects of DBS for CCH on patient-reported quality of life, disability and mood.

Following from this, we strived to elucidate the optimum target for stimulation and the involved network. Active contact DBS activation in responders lay on the trigemino-hypothalamic tract, connecting the trigeminal system and other brainstem nuclei linked with nociception and pain modulation with the hypothalamus, prefrontal and mesial temporal areas. This is a novel finding that helps us in understanding the mechanism of action of VTa-DBS as well as in shedding a light on the pathophysiology of CH and possibly other TACs.

10.2: Limitations of the thesis

This thesis draws upon several experimental methodologies and patient groups to explore the application of connectivity studies in functional neurosurgery. There are numerous limitations and caveats to these methodologies, each discussed in the relevant chapters. One conspicuous issue is that of reproducibility. In contrast to studies that explore a therapeutic intervention, whether pharmacological or surgical where the treatment can often be standardised and verified; connectivity imaging studies are inherently difficult to reproduce. This is attributed to the plethora of MRI acquisition and processing techniques. Furthermore, by employing multiple registration steps, errors are introduced to the system. Nonetheless; meticulous confirmation of registration accuracy at each step can alleviate the impact of this issue.

In this thesis, we used state of the art MRI sequences to achieve the spatial resolution and SNR necessary to run the experiments. Unfortunately, this meant that the acquisition time was rather lengthy. This poses difficulties for many patients undergoing DBS surgery, mainly those undergoing surgery for movement disorders. The patients who participated in

the studies here were all very carefully selected and vetted before recruitment. Despite all of this, a small number could not tolerate the lengthy imaging protocol and the scan was therefore abandoned. This may be acceptable in group studies aiming to explore pathophysiological models but not in clinical applications in individual patients. Novel MRI acquisition techniques, such as Simultaneous Multi-Slice Imaging and Multi-Band Imaging [303], have been developed since the commencement of this work that will allow future studies to run similar protocols within half the time without compromising the SNR.

Another limitation is the use of a patient specific, finite element model to create DBS volumes of tissue activated [143]. This is a simplified linear model that does not account for local impedance inhomogeneity. While it is important that efforts are put into improving models of DBS to resemble reality as much as possible, it may not help to add details to a rough model when the basic knowledge of the DBS mechanisms of actions are still debated. Indeed, various models over- or under-estimate the VTA [142]. The presence of axons of different diameters and cell bodies, with variable action-potential thresholds, in the DBS region, complicates matters further. Other justification for not using a more ***complex*** model is the fact that minute variations in VTAs are unlikely to have a large effect on statistical analysis and tractography results, due to the relatively coarse spatial resolution of our structural and diffusion MRI data. Lastly, the package used to generate the VTAs is not yet commercially available. This make reproducing these models, albeit theoretically, difficult. With time, the software mentioned is likely to be mainstream, alleviating this problem.

There are also limitations associated with some of the techniques used, especially functional connectivity, which is largely limited to group-level analysis. While this is useful in exploring group-wise changes, inferences on the individual level cannot be readily made, especially on a diagnostic/predictive capacity. This may limit the clinical application of the technique in individual patients.

Lastly, one of the principal weakness in this thesis is the relatively small number of patients and the mixed aetiologies. Some of the disorders included orphan conditions (CH

prevalence is 0.1-0.2%, with only 10-15% of sufferers developing the chronic form, a small minority of which will be refractory to medical therapies and hence qualify for neuromodulation [400-404]). This makes recruitment rather difficult. Additionally, to achieve the required postoperative follow-up period prior to carrying out the analysis, limited recruitment is possible in the time span of a PhD project.

10.3: Future challenges

10.3.1: Standardisation of methods

Method standardisation is by far the biggest challenge facing the field. Diffusion data are noisy and the sequences are highly variable and configurable. Moreover, data analysis is based on statistics and has many options and alternatives with more than one "right" way (but many wrong ways) of analysis [80]. This, combined with the relative paucity of patients undergoing connectivity studies and functional neurosurgery, makes it essential rather than desirable to have standardized imaging paradigms and processing in order to reproduce and validate the results of these studies.

10.3.2: Quantification of connectivity (functional and structural)

A real challenge in connectivity studies, especially in measuring grey matter connectivity, is coming up with a quantifiable measure of connectivity [102]. We proposed a connectivity index in **chapter 4** using normalised streamline count. This is by no means a perfect solution. Tractography has many biases and can result in false positive/ negative tracts. It is also affected by crossing fibres, distance, size of seed/ target masks and the straightness/ curvature of the streamlines.

10.3.3: DBS volume of tissue activation

This is certainly a challenging area that will require further development. The available models including the one used in this thesis are oversimplified and often do not consider inhomogeneity in local impedance [502]. Improving the existing models cannot, however, rely only on improving the mathematical model as it depends on a better understanding of the

mechanism of action of DBS therapy itself [162]. It is likely that the emergence of more 'steered' stimulation with directional electrodes will enrich the available models by providing more specific efficacy and side-effect data to correlate with virtual stimulation models. We attempted to verify the finite element VTA model used in this thesis in **chapter 9**.

10.3.4: Clinical applications in functional neurosurgery

The next step, and indeed the ultimate aim of this work is to use the proposed methods in clinical practice. Some of the challenges that this poses are related to multimodal image fusion and integration within commercially available neuronavigation and targeting packages. We have presented an example of integrating tractography data (segmented VIM) within Renishaw's Neuroinspire package in **chapter 6**. Improved image fusion and coregistration is essential, especially when spatial distortion must be kept at a minimum in stereotactic surgery. This will be achieved with improved diffusion and BOLD data noise and artifact, amalgamated with better distortion correction and coregistration algorithms. Improving structural MRI data will also help better segment deep brain structures (e.g. the STN). This will help focus registration, as well as reducing observer error in manual segmentation in group studies **(Chapter 4 and 5)**. Acquiring 'stereotactic' diffusion and fMRI data in the future, with newly developed MR safe frames is bound to improve spatial accuracy by improving co-registration. The newest iteration of the Leksell frame is 3T MRI safe. The frame is made from plastic resin and therefore does not cause artifact with EPI sequences. As surgery is increasingly performed under general anaesthesia, stereotactic diffusion/ fMRI data could be acquired at the same time as stereotactic planning MRI and instantaneously processed and integrated with structural imaging to aid with targeting (e.g. VIM DBS for tremor).

10.4: Future developments

Perhaps the biggest development in the field of brain connectivity will come from the completion of the Human Connectome Project next year [117,503]. The 5-year project has set

out to provide data and analysis pipelines of very high quality to map the macroscopic brain connections and their variability in healthy adults for a large population of 1,200 subjects. By doing so, the findings will provide a frame of reference for future studies on pathological brains, not to mention new standards in image acquisition and connectivity processing.

Other developments are certain to arise from the continuous progress in MRI, which may be improvements in structural, diffusion or functional imaging. Higher spatial resolution and SNR with shorter acquisition times are bound to provide better data and applicability in clinical settings. There has been already a big stride forward with Simultaneous Multi-Slice Imaging and Multi-Band Imaging techniques [303]. Since the completion of the experiments in this thesis, the Siemens Trio 3T MRI scanner used has been upgraded to a Siemens Magnetom Prisma 3T MRI scanner with upgraded gradient magnets. We have tested Multi-Band diffusion MRI sequences utilising three and two bands along with single band acquisitions on both the Prisma and the Trio (used in this thesis). The sequences had the same imaging parameters. It seemed appropriate that the subject whose brain was studied was the writer. The three-band (3B) sequence took only 15 minutes to acquire, the two-band sequence (2B) took 30 minutes whilst the single band (1B) took 45 minutes on the Prisma. These times compare favourably with the 61 minute (1B) acquisition time on the Trio. Three fibre modelling was achieved as per standard methodology described in this thesis, the results of which are shown in **Figure 10-1.**

Perhaps not surprisingly the best SNR and quality of crossing fibre modelling was seen in the 1B scan on the Prisma. Nevertheless, the 2B scan, which took only 30 minutes, was visually comparable, if not of better quality than the 1B scan on the Trio scanner **(Figure 10-1).**

Machine learning and artificial intelligence (AI) are likely to change the way multimodal data are analysed in the future [504]. Multivariate pattern analysis of neuroimaging data achieves increased sensitivity in detecting spatially distributed effects not usually detected by univariate analysis [504]. Using machine learning algorithms will allow for the use of data from group studies (such as in **chapter 3.1**) to apply to individual datasets. This can significantly

increase the clinical applicability of connectivity studies, which often require large groups to overcome biases from the spatial reconstruction of connections resulting in false positive and/ or false negative results [102,283].

Another important development will come from further advances in computational power and GPU parallel processing techniques. This has already led to a substantial reductions in big dataset processing time (as demonstrated in this thesis), allowing the use of connectivity studies in clinical settings [160].

Figure 10-1: Diffusion MRI acquisitions at 3B, 2B and 1B (Trio - Prisma) along with preprocessed images

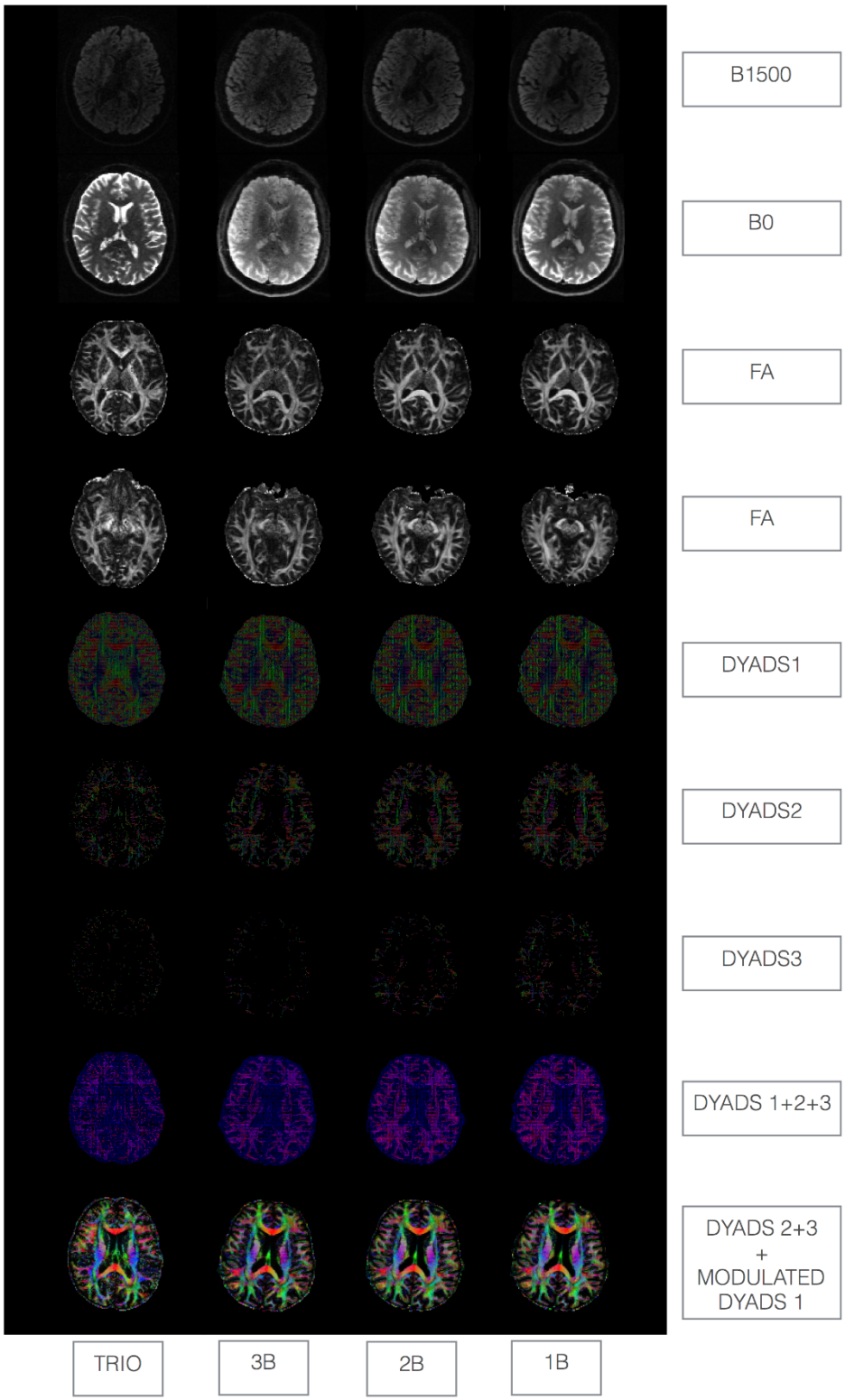

FA: fractional anisotropy; DYADS: distribution of mean diffusion direction vector (1 = principal, 2 = secondary and 3 = tertiary); B: band

10.5: Conclusions

Progress in functional neurosurgery has been inextricably linked to progress in neuroimaging techniques. Advances in MRI have made it possible to directly target deep brain structures with DBS or ablative surgery and confirm the result as well as improve safety. The use of advanced MRI connectivity studies take our understanding of brain networks to the next level and provide us with new tools to refine targeting and patient selection, as well as to better understand the treatment mechanisms of action and disease pathophysiology.

The use of these techniques should come with caution. Heavy reliance on complex statistical methods and variability in image acquisition and analysis pose real challenges. Clinicians delving into this world ought to have a good understanding of the science and the methods in order to achieve accurate results and meaningful outcomes. Doing otherwise will not only result in erroneous interpretations of the data thus potentially harming patients, but can also cause harm to the reliability of the techniques themselves, jeopardising progress in this exciting field.

"Concern for man and his fate must always form the chief interest of all technical endeavors. Never forget this in the midst of your diagrams and equations."

Albert Einstein (1879 – 1955)

Appendix 1:

MRI acquisition parameters

DIFFUSION IMAGE ACQUISITION			
Coil	32 Ch T&R	Reference Scan Mode	single-shot EPI
Voxel size	1.5×1.5×1.5 mm	Distortion Corr.	Off
TA	04:41	Prescan Normalize	Off
Slices	85	Raw filter	Off
Dist. factor	0%	Elliptical filter	Off
Position	L4.0 A11.0 F25.7	Hamming	Off
Orientation	T > C-8.2 > S-1.5	Coil Combine Mode	Adaptive Combine
Phase enc. dir.	R >> L (6) + L >> R (6)	Auto Coil Select	Default
Rotation	90.00 / -90.00 deg	Shim mode	Standard
Phase oversampling	0%	? Ref. amplitude 1H	0.000 V
FoV read	219 mm	Adjustment Tolerance	Auto
FoV phase	80.8%	**Physio**	
Slice thickness	1.5 mm	1st Signal/Mode	None
TR	12200 ms	PMU Recording	off
TE	99.6 ms	Resp. control	Off
Averages	1	**Diff**	
Concatenations	1	Diffusion mode	Free
Filter	None	Diff. weightings	1
Coil elements	HEA;HEP	b-value	1500 s/mm²
Contrast		Diff. weighted images	On
MTC	Off	Trace weighted images	On
Magn. preparation	None	Average ADC maps	On
Fat suppr.	Fat sat.	Individual ADC maps	On
Extra Fat Suppr.	on	FA maps	On
Saturation Mode	standard	Mosaic	On
Averaging mode	Long term	Tensor	On
Reconstruction	Magnitude	Noise level	40
Delay in TR	0 ms	Diff. directions	270 (14 B0)
Multiple series	Off	**Sequence**	
Resolution		Introduction	Off
Base resolution	146	Bandwidth	1426 Hz/Px
Phase resolution	100%	Optimization	None
Phase partial Fourier	6/8	Free echo spacing	On
Interpolation	Off	Echo spacing	0.89 ms
PAT mode	GRAPPA	EPI factor	118
Accel. factor PE	2	RF pulse type	Normal
Ref. lines PE	30	Gradient mode	Fast*
Matrix Coil Mode	Auto (Triple)	Add. FFT Scale Factor	1.0

B1 IMAGE ACQUISITION			
TA	03:00	Matrix Coil Mode	Auto (Triple)
Voxel size	4.0×4.0×4.0 mm	Reference scan mode	Separate
Slabs	1	Image Filter	Off
Position	L3.0 A18.5 F41.4	Distortion Corr.	Off
Orientation	Transversal	Prescan Normalize	Off
Phase enc. dir.	R >> L	Normalize	Off
Rotation	90.00 deg	B1 filter	Off
Phase oversampling	0%	Raw filter	Off
Slice oversampling	0%	Elliptical filter	Off
Slices per slab	48	Coil Combine Mode	Sum of Squares
FoV read	256 mm	Auto Coil Select	Default
FoV phase	75.00%	Shim mode	Standard
Slice thickness	4.0 mm	Adjust with body coil	Off
TR	500.00 ms	Assume Silicone	Off
TE 1	39.06 ms	? Ref. amplitude 1H	0.000 V
TE 2	19.53 ms	Adjustment Tolerance	Auto
Concatenations	1	**Sequence**	
Filter	None	Dimension	3D
Coil elements	HEA;HEP	Contrasts	2
Contrast		Bandwidth	2298 Hz/Px
Fat suppr.	Fat sat.	RF spoiling	Off
Reconstruction	Magnitude	Refoc. Corr	6.0 [%]
Measurements	11	Scale s. gradient	15.0 [%]
Resolution		Mixing time	33800 [us]
Base resolution	64	Max refoc. angle	230 [deg]
Phase resolution	100%	Dec refoc. angle	10 [deg]
Slice resolution	100%	Flip angle for ref scans	230 [deg]
Phase partial Fourier	Off	Dur per 5 degrees	140 [us]
PAT mode	GRAPPA	BWT SE/STE factor	6 [us]
Accel. factor PE	2	No dummy scans	0
Ref. lines PE	48	RF spoil incr.	50.0 [deg]
Accel. factor 3D	2	Crushers permutation	On
Ref. lines 3D	48	Optimized RF duration	On

GRADIENT FIELD MAPPING ACQUISITION			
TA	02:14	**Resolution**	
Voxel size	3.0×3.0×2.0 mm	Base resolution	64
Slices	64	Phase resolution	100%
Dist. factor	50%	Phase partial Fourier	Off
Position	L3.0 A9.2 F41.4	Interpolation	Off
Orientation	Transversal	Matrix Coil Mode	Auto (CP)
Phase enc. dir.	R >> L	Image Filter	Off
Rotation	90.00 deg	Distortion Corr.	Off
Phase oversampling	0%	Prescan Normalize	Off
FoV read	192 mm	Normalize	Off
FoV phase	100.00%	B1 filter	Off
Slice thickness	2.0 mm	Raw filter	Off
TR	1020 ms	Elliptical filter	Off
TE 1	10.00 ms	Shim mode	Standard
TE 2	12.46 ms	Adjust with body coil	Off
Averages	1	Assume Silicone	Off
Concatenations	1	? Ref. amplitude 1H	0.000 V
Filter	None	Adjustment Tolerance	Auto
Coil elements	HEA;HEP	**Sequence**	
Contrast		Introduction	On
MTC	Off	Dimension	2D
Flip angle	90 deg	Asymmetric echo	Off
Fat suppr.	None	Contrasts	2
Averaging mode	Long term	Bandwidth	260 Hz/Px
Reconstruction	Magn./Phase	Flow comp.	Yes
Measurements	1	RF pulse type	Normal
Multiple series	Off	Gradient mode	Fast
		RF spoiling	On

MT IMAGE ACQUISITION			
TA	07:00	Ref. lines PE	18
Voxel size	1.0×1.0×1.0 mm	Accel. factor 3D	1
Slabs	1	Matrix Coil Mode	Auto (Triple)
Position	L3.4 A24.0 F52.3	Reference scan mode	Integrated
Orientation	Sagittal	Image Filter	Off
Phase enc. dir.	A >> P	Distortion Corr.	Off
Rotation	0.00 deg	Prescan Normalize	Off
Slice oversampling	0.00%	Normalize	Off
Slices per slab	176	B1 filter	Off
FoV read	256 mm	Raw filter	Off
FoV phase	93.80%	Elliptical filter	Off
Slice thickness	1.00 mm	Shim mode	Standard
TR	24.50 ms	Adjust with body coil	Off
TE 1	2.34 ms	Assume Silicone	Off
TE 2	4.68 ms	? Ref. amplitude 1H	0.000 V
TE 3	7.02 ms	Adjustment Tolerance	Auto
TE 4	9.36 ms	**Sequence**	
TE 5	11.70 ms	Dimension	3D
TE 6	14.04 ms	Contrasts	6
Concatenations	1	Bandwidth	465 Hz/Px
Filter	None	RF spoiling	On
Coil elements	HEA;HEP	MT repetition factor	1
Contrast		FA Gaussian	220 [deg]
MTC	On	Duration Gaussian	4000 [us]
Flip angle	6 deg	Off-resonance Gaussian]	2000 [Hz
Reconstruction	Magn./Phase	Flat Top MT spoiler	1000 [us]
Resolution		Dur. Prew. Ramp	150 [us]
Base resolution	256	Dur. Prew. Flat	600 [us]
Phase resolution	100%	Dur. RO Ramp	80 [us]
Slice resolution	100%	RF spoil incr.	137.0 [deg]
Phase partial Fourier	Off	RF excitation	Sinc (non-sel.)
Slice partial Fourier	6/8	Rec: fixed duration	30 [us]
PAT mode	GRAPPA	Sinc: fixed duration	160 [us]
Accel. factor PE	2	BWT of sinc	6 [int]

PROTON DENSITY IMAGE ACQUISITION			
TA	07:00	Accel. factor PE	2
Voxel size	1.0×1.0×1.0 mm	Ref. lines PE	18
Slabs	1	Accel. factor 3D	1
Position	L3.4 A24.0 F52.3	Matrix Coil Mode	Auto (Triple)
Orientation	Sagittal	Reference scan mode	Integrated
Phase enc. dir.	A >> P	Image Filter	Off
Rotation	0.00 deg	Distortion Corr.	Off
Slice oversampling	0.00%	Prescan Normalize	Off
Slices per slab	176	Normalize	Off
FoV read	256 mm	B1 filter	Off
FoV phase	93.80%	Raw filter	Off
Slice thickness	1.00 mm	Elliptical filter	Off
TR	24.50 ms	Shim mode	Standard
TE 1	2.34 ms	Adjust with body coil	Off
TE 2	4.68 ms	Assume Silicone	Off
TE 3	7.02 ms	? Ref. amplitude 1H	0.000 V
TE 4	9.36 ms	Adjustment Tolerance	Auto
TE 5	11.70 ms	**Sequence**	
TE 6	14.04 ms	Dimension	3D
TE 7	16.38 ms	Contrasts	8
TE 8	18.72 ms	Bandwidth	465 Hz/Px
Concatenations	1	RF spoiling	On
Filter	None	MT repetition factor	1
Coil elements	HEA;HEP	FA Gaussian	220 [deg]
Contrast		Duration Gaussian	4000 [us]
MTC	Off	Off-resonance Gaussian	2000 [Hz]
Flip angle	6 deg	Flat Top MT spoiler	1000 [us]
Reconstruction	Magn./Phase	Dur. Prew. Ramp	150 [us]
Resolution		Dur. Prew. Flat	600 [us]
Base resolution	256	Dur. RO Ramp	80 [us]
Phase resolution	100%	RF spoil incr.	137.0 [deg]
Slice resolution	100%	RF excitation	Sinc (non-sel.)
Phase partial Fourier	Off	Rec: fixed duration	30 [us]
Slice partial Fourier	6/8	Sinc: fixed duration	160 [us]
PAT mode	GRAPPA	BWT of sinc	6 [int]

T1 IMAGE ACQUISITION			
TA	07:00	Accel. factor PE	2
Voxel size	1.0×1.0×1.0 mm	Ref. lines PE	18
Routine		Accel. factor 3D	1
Slabs	1	Matrix Coil Mode	Auto (Triple)
Position	L3.4 A24.0 F52.3	Reference scan mode	Integrated
Orientation	Sagittal	Image Filter	Off
Phase enc. dir.	A >> P	Distortion Corr.	Off
Rotation	0.00 deg	Prescan Normalize	Off
Slice oversampling	0.00%	Normalize	Off
Slices per slab	176	B1 filter	Off
FoV read	256 mm	Raw filter	Off
FoV phase	93.80%	Elliptical filter	Off
Slice thickness	1.00 mm	Shim mode	Standard
TR	24.50 ms	Adjust with body coil	Off
TE 1	2.34 ms	Assume Silicone	Off
TE 2	4.68 ms	? Ref. amplitude 1H	0.000 V
TE 3	7.02 ms	Adjustment Tolerance	Auto
TE 4	9.36 ms	**Sequence**	
TE 5	11.70 ms	Dimension	3D
TE 6	14.04 ms	Contrasts	8
TE 7	16.38 ms	Bandwidth	465 Hz/Px
TE 8	18.72 ms	RF spoiling	On
Concatenations	1	MT repetition factor	1
Filter	None	FA Gaussian	220 [deg]
Coil elements	HEA;HEP	Duration Gaussian	4000 [us]
Contrast		Off-resonance Gaussian	2000 [Hz]
MTC	Off	Flat Top MT spoiler	1000 [us]
Flip angle	21 deg	Dur. Prew. Ramp	150 [us]
Reconstruction	Magn./Phase	Dur. Prew. Flat	600 [us]
Resolution		Dur. RO Ramp	80 [us]
Base resolution	256	RF spoil incr.	137.0 [deg]
Phase resolution	100%	RF excitation	Sinc (non-sel.)
Slice resolution	100%	Rec: fixed duration	100 [us]
Phase partial Fourier	Off	Sinc: fixed duration	580 [us]
Slice partial Fourier	6/8	BWT of sinc	6 [int]
PAT mode	GRAPPA		

RESTING STATE FMRI ACQUISITION			
TA	08:01	Adjustment Tolerance	Auto
Voxel size	3.0×3.0×2.5 mm	GLM Statistics	Off
Slices	45	Dynamic t-maps	Off
Dist. factor	20%	Starting ignore meas	0
Position	L4.0 A11.8 F30.3	Ignore after transition	0
Orientation	T > C-8.2 > S-1.5	Model transition states	On
Phase enc. dir.	P >> A	Temp. highpass filter	On
Rotation	-180.00 deg	Threshold	4
Phase oversampling	0%	Paradigm size	5
FoV read	192 mm	Meas[1]	Baseline
FoV phase	100.00%	Meas[2]	Baseline
Slice thickness	2.5 mm	Meas[3]	Baseline
TR	60.0 ms	Meas[4]	Baseline
TE 1	30.00 ms	Meas[5]	Active
TE 2	30.00 ms	Motion correction	On
TE 3	30.00 ms	Interpolation	3D-K-space
Concatenations	1	Spatial filter	Off
Filter	None	**Sequence**	
Coil elements	HEA;HEP	Dimension	2D
Contrast		Contrasts	1
Flip angle	90.0 deg	Bandwidth	2298 Hz/Px
Fat suppr.	Fat sat.	Output Data Type	Image Data
Reconstruction	Magnitude	Trigger Output	Cogent
Measurements	3	Phase Correction Mode	Point/Point
Pause after meas. 1	0.000 s	Read Gradient	Normal
Pause after meas. 2	0.000 s	Phase Gradient	Normal
Resolution		Phase FoV	Normal
Base resolution	64	PE direction	Positive
Phase resolution	100%	RO Waveform	Trapezoidal
PAT mode	None	Refoc. Corr	2.0 [%]
Matrix Coil Mode	Auto (CP)	Multi-echo full FOV	Off
Image Filter	Off	FatSat FA	130 [deg]
Distortion Corr.	Off	X-Shim 1	0.0 [mT/m*ms]
Prescan Normalize	Off	X-Shim 2	0.0 [mT/m*ms]
Normalize	Off	X-Shim 3	0.0 [mT/m*ms]
B1 filter	Off	Y-Shim 1	0.0 [mT/m*ms]
Raw filter	Off	Y-Shim 2	0.0 [mT/m*ms]
Elliptical filter	Off	Y-Shim 3	0.0 [mT/m*ms]
Shim mode	Standard	Z-Shim 1	0.0 [mT/m*ms]
Adjust with body coil	Off	Z-Shim 2	0.0 [mT/m*ms]
Assume Silicone	Off	Z-Shim 3	0.0 [mT/m*ms]

ALTERNATIVE RESTING STATE FMRI (LOW SAR)			
TA	06:53	Adjustment Tolerance	Auto
Voxel size	3.0×3.0×2.5 mm	GLM Statistics	Off
Slices	45	Dynamic t-maps	Off
Dist. factor	20%	Starting ignore meas	0
Position	L4.0 A11.8 F30.3	Ignore after transition	0
Orientation	T > C-8.2 > S-1.5	Model transition states	On
Phase enc. dir.	A >> P	Temp. highpass filter	On
Rotation	0.00 deg	Threshold	4
Phase oversampling	0%	Paradigm size	5
FoV read	192 mm	Meas[1]	Baseline
FoV phase	100.00%	Meas[2]	Baseline
Slice thickness	2.5 mm	Meas[3]	Baseline
TR	60.0 ms	Meas[4]	Baseline
TE 1	30.00 ms	Meas[5]	Active
TE 2	30.00 ms	Motion correction	On
TE 3	30.00 ms	Interpolation	3D-K-space
Concatenations	1	Spatial filter	Off
Filter	None	**Sequence**	
Coil elements	HEA;HEP	Dimension	2D
Contrast		Contrasts	1
Flip angle	90.0 deg	Bandwidth	2298 Hz/Px
Fat suppr.	Fat sat.	Output Data Type	Image Data
Reconstruction	Magnitude	Trigger Output	Cogent
Measurements	153	Phase Correction Mode	Point/Point
Pause after meas.	0.000 s	Read Gradient	Normal
Resolution		Phase Gradient	Normal
Base resolution	64	Phase FoV	Normal
Phase resolution	100%	PE direction	Positive
PAT mode	None	RO Waveform	Trapezoidal
Matrix Coil Mode	Auto (CP)	Refoc. Corr	2.0 [%]
Image Filter	Off	Multi-echo full FOV	Off
Distortion Corr.	Off	FatSat FA	130 [deg]
Prescan Normalize	Off	X-Shim 1	0.0 [mT/m*ms]
Normalize	Off	X-Shim 2	0.0 [mT/m*ms]
B1 filter	Off	X-Shim 3	0.0 [mT/m*ms]
Raw filter	Off	Y-Shim 1	0.0 [mT/m*ms]
Elliptical filter	Off	Y-Shim 2	0.0 [mT/m*ms]
Shim mode	Standard	Y-Shim 3	0.0 [mT/m*ms]
Adjust with body coil	Off	Z-Shim 1	0.0 [mT/m*ms]
Assume Silicone	Off	Z-Shim 2	0.0 [mT/m*ms]
Ref. amplitude 1H	0.000 V	Z-Shim 3	0.0 [mT/m*ms]

Appendix 2:

DBS screening sheet

DBS SCREENING SHEET	Patient Name:	Hospital number	DOB:
Date:	Diagnosis	Screened By:	

Baseline		**Rigidity**	**Global bradykinesia**	**Tremor**	**Gait**	**Others**	**Side effect 1= transient 2= Persistent**				
							Speech	**Pulling on face**	**Sensory (i.e. Tingling)**	**Others**	**comment**
Contact	**Parameter**										

Best contact		Second best contact		Comments:

Appendix 3:

Patient information sheet and consent

University College London Hospitals NHS
NHS Trust

The National Hospital for Neurology and Neurosurgery
Queen Square
LONDON
WC1N 3BG

Telephone 0207837 3611
Fax 020 7278 5616

Information for surgical patients (version 3.0-08 February 2016)

Basal Ganglia Connectivity

Introduction
You are being invited to take part in a research study. Before you decide, it is important for you to understand why the research is being done and what it will involve. Please take time to read the following information carefully and discuss it with others if you wish. Ask us if there is anything that is not clear or if you would like more information.

What is the purpose of the study?
The basal ganglia are a collection of structures deep within the brain. They play a critical role in mediating normal movements, and also are involved in the regulation of memory, impulsivity and behaviour. Normally the communication between these structures is highly organised, but can become disrupted in certain movement, behavioural or psychiatric disorders such as Parkinson's disease, Dystonia and Tourette's syndrome. Diffusion Tensor Imaging (DTI) is a Magnetic Resonance Imaging (MRI) technique that allows researchers to trace the connections between different brain structures. We are seeking to better map the connections between the basal ganglia and the rest of the brain.

You are about to undergo a surgical operation to implant a deep brain stimulator into certain structures of the basal ganglia, or to create a surgical lesion to disrupt brain connections between these structures. The exact site depends on the reason you are having the surgery. We want to examine our results with the clinical effect of the treatment you are going to receive. As a normal part of this procedure, you will have MRI scans both before and during the surgery. We will combine our results with these scans in an attempt to understand which parts of the brain are affected by the treatment. The hope is this will lead to a better understanding of normal basal ganglia function, how your disease affects it and allows us to develop more accurate ways of targeting these structures in the future.

The proposed study is outlined in detail over the next few pages. In summary, we will:

1) Perform an extra MRI scan before your operation that will allow us to map the connections from the area affected by the surgery.
2) Perform questionnaires both before and after the treatment to examine for changes in mood and impulsivity
3) Document carefully the effect of the treatment following surgery.
4) Look for a link between the changes seen due to the treatment, and the connections identified using the specialised MRI scan.
5)

Do I have to take part?
We have approached you because you are going to undergo a functional neurosurgery procedure that involves the implantation of a deep brain stimulator or the creation of a surgical brain lesion. We will be asking everyone due to undergo this procedure over the next 18 months. If you do decide to take part you will be given this information sheet to keep and be asked to sign a consent form, which you will also be given to keep. Your participation in this trial is entirely voluntary. Even if you decide to take part you are still free to withdraw at any time and without giving a reason. A decision to withdraw at any time, or a decision not to take part, will not affect the standard of care you receive.

What is involved in the study?

1. A 35-minute, DTI scan prior to your operation to allow us to map the white matter connections. This will be timed to occur at the same time you attend for other routine pre-operative investigations. In some selected patients, a longer and more detailed scan will be done.
2. Following surgery, you will undergo a series of routine clinical tests and questionnaires, which will take approximately 20 minutes to complete. This is the standard practice after this type of surgery, and we will collect copies of this data.
3. The normal procedure when the deep brain stimulator is switched on is to test each electrode contact in turn, and carefully document the response you have – During this the clinical researcher (Mr Akram) will also be present, to document these results.
4. Whilst you are still in hospital, between 2-5 days after the stimulator settings have been set, it is routine to repeat some of the earlier questionnaires which will take around 20 minutes to complete – We will collect copies of this data
5. If you are having an ablative surgical procedure (surgical lesioning), you will be invited to have a post-operative scan, identical to the pre-operative one, 6 months after surgery. This scan will be used to examine the changes in the brain connections following the surgical procedure.

Diffusion Tensor Imaging (DTI)
As noted above, you will undergo a special type of MRI scan called diffusion tensor imaging (DTI). This is a specialised scan that allows us to map the connections between different areas of the brain. You will lie on a couch inside the scanner, with your head in a specially designed headrest, which is cushioned for comfort. Inside the scanner there are speakers, an intercom so that you can speak to us and a screen on which a film can be shown. The scanner makes a loud clicking noise so we will give you earplugs to wear. The scan can be stopped at any time.

Is it safe?
To be eligible for the surgical procedure you are about to have, you have already been assessed for MRI compatibility, and have probably had MRI scans in the past. The DTI scan is a form of MRI and hence poses no additional risk.

The researcher (Mr Akram) is legally obliged to recheck your compatibility for MRI prior to any scanning for safety purposes. Please inform us if any of the following apply to you:

- **You have a pacemaker**
- **You have an implanted medication pump**
- **You have a metal plate in the skull or metal objects inside the eye or skull (for example after brain surgery or an accident)**
- **You have any tattoos anywhere except the ankle and foot.**

MRI is a painless and safe technique, which can obtain detailed pictures of the brain. As the name implies it uses magnetic fields to generate the pictures and unlike X-ray techniques there is no ionising radiation used. As long as people with any magnetic metal implants are excluded (see above), there are no known risks.

What would happen to the information about me that is collected? Who would have access to it?

All information which is collected about you during the course of the research will be kept strictly confidential. Any information about you which leaves the hospital / institute will have your name and address, date of birth and all identifiable information (including patient/hospital/NHS number) removed so that you cannot be recognised from it. The information held would include a brief summary of your symptoms and of your medical history and the results of the assessment outlined above. The 'data controllers' (i.e. the organisations collecting, storing, handling and processing the information) would be the National Hospital for Neurology and Neurosurgery and the Institute of Neurology. As principal investigator, Mr Ludvic Zrinzo would be responsible by law for the safety and security of this information. Your medical records may be inspected by competent authorities and properly authorized persons, but if any information is released this will be done in coded form with your name removed from the records so that your confidentiality is strictly maintained. The information collected about you may also be shown to authorised people from the UK Regulatory Authority (the Medicines and Healthcare Products Regulatory Authority) and Research Ethics Committee; this is to ensure that the study is carried out to the highest possible scientific standards. All will have a duty of confidentiality to you as a research participant. The results of the study will be stored on a secured computer database for a minimum of 20 years.

It is important that your GP is aware that you are taking part in a research project. With your permission, your GP would therefore be informed by letter on a strictly confidential basis.

What will happen if the findings may affect me personally?

The tests used in this study are currently research tools only and of uncertain significance. Potentially, unusually high levels of impulsivity may be found on the questionnaires. If this occurs then your doctors (Dr Foltynie/Dr Limousin) would be informed and any further formal assessments arranged as required.

Who is organising and funding the research?

This project is being organised by the Institute of Neurology, in conjunction with the National Hospital for Neurology and Neurosurgery. The costs of research (including researchers' salaries and equipment) are being paid by a grant from the Brain Research Trust (BRT).

How do you find us?

We are close to Russell Square tube station, on the Piccadilly line. We can reimburse travel expenses for you and a companion, so keep any receipts you have to enable us to do this as quickly as possible.

What happens if something goes wrong?

If you have a concern or complaint about any aspect of this study, you should initially speak to the researcher (Mr Akram, telephone-07709093929 or to Mr Ludvic Zrinzo telephone 0203 108 0026) who will do their best to answer your questions. Any complaint about the way you have been dealt with during the study or any possible harm you might suffer will be addressed as far as possible.

If you remain unhappy and wish to complain formally, you can do this through the NHS Complaints Procedure. If you are harmed by taking part in this research project, there are no special compensation arrangements. If you are harmed due to someone's negligence, then you may have grounds for taking legal action but you may have to pay the legal costs. Regardless of this, if you wish to complain, or have any concerns about this study, the normal National Health Service complaints mechanism should be available to you. At this hospital the person to contact would be:

Ms Jennifer Fraser
Complaints Coordinator, Box 52
National Hospital for Neurology and Neurosurgery
Queen Square, London WC1N 3BG
Tel: 0207 829 8765

Further information
If you would like to volunteer or would like to know more about the study, please contact:

Mr Harith Akram

The Unit of Functional Neurosurgery - Institute of Neurology
33 Queen Square
London
WC1N 3BG

Telephone: 02031080034

For out of hours contact please call Mr Harith Akram on 07709093929

Thank you for taking the time to read this information sheet

University College London Hospitals NHS
NHS Trust

The National Hospital for Neurology and Neurosurgery
Queen Square
LONDON
WC1N 3BG

Telephone 0207837 3611
Fax 020 7278 5616

Patient Identification Number for this Study: ……..
Consent Form Version Number and Date: ……..

PATIENT INFORMED CONSENT FORM (version:3 – 8/2/2016)

Title of Study: ……Basal Ganglia Connectivity……,……
Name of Chief / Principal Investigator (C/PI):……..Mr Ludvic Zrinzo…..…….

Please initial box

1. I confirm that I have read and understand the information sheet dated…….. (version:3 – 8/2/2016) for the above study. I have had the opportunity to consider the information, ask questions and have had these answered satisfactorily. ☐
2. I confirm that I have had sufficient time to consider whether or not I want to be included in the study. ☐
3. I understand that my participation is voluntary and that I am free to withdraw at any time, without giving any reason, without my medical care or legal rights being affected. ☐
4. I understand that relevant sections of any of my medical notes (only applicable for NHS patients) and data collected during the study, may be looked at by responsible individuals from the Institute of Neurology, from regulatory authorities, from the NHS Trust or representatives of the sponsor for purposes of monitoring and auditing, where it is relevant to my taking part in this research. I give permission for these individuals to have access to my records. ☐
5. I agree to my GP being informed of my participation in the study (only applicable for NHS patients). ☐
6. I agree to take part in the above study. ☐

……	……	…….
Name of Patient	Date	Signature
……	……	…….
Name of Person taking consent (if different from C/PI)	Date	Signature
……	……	…….
C/PI (to be contacted if there are any problems)	Email	Phone No:

Comments or concerns during the study:
If you have any comments or concerns you may discuss these with the investigator. If you wish to go further and complain about any aspect of the way you have been approached or treated during the course of the study, you should write or get in touch with the Complaints Manager, UCL hospitals. Please quote the UCLH project number at the top this consent form.

When completed, 1 form for the patient; 1 to be kept as part of the study documentation for the trial master / investigator site file at the Ion; 1 original to be kept with the hospital medical notes.

Bibliography

1. Okun, M. S. Deep-brain stimulation for Parkinson's disease. *N Engl J Med* **367,** 1529–1538 (2012).
2. Miocinovic, S., Somayajula, S., Chitnis, S. & Vitek, J. L. History, applications, and mechanisms of deep brain stimulation. *JAMA Neurol* **70,** 163–171 (2013).
3. Coenen, V. A., Amtage, F., Volkmann, J. & Schläpfer, T. E. Deep Brain Stimulation in Neurological and Psychiatric Disorders. *Dtsch Arztebl Int* **112,** 519–526 (2015).
4. Hariz, M. I., Blomstedt, P. & Zrinzo, L. Deep brain stimulation between 1947 and 1987: the untold story. *Neurosurgical FOCUS* **29,** E1 (2010).
5. Hariz, M. Deep brain stimulation: new techniques. *Parkinsonism and Related Disorders* **20 Suppl 1,** S192–6 (2014).
6. Hariz, M., Blomstedt, P. & Zrinzo, L. Future of brain stimulation: new targets, new indications, new technology. *Mov Disord.* **28,** 1784–1792 (2013).
7. Benabid, A. L., Pollak, P., Louveau, A., Henry, S. & de Rougemont, J. Combined (thalamotomy and stimulation) stereotactic surgery of the VIM thalamic nucleus for bilateral Parkinson disease. *Appl Neurophysiol* **50,** 344–346 (1987).
8. Limousin, P. *et al.* Effect of parkinsonian signs and symptoms of bilateral subthalamic nucleus stimulation. *The Lancet* **345,** 91–95 (1995).
9. Pollak, P. *et al.* [Effects of the stimulation of the subthalamic nucleus in Parkinson disease]. *Rev. Neurol. (Paris)* **149,** 175–176 (1993).
10. Coubes, P. *et al.* [Treatment of early-onset generalized dystonia by chronic bilateral stimulation of the internal globus pallidus. Apropos of a case]. *Neurochirurgie* **45,** 139–144 (1999).
11. Krauss, J. K., Pohle, T., Weber, S., Ozdoba, C. & Burgunder, J. M. Bilateral stimulation of globus pallidus internus for treatment of cervical dystonia. *The Lancet* **354,** 837–838 (1999).
12. Volkmann, J., Chabardes, S., Steinke, G. K. & Carcieri, S. 375 DIRECT DBS: A Prospective, Multicenter Clinical Trial With Blinding for a Directional Deep Brain Stimulation Lead. *Neurosurgery* **63 Suppl 1,** 211–212 (2016).
13. Steigerwald, F., Müller, L., Johannes, S., Matthies, C. & Volkmann, J. Directional deep brain stimulation of the subthalamic nucleus: A pilot study using a novel neurostimulation device. *Mov Disord.* **31,** 1240–1243 (2016).
14. Rengachary, S. S. & Ellenbogen, R. G. *Principles of Neurosurgery*. (Mosby Incorporated, 2005).
15. Porter, R. *The Cambridge History of Medicine*. (Cambridge University Press, 2006).
16. Brothwell, D. R. *Digging Up Bones*. (Cornell University Press, 1981).
17. Weber, J. & Czarnetzki, A. Trepanations from the early medieval period of southwestern Germany--indications, complications and outcome. *Zentralbl. Neurochir.* **62,** 10–14 (2001).
18. Horsley, V. The Linacre Lecture '*On the function of the so-called motor area of the brain*': Delivered to the Master and Fellows of St. John's College, Cambridge, May 6th, 1909. *Br Med J* **2,** 121–132 (1909).
19. Bucy, P. C. & Buchanan, D. N. Athetosis. *Brain* **55,** 479–492 (1932).
20. Walker, A. E. Cerebral pedunculotomy for the relief of involuntary movements; hemiballismus. *Acta Psychiatr Neurol* **24,** 723–729 (1949).
21. Walker, A. E. Cerebral pedunculotomy for the relief of involuntary movements. II. Parkinsonian tremor. *J. Nerv. Ment. Dis.* **116,** 766–775 (1952).
22. Broadbent, W. H. Remarks on the Pathology of Chorea. *Br Med J* **1,** 369–371 (1869).
23. Gildenberg, P. L. Evolution of Basal Ganglia Surgery for Movement Disorders. *Stereotact Funct Neurosurg* **84,** 131–135 (2006).
24. Oppolzer, R. *Fall von Paralysis agitans*. (Wien. med. Wschr, 1861).

25. Marmaduke, M. E. D., Awad, I. A. & Edward R Laws, J. *Walter Dandy: The Personal Side of a Premier Neurosurgeon, Revised Edition*. (Lippincott Williams & Wilkins, 2015).
26. Meyers, R. *Surgical procedure for postencephalitic tremor, with notes on the physiology of premotor fibers*. (Arch Neurol Psychiatry, 1940).
27. Guiot, G. & Brion, S. *[Neurosurgery of choreoathetosic and Parkinsonian syndromes.]*. (La semaine des hopitaux: organe fonde par l' …, 1952).
28. Meyers, R. Surgical experiments in the therapy of certain 'extrapyramidal' diseases: a current evaluation. *Acta Psychiatr Neurol Suppl* **67,** 1–42 (1951).
29. Vinken, P. J. & Bruyn, G. W. *Diseases of the Basal Ganglia*. (1968).
30. Fenelon, F. [Neurosurgery of parkinsonian syndrome by direct intervention on the extrapyramidal tracts immediately below the lenticular nucleus. Communication followed by film showing patient before and after intervention]. *Rev. Neurol. (Paris)* **83,** 437–440 (1950).
31. Cooper, I. S. Anterior chorodial artery ligation for involuntary movements. *Science* **118,** 193 (1953).
32. Cooper, I. S. Intracerebral injection of procaine into the globus pallidus in hyperkinetic disorders. *Science* **119,** 417–418 (1954).
33. Cooper, I. S. Surgical alleviation of Parkinsonism; effects of occlusion of the anterior choroidal artery. *J Am Geriatr Soc* **2,** 691–718 (1954).
34. Cooper, I. S. & BRAVO, G. Chemopallidectomy and chemothalamectomy. *Journal of Neurosurgery* **15,** 244–250 (1958).
35. Gildenberg, P. L. The history of surgery for movement disorders. *Neurosurgery Clinics of NA* **9,** 283–294 (1998).
36. Leppik, I. E. *Contemporary Diagnosis and Management of the Patient with Epilepsy*. (Handbooks in Health Care, 2006).
37. Rontgen, W. K. On A New Kind of Rays. *CA: A Cancer Journal for Clinicians* **22,** 153–157 (1972).
38. Giller, C. A., Mornet, P. & Moreau, J.-F. The first formulation of image-based stereotactic principles: the forgotten work of Gaston Contremoulins. *Journal of Neurosurgery* 1–10 (2017). doi:10.3171/2016.10.JNS161966
39. Clarke, R. H. & Horsley, V. THE CLASSIC: On a method of investigating the deep ganglia and tracts of the central nervous system (cerebellum). Br Med J 1906:1799-1800. *Clin. Orthop. Relat. Res.* **463,** 3–6 (2007).
40. Spiegel, E. A., Wycis, H. T., Marks, M. & Lee, A. J. Stereotaxic Apparatus for Operations on the Human Brain. *Science* **106,** 349–350 (1947).
41. Spiegel, E. Atlas d'anatomie stéréotaxique (anatomic stereotaxic atlas). *Electroencephalography and Clinical Neurophysiology* **10,** 791 (1958).
42. Leksell, L. *A stereotaxic apparatus for intracerebral surgery*. (Acta Chirurgica Scandinavica, 1950).
43. Martínez, R. & Vaquero, J. Image-directed functional neurosurgery with the Cosman-Roberts-Wells stereotactic instrument. *Acta Neurochir* **113,** 176–179 (1991).
44. UCL - London's Global University. (1949).
45. Spiegel, E. A. & Wycis, H. T. Pallidothalamotomy in chorea. *Arch Neurol Psychiatry* **64,** 295–296 (1950).
46. Benabid, A. L. *et al. Functional neurosurgery for movement disorders a historical perspective*. *Progress in Brain Research* **175,** 379–391 (Elsevier, 2009).
47. Nashold, B. S. Stereotactic neurosurgery: the present and future. *Am Surg* **36,** 91–93 (1970).
48. Laitinen, L. V., Bergenheim, A. T. & Hariz, M. I. Ventroposterolateral pallidotomy can abolish all parkinsonian symptoms. *Stereotact Funct Neurosurg* **58,** 14–21 (1992).
49. Laitinen, L. V., Bergenheim, A. T. & Hariz, M. I. Leksell's posteroventral pallidotomy in the treatment of Parkinson's disease. *Journal of Neurosurgery* **76,** 53–61 (1992).
50. Hariz, M. I. & Hariz, G.-M. Therapeutic stimulation versus ablation. *Handb Clin Neurol* **116,** 63–71 (2013).
51. Hariz, M. I. Psychosurgery, Deep Brain Stimulation, and the Re-writing of History. *Neurosurgery* **63,** E820 (2008).

52. Hosobuchi, Y. Subcortical electrical stimulation for control of intractable pain in humans. Report of 122 cases (1970-1984). *Journal of Neurosurgery* **64,** 543–553 (1986).
53. Valenstein, E. S. Brain stimulation and behavior control. *Nebr Symp Motiv* **22,** 251–292 (1975).
54. Guridi, J. & Manrique, M. in *Textbook of Stereotactic and Functional Neurosurgery* 179–191 (Springer Berlin Heidelberg, 2009). doi:10.1007/978-3-540-69960-6_14
55. Sem-Jacobsen, C. W. Depth-electrographic neurosurgical treatment of extrapyramidal disturbances. Dangers and necessary precautions. *Acta Neurologica Scandinavica* **39,** 230–230 (2009).
56. Baumeister, A. The Tulane Electrical Brain Stimulation Program A Historical Case Study in Medical Ethics. *Journal of the History of the Neurosciences* **9,** 262–278 (2000).
57. Hariz, M. I. in *Deep Brain Stimulation* 289–294 (Springer, Berlin, Heidelberg, 2012). doi:10.1007/978-3-642-30991-5_26
58. Haber, S. N., Fudge, J. L. & McFarland, N. R. Striatonigrostriatal pathways in primates form an ascending spiral from the shell to the dorsolateral striatum. *Journal of Neuroscience* **20,** 2369–2382 (2000).
59. Ashkan, K. *et al.* Variability of the subthalamic nucleus: The case for direct MRI guided targeting. *Br J Neurosurg* **21,** 197–200 (2007).
60. O'Gorman, R. L. *et al.* CT/MR image fusion in the postoperative assessment of electrodes implanted for deep brain stimulation. *Stereotact Funct Neurosurg* **87,** 205–210 (2009).
61. Foltynie, T. *et al.* MRI-guided STN DBS in Parkinson's disease without microelectrode recording: efficacy and safety. *Journal of Neurology, Neurosurgery & Psychiatry* **82,** 358–363 (2011).
62. Hariz, M. I. *et al.* A Quick and Universal Method for Stereotactic Visualization of the Subthalamic Nucleus before and after Implantation of Deep Brain Stimulation Electrodes. *Stereotact Funct Neurosurg* **80,** 96–101 (2003).
63. Zrinzo, L. *et al.* Clinical safety of brain magnetic resonance imaging with implanted deep brain stimulation hardware: large case series and review of the literature. *WNEU* **76,** 164–72– discussion 69–73 (2011).
64. Yelnik, J. *et al.* A three-dimensional, histological and deformable atlas of the human basal ganglia. I. Atlas construction based on immunohistochemical and MRI data. *NeuroImage* **34,** 618–638 (2007).
65. Bour, L. J. *et al.* Long-term experience with intraoperative microrecording during DBS neurosurgery in STN and GPi. *Acta Neurochir* **152,** 2069–2077 (2010).
66. Wodarg, F. *et al.* Stimulation site within the MRI-defined STN predicts postoperative motor outcome. *Mov Disord.* **27,** 874–879 (2012).
67. Aviles-Olmos, I. *et al.* Long-term outcome of subthalamic nucleus deep brain stimulation for Parkinson's disease using an MRI-guided and MRI-verified approach. *Journal of Neurology, Neurosurgery & Psychiatry* **85,** 1419–1425 (2014).
68. Schoenen, J. Hypothalamic stimulation in chronic cluster headache: a pilot study of efficacy and mode of action. *Brain* **128,** 940–947 (2005).
69. Zrinzo, L., Foltynie, T., Limousin, P. & Hariz, M. I. Reducing hemorrhagic complications in functional neurosurgery: a large case series and systematic literature review. *Journal of Neurosurgery* **116,** 84–94 (2012).
70. Tripoliti, E. *et al.* Effects of subthalamic stimulation on speech of consecutive patients with Parkinson disease. *Neurology* **76,** 80–86 (2011).
71. Nakajima, T. *et al.* MRI-Guided Subthalamic Nucleus Deep Brain Stimulation without Microelectrode Recording: Can We Dispense with Surgery under Local Anaesthesia. *Stereotact Funct Neurosurg* **89,** 318–325 (2011).
72. Richardson, R. M., Ostrem, J. L. & Starr, P. A. Surgical Repositioning of Misplaced Subthalamic Electrodes in Parkinson’s Disease: Location of Effective and Ineffective Leads. *Stereotact Funct Neurosurg* **87,** 297–303 (2009).
73. Van Horn, G. *et al.* Pallidotomy: a comparison of responders and nonresponders. *Neurosurgery* **48,** 263–71– discussion 271–3 (2001).

74. Schiff, S. J., Dunagan, B. K. & Worth, R. M. Failure of single-unit neuronal activity to differentiate globus pallidus internus and externus in Parkinson disease. *Journal of Neurosurgery* **97,** 119–128 (2002).
75. Rodriguez-Oroz, M. C. *et al.* Neuronal activity of the red nucleus in Parkinson's disease. *Mov Disord.* **23,** 908–911 (2008).
76. Weise, L. M. *et al.* Correlation of active contact positions with the electrophysiological and anatomical subdivisions of the subthalamic nucleus in deep brain stimulation. *Stereotact Funct Neurosurg* **91,** 298–305 (2013).
77. Johnsen, E. L., Sunde, N., Mogensen, P. H. & Østergaard, K. MRI verified STN stimulation site - gait improvement and clinical outcome. *Eur J Neurol* **17,** 746–753 (2010).
78. Sarem-Aslani, A. & Mullett, K. Industrial perspective on deep brain stimulation: history, current state, and future developments. *Front. Integr. Neurosci.* **5,** 46 (2011).
79. Henderson, J. M. 'Connectomic surgery': diffusion tensor imaging (DTI) tractography as a targeting modality for surgical modulation of neural networks. *Front. Integr. Neurosci.* **6,** 15 (2012).
80. Ramnani, N., Behrens, T. E. J., Penny, W. & Matthews, P. M. New approaches for exploring anatomical and functional connectivity in the human brain. *BPS* **56,** 613–619 (2004).
81. Hoy, A. R. & Alexander, A. L. *Diffusion MRI. Brain Mapping An Encyclopedic Reference* **1,** 47–52 (Elsevier, 2015).
82. van der Kolk, A. G., Hendrikse, J., Zwanenburg, J. J. M., Visser, F. & Luijten, P. R. Clinical applications of 7 T MRI in the brain. *Eur J Radiol* **82,** 708–718 (2013).
83. Jensen, J. H., Helpern, J. A., Ramani, A., Lu, H. & Kaczynski, K. Diffusional kurtosis imaging: the quantification of non-gaussian water diffusion by means of magnetic resonance imaging. *Magn. Reson. Med.* **53,** 1432–1440 (2005).
84. Wedeen, V. J. *et al.* Diffusion spectrum magnetic resonance imaging (DSI) tractography of crossing fibers. *NeuroImage* **41,** 1267–1277 (2008).
85. Wu, Y.-C. & Alexander, A. L. Hybrid diffusion imaging. *NeuroImage* **36,** 617–629 (2007).
86. Assaf, Y., Freidlin, R. Z., Rohde, G. K. & Basser, P. J. New modeling and experimental framework to characterize hindered and restricted water diffusion in brain white matter. *Magn. Reson. Med.* **52,** 965–978 (2004).
87. Zhang, H., Schneider, T., Wheeler-Kingshott, C. A. & Alexander, D. C. NODDI: practical in vivo neurite orientation dispersion and density imaging of the human brain. *NeuroImage* **61,** 1000–1016 (2012).
88. Wang, X. *et al.* Diffusion basis spectrum imaging detects and distinguishes coexisting subclinical inflammation, demyelination and axonal injury in experimental autoimmune encephalomyelitis mice. *NMR Biomed* **27,** 843–852 (2014).
89. Basser, P. J., Mattiello, J. & LeBihan, D. Estimation of the effective self-diffusion tensor from the NMR spin echo. *J Magn Reson B* **103,** 247–254 (1994).
90. Tuch, D. S. *et al.* High angular resolution diffusion imaging reveals intravoxel white matter fiber heterogeneity. *Magn. Reson. Med.* **48,** 577–582 (2002).
91. Behrens, T. E. J. *et al.* Characterization and propagation of uncertainty in diffusion-weighted MR imaging. *Magn. Reson. Med.* **50,** 1077–1088 (2003).
92. Dyrby, T. B. *et al.* Validation of in vitro probabilistic tractography. *NeuroImage* **37,** 1267–1277 (2007).
93. Johansen-Berg, H. Functional-Anatomical Validation and Individual Variation of Diffusion Tractography-based Segmentation of the Human Thalamus. *Cerebral Cortex* **15,** 31–39 (2004).
94. Behrens, T. E. J. *et al.* Non-invasive mapping of connections between human thalamus and cortex using diffusion imaging. *Nat Neurosci* **6,** 750–757 (2003).
95. Draganski, B. *et al.* Evidence for Segregated and Integrative Connectivity Patterns in the Human Basal Ganglia. *Journal of Neuroscience* **28,** 7143–7152 (2008).
96. Lambert, C. *et al.* Confirmation of functional zones within the human subthalamic nucleus: Patterns of connectivity and sub-parcellation using diffusion weighted imaging. *NeuroImage* 1–12 (2011). doi:10.1016/j.neuroimage.2011.11.082

97. Chowdhury, R., Lambert, C., Dolan, R. J. & Düzel, E. Parcellation of the human substantia nigra based on anatomical connectivity to the striatum. *NeuroImage* **81,** 191–198 (2013).
98. Catani, M., Howard, R. J., Pajevic, S. & Jones, D. K. Virtual in vivo interactive dissection of white matter fasciculi in the human brain. *NeuroImage* **17,** 77–94 (2002).
99. Behrens, T. E. J. & Jbabdi, S. in *Diffusion MRI* 333–351 (Elsevier, 2009). doi:10.1016/B978-0-12-374709-9.00015-8
100. Petersen, M. V. *et al.* Probabilistic versus deterministic tractography for delineation of the cortico-subthalamic hyperdirect pathway in patients with Parkinson disease selected for deep brain stimulation. *Journal of Neurosurgery* 1–12 (2016). doi:10.3171/2016.4.JNS1624
101. Maier-Hein, K. H. *et al.* The challenge of mapping the human connectome based on diffusion tractography. *Nat Commun* **8,** 1349 (2017).
102. Sotiropoulos, S. N. *et al.* Advances in diffusion MRI acquisition and processing in the Human Connectome Project. *NeuroImage* **80,** 125–143 (2013).
103. Behrens, T. E. J., Berg, H. J., Jbabdi, S., Rushworth, M. F. S. & Woolrich, M. W. Probabilistic diffusion tractography with multiple fibre orientations: What can we gain? *NeuroImage* **34,** 144–155 (2007).
104. Lambert, C., Lutti, A., Helms, G., Frackowiak, R. & Ashburner, J. Multiparametric brainstem segmentation using a modified multivariate mixture of Gaussians. *Neuroimage Clin* **2,** 684–694 (2013).
105. Lambert, C. *et al.* Characterizing aging in the human brainstem using quantitative multimodal MRI analysis. *Front Hum Neurosci* **7,** 462 (2013).
106. Tye, K. M. & Deisseroth, K. Optogenetic investigation of neural circuits underlying brain disease in animal models. *Nat Rev Neurosci* **13,** 251–266 (2012).
107. Beckmann, M., Johansen-Berg, H. & Rushworth, M. F. S. Connectivity-Based Parcellation of Human Cingulate Cortex and Its Relation to Functional Specialization. *Journal of Neuroscience* **29,** 1175–1190 (2009).
108. Owen, S. L. F. *et al.* Pre-operative DTI and probabilisitic tractography in four patients with deep brain stimulation for chronic pain. *J Clin Neurosci* **15,** 801–805 (2008).
109. Owen, S. L. F., Heath, J., Kringelbach, M. L., Stein, J. F. & Aziz, T. Z. Preoperative DTI and probabilistic tractography in an amputee with deep brain stimulation for lower limb stump pain. *Br J Neurosurg* **21,** 485–490 (2007).
110. Gutman, D. A., Holtzheimer, P. E., Behrens, T. E. J., Johansen-Berg, H. & Mayberg, H. S. A Tractography Analysis of Two Deep Brain Stimulation White Matter Targets for Depression. *BPS* **65,** 276–282 (2009).
111. Lujan, J. L., Chaturvedi, A. & McIntyre, C. C. Tracking the mechanisms of deep brain stimulation for neuropsychiatric disorders. *Front. Biosci.* **13,** 5892–5904 (2008).
112. Johansen-Berg, H. *et al.* Anatomical Connectivity of the Subgenual Cingulate Region Targeted with Deep Brain Stimulation for Treatment-Resistant Depression. *Cerebral Cortex* **18,** 1374–1383 (2008).
113. Grover, P. J. *et al.* Deep brain stimulation for cluster headache. *Journal of Clinical Neuroscience* **16,** 861–866 (2009).
114. Sedrak, M. *et al.* The role of modern imaging modalities on deep brain stimulation targeting for mental illness. *Acta Neurochir. Suppl.* **101,** 3–7 (2008).
115. Anderson, J. S. *et al.* Functional connectivity targeting for deep brain stimulation in essential tremor. *American Journal of Neuroradiology* **32,** 1963–1968 (2011).
116. Hyam, J. A. *et al.* Contrasting Connectivity of the Ventralis Intermedius and Ventralis Oralis Posterior Nuclei of the Motor Thalamus Demonstrated by Probabilistic Tractography. *Neurosurgery* **70,** 162–169 (2012).
117. Van Essen, D. C. *et al.* The Human Connectome Project: A data acquisition perspective. *NeuroImage* **62,** 2222–2231 (2012).
118. Horn, A. & Kühn, A. A. Lead-DBS: A toolbox for deep brain stimulation electrode localizations and visualizations. *NeuroImage* (2014). doi:10.1016/j.neuroimage.2014.12.002
119. Horn, A. *et al.* Connectivity Predicts deep brain stimulation outcome in Parkinson disease. *Ann Neurol.* **82,** 67–78 (2017).

120. Owen, S. L. F. *et al.* Connectivity of an effective hypothalamic surgical target for cluster headache. *Journal of Clinical Neuroscience* **14,** 955–960 (2007).
121. May, A., Bahra, A., Büchel, C., Frackowiak, R. S. & Goadsby, P. J. Hypothalamic activation in cluster headache attacks. *The Lancet* **352,** 275–278 (1998).
122. May, A. *et al.* Correlation between structural and functional changes in brain in an idiopathic headache syndrome. *Nature Medicine* **5,** 836–838 (1999).
123. Leone, M., Franzini, A. & Bussone, G. Stereotactic stimulation of posterior hypothalamic gray matter in a patient with intractable cluster headache. *N Engl J Med* **345,** 1428–1429 (2001).
124. Franzini, A., Ferroli, P., Leone, M. & Broggi, G. Stimulation of the Posterior Hypothalamus for Treatment of Chronic Intractable Cluster Headaches: First Reported Series. *Neurosurgery* **52,** 1095–1101 (2003).
125. Larson, P. S. Deep brain stimulation for psychiatric disorders. *NURT* **5,** 50–58 (2008).
126. Mayberg, H. S. *et al.* Deep Brain Stimulation for Treatment-Resistant Depression. *Neuron* **45,** 651–660 (2005).
127. Blomstedt, P., Sjöberg, R. L., Hansson, M., Bodlund, O. & Hariz, M. I. Deep brain stimulation in the treatment of depression. *Acta Psychiatrica Scandinavica* **123,** 4–11 (2010).
128. Voon, V., Kubu, C., Krack, P., Houeto, J.-L. & Tröster, A. I. Deep brain stimulation: Neuropsychological and neuropsychiatric issues. *Mov Disord.* **21,** S305–S327 (2006).
129. Hariz, M. I. & Hariz, G. M. Hyping deep brain stimulation in psychiatry could lead to its demise. *BMJ* **345,** e5447–e5447 (2012).
130. Steele, J. D., Christmas, D., Eljamel, M. S. & Matthews, K. Anterior cingulotomy for major depression: clinical outcome and relationship to lesion characteristics. *Biological Psychiatry* **63,** 670–677 (2008).
131. Bhatia, K. D., Henderson, L., Ramsey-Stewart, G. & May, J. Diffusion Tensor Imaging to Aid Subgenual Cingulum Target Selection for Deep Brain Stimulation in Depression. *Stereotact Funct Neurosurg* **90,** 225–232 (2012).
132. Coenen, V. A. *et al.* Modulation of the cerebello-thalamo-cortical network in thalamic deep brain stimulation for tremor: a diffusion tensor imaging study. *Neurosurgery* **75,** 657–69– discussion 669–70 (2014).
133. Yamada, K. *et al.* MR Imaging of Ventral Thalamic Nuclei. *American Journal of Neuroradiology* **31,** 732–735 (2010).
134. Aravamuthan, B. R., Stein, J. F. & Aziz, T. Z. The anatomy and localization of the pedunculopontine nucleus determined using probabilistic diffusion tractagrophy. *Br J Neurosurg* **22,** S25–S32 (2008).
135. Barkhoudarian, G. *et al.* A role of diffusion tensor imaging in movement disorder surgery. *Acta Neurochir* **152,** 2089–2095 (2010).
136. Coenen, V. A., Mädler, B., Schiffbauer, H., Urbach, H. & Allert, N. Individual fiber anatomy of the subthalamic region revealed with diffusion tensor imaging: a concept to identify the deep brain stimulation target for tremor suppression. *Neurosurgery* **68,** 1069–75– discussion 1075–6 (2011).
137. Coenen, V. A., Allert, N. & Mädler, B. A role of diffusion tensor imaging fiber tracking in deep brain stimulation surgery: DBS of the dentato-rubro-thalamic tract (drt) for the treatment of therapy-refractory tremor. *Acta Neurochir* **153,** 1579–1585 (2011).
138. Pouratian, N. *et al.* Multi-institutional evaluation of deep brain stimulation targeting using probabilistic connectivity-based thalamic segmentation. *Journal of Neurosurgery* **115,** 995–1004 (2011).
139. Klein, J. C. *et al.* The tremor network targeted by successful VIM deep brain stimulation in humans. *Neurology* **78,** 787–795 (2012).
140. Groppa, S. *et al.* Physiological and anatomical decomposition of subthalamic neurostimulation effects in essential tremor. *Brain* **137,** 109–121 (2014).
141. Anthofer, J. *et al.* The variability of atlas-based targets in relation to surrounding major fibre tracts in thalamic deep brain stimulation. *Acta Neurochir* **156,** 1497–504– discussion 1504 (2014).

142. Maks, C. B., Butson, C. R., Walter, B. L., Vitek, J. L. & McIntyre, C. C. Deep brain stimulation activation volumes and their association with neurophysiological mapping and therapeutic outcomes. *Journal of Neurology, Neurosurgery & Psychiatry* **80,** 659–666 (2009).
143. Åström, M. *et al.* Method for patient-specific finite element modeling and simulation of deep brain stimulation. *Med Biol Eng Comput* **47,** 21–28 (2008).
144. Schweder, P. M. *et al.* Chronic pedunculopontine nucleus stimulation restores functional connectivity. *NeuroReport* **21,** 1065–1068 (2010).
145. Figee, M. *et al.* Deep brain stimulation restores frontostriatal network activity in obsessive-compulsive disorder. *Nature Publishing Group* – (2013). doi:doi:10.1038/nn.3344
146. Riva-Posse, P. *et al.* Defining Critical White Matter Pathways Mediating Successful Subcallosal Cingulate Deep Brain Stimulation for Treatment-Resistant Depression. *Biological Psychiatry* **0,** – (2014).
147. McNab, J. A. *et al.* Reduced limbic connections may contraindicate subgenual cingulate deep brain stimulation for intractable depression. *Journal of Neurosurgery* **111,** 780–784 (2009).
148. Lenglet, C. *et al.* Comprehensive in vivo mapping of the human basal ganglia and thalamic connectome in individuals using 7T MRI. *PLoS ONE* **7,** e29153 (2012).
149. Accolla, E. A. *et al.* Brain tissue properties differentiate between motor and limbic basal ganglia circuits. *Hum. Brain Mapp.* **35,** 5083–5092 (2014).
150. Brunenberg, E. J. L. *et al.* Structural and resting state functional connectivity of the subthalamic nucleus: identification of motor STN parts and the hyperdirect pathway. *PLoS ONE* **7,** e39061 (2012).
151. Weiskopf, N. *et al.* Quantitative multi-parameter mapping of R1, PD(*), MT, and R2(*) at 3T: a multi-center validation. *Front Neurosci* **7,** 95 (2013).
152. Helms, G., Draganski, B., Frackowiak, R., Ashburner, J. & Weiskopf, N. Improved segmentation of deep brain grey matter structures using magnetization transfer (MT) parameter maps. *NeuroImage* **47,** 194–198 (2009).
153. Weiskopf, N. *et al.* Unified segmentation based correction of R1 brain maps for RF transmit field inhomogeneities (UNICORT). *NeuroImage* **54,** 2116–2124 (2011).
154. Helms, G., Dathe, H. & Dechent, P. Quantitative FLASH MRI at 3T using a rational approximation of the Ernst equation. *Magn. Reson. Med.* **59,** 667–672 (2008).
155. Heiervang, E., Behrens, T. E. J., Mackay, C. E., Robson, M. D. & Johansen-Berg, H. Between session reproducibility and between subject variability of diffusion MR and tractography measures. *NeuroImage* **33,** 867–877 (2006).
156. Andersson, J. L. R., Skare, S. & Ashburner, J. How to correct susceptibility distortions in spin-echo echo-planar images: application to diffusion tensor imaging. *NeuroImage* **20,** 870–888 (2003).
157. Smith, S. M. *et al.* Advances in functional and structural MR image analysis and implementation as FSL. *NeuroImage* **23 Suppl 1,** S208–19 (2004).
158. Andersson, J. L. R. & Sotiropoulos, S. N. An integrated approach to correction for off-resonance effects and subject movement in diffusion MR imaging. *NeuroImage* **125,** 1063–1078 (2016).
159. Jbabdi, S., Sotiropoulos, S. N., Savio, A. M., Graña, M. & Behrens, T. E. J. Model-based analysis of multishell diffusion MR data for tractography: how to get over fitting problems. *Magn. Reson. Med.* **68,** 1846–1855 (2012).
160. Hernandez, M. *et al.* Accelerating fibre orientation estimation from diffusion weighted magnetic resonance imaging using GPUs. *PLoS ONE* **8,** e61892 (2013).
161. Gunalan, K., Howell, B. & McIntyre, C. C. Quantifying axonal responses in patient-specific models of subthalamic deep brain stimulation. *NeuroImage* **172,** 263–277 (2018).
162. Åström, M., Diczfalusy, E., Martens, H. & Wårdell, K. Relationship between neural activation and electric field distribution during deep brain stimulation. *IEEE Trans. Biomed. Eng.* **62,** 664–672 (2015).
163. Howell, B. & McIntyre, C. C. Role of Soft-Tissue Heterogeneity in Computational Models of Deep Brain Stimulation. *Brain Stimulation* **10,** 46–50 (2017).

164. Smith, S. M. & Nichols, T. E. Threshold-free cluster enhancement: addressing problems of smoothing, threshold dependence and localisation in cluster inference. *NeuroImage* **44,** 83–98 (2009).
165. Winkler, A. M., Ridgway, G. R., Webster, M. A., Smith, S. M. & Nichols, T. E. Permutation inference for the general linear model. *NeuroImage* **92,** 381–397 (2014).
166. Mackenzie, I. Observations On the Parkinsonian syndrome in lethargic encephalitis: A pathological posture. *The Lancet* **202,** 1385–1390 (1923).
167. Braak, H. *et al.* Staging of brain pathology related to sporadic Parkinson's disease. *Neurobiol. Aging* **24,** 197–211 (2003).
168. Lees, A. J., Hardy, J. & Revesz, T. Parkinson's disease. *Lancet* **373,** 2055–2066 (2009).
169. Hoehn, M. M. & Yahr, M. D. Parkinsonism: onset, progression and mortality. *Neurology* **17,** 427–442 (1967).
170. Alexander, G. E., DeLong, M. R. & Strick, P. L. Parallel organization of functionally segregated circuits linking basal ganglia and cortex. *Annu. Rev. Neurosci.* **9,** 357–381 (1986).
171. Albin, R. L., Young, A. B. & Penney, J. B. The functional anatomy of basal ganglia disorders. *Trends in Neurosciences* **12,** 366–375 (1989).
172. Alexander, G. E. & Crutcher, M. D. Functional architecture of basal ganglia circuits: neural substrates of parallel processing. *Trends in Neurosciences* **13,** 266–271 (1990).
173. Bergman, H. *et al.* Physiological aspects of information processing in the basal ganglia of normal and parkinsonian primates. *Trends in Neurosciences* **21,** 32–38 (1998).
174. Eusebio, A. *et al.* Resonance in subthalamo-cortical circuits in Parkinson's disease. *Brain* **132,** 2139–2150 (2009).
175. Litvak, V. *et al.* Resting oscillatory cortico-subthalamic connectivity in patients with Parkinson's disease. *Brain* **134,** 359–374 (2011).
176. Hirschmann, J. *et al.* Distinct oscillatory STN-cortical loops revealed by simultaneous MEG and local field potential recordings in patients with Parkinson's disease. *NeuroImage* **55,** 1159–1168 (2011).
177. Hammond, C., Bergman, H. & Brown, P. Pathological synchronization in Parkinson's disease: networks, models and treatments. *Trends in Neurosciences* **30,** 357–364 (2007).
178. Lalo, E. *et al.* Patterns of bidirectional communication between cortex and basal ganglia during movement in patients with Parkinson disease. *Journal of Neuroscience* **28,** 3008–3016 (2008).
179. Shimamoto, S. A. *et al.* Subthalamic nucleus neurons are synchronized to primary motor cortex local field potentials in Parkinson's disease. *Journal of Neuroscience* **33,** 7220–7233 (2013).
180. Brown, P. Oscillatory nature of human basal ganglia activity: relationship to the pathophysiology of Parkinson's disease. *Mov Disord.* **18,** 357–363 (2003).
181. Nambu, A., Tokuno, H. & Takada, M. Functional significance of the cortico-subthalamo-pallidal 'hyperdirect' pathway. *Neuroscience Research* **43,** 111–117 (2002).
182. Obeso, J. A. *et al.* Functional organization of the basal ganglia: therapeutic implications for Parkinson's disease. *Mov Disord.* **23 Suppl 3,** S548–59 (2008).
183. Brown, P. *et al.* Dopamine dependency of oscillations between subthalamic nucleus and pallidum in Parkinson's disease. *Journal of Neuroscience* **21,** 1033–1038 (2001).
184. Williams, D. *et al.* Dopamine-dependent changes in the functional connectivity between basal ganglia and cerebral cortex in humans. *Brain* **125,** 1558–1569 (2002).
185. Zhang, D. & Raichle, M. E. Disease and the brain's dark energy. *Nature Reviews Neurology* **6,** 15–28 (2010).
186. Biswal, B., Yetkin, F. Z., Haughton, V. M. & Hyde, J. S. Functional connectivity in the motor cortex of resting human brain using echo-planar MRI. *Magn. Reson. Med.* **34,** 537–541 (1995).

187. Rogers, B. P., Morgan, V. L., Newton, A. T. & Gore, J. C. Assessing functional connectivity in the human brain by fMRI. *Magnetic Resonance Imaging* **25,** 1347–1357 (2007).
188. Fox, M. D. & Greicius, M. Clinical applications of resting state functional connectivity. *Front Syst Neurosci* **4,** 19 (2010).
189. Sorg, C. *et al.* Selective changes of resting-state networks in individuals at risk for Alzheimer's disease. *Proc. Natl. Acad. Sci. U.S.A.* **104,** 18760–18765 (2007).
190. Greicius, M. D. *et al.* Resting-state functional connectivity in major depression: abnormally increased contributions from subgenual cingulate cortex and thalamus. *BPS* **62,** 429–437 (2007).
191. van den Heuvel, M., Mandl, R., Luigjes, J. & Hulshoff Pol, H. Microstructural organization of the cingulum tract and the level of default mode functional connectivity. *Journal of Neuroscience* **28,** 10844–10851 (2008).
192. Greicius, M. D., Supekar, K., Menon, V. & Dougherty, R. F. Resting-state functional connectivity reflects structural connectivity in the default mode network. *Cerebral Cortex* **19,** 72–78 (2009).
193. Honey, C. J. *et al.* Predicting human resting-state functional connectivity from structural connectivity. *Proc. Natl. Acad. Sci. U.S.A.* **106,** 2035–2040 (2009).
194. Zhang, D., Snyder, A. Z., Shimony, J. S., Fox, M. D. & Raichle, M. E. Noninvasive functional and structural connectivity mapping of the human thalamocortical system. *Cerebral Cortex* **20,** 1187–1194 (2010).
195. Leopold, D. A., Murayama, Y. & Logothetis, N. K. Very slow activity fluctuations in monkey visual cortex: implications for functional brain imaging. *Cereb. Cortex* **13,** 422–433 (2003).
196. Laufs, H. *et al.* EEG-correlated fMRI of human alpha activity. *NeuroImage* **19,** 1463–1476 (2003).
197. He, B. J., Snyder, A. Z., Zempel, J. M., Smyth, M. D. & Raichle, M. E. Electrophysiological correlates of the brain's intrinsic large-scale functional architecture. *Proc. Natl. Acad. Sci. U.S.A.* **105,** 16039–16044 (2008).
198. de Munck, J. C., Gonçalves, S. I., Mammoliti, R., Heethaar, R. M. & Lopes da Silva, F. H. Interactions between different EEG frequency bands and their effect on alpha-fMRI correlations. *NeuroImage* **47,** 69–76 (2009).
199. Wu, T. *et al.* Changes of functional connectivity of the motor network in the resting state in Parkinson's disease. *Neurosci. Lett.* **460,** 6–10 (2009).
200. Helmich, R. C. *et al.* Spatial remapping of cortico-striatal connectivity in Parkinson's disease. *Cerebral Cortex* **20,** 1175–1186 (2010).
201. Baudrexel, S. *et al.* Resting state fMRI reveals increased subthalamic nucleus-motor cortex connectivity in Parkinson's disease. *NeuroImage* **55,** 1728–1738 (2011).
202. Wu, T. *et al.* Functional connectivity of cortical motor areas in the resting state in Parkinson's disease. *Hum. Brain Mapp.* **32,** 1443–1457 (2011).
203. Hacker, C. D., Perlmutter, J. S., Criswell, S. R., Ances, B. M. & Snyder, A. Z. Resting state functional connectivity of the striatum in Parkinson's disease. *Brain* **135,** 3699–3711 (2012).
204. Esposito, F. *et al.* Rhythm-specific modulation of the sensorimotor network in drug-naive patients with Parkinson's disease by levodopa. *Brain* **136,** 710–725 (2013).
205. Li, J. *et al.* Parkinson's disease-related modulation of functional connectivity associated with the striatum in the resting state in a nonhuman primate model. *Brain Research* **1555,** 10–19 (2014).
206. Cerasa, A. *et al.* A network centred on the inferior frontal cortex is critically involved in levodopa-induced dyskinesias. *Brain* **138,** 414–427 (2015).
207. Onu, M., Badea, L., Roceanu, A., Tivarus, M. & Bajenaru, O. Increased connectivity between sensorimotor and attentional areas in Parkinson's disease. *Neuroradiology* 1–12 (2015). doi:10.1007/s00234-015-1556-y
208. Lang, A. E. *et al.* Deep brain stimulation: Preoperative issues. *Mov Disord.* **21,** S171–S196 (2006).
209. Ashburner, J. & Friston, K. J. Unified segmentation. *NeuroImage* **26,** 839–851 (2005).

210. Behzadi, Y., Restom, K., Liau, J. & Liu, T. T. A component based noise correction method (CompCor) for BOLD and perfusion based fMRI. *NeuroImage* **37,** 90–101 (2007).
211. Whitfield-Gabrieli, S. & Nieto-Castanon, A. Conn: a functional connectivity toolbox for correlated and anticorrelated brain networks. *Brain Connectivity* **2,** 125–141 (2012).
212. Power, J. D. *et al.* Methods to detect, characterize, and remove motion artifact in resting state fMRI. *NeuroImage* **84,** 320–341 (2014).
213. Forstmann, B. U. *et al.* Cortico-subthalamic white matter tract strength predicts interindividual efficacy in stopping a motor response. *NeuroImage* **60,** 370–375 (2012).
214. Wichmann, T. & DeLong, M. R. Functional and pathophysiological models of the basal ganglia. *Current Opinion in Neurobiology* **6,** 751–758 (1996).
215. DeLong, M. R. Primate models of movement disorders of basal ganglia origin. *Trends in Neurosciences* **13,** 281–285 (1990).
216. Nyholm, D. & Lennernäs, H. Irregular gastrointestinal drug absorption in Parkinson's disease. *Expert Opin Drug Metab Toxicol* **4,** 193–203 (2008).
217. Leenders, K. L., Poewe, W. H., Palmer, A. J., Brenton, D. P. & Frackowiak, R. S. Inhibition of L-[18F]fluorodopa uptake into human brain by amino acids demonstrated by positron emission tomography. *Ann Neurol.* **20,** 258–262 (1986).
218. Lennernäs, H. *et al.* The effect of L-leucine on the absorption of levodopa, studied by regional jejunal perfusion in man. *Br J Clin Pharmacol* **35,** 243–250 (1993).
219. Huang, C. *et al.* Changes in network activity with the progression of Parkinson's disease. *Brain* **130,** 1834–1846 (2007).
220. Ma, Y., Tang, C., Spetsieris, P. G., Dhawan, V. & Eidelberg, D. Abnormal metabolic network activity in Parkinson's disease: test-retest reproducibility. *J Cereb Blood Flow Metab* **27,** 597–605 (2007).
221. Eidelberg, D. Metabolic brain networks in neurodegenerative disorders: a functional imaging approach. *Trends in Neurosciences* **32,** 548–557 (2009).
222. Herz, D. M., Eickhoff, S. B., Løkkegaard, A. & Siebner, H. R. Functional neuroimaging of motor control in Parkinson's disease: a meta-analysis. *Hum. Brain Mapp.* **35,** 3227–3237 (2014).
223. Gauggel, S., Rieger, M. & Feghoff, T.-A. Inhibition of ongoing responses in patients with Parkinson's disease. *Journal of Neurology, Neurosurgery & Psychiatry* **75,** 539–544 (2004).
224. Aron, A. R. & Poldrack, R. A. Cortical and subcortical contributions to Stop signal response inhibition: role of the subthalamic nucleus. *Journal of Neuroscience* **26,** 2424–2433 (2006).
225. Swick, D., Ashley, V. & Turken, A. U. Left inferior frontal gyrus is critical for response inhibition. *BMC Neurosci* **9,** 102 (2008).
226. Li, C.-S. R., Yan, P., Sinha, R. & Lee, T.-W. Subcortical processes of motor response inhibition during a stop signal task. *NeuroImage* **41,** 1352–1363 (2008).
227. Levy, B. J. & Wagner, A. D. Cognitive control and right ventrolateral prefrontal cortex: reflexive reorienting, motor inhibition, and action updating. *Ann. N. Y. Acad. Sci.* **1224,** 40–62 (2011).
228. Aron, A. R., Robbins, T. W. & Poldrack, R. A. Inhibition and the right inferior frontal cortex: one decade on. *Trends Cogn. Sci. (Regul. Ed.)* **18,** 177–185 (2014).
229. Jahanshahi, M., Obeso, I., Rothwell, J. C. & Obeso, J. A. A fronto-striato-subthalamic-pallidal network for goal-directed and habitual inhibition. *Nat Rev Neurosci* (2015). doi:10.1038/nrn4038
230. Koller, W. C. & Biary, N. M. Volitional control of involuntary movements. *Mov Disord.* **4,** 153–156 (1989).
231. Aron, A. R. From reactive to proactive and selective control: developing a richer model for stopping inappropriate responses. *Biological Psychiatry* **69,** e55–68 (2011).
232. Chen, Y. *et al.* Discriminative analysis of Parkinson's disease based on whole-brain functional connectivity. *PLoS ONE* **10,** e0124153 (2015).

233. Murphy, K., Birn, R. M., Handwerker, D. A., Jones, T. B. & Bandettini, P. A. The impact of global signal regression on resting state correlations: Are anti-correlated networks introduced? *NeuroImage* **44,** 893–905 (2009).
234. Fox, M. D., Zhang, D., Snyder, A. Z. & Raichle, M. E. The global signal and observed anticorrelated resting state brain networks. *Journal of Neurophysiology* **101,** 3270–3283 (2009).
235. Buckner, R. L., Krienen, F. M. & Yeo, B. T. T. Opportunities and limitations of intrinsic functional connectivity MRI. *Nature Publishing Group* **16,** 832–837 (2013).
236. Weissenbacher, A. *et al.* Correlations and anticorrelations in resting-state functional connectivity MRI: a quantitative comparison of preprocessing strategies. *NeuroImage* **47,** 1408–1416 (2009).
237. Chang, C. & Glover, G. H. Effects of model-based physiological noise correction on default mode network anti-correlations and correlations. *NeuroImage* **47,** 1448–1459 (2009).
238. Chai, X. J., Castañón, A. N., Ongür, D. & Whitfield-Gabrieli, S. Anticorrelations in resting state networks without global signal regression. *NeuroImage* **59,** 1420–1428 (2012).
239. Krack, P. *et al.* Five-year follow-up of bilateral stimulation of the subthalamic nucleus in advanced Parkinson's disease. *N Engl J Med* **349,** 1925–1934 (2003).
240. Williams, A. *et al.* Deep brain stimulation plus best medical therapy versus best medical therapy alone for advanced Parkinson's disease (PD SURG trial): a randomised, open-label trial. *The Lancet Neurology* **9,** 581–591 (2010).
241. Haynes, W. I. A. & Haber, S. N. The organization of prefrontal-subthalamic inputs in primates provides an anatomical substrate for both functional specificity and integration: implications for Basal Ganglia models and deep brain stimulation. *Journal of Neuroscience* **33,** 4804–4814 (2013).
242. Nambu, A., Tokuno, H., Inase, M. & Takada, M. Corticosubthalamic input zones from forelimb representations of the dorsal and ventral divisions of the premotor cortex in the macaque monkey: comparison with the input zones from the primary motor cortex and the supplementary motor area. *Neuroscience Letters* **239,** 13–16 (1997).
243. Nambu, A., Takada, M., Inase, M. & Tokuno, H. Dual somatotopical representations in the primate subthalamic nucleus: evidence for ordered but reversed body-map transformations from the primary motor cortex and the supplementary motor area. *J. Neurosci.* **16,** 2671–2683 (1996).
244. Nakano, K. *et al.* Topographical projections from the thalamus, subthalamic nucleus and pedunculopontine tegmental nucleus to the striatum in the Japanese monkey, Macaca fuscata. *Brain Research* **537,** 54–68 (1990).
245. Lambert, C. *et al.* Confirmation of functional zones within the human subthalamic nucleus: patterns of connectivity and sub-parcellation using diffusion weighted imaging. *NeuroImage* **60,** 83–94 (2012).
246. Garcia-Garcia, D. *et al.* Stimulation sites in the subthalamic nucleus and clinical improvement in Parkinson's disease: a new approach for active contact localization. *Journal of Neurosurgery* 1–12 (2016). doi:10.3171/2015.9.JNS15868
247. Zheng, Z. *et al.* Subthalamic deep brain stimulation for Parkinson's disease: correlation of active contacts and electrophysiologically mapped subthalamic nucleus. *Chin. Med. J.* **122,** 2419–2422 (2009).
248. Vergani, F. *et al.* Anatomical identification of active contacts in subthalamic deep brain stimulation. *Surgical Neurology* **67,** 140–146 (2007).
249. Godinho, F. *et al.* Subthalamic nucleus stimulation in Parkinson's disease : anatomical and electrophysiological localization of active contacts. *J Neurol* **253,** 1347–1355 (2006).
250. Plaha, P. Stimulation of the caudal zona incerta is superior to stimulation of the subthalamic nucleus in improving contralateral parkinsonism. *Brain* **129,** 1732–1747 (2006).
251. Yelnik, J. *et al.* Localization of stimulating electrodes in patients with Parkinson disease by using a three-dimensional atlas-magnetic resonance imaging coregistration method. *Journal of Neurosurgery* **99,** 89–99 (2003).

252. Cintas, P. *et al.* Deep brain stimulation for parkinson's disease: correlation between intraoperative subthalamic nucleus neurophysiology and most effective contacts. *Stereotact Funct Neurosurg* **80,** 108–113 (2003).
253. Voges, J. *et al.* Bilateral high-frequency stimulation in the subthalamic nucleus for the treatment of Parkinson disease: correlation of therapeutic effect with anatomical electrode position. *Journal of Neurosurgery* **96,** 269–279 (2002).
254. Zonenshayn, M., Sterio, D., Kelly, P. J., Rezai, A. R. & Beric, A. Location of the active contact within the subthalamic nucleus (STN) in the treatment of idiopathic Parkinson's disease. *Surgical Neurology* **62,** 216–225 (2004).
255. Herzog, J. *et al.* Most effective stimulation site in subthalamic deep brain stimulation for Parkinson's disease. *Mov Disord.* **19,** 1050–1054 (2004).
256. Hamel, W. *et al.* Deep brain stimulation of the subthalamic nucleus in Parkinson's disease: evaluation of active electrode contacts. *Journal of Neurology, Neurosurgery & Psychiatry* **74,** 1036–1046 (2003).
257. Lanotte, M. M. *et al.* Deep brain stimulation of the subthalamic nucleus: anatomical, neurophysiological, and outcome correlations with the effects of stimulation. *Journal of Neurology, Neurosurgery & Psychiatry* **72,** 53–58 (2002).
258. Yokoyama, T. *et al.* The Optimal Stimulation Site for Chronic Stimulation of the Subthalamic Nucleus in Parkinson’s Disease. *Stereotact Funct Neurosurg* **77,** 61–67 (2001).
259. Cho, Z.-H. *et al.* Direct visualization of deep brain stimulation targets in Parkinson disease with the use of 7-tesla magnetic resonance imaging. *Journal of Neurosurgery* **113,** 639–647 (2010).
260. Petersen, E. A. *et al.* Minimizing brain shift in stereotactic functional neurosurgery. *Neurosurgery* **67,** ons213–21– discussion ons221 (2010).
261. Hamani, C. The subthalamic nucleus in the context of movement disorders. *Brain* **127,** 4–20 (2004).
262. Schaltenbrand, G., Wahren, W. & Hassler, R. *Atlas for Stereotaxy of the Human Brain*. (Thieme Medical Publishers, 1977).
263. Coenen, V. A., Prescher, A., Schmidt, T., Picozzi, P. & Gielen, F. L. H. What is dorso-lateral in the subthalamic Nucleus (STN)?—a topographic and anatomical consideration on the ambiguous description of today's primary target for deep brain stimulation (DBS) surgery. *Acta Neurochir* **150,** 1163–1165 (2008).
264. Hardman, C. D. *et al.* Comparison of the basal ganglia in rats, marmosets, macaques, baboons, and humans: Volume and neuronal number for the output, internal relay, and striatal modulating nuclei. *J. Comp. Neurol.* **445,** 238–255 (2002).
265. Sotiropoulos, S. N. & Steinmetz, P. N. Assessing the direct effects of deep brain stimulation using embedded axon models. *J. Neural Eng.* **4,** 107–119 (2007).
266. Schmidt, C. & van Rienen, U. Modeling the field distribution in deep brain stimulation: the influence of anisotropy of brain tissue. *IEEE Trans. Biomed. Eng.* **59,** 1583–1592 (2012).
267. Lumsden, D. E. *et al.* Observation and modeling of deep brain stimulation electrode depth in the pallidal target of the developing brain. *WNEU* **83,** 438–446 (2015).
268. Zhang, T. C. & Grill, W. M. Modeling deep brain stimulation: point source approximation versus realistic representation of the electrode. *J. Neural Eng.* **7,** 066009 (2010).
269. Gradinaru, V., Mogri, M., Thompson, K. R., Henderson, J. M. & Deisseroth, K. Optical deconstruction of parkinsonian neural circuitry. *Science* **324,** 354–359 (2009).
270. Kitai, S. T. & Kita, H. in *The Basal Ganglia II: Structure and Function—Current Concepts* (eds. Carpenter, M. B. & Jayaraman, A.) 357–373 (Springer US, 1987). doi:10.1007/978-1-4684-5347-8_25
271. Parent, A. & Hazrati, L. N. Functional anatomy of the basal ganglia. II. The place of subthalamic nucleus and external pallidum in basal ganglia circuitry. *Brain Res. Brain Res. Rev.* **20,** 128–154 (1995).
272. Alexander, G. E., Crutcher, M. D. & DeLong, M. R. Basal ganglia-thalamocortical circuits: parallel substrates for motor, oculomotor, "prefrontal" and 'limbic' functions. *Prog. Brain Res.* **85,** 119–146 (1990).

273. Hughes, A. J., Daniel, S. E., Kilford, L. & Lees, A. J. Accuracy of clinical diagnosis of idiopathic Parkinson's disease: a clinico-pathological study of 100 cases. *Journal of Neurology, Neurosurgery & Psychiatry* **55,** 181–184 (1992).
274. Holl, E. M. *et al.* Improving Targeting in Image-Guided Frame-Based Deep Brain Stimulation. *Neurosurgery* **67,** ons437–ons447 (2010).
275. Foltynie, T. *et al.* MRI-guided STN DBS in Parkinson's disease without microelectrode recording: efficacy and safety. *Journal of Neurology, Neurosurgery & Psychiatry* **82,** 358–363 (2011).
276. Bejjani, B. P. *et al.* Bilateral subthalamic stimulation for Parkinson's disease by using three-dimensional stereotactic magnetic resonance imaging and electrophysiological guidance. *Journal of Neurosurgery* **92,** 615–625 (2000).
277. Smith, S. M. Fast robust automated brain extraction. *Hum. Brain Mapp.* **17,** 143–155 (2002).
278. Grabner, G. *et al.* Symmetric atlasing and model based segmentation: an application to the hippocampus in older adults. *Med Image Comput Comput Assist Interv* **9,** 58–66 (2006).
279. Jenkinson, M., Bannister, P., Brady, M. & Smith, S. Improved optimization for the robust and accurate linear registration and motion correction of brain images. *NeuroImage* **17,** 825–841 (2002).
280. Jenkinson, M. & Smith, S. A global optimisation method for robust affine registration of brain images. *Med Image Anal* **5,** 143–156 (2001).
281. Andersson, J. L. R., Jenkinson, M. & Smith, S. Non-linear registration aka Spatial normalisation. (2007). Available at: http://www.fmrib.ox.ac.uk/analysis/techrep/tr07ja2/tr07ja2.pdf. (Accessed: 18 May 2016)
282. Hernandez-Fernandez, M. *et al.* A fast and flexible toolbox for tracking brain connections in diffusion MRI datasets using GPUs. in **22nd Annual Meeting,** (2016).
283. Jbabdi, S. & Johansen-Berg, H. Tractography: where do we go from here? *Brain Connectivity* **1,** 169–183 (2011).
284. Plaha, P., Khan, S. & Gill, S. S. Bilateral stimulation of the caudal zona incerta nucleus for tremor control. *Journal of Neurology, Neurosurgery & Psychiatry* **79,** 504–513 (2008).
285. Tripoliti, E., Akram, H. & Holl, E. *A Subtle Change In MRI-verified Targeting Significantly Improves Long-term Speech Outcome After STN-DBS*. (…, 2013).
286. Zaidel, A., Bergman, H., Ritov, Y. & MD, Z. I. Levodopa and subthalamic deep brain stimulation responses are not congruent. *Mov Disord.* **25,** 2379–2386 (2010).
287. Vickers, A. J. The use of percentage change from baseline as an outcome in a controlled trial is statistically inefficient: a simulation study. *BMC Med Res Methodol* **1,** 6 (2001).
288. Avecillas-Chasin, J. M., Rascón-Ramírez, F. & Barcia, J. A. Tractographical model of the cortico-basal ganglia and corticothalamic connections: Improving Our Understanding of Deep Brain Stimulation. *Clin Anat* **29,** 481–492 (2016).
289. Vanegas-Arroyave, N. *et al.* Tractography patterns of subthalamic nucleus deep brain stimulation. *Brain* **139,** 1200–1210 (2016).
290. Aravamuthan, B. R., Muthusamy, K. A., Stein, J. F., Aziz, T. Z. & Johansen-Berg, H. Topography of cortical and subcortical connections of the human pedunculopontine and subthalamic nuclei. *NeuroImage* **37,** 694–705 (2007).
291. Rektor, I., Bočková, M., Chrastina, J., Rektorová, I. & Baláž, M. The modulatory role of subthalamic nucleus in cognitive functions - a viewpoint. *Clin Neurophysiol* **126,** 653–658 (2015).
292. Obeso, I. *et al.* Stimulation of the pre-SMA influences cerebral blood flow in frontal areas involved with inhibitory control of action. *Brain Stimulation* **6,** 769–776 (2013).
293. Jahanshahi, M., Obeso, I., Baunez, C., Alegre, M. & Krack, P. Parkinson's disease, the subthalamic nucleus, inhibition, and impulsivity. *Mov Disord.* **30,** 128–140 (2015).
294. Obeso, I., Wilkinson, L., Rodriguez-Oroz, M. C., Obeso, J. A. & Jahanshahi, M. Bilateral stimulation of the subthalamic nucleus has differential effects on reactive and proactive inhibition and conflict-induced slowing in Parkinson's disease. *Exp Brain Res* **226,** 451–462 (2013).

295. Hallett, M. Parkinson's disease tremor: pathophysiology. *Parkinsonism and Related Disorders* **18 Suppl 1,** S85–6 (2012).
296. Ni, Z., Pinto, A. D., Lang, A. E. & Chen, R. Involvement of the cerebellothalamocortical pathway in Parkinson disease. *Ann Neurol.* **68,** 816–824 (2010).
297. Bostan, A. C., Dum, R. P. & Strick, P. L. The basal ganglia communicate with the cerebellum. *Proc. Natl. Acad. Sci. U.S.A.* **107,** 8452–8456 (2010).
298. Timmermann, L. *et al.* The cerebral oscillatory network of parkinsonian resting tremor. *Brain* **126,** 199–212 (2003).
299. Helmich, R. C., Janssen, M. J. R., Oyen, W. J. G., Bloem, B. R. & Toni, I. Pallidal dysfunction drives a cerebellothalamic circuit into Parkinson tremor. *Ann Neurol.* **69,** 269–281 (2011).
300. Kahan, J. *et al.* Resting state functional MRI in Parkinson's disease: the impact of deep brain stimulation on “effective” connectivity. *Brain* **137,** 1130–1144 (2014).
301. Eitan, R. *et al.* Asymmetric right/left encoding of emotions in the human subthalamic nucleus. *Front Syst Neurosci* **7,** 69 (2013).
302. Kriegeskorte, N., Bodurka, J. & Bandettini, P. Artifactual time-course correlations in echo-planar fMRI with implications for studies of brain function. *International Journal of Imaging Systems and Technology* **18,** 345–349 (2008).
303. Feinberg, D. A. & Setsompop, K. Ultra-fast MRI of the human brain with simultaneous multi-slice imaging. *J. Magn. Reson.* **229,** 90–100 (2013).
304. Limousin, P. *et al.* Electrical stimulation of the subthalamic nucleus in advanced Parkinson's disease. *N Engl J Med* **339,** 1105–1111 (1998).
305. Deuschl, G. *et al.* A randomized trial of deep-brain stimulation for Parkinson's disease. *N Engl J Med* **355,** 896–908 (2006).
306. Fox, S. H. *et al.* The Movement Disorder Society Evidence-Based Medicine Review Update: Treatments for the motor symptoms of Parkinson's disease. *Mov Disord.* **26 Suppl 3,** S2–41 (2011).
307. Lawrence, D. G. & Hopkins, D. A. The development of motor control in the rhesus monkey: evidence concerning the role of corticomotoneuronal connections. *Brain* **99,** 235–254 (1976).
308. Pan, C., Peck, K. K., Young, R. J. & Holodny, A. I. Somatotopic organization of motor pathways in the internal capsule: a probabilistic diffusion tractography study. *American Journal of Neuroradiology* **33,** 1274–1280 (2012).
309. Cao, C. *et al.* Subthalamus deep brain stimulation for primary dystonia patients: a long-term follow-up study. *Mov Disord.* **28,** 1877–1882 (2013).
310. Ashby, P., Kim, Y. J., Kumar, R., Lang, A. E. & Lozano, A. M. Neurophysiological effects of stimulation through electrodes in the human subthalamic nucleus. *Brain* **122 (Pt 10),** 1919–1931 (1999).
311. Tommasi, G. *et al.* Pyramidal tract side effects induced by deep brain stimulation of the subthalamic nucleus. *Journal of Neurology, Neurosurgery & Psychiatry* **79,** 813–819 (2008).
312. Baizabal Carvallo, J. F. & Jankovic, J. Movement disorders induced by deep brain stimulation. *Parkinsonism and Related Disorders* **25,** 1–9 (2016).
313. Jung, Y. J. *et al.* An 8-Year Follow-up on the Effect of Subthalamic Nucleus Deep Brain Stimulation on Pain in Parkinson Disease. *JAMA Neurol* **72,** 504–510 (2015).
314. Tripoliti, E. *et al.* Predictive factors of speech intelligibility following subthalamic nucleus stimulation in consecutive patients with Parkinson's disease. *Mov Disord.* **29,** 532–538 (2014).
315. Tsuboi, T. *et al.* Distinct phenotypes of speech and voice disorders in Parkinson's disease after subthalamic nucleus deep brain stimulation. *Journal of Neurology, Neurosurgery & Psychiatry* **86,** 856–864 (2015).
316. Strafella, A. *et al.* Inhibition of voluntary activity by thalamic stimulation in humans: relevance for the control of tremor. *Mov Disord.* **12,** 727–737 (1997).
317. Hanajima, R. *et al.* Somatosensory evoked potentials (SEPs) recorded from deep brain stimulation (DBS) electrodes in the thalamus and subthalamic nucleus (STN). *Clin Neurophysiol* **115,** 424–434 (2004).

318. Costa, J., Valls-Sole, J., Valldeoriola, F., Rumia, J. & Tolosa, E. Motor responses of muscles supplied by cranial nerves to subthalamic nucleus deep brain stimuli. *Brain* **130,** 245–255 (2006).
319. Yorkston, K. M., Beukelman, D. R. & Honsinger, M. J. Perceived articulatory adequacy and velopharyngeal function in dysarthric speakers. *Arch Phys Med Rehabil* **70,** 313–317 (1989).
320. Yousry, T. A. *et al.* Localization of the motor hand area to a knob on the precentral gyrus. A new landmark. *Brain* **120,** 141–157 (1997).
321. Meyer, B. U., Werhahn, K., Rothwell, J. C., Roericht, S. & Fauth, C. Functional organisation of corticonuclear pathways to motoneurones of lower facial muscles in man. *Exp Brain Res* **101,** 465–472 (1994).
322. Triggs, W. J., Ghacibeh, G., Springer, U. & Bowers, D. Lateralized asymmetry of facial motor evoked potentials. *Neurology* **65,** 541–544 (2005).
323. Ranck, J. B. Which elements are excited in electrical stimulation of mammalian central nervous system: a review. *Brain Research* **98,** 417–440 (1975).
324. Reich, M. M. *et al.* Short pulse width widens the therapeutic window of subthalamic neurostimulation. *Ann Clin Transl Neurol* **2,** 427–432 (2015).
325. Gordon, T., Thomas, C. K., Munson, J. B. & Stein, R. B. The resilience of the size principle in the organization of motor unit properties in normal and reinnervated adult skeletal muscles. *Can. J. Physiol. Pharmacol.* **82,** 645–661 (2004).
326. Whitmer, D. *et al.* High frequency deep brain stimulation attenuates subthalamic and cortical rhythms in Parkinson's disease. *Front Hum Neurosci* **6,** 155 (2012).
327. Ozaki, I., Baba, M., Narita, S., Matsunaga, M. & Takebe, K. Pure dysarthria due to anterior internal capsule and/or corona radiata infarction: a report of five cases. *Journal of Neurology, Neurosurgery & Psychiatry* **49,** 1435–1437 (1986).
328. Åström, M. *et al.* Patient-Specific Model-Based Investigation of Speech Intelligibility and Movement during Deep Brain Stimulation. *Stereotact Funct Neurosurg* **88,** 224–233 (2010).
329. Pahwa, R. *et al.* Comparison of thalamotomy to deep brain stimulation of the thalamus in essential tremor. *Mov Disord.* **16,** 140–143 (2001).
330. Berk, C., Carr, J., Sinden, M., Martzke, J. & Honey, C. R. Assessing tremor reduction and quality of life following thalamic deep brain stimulation for the treatment of tremor in multiple sclerosis. *Journal of Neurology, Neurosurgery & Psychiatry* **75,** 1210–author reply 1210–1 (2004).
331. Benabid, A. L. *et al.* [Treatment of Parkinson tremor by chronic stimulation of the ventral intermediate nucleus of the thalamus]. *Rev. Neurol. (Paris)* **145,** 320–323 (1989).
332. Benabid, A. L. *et al.* Long-term suppression of tremor by chronic stimulation of the ventral intermediate thalamic nucleus. *The Lancet* **337,** 403–406 (1991).
333. Pollak, P. *et al.* Long-term effects of chronic stimulation of the ventral intermediate thalamic nucleus in different types of tremor. *Adv Neurol* **60,** 408–413 (1993).
334. Benabid, A. L. *et al.* Chronic VIM thalamic stimulation in Parkinson's disease, essential tremor and extra-pyramidal dyskinesias. *Acta Neurochir Suppl (Wien)* **58,** 39–44 (1993).
335. Schuurman, P. R., Bosch, D. A., Merkus, M. P. & Speelman, J. D. Long-term follow-up of thalamic stimulation versus thalamotomy for tremor suppression. *Mov Disord.* **23,** 1146–1153 (2008).
336. Hariz, M. I. *et al.* Multicentre European study of thalamic stimulation for parkinsonian tremor: a 6 year follow-up. *Journal of Neurology, Neurosurgery & Psychiatry* **79,** 694–699 (2007).
337. Murata, J.-I. *et al.* Electrical stimulation of the posterior subthalamic area for the treatment of intractable proximal tremor. *Journal of Neurosurgery* **99,** 708–715 (2003).
338. Blomstedt, P., Sandvik, U., Fytagoridis, A. & Tisch, S. The posterior subthalamic area in the treatment of movement disorders: past, present, and future. *Neurosurgery* **64,** 1029–38– discussion 1038–42 (2009).

339. Blomstedt, P., Sandvik, U. & Tisch, S. Deep brain stimulation in the posterior subthalamic area in the treatment of essential tremor. *Mov Disord.* **25,** 1350–1356 (2010).
340. Blomstedt, P., Hariz, G. M., Hariz, M. I. & Koskinen, L. O. D. Thalamic deep brain stimulation in the treatment of essential tremor: a long-term follow-up. *Br J Neurosurg* **21,** 504–509 (2007).
341. Gallay, M. N., Jeanmonod, D., Liu, J. & Morel, A. Human pallidothalamic and cerebellothalamic tracts: anatomical basis for functional stereotactic neurosurgery. *Brain Struct Funct* **212,** 443–463 (2008).
342. McIntyre, C. C. & Hahn, P. J. Network perspectives on the mechanisms of deep brain stimulation. *Neurobiology of Disease* **38,** 329–337 (2010).
343. Jörntell, H. & Ekerot, C. F. Topographical organization of projections to cat motor cortex from nucleus interpositus anterior and forelimb skin. *The Journal of Physiology* **514 (Pt 2),** 551–566 (1999).
344. Dum, R. P. & Strick, P. L. An unfolded map of the cerebellar dentate nucleus and its projections to the cerebral cortex. *Journal of Neurophysiology* **89,** 634–639 (2003).
345. Helmich, R. C., Hallett, M., Deuschl, G., Toni, I. & Bloem, B. R. Cerebral causes and consequences of parkinsonian resting tremor: a tale of two circuits? *Brain* **135,** 3206–3226 (2012).
346. Baker, K. B., Schuster, D., Cooperrider, J. & Machado, A. G. Deep brain stimulation of the lateral cerebellar nucleus produces frequency-specific alterations in motor evoked potentials in the rat in vivo. *Experimental Neurology* **226,** 259–264 (2010).
347. Lemaire, J.-J. *et al.* Anatomy of the human thalamus based on spontaneous contrast and microscopic voxels in high-field magnetic resonance imaging. *Neurosurgery* **66,** 161–172 (2010).
348. Deistung, A. *et al.* Toward in vivo histology: A comparison of quantitative susceptibility mapping (QSM) with magnitude-, phase-, and $R2_*$-imaging at ultra-high magnetic field strength. *NeuroImage* **65,** 299–314 (2013).
349. Traynor, C. R., Barker, G. J., Crum, W. R., Williams, S. C. R. & Richardson, M. P. Segmentation of the thalamus in MRI based on T1 and T2. *NeuroImage* **56,** 939–950 (2011).
350. Vassal, F. *et al.* Direct stereotactic targeting of the ventrointermediate nucleus of the thalamus based on anatomic 1.5-T MRI mapping with a white matter attenuated inversion recovery (WAIR) sequence. *Brain Stimulation* **5,** 625–633 (2012).
351. Gross, R. E., Krack, P., Rodriguez-Oroz, M. C., Rezai, A. R. & Benabid, A. L. Electrophysiological mapping for the implantation of deep brain stimulators for Parkinson's disease and tremor. *Mov Disord.* **21,** S259–S283 (2006).
352. Witjas, T. *et al.* A prospective single-blind study of Gamma Knife thalamotomy for tremor. *Neurology* **85,** 1562–1568 (2015).
353. Elias, W. J. *et al.* A Randomized Trial of Focused Ultrasound Thalamotomy for Essential Tremor. *N Engl J Med* **375,** 730–739 (2016).
354. Spiegelmann, R., Nissim, O., Daniels, D., Ocherashvilli, A. & Mardor, Y. Stereotactic Targeting of the Ventrointermediate Nucleus of the Thalamus by Direct Visualization with High-Field MRI. *Stereotact Funct Neurosurg* **84,** 19–23 (2006).
355. Lefranc, M., Carron, R. & Régis, J. Prelemniscal Radiations: A New Reliable Landmark of the Thalamic Nucleus Ventralis Intermedius Location. *Stereotact Funct Neurosurg* **93,** 400–406 (2015).
356. Sedrak, M. *et al.* Diffusion tensor imaging and colored fractional anisotropy mapping of the ventralis intermedius nucleus of the thalamus. *Neurosurgery* **69,** 1124–9–discussion 1129–30 (2011).
357. Sammartino, F. *et al.* Tractography-Based Ventral Intermediate Nucleus Targeting: Novel Methodology and Intraoperative Validation. *Mov Disord.* **31,** 1217–1225 (2016).
358. Coenen, V. A. *et al.* One-pass deep brain stimulation of dentato-rubro-thalamic tract and subthalamic nucleus for tremor-dominant or equivalent type Parkinson's disease. *Acta Neurochir* **158,** 773–781 (2016).

359. Lambert, C., Simon, H., Colman, J. & Barrick, T. R. Defining Thalamic Nuclei and Topographic Connectivity Gradients in vivo. *NeuroImage* (2016). doi:10.1016/j.neuroimage.2016.08.028
360. Calabrese, E. *et al.* Postmortem diffusion MRI of the human brainstem and thalamus for deep brain stimulator electrode localization. *Hum. Brain Mapp.* **36,** 3167–3178 (2015).
361. Miller, K. L. *et al.* Diffusion imaging of whole, post-mortem human brains on a clinical MRI scanner. *NeuroImage* **57,** 167–181 (2011).
362. Jankovic, J. & Tolosa, E. *Parkinson's disease and movement disorders*. (2007).
363. Hess, C. W. & Pullman, S. L. Tremor: clinical phenomenology and assessment techniques. *Tremor Other Hyperkinet Mov (N Y)* **2,** (2012).
364. Hirabayashi, H., Tengvar, M. & Hariz, M. I. Stereotactic imaging of the pallidal target. *Mov Disord.* **17,** S130–S134 (2002).
365. Yushkevich, P. A. *et al.* User-guided 3D active contour segmentation of anatomical structures: significantly improved efficiency and reliability. *NeuroImage* **31,** 1116–1128 (2006).
366. Jones, D. K., Simmons, A., Williams, S. C. & Horsfield, M. A. Non-invasive assessment of axonal fiber connectivity in the human brain via diffusion tensor MRI. *Magn. Reson. Med.* **42,** 37–41 (1999).
367. Morel, A., Magnin, M. & Jeanmonod, D. Multiarchitectonic and stereotactic atlas of the human thalamus. *J. Comp. Neurol.* **387,** 588–630 (1997).
368. Jones, E. G. *The Thalamus*. (Springer Science & Business Media, 2012).
369. Tanaka, D. Thalamic projections of the dorsomedial prefrontal cortex in the rhesus monkey (Macaca mulatta). *Brain Research* **110,** 21–38 (1976).
370. Tobias, T. J. Afferents to prefrontal cortex from the thalamic mediodorsal nucleus in the rhesus monkey. *Brain Research* **83,** 191–212 (1975).
371. Markowitsch, H. J., Irle, E. & Emmans, D. Cortical and subcortical afferent connections of the squirrel monkey's (lateral) premotor cortex: evidence for visual cortical afferents. *Int J Neurosci* **37,** 127–148 (1987).
372. Yarita, H., Iino, M., Tanabe, T., Kogure, S. & Takagi, S. F. A transthalamic olfactory pathway to orbitofrontal cortex in the monkey. *Journal of Neurophysiology* **43,** 69–85 (1980).
373. Russchen, F. T., Amaral, D. G. & Price, J. L. The afferent input to the magnocellular division of the mediodorsal thalamic nucleus in the monkey, Macaca fascicularis. *J. Comp. Neurol.* **256,** 175–210 (1987).
374. Jones, E. G. & Powell, T. P. Connexions of the somatic sensory cortex of the rhesus monkey. 3. Thalamic connexions. *Brain* **93,** 37–56 (1970).
375. Jones, E. G., Wise, S. P. & Coulter, J. D. Differential thalamic relationships of sensory-motor and parietal cortical fields in monkeys. *J. Comp. Neurol.* **183,** 833–881 (1979).
376. Johansen-Berg, H. Functional-Anatomical Validation and Individual Variation of Diffusion Tractography-based Segmentation of the Human Thalamus. *Cerebral Cortex* **15,** 31–39 (2004).
377. Hyam, J. A. *et al.* Contrasting Connectivity of the Ventralis Intermedius and Ventralis Oralis Posterior Nuclei of the Motor Thalamus Demonstrated by Probabilistic Tractography. *Neurosurgery* **70,** 162–169 (2012).
378. Nieuwenhuys, R., Voogd, J. & van Huijzen, C. *The Human Central Nervous System*. (Springer Science & Business Media, 2013).
379. Parent, A. & De Bellefeuille, L. Organization of efferent projections from the internal segment of globus pallidus in primate as revealed by fluorescence retrograde labeling method. *Brain Research* **245,** 201–213 (1982).
380. Sakai, S. T., Stepniewska, I., Qi, H. X. & Kaas, J. H. Pallidal and cerebellar afferents to pre-supplementary motor area thalamocortical neurons in the owl monkey: a multiple labeling study. *J. Comp. Neurol.* **417,** 164–180 (2000).
381. DeVito, J. L. & Anderson, M. E. An autoradiographic study of efferent connections of the globus pallidus in Macaca mulatta. *Exp Brain Res* **46,** 107–117 (1982).

382. Sakai, S. T., Inase, M. & Tanji, J. Pallidal and cerebellar inputs to thalamocortical neurons projecting to the supplementary motor area in Macaca fuscata: a triple-labeling light microscopic study. *Anat. Embryol.* **199,** 9–19 (1999).
383. Nauta, H. J. Projections of the pallidal complex: an autoradiographic study in the cat. *NSC* **4,** 1853–1873 (1979).
384. Kuo, J. S. & Carpenter, M. B. Organization of pallidothalamic projections in the rhesus monkey. *J. Comp. Neurol.* **151,** 201–236 (1973).
385. Schell, G. R. & Strick, P. L. The origin of thalamic inputs to the arcuate premotor and supplementary motor areas. *J. Neurosci.* **4,** 539–560 (1984).
386. Strick, P. L. Light microscopic analysis of the cortical projection of the thalamic ventrolateral nucleus in the cat. *Brain Research* **55,** 1–24 (1973).
387. Asanuma, C., Thach, W. T. & Jones, E. G. Distribution of cerebellar terminations and their relation to other afferent terminations in the ventral lateral thalamic region of the monkey. *Brain Research* **286,** 237–265 (1983).
388. Percheron, G. *et al.* The primate motor thalamus analysed with reference to subcortical afferent territories. *Stereotact Funct Neurosurg* **60,** 32–41 (1993).
389. Hassler, R. [Anatomy of the thalamus]. *Arch Psychiatr Nervenkr Z Gesamte Neurol Psychiatr* **184,** 249–256 (1950).
390. Hirai, T. & Jones, E. G. A new parcellation of the human thalamus on the basis of histochemical staining. *Brain Res. Brain Res. Rev.* **14,** 1–34 (1989).
391. Deuschl, G., Raethjen, J., Lindemann, M. & Krack, P. The pathophysiology of tremor. *Muscle Nerve* **24,** 716–735 (2001).
392. Deuschl, G. *et al.* The pathophysiology of parkinsonian tremor: a review. *J Neurol* **247 Suppl 5,** V33–48 (2000).
393. Deuschl, G. & Elble, R. J. The pathophysiology of essential tremor. *Neurology* **54,** S14–20 (2000).
394. Elble, R. *et al.* Reliability of a new scale for essential tremor. *Mov Disord.* **27,** 1567–1569 (2012).
395. Elble, R. *et al.* Task force report: scales for screening and evaluating tremor: critique and recommendations. *Mov Disord.* **28,** 1793–1800 (2013).
396. Stacy, M. A. *et al.* Assessment of interrater and intrarater reliability of the Fahn-Tolosa-Marin Tremor Rating Scale in essential tremor. *Mov Disord.* **22,** 833–838 (2007).
397. Headache Classification Subcommittee of the International Headache Society. The International Classification of Headache Disorders: 2nd edition. *Cephalalgia* **24 Suppl 1,** 9–160 (2004).
398. Donnet, A. *et al.* Chronic cluster headache: a French clinical descriptive study. *Journal of Neurology, Neurosurgery & Psychiatry* **78,** 1354–1358 (2007).
399. Rothrock, J. Cluster: A Potentially Lethal Headache Disorder. *Headache: The Journal of Head and Face Pain* **46,** 327–327 (2006).
400. May, A. Cluster headache: pathogenesis, diagnosis, and management. *Lancet* **366,** 843–855 (2005).
401. Leroux, E. & Ducros, A. Cluster headache. *Orphanet J Rare Dis* **3,** 20 (2008).
402. Russell, M. B. Epidemiology and genetics of cluster headache. *The Lancet Neurology* **3,** 279–283 (2004).
403. Bahra, A., May, A. & Goadsby, P. J. Cluster headache: a prospective clinical study with diagnostic implications. *Neurology* **58,** 354–361 (2002).
404. Fischera, M., Marziniak, M., Gralow, I. & Evers, S. The incidence and prevalence of cluster headache: a meta-analysis of population-based studies. *Cephalalgia* **28,** 614–618 (2008).
405. May, A. *et al.* EFNS guidelines on the treatment of cluster headache and other trigeminal-autonomic cephalalgias. *European Journal of Neurology* **13,** 1066–1077 (2006).
406. Magis, D. & Schoenen, J. Advances and challenges in neurostimulation for headaches. *The Lancet Neurology* **11,** 708–719 (2012).
407. Clelland, C. D., Zheng, Z., Kim, W., Bari, A. & Pouratian, N. Common cerebral networks associated with distinct deep brain stimulation targets for cluster headache. *Cephalalgia* (2013). doi:10.1177/0333102413509431

408. Schoenen, J. *et al.* Stimulation of the sphenopalatine ganglion (SPG) for cluster headache treatment. Pathway CH-1: a randomized, sham-controlled study. *Cephalalgia* **33,** 816–830 (2013).
409. Goadsby, P. J., Schoenen, J., Ferrari, M. D., Silberstein, S. D. & Dodick, D. Towards a definition of intractable headache for use in clinical practice and trials. *Cephalalgia* **26,** 1168–1170 (2006).
410. Dworkin, R. H. *et al.* Interpreting the clinical importance of treatment outcomes in chronic pain clinical trials: IMMPACT recommendations. in **9,** 105–121 (2008).
411. Mueller, O. M. *et al.* Occipital nerve stimulation for the treatment of chronic cluster headache - lessons learned from 18 months experience. *Cen Eur Neurosurg* **72,** 84–89 (2011).
412. Stewart, W. F., Lipton, R. B., Kolodner, K., Liberman, J. & Sawyer, J. Reliability of the migraine disability assessment score in a population-based sample of headache sufferers. *Cephalalgia* **19,** 107–14– discussion 74 (1999).
413. Kosinski, M. *et al.* A six-item short-form survey for measuring headache impact: the HIT-6. *Qual Life Res* **12,** 963–974 (2003).
414. Burns, B., Watkins, L. & Goadsby, P. J. Treatment of hemicrania continua by occipital nerve stimulation with a bion device: long-term follow-up of a crossover study. *The Lancet Neurology* **7,** 1001–1012 (2008).
415. Schwedt, T. J., Dodick, D. W., Hentz, J., Trentman, T. L. & Zimmerman, R. S. Occipital nerve stimulation for chronic headache--long-term safety and efficacy. *Cephalalgia* **27,** 153–157 (2007).
416. Mykletun, A., Stordal, E. & Dahl, A. A. Hospital Anxiety and Depression (HAD) scale: factor structure, item analyses and internal consistency in a large population. *Br J Psychiatry* **179,** 540–544 (2001).
417. May, A. Hypothalamic Deep Brain Stimulation in Positron Emission Tomography. *Journal of Neuroscience* **26,** 3589–3593 (2006).
418. Matharu, M. S. & Zrinzo, L. Deep Brain Stimulation in Cluster Headache: Hypothalamus or Midbrain Tegmentum? *Curr Pain Headache Rep* **14,** 151–159 (2010).
419. Leone, M., Franzini, A., Cecchini, A. P. & Bussone, G. Success, failure, and putative mechanisms in hypothalamic stimulation for drug-resistant chronic cluster headache. *PAIN* **154,** 89–94 (2013).
420. *Joint Formulary Committee. British National Formulary (online) London: BMJ Group and Pharmaceutical Press <http://www.medicinescomplete.com> [Accessed March 2015])*. (2015).
421. Sano, K., Mayanagi, Y., Sekino, H., Ogashiwa, M. & Ishijima, B. Results of stimulation and destruction of the posterior hypothalamus in man. *Journal of Neurosurgery* **33,** 689–707 (1970).
422. Fontaine, D. *et al.* Anatomical location of effective deep brain stimulation electrodes in chronic cluster headache. *Brain* **133,** 1214–1223 (2010).
423. Schlaepfer, T. E., Bewernick, B. H., Kayser, S., Mädler, B. & Coenen, V. A. Rapid effects of deep brain stimulation for treatment-resistant major depression. *Biological Psychiatry* **73,** 1204–1212 (2013).
424. Headache Classification Committee of the International Headache Society (IHS). The International Classification of Headache Disorders, 3rd edition (beta version). *Cephalalgia* **33,** 629–808 (2013).
425. Black, D. F. & Dodick, D. W. Two cases of medically and surgically intractable SUNCT: a reason for caution and an argument for a central mechanism. *Cephalalgia* **22,** 201–204 (2002).
426. Leone, M. *et al.* Deep brain stimulation to relieve drug-resistant SUNCT. *Ann Neurol.* **57,** 924–927 (2005).
427. Lyons, M. K., Dodick, D. W. & Evidente, V. G. H. Responsiveness of short-lasting unilateral neuralgiform headache with conjunctival injection and tearing to hypothalamic deep brain stimulation. *Journal of Neurosurgery* **110,** 279–281 (2009).
428. Bartsch, T. *et al.* Deep brain stimulation of the posterior hypothalamic area in intractable short-lasting unilateral neuralgiform headache with conjunctival injection and tearing (SUNCT). *Cephalalgia* **31,** 1405–1408 (2011).

429. Lambru, G., Shanahan, P., Watkins, L. & Matharu, M. S. Occipital nerve stimulation in the treatment of medically intractable SUNCT and SUNA. *Pain Physician* **17,** 29–41 (2014).
430. Olesen, J. & Steiner, T. J. The International classification of headache disorders, 2nd edn (ICDH-II). *Journal of Neurology, Neurosurgery & Psychiatry* **75,** 808–811 (2004).
431. Antonaci, F. *et al.* Parenteral indomethacin (the INDOTEST) in cluster headache. *Cephalalgia* **23,** 193–196 (2003).
432. Cohen, A. S. Short-lasting unilateral neuralgiform headache attacks with conjunctival injection and tearing (SUNCT) or cranial autonomic features (SUNA)--a prospective clinical study of SUNCT and SUNA. *Brain* **129,** 2746–2760 (2006).
433. Williams, M. H. & Broadley, S. A. SUNCT and SUNA: clinical features and medical treatment. *J Clin Neurosci* **15,** 526–534 (2008).
434. Levy, M. J. *et al.* Pituitary volume and headache: size is not everything. *Arch Neurol* **61,** 721–725 (2004).
435. Burns, B., Watkins, L. & Goadsby, P. J. Treatment of intractable chronic cluster headache by occipital nerve stimulation in 14 patients. *Neurology* **72,** 341–345 (2009).
436. Smelt, A. F. H., Assendelft, W. J. J., Terwee, C. B., Ferrari, M. D. & Blom, J. W. What is a clinically relevant change on the HIT-6 questionnaire? An estimation in a primary-care population of migraine patients. *Cephalalgia* **34,** 29–36 (2014).
437. May, A., Bahra, A., Büchel, C., Turner, R. & Goadsby, P. J. Functional magnetic resonance imaging in spontaneous attacks of SUNCT: short-lasting neuralgiform headache with conjunctival injection and tearing. *Ann Neurol.* **46,** 791–794 (1999).
438. Bartsch, T. *et al.* Hypothalamic deep brain stimulation for cluster headache: experience from a new multicase series. *Cephalalgia* **28,** 285–295 (2008).
439. Magis, D., Gérardy, P.-Y., Remacle, J.-M. & Schoenen, J. Sustained Effectiveness of Occipital Nerve Stimulation in Drug-Resistant Chronic Cluster Headache. *Headache: The Journal of Head and Face Pain* **51,** 1191–1201 (2011).
440. Solomon, G. D. Evolution of the measurement of quality of life in migraine. *Neurology* **48,** S10–5 (1997).
441. Fontaine, D. *et al.* Safety and efficacy of deep brain stimulation in refractory cluster headache: a randomized placebo-controlled double-blind trial followed by a 1-year open extension. *J Headache Pain* **11,** 23–31 (2009).
442. Chabardes, S. *et al.* Endoventricular Deep Brain Stimulation of the Third Ventricle: Proof of Concept and Application to Cluster Headache. *Neurosurgery* **79,** 806–815 (2016).
443. Büttner-Ennever, J. A., Büttner, U., Cohen, B. & Baumgartner, G. Vertical glaze paralysis and the rostral interstitial nucleus of the medial longitudinal fasciculus. *Brain* **105,** 125–149 (1982).
444. Lipton, R. B., Goadsby, P. J. & Cady, R. K. *PRISM study: occipital nerve stimulation for treatment-refractory migraine*. (…, 2009).
445. Saper, J. R. *et al.* Occipital nerve stimulation for the treatment of intractable chronic migraine headache: ONSTIM feasibility study. *Cephalalgia* **31,** 271–285 (2011).
446. Silberstein, S. D. *et al.* Safety and efficacy of peripheral nerve stimulation of the occipital nerves for the management of chronic migraine: results from a randomized, multicenter, double-blinded, controlled study. *Cephalalgia* **32,** 1165–1179 (2012).
447. Sebastian, S., Schweitzer, D., Tan, L. & Broadley, S. A. Role of trigeminal microvascular decompression in the treatment of SUNCT and SUNA. *Curr Pain Headache Rep* **17,** 332 (2013).
448. Akram, H. *et al.* Ventral tegmental area deep brain stimulation for refractory chronic cluster headache. *Neurology* **86,** 1676–1682 (2016).
449. Fontaine, D., Vandersteen, C., Magis, D. & Lantéri-Minet, M. Neuromodulation in cluster headache. *Adv Tech Stand Neurosurg* **42,** 3–21 (2015).
450. de Tommaso, M. & Vecchio, E. Primary headaches and trigeminal neuralgia: neuropathic pain yes or not? Evidences from neurophysiological procedures. *Expert Rev Neurotherapeutics* **13,** 1031–1039 (2013).
451. Goadsby, P. J. Trigeminal autonomic cephalalgias. *Continuum (Minneap Minn)* **18,** 883–895 (2012).

452. Holle, D. & Obermann, M. Cluster headache and the hypothalamus: causal relationship or epiphenomenon? *Expert Rev Neurotherapeutics* **11,** 1255–1263 (2011).
453. Waldenlind, E. & Sjöstrand, C. Pathophysiology of cluster headache and other trigeminal autonomic cephalalgias. *Handb Clin Neurol* **97,** 389–411 (2010).
454. Holland, P. R. Modulation of trigeminovascular processing: novel insights into primary headache disorders. *Cephalalgia* **29 Suppl 3,** 1–6 (2009).
455. Leone, M. & Bussone, G. Pathophysiology of trigeminal autonomic cephalalgias. *The Lancet Neurology* **8,** 755–764 (2009).
456. Bussone, G. Cluster headache: from treatment to pathophysiology. *Neurol Sci* **29,** 1–6 (2008).
457. Nardone, R. *et al.* Trigemino-cervical reflex abnormalities in patients with migraine and cluster headache. *Headache* **48,** 578–585 (2008).
458. Waldenlind, E., Gustafsson, S. A., Ekbom, K. & Wetterberg, L. Circadian secretion of cortisol and melatonin in cluster headache during active cluster periods and remission. *Journal of Neurology, Neurosurgery & Psychiatry* **50,** 207–213 (1987).
459. Leone, M. & Bussone, G. A review of hormonal findings in cluster headache. Evidence for hypothalamic involvement. *Cephalalgia* **13,** 309–317 (1993).
460. Cutrer, F. M. Functional imaging in primary headache disorders. *Headache* **48,** 704–706 (2008).
461. Goadsby, P. J. & Lipton, R. B. A review of paroxysmal hemicranias, SUNCT syndrome and other short-lasting headaches with autonomic feature, including new cases. *Brain* **120 (Pt 1),** 193–209 (1997).
462. Matharu, M. S. & Zrinzo, L. Deep brain stimulation in cluster headache. *Expert Rev Neurotherapeutics* **11,** 473–475 (2011).
463. Bartsch, T. & Goadsby, P. J. Stimulation of the greater occipital nerve induces increased central excitability of dural afferent input. *Brain* **125,** 1496–1509 (2002).
464. Wolter, T. & Kaube, H. Spinal cord stimulation in cluster headache. *Curr Pain Headache Rep* **17,** 324 (2013).
465. Malick, A., Strassman, R. M. & Burstein, R. Trigeminohypothalamic and reticulohypothalamic tract neurons in the upper cervical spinal cord and caudal medulla of the rat. *Journal of Neurophysiology* **84,** 2078–2112 (2000).
466. Bartsch, T., Levy, M. J., Knight, Y. E. & Goadsby, P. J. Differential modulation of nociceptive dural input to [hypocretin] orexin A and B receptor activation in the posterior hypothalamic area. *PAIN* **109,** 367–378 (2004).
467. Bailey, D. L., Townsend, D. W., Valk, P. E. & Maisey, M. N. *Positron Emission Tomography*. (Springer Science & Business Media, 2006).
468. Sprenger, T. *et al.* Specific hypothalamic activation during a spontaneous cluster headache attack. *Neurology* **62,** 516–517 (2004).
469. Morelli, N. *et al.* Functional magnetic resonance imaging in episodic cluster headache. *J Headache Pain* **10,** 11–14 (2008).
470. Starr, P. A., Barbaro, N. M., Raskin, N. H. & Ostrem, J. L. Chronic stimulation of the posterior hypothalamic region for cluster headache: technique and 1-year results in four patients. *Journal of Neurosurgery* **106,** 999–1005 (2007).
471. May, A. Hypothalamic deep-brain stimulation: target and potential mechanism for the treatment of cluster headache. *Cephalalgia* **28,** 799–803 (2008).
472. Eller, M. & Goadsby, P. J. Trigeminal autonomic cephalalgias. *Oral Dis* **22,** 1–8 (2016).
473. Jürgens, T. P. *et al.* Hypothalamic deep-brain stimulation modulates thermal sensitivity and pain thresholds in cluster headache. *PAIN* 1–7 (2009). doi:10.1016/j.pain.2009.07.006
474. Broggi, G., Franzini, A., Leone, M. & Bussone, G. Update on neurosurgical treatment of chronic trigeminal autonomic cephalalgias and atypical facial pain with deep brain stimulation of posterior hypothalamus: results and comments. *Neurol Sci* **28,** S138–S145 (2007).
475. Bernard, J. F. & Besson, J. M. The spino(trigemino)pontoamygdaloid pathway: electrophysiological evidence for an involvement in pain processes. *Journal of Neurophysiology* **63,** 473–490 (1990).

476. Kannan, H., Osaka, T., Kasai, M., Okuya, S. & Yamashita, H. Electrophysiological properties of neurons in the caudal ventrolateral medulla projecting to the paraventricular nucleus of the hypothalamus in rats. *Brain Research* **376,** 342–350 (1986).
477. Pan, B., Castro-Lopes, J. M. & Coimbra, A. Central afferent pathways conveying nociceptive input to the hypothalamic paraventricular nucleus as revealed by a combination of retrograde labeling and c-fos activation. *J. Comp. Neurol.* **413,** 129–145 (1999).
478. Person, R. J. Somatic and vagal afferent convergence on solitary tract neurons in cat: electrophysiological characteristics. *NSC* **30,** 283–295 (1989).
479. Zhang, X., Fogel, R. & Renehan, W. E. Physiology and morphology of neurons in the dorsal motor nucleus of the vagus and the nucleus of the solitary tract that are sensitive to distension of the small intestine. *J. Comp. Neurol.* **323,** 432–448 (1992).
480. Cechetto, D. F., Standaert, D. G. & Saper, C. B. Spinal and trigeminal dorsal horn projections to the parabrachial nucleus in the rat. *J. Comp. Neurol.* **240,** 153–160 (1985).
481. Saper, C. B. & Loewy, A. D. Efferent connections of the parabrachial nucleus in the rat. *Brain Research* **197,** 291–317 (1980).
482. Slugg, R. M. & Light, A. R. Spinal cord and trigeminal projections to the pontine parabrachial region in the rat as demonstrated with Phaseolus vulgaris leucoagglutinin. *J. Comp. Neurol.* **339,** 49–61 (1994).
483. Menétrey, D. & Basbaum, A. I. Spinal and trigeminal projections to the nucleus of the solitary tract: a possible substrate for somatovisceral and viscerovisceral reflex activation. *J. Comp. Neurol.* **255,** 439–450 (1987).
484. Ricardo, J. A. & Koh, E. T. Anatomical evidence of direct projections from the nucleus of the solitary tract to the hypothalamus, amygdala, and other forebrain structures in the rat. *Brain Research* **153,** 1–26 (1978).
485. Beitz, A. J. The organization of afferent projections to the midbrain periaqueductal gray of the rat. *NSC* **7,** 133–159 (1982).
486. Eberhart, J. A., Morrell, J. I., Krieger, M. S. & Pfaff, D. W. An autoradiographic study of projections ascending from the midbrain central gray, and from the region lateral to it, in the rat. *J. Comp. Neurol.* **241,** 285–310 (1985).
487. Lima, D. & Coimbra, A. Morphological types of spinomesencephalic neurons in the marginal zone (lamina I) of the rat spinal cord, as shown after retrograde labelling with cholera toxin subunit B. *J. Comp. Neurol.* **279,** 327–339 (1989).
488. Liu, R. P. Laminar origins of spinal projection neurons to the periaqueductal gray of the rat. *Brain Research* **264,** 118–122 (1983).
489. Lima, D., Mendes-Ribeiro, J. A. & Coimbra, A. The spino-latero-reticular system of the rat: projections from the superficial dorsal horn and structural characterization of marginal neurons involved. *NSC* **45,** 137–152 (1991).
490. Sawchenko, P. E. & Swanson, L. W. Central noradrenergic pathways for the integration of hypothalamic neuroendocrine and autonomic responses. *Science* **214,** 685–687 (1981).
491. Owen, S. L. F. *et al.* Connectivity of an effective hypothalamic surgical target for cluster headache. *J Clin Neurosci* **14,** 955–960 (2007).
492. Goadsby, P. J. Lacrimation, conjunctival injection, nasal symptoms... cluster headache, migraine and cranial autonomic symptoms in primary headache disorders -- what's new? *Journal of Neurology, Neurosurgery & Psychiatry* **80,** 1057–1058 (2009).
493. May, A. & Goadsby, P. J. The trigeminovascular system in humans: pathophysiologic implications for primary headache syndromes of the neural influences on the cerebral circulation. *J Cereb Blood Flow Metab* **19,** 115–127 (1999).
494. Frese, A., Evers, S. & May, A. Autonomic activation in experimental trigeminal pain. *Cephalalgia* **23,** 67–68 (2003).
495. Goadsby, P. J. & Hoskin, K. L. The distribution of trigeminovascular afferents in the nonhuman primate brain Macaca nemestrina: a c-fos immunocytochemical study. *J. Anat.* **190 (Pt 3),** 367–375 (1997).

496. Knight, Y. E. *et al.* Patterns of fos expression in the rostral medulla and caudal pons evoked by noxious craniovascular stimulation and periaqueductal gray stimulation in the cat. *Brain Research* **1045,** 1–11 (2005).
497. Goadsby, P. J., Lambert, G. A. & Lance, J. W. Effects of locus coeruleus stimulation on carotid vascular resistance in the cat. *Brain Research* **278,** 175–183 (1983).
498. Goadsby, P. J. Pathophysiology of cluster headache: a trigeminal autonomic cephalgia. *The Lancet Neurology* **1,** 251–257 (2002).
499. Lipton, R. B. *et al.* Guidelines for controlled trials of drugs in cluster headache. *Cephalalgia* **15,** 452–462 (1995).
500. Little, S. *et al.* Bilateral adaptive deep brain stimulation is effective in Parkinson's disease. *Journal of Neurology, Neurosurgery & Psychiatry* **87,** 717–721 (2016).
501. Little, S. *et al.* Adaptive deep brain stimulation for Parkinson's disease demonstrates reduced speech side effects compared to conventional stimulation in the acute setting. *Journal of Neurology, Neurosurgery & Psychiatry* **87,** jnnp–2016–313518–1389 (2016).
502. Åström, M., Lemaire, J.-J. & Wårdell, K. Influence of heterogeneous and anisotropic tissue conductivity on electric field distribution in deep brain stimulation. *Med Biol Eng Comput* **50,** 23–32 (2012).
503. Marcus, D. S. *et al.* Informatics and data mining tools and strategies for the human connectome project. *Front Neuroinform* **5,** 4 (2011).
504. Schrouff, J. *et al.* PRoNTo: pattern recognition for neuroimaging toolbox. *Neuroinformatics* **11,** 319–337 (2013).